



HAL
open science

Experimental investigation of the phase diagram of ammonia monohydrate at high pressure and temperature

Haiwa Zhang

► **To cite this version:**

Haiwa Zhang. Experimental investigation of the phase diagram of ammonia monohydrate at high pressure and temperature. Materials Science [cond-mat.mtrl-sci]. Sorbonne Université, 2019. English. NNT : 2019SORUS410 . tel-03459424

HAL Id: tel-03459424

<https://theses.hal.science/tel-03459424>

Submitted on 1 Dec 2021

HAL is a multi-disciplinary open access archive for the deposit and dissemination of scientific research documents, whether they are published or not. The documents may come from teaching and research institutions in France or abroad, or from public or private research centers.

L'archive ouverte pluridisciplinaire **HAL**, est destinée au dépôt et à la diffusion de documents scientifiques de niveau recherche, publiés ou non, émanant des établissements d'enseignement et de recherche français ou étrangers, des laboratoires publics ou privés.

Sorbonne Université

Ecole doctorale 397 Physique et Chimie des Matériaux

Laboratoire: Institut de minéralogie, de physique des matériaux et de cosmochimie

Experimental investigation of the phase diagram of ammonia monohydrate at high pressure and temperature

Par Haiwa ZHANG

Thèse de doctorat en Science des Matériaux

Dirigée par Frédéric DATCHI

Présentée et soutenue publiquement le 29 Novembre 2019

Devant un jury composé de:

Mme Agnès DEWAELE	Ingénieur-Chercheur, CEA	Rapporteur
M. Volodymyr SVITLYK	Scientifique de ligne, ESRF	Rapporteur
M. Frédéric DECREMPS	Professeur, Sorbonne Université	Examineur
M. Jean-Paul ITIÉ	Directeur de Recherche, CNRS	Examineur
M. Frédéric DATCHI	Directeur de Recherche CNRS	Directeur de thèse
Mme Sandra NINET	Maître de Conférences, Sorbonne Université	Encadrant de thèse

Acknowledgments

Upon finishing this thesis, I would like to express my great gratitude towards all those who have offered me sincere assistance in the four years.

First and foremost, I want to extend my heartfelt gratitude to my supervisor, Professor Frédéric DATCHI, whose patient guidance, valuable suggestions and constant encouragement make me complete this thesis. His conscientious academic spirit inspires me in academic study. The experience and profit I obtained will be of grand importance to my further studies.

I would also like to express my sincere gratitude to Professor Sandra NINET. She has provided a lot of help in my experiments and data analysis. In the preparation of this thesis, she has spent much time correcting my thesis and provided me with inspiring advice.

I would also like to thank several friends of the same research group: Jean-Antoine QUEYROUX, Guozhao ZHANG and Leon ANDRIAMBARIJAONA. They gave me a lot of help and support in my experiments and life.

My thanks also go to Professor Stefan KLOTZ and Livia BOVE who provide support and advice in QENS experiments.

In the past four years, I have met many people who have provided me with selfless help, too many to name individually, and I would like to thank them all as well. I would like to thank all the staff of IMPMC for the help in my work and life. I would also like to thank the technical staff at ESRF, SOLEIL and ILL who have all helped in the data collection process at various different experiments over the years.

Also, I owe many thanks to the China Scholarship Council for financial support. Without their funding, I would not successfully complete my P.hD, and I am very grateful.

Last but not least, I am deeply indebted to my family and friends, who have helped me and shared with me my worries, frustrations, and happiness.

Abstract

This thesis in experimental physics investigates the phase diagram of ammonia monohydrate (AMH) at high pressure ($0 < P < 70$ GPa) and temperature ($300 < T < 800$ K). AMH is a solid compound formed of equal amounts of water (H_2O) and ammonia (NH_3). Its study under extreme P-T conditions is of great interest for the understanding and modeling of planetary interiors of giant icy planets and satellites, as well as for the understanding of density effects on hydrogen bonds. In this work, we mainly use x-ray diffraction and Raman spectroscopy to study the stable solid phases as a function of pressure and temperature. We evidence a partial ionization of the compound above 7.4 GPa at 300 K, and the existence of two new phases, AMH-VII and VIII, stable at high T. The solid-solid and solid-liquid transition lines are disclosed. The plastic nature of phase VII is demonstrated by quasi-elastic neutron scattering. The superionic nature of the solid at high P-T is suggested by the measured evolution of the infrared spectra.

Keywords: water-ammonia system; extreme condition; phase diagram; ionization; plastic solid; superionic solid

Contents

Acknowledgments	i
Abstract.....	ii
Contents.....	iii
Introduction	1
Chapter 1: Water, ammonia and ammonia hydrates: State of the art.....	3
Contents	3
1.1 Introduction.....	5
1.2 The Hydrogen Bond.....	5
1.3 The ammonia-water system in icy bodies of our solar system	7
1.3.1 The evidence of ammonia-water system in icy bodies of our solar system.....	7
1.3.2 Interior models of Uranus and Neptune	8
1.4 Water ice.....	9
1.4.1 The water molecule	9
1.4.2 The phase diagram of water	10
1.4.2.1 Ice VII and VII'	11
1.4.2.2 Ice X	12
1.4.2.3 Plastic ice VII	12
1.4.2.4 Superionic ice	13
1.5 Ammonia ice	14
1.5.1 The ammonia molecule	14
1.5.2 The phase diagram of ammonia	15
1.5.2.1 Phase I	15
1.5.2.2 Phase II.....	16
1.5.2.3 Phase III.....	16

1.5.2.4 Phase IV and V	16
1.5.2.5 The ionic β phase	17
1.5.2.6 Superionic ammonia.....	18
1.6 The ammonia-water system	18
1.6.1 The phase diagram of ammonia monohydrate	19
1.6.1.1 AMH I	19
1.6.1.2 AMH-II.....	20
1.6.1.3 AMH-V.....	20
1.6.1.4 AMH-VI	21
1.6.1.5 Theoretical ionic and superionic structures.....	23
1.6.1.6 Melting curve of ammonia monohydrate	25
1.6.2 The phase diagram of ammonia dihydrate	25
1.6.2.1 Experimental phase diagram	26
1.6.2.2 Theoretical predictions	26
1.6.3 The phase diagram of ammonia hemihydrate	28
1.6.3.1 Experimental phase diagram	28
1.6.3.2 Theoretical predictions	30
1.7 Conclusions and aims of the thesis work	30
References	32
Chapter 2: Experimental methods.....	37
Contents	37
2.1 Introduction.....	38
2.2 High-pressure and high-temperature device	38
2.2.1 The diamond anvil cell.....	38
2.2.2 High temperature experiments in the DAC.....	39
2.3 Measuring the sample pressure in the DAC.....	40
2.3.1 Luminescent sensors	40
2.3.1.1 Ruby	40
2.3.1.2 Samarium-doped strontium tetraborate.....	42
2.3.2 The diamond Raman gauge.....	43

2.3.3 Pressure measurement by x-ray diffraction.....	44
2.4 Sample preparation and loading.....	45
2.4.1 Sample preparation.....	45
2.4.2 Loading the sample	46
2.5 Analytical techniques	47
2.5.1 X-ray diffraction.....	47
2.5.1.1 Principle of powder x-ray diffraction.....	47
2.5.1.2 X-ray diffraction setups.....	48
2.5.2 Optical vibrational spectroscopies	49
2.5.2.1 Principle of Raman spectroscopy	49
2.5.2.2 Raman spectroscopy setup	51
2.5.2.3 Principle of infrared spectroscopy.....	51
2.5.2.4 Infrared spectroscopy setups	52
2.5.3 Quasi-elastic incoherent neutron scattering	52
2.5.3.1 Basic principles	53
2.5.3.2 Experimental methods for high-pressure QENS experiments	59
References	62

Chapter 3: Observation of a disordered ionic-molecular alloy in ammonia monohydrate 65

Contents	65
3.1 Introduction.....	66
3.2 Experimental methods.....	66
3.3 Results.....	66
3.3.1 Ionisation at mild pressure	66
3.3.2 Evolution of the IR spectra with pressure.....	68
3.3.3 X-ray and neutron diffraction results	71
3.3.3.1 Equation of state of AMH at 300 K.....	74
3.3.3.2 Ionic-molecular transition on decompression	75
3.3.4 The disordered ionic-molecular crystal.....	76
3.4 Conclusions.....	80
References	82

Chapter 4: Melting curve of ammonia monohydrate	84
Contents	84
4.1 Introduction	85
4.2 Experimental protocol.....	85
4.3 Results.....	86
4.3.1 Observation and characterization of the non-congruent melting line ($T < 324$ K).....	87
4.3.2 Observation and characterization of the congruent melting line ($T > 324$ K)	89
4.4 Discussion	93
4.4.1 Comparison with literature.....	93
4.4.2 Comparison with pure water and ammonia	94
4.5 Conclusions.....	96
References.....	97
Chapter 5: A plastic solid phase of ammonia hydrate at high P-T.....	98
Contents	98
5.1 Introduction.....	99
5.2 Structure of AMH-phase VII.....	99
5.3 Stability field of AMH-VII below 10 GPa.....	103
5.4 Evidence for the plastic nature of AMH-VII.....	104
5.4.1 Similitudes with the plastic phases of NH_3 and H_2O	104
5.4.2 QENS experiments.....	105
5.4.2.1 Experimental protocol.....	105
5.4.2.2 Results	107
5.5 Conclusions.....	116
References.....	117
Chapter 6: High pressure-temperature phase diagram of AMH	118
Contents	118
6.1 Introduction.....	119
6.2 Overview of the high P-T phase diagram	119
6.3 Evolution of AMH-VI (DIMA+P4/nmm) at high temperature.....	121

6.3.1 Evolution below 18 GPa	122
6.3.2 Evolution above 18 GPa.....	126
6.4 Cooling and compression of AMH-VII.....	128
6.4.1 Formation of AMH-VIII	129
6.4.2 Structure of AMH-VIII	131
6.4.3 Raman spectra of AMH-VIII	136
6.4.4 Transition line between AMH-VII and VIII.....	137
6.4.5 Stability range of AMH-VIII.....	138
6.5 Stability of the DIMA phase above 18 GPa	139
6.6 Stability of AMH-VII at high pressure and high temperature.....	142
6.7 Signature of superionicity in AMH-VII?	144
6.8 Conclusions	148
References	150
Conclusions	151
References	154
Résumé en français de la thèse	155

Introduction

Water, ammonia and methane are considered major components of the interiors of the giant icy planets Neptune and Uranus and their satellites, the icy satellites of Saturn (Titan, Enceladus) and Jupiter (Ganymede), and of the “Ocean” exoplanets recently discovered. Present models of the interior of Neptune and Uranus assume the existence of a thick layer composed of these ices submitted to extreme conditions of pressure (20-700 GPa) and temperature (2000-6000 K). Knowing the physical and chemical state and the behavior of these compounds over a large range of pressure and temperature is therefore needed to build robust interior models which can be compared to observations such as the magnetic field, the gravitational moments and the atmospheric composition, collected from Earth or from space missions.

Additionally, from a fundamental perspective, the simple molecular ices water and ammonia and their mixtures are the simplest systems containing hydrogen (H) bonds that bind these molecules together. Hydrogen bonds are found in many other, more complex substances, such as DNA, and largely affect their properties. Therefore, studying the evolution of hydrogen bonds of simple ices as a function of pressure and temperature should help understand the properties of H-bonded systems from a microscopic point of view.

In the past few decades, the high pressure and temperature (up to about 200 GPa and 2500 K) properties of the pure ice compounds have been the focus of many investigations, which have revealed a rich polymorphism and several “exotic” solid phases, such as superionic water and ammonia, ionic ammonia and the symmetric phase of water. By contrast, the study of their mixtures has remained limited to modest pressures, mostly below 10 GPa, and low temperatures, below 300 K. This is somehow surprising as these mixtures are more realistic planetary “minerals” than the pure systems. Moreover, these mixtures are the simplest solids which bind through the heteronuclear H-bonds $\text{O-H}\cdots\text{N}$ and $\text{N-H}\cdots\text{O}$ of utmost importance in proteins.

The ammonia-water system may crystallize in three different hydrates, depending on the concentration: ammonia dihydrate, with a (1:2) ammonia-water ratio, ammonia monohydrate (1:1) and ammonia hemihydrate (2:1). At the start of this thesis, the phase diagrams of these hydrates had been investigated up to about 9 GPa and at temperatures 100-300 K, mostly by neutron diffraction methods. The purpose of this thesis has been to extend the experimental exploration of the high-pressure and high-temperature phases and properties of ammonia monohydrate (AMH) to higher pressures and temperatures. The motivations behind this work will be exposed in **Chapter 1**, followed by the presentation of the state-of-the-art knowledge on the high P-T phase diagrams of water, ammonia and ammonia hydrates.

In **Chapter 2**, the experimental methods used in the present work will be exposed. This includes the presentation of the high-pressure and high-temperature apparatuses, the procedures for sample loading, the P-T metrologies and the sample characterization techniques.

Chapter 3 will present our investigations of solid AMH at room and low temperature. We will show that a partial ionization occurs in the solid phase of AMH previously described as a

disordered molecular alloy. This ionization results from proton transfer between ammonia and water and are observed at moderate pressure, 7.4 GPa, compared to pure ices.

Chapter 4 relates to our study of the melting properties of AMH. We will see in particular that melting evolves from non-congruent to congruent, and discloses the existence of a new high-temperature phase of AMH called AMH-VII.

Chapter 5 focusses on the nature and properties of AMH-VII below 10 GPa. We show in particular, using high pressure quasi-elastic incoherent neutron scattering, that phase VII is a plastic solid.

Chapter 6 presents the results of our investigations of the solid phase diagram of AMH at high P-T, up to 70 GPa and 760 K. The building of this phase diagram turned out to be a rather complex task, as different phases can be observed at the same P-T condition depending on the followed thermodynamic path. We will describe the information gathered for all the observed phases and the transition lines separating them.

Chapter 1: Water, ammonia and ammonia hydrates: State of the art

Contents

1.1 Introduction.....	5
1.2 The Hydrogen Bond.....	5
1.3 The ammonia-water system in icy bodies of our solar system	7
1.3.1 The evidence of ammonia-water system in icy bodies of our solar system.....	7
1.3.2 Interior models of Uranus and Neptune	8
1.4 Water ice.....	9
1.4.1 The water molecule	9
1.4.2 The phase diagram of water	10
1.4.2.1 Ice VII and VII'	11
1.4.2.2 Ice X	12
1.4.2.3 Plastic ice VII	12
1.4.2.4 Superionic ice	13
1.5 Ammonia ice	14
1.5.1 The ammonia molecule	14
1.5.2 The phase diagram of ammonia	15
1.5.2.1 Phase I	15
1.5.2.2 Phase II.....	16
1.5.2.3 Phase III.....	16
1.5.2.4 Phase IV and V	16
1.5.2.5 The ionic β phase	17
1.5.2.6 Superionic ammonia.....	18
1.6 The ammonia-water system	18
1.6.1 The phase diagram of ammonia monohydrate	19
1.6.1.1 AMH I	19
1.6.1.2 AMH-II.....	20

1.6.1.3 AMH-V.....	20
1.6.1.4 AMH-VI	21
1.6.1.5 Theoretical ionic and superionic structures.....	23
1.6.1.6 Melting curve of ammonia monohydrate	25
1.6.2 The phase diagram of ammonia dihydrate	25
1.6.2.1 Experimental phase diagram	26
1.6.2.2 Theoretical predictions	26
1.6.3 The phase diagram of ammonia hemihydrate	28
1.6.3.1 Experimental phase diagram	28
1.6.3.2 Theoretical predictions	30
1.7 Conclusions and aims of the thesis work	30
References	32

1.1 Introduction

As stated in the Introduction, the present thesis focusses on the properties of the $\text{NH}_3\text{-H}_2\text{O}$ system at high pressure and temperature, and more specifically on the solid forms of ammonia monohydrate (AMH). There are two main scientific motivations driving the research on the $\text{NH}_3\text{-H}_2\text{O}$ system. The first is microscopic, and relates to the force that binds these molecules together, the hydrogen bond. The second is macroscopic, and relates to the role these solids play as the building blocks of planets and moons in the outer solar system.

In this chapter, we present in more detail the motivation behind this work, by describing, first, the nature and importance of the hydrogen bond, and second, the evidence and role of the ammonia-water system in icy planetary bodies of the solar system. We then proceed by presenting the state-of-art knowledge on the phase diagrams of water, ammonia and ammonia hydrates. The conclusions and aims of the present work will be presented in the final part.

1.2 The Hydrogen Bond

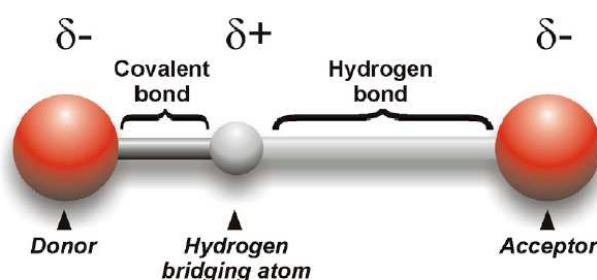


Figure 1.1. Cartoon illustration of a hydrogen bond. The δ^- and δ^+ denote small electrical charges that occur in the formation of the bond. The arrangement is written as $X\text{-H}\cdots Y$, where $X\text{-H}$ is a strong covalent bond and $\text{H}\cdots Y$ is the hydrogen bond. The hydrogen bond (noted H-bond), also called the hydrogen bridge, is a primarily electrostatic interaction between a hydrogen atom which is covalently bound to a more electronegative atom or group, and another electronegative atom bearing a lone pair of electrons^[1] as illustrated in Figure 1.1. The covalent bond length is typically 0.97-1.03 Å and the H-bond length is typically 1.75-2.50 Å^[2]. H-bonds can be intermolecular (occurring between separate molecules, as for example two HF molecules) or intramolecular (occurring among parts of the same molecule, like in 2-Nitrophenol).

The H-bond strength is intermediate between the weaker Van der Waals force (less than 5 kJ/mol) and the much stronger covalent and ionic bonds (in the range of 500-1000 kJ/mol). Depending on the nature of the donor (X) and acceptor (Y) atoms which constitute the bond, their geometry, and environment, hydrogen bonds can vary in strength from weak (1–2 kJ/mol) to strong (100-150 kJ/mol) and most of them are between 25 to 40 kJ/mol^[3]. The average strength of hydrogen bonds between water molecules is about 21 kJ/mol, while that between ammonia molecules is about 13 kJ/mol.

The existence of H-bonds affects many properties of matter, such as the melting and boiling points, the solubility, the viscosity, the density and the structure. For example, the larger strength of H-bonds in water compared to those in ammonia has for consequence that water has a higher melting point (MP=273.15 K) and boiling point (BP=373.15 K) than ammonia (MP = 195.41 K, BP = 239.82 K). Likewise, the MP and BP of both water and ammonia are much higher than those of methane (MP = 90.70 K, BP = 111.67 K), which is not hydrogen bonded.

There are many substances capable of forming hydrogen bonds, such as water, hydrates, amines, inorganic acids, and certain organic compounds. This thesis is only concerned with the two kinds of hydrogen bonds and two donor/acceptor species which are found in the ammonia-water system. These species are nitrogen and oxygen, and the H-bond types are homonuclear (O-H \cdots O and N-H \cdots N) and heteronuclear (O-H \cdots N and N-H \cdots O).

These four intermolecular H-bonds, O-H \cdots O, O-H \cdots N, N-H \cdots O, and N-H \cdots N, are arguably among the most important in chemistry. Indeed, the properties of the most abundant liquid at the Earth's surface, the 'universal solvent,' water, are determined by the O-H \cdots O hydrogen bond. Without it, life as we know it would be impossible; its melting and boiling points would be more than 200 K lower. The remaining three hydrogen bonds (O-H \cdots N, N-H \cdots O, and N-H \cdots N) play a central role in biology too. Hydrogen bonds between the amine and hydroxyl groups form the scaffolding that holds proteins and enzymes in shape (Figs. 1.2, right). Such hydrogen bonds also link together the nucleic acid base pairs in DNA and RNA (Fig. 1.2, left). Without the N-H \cdots O bond, there would be no genetics.

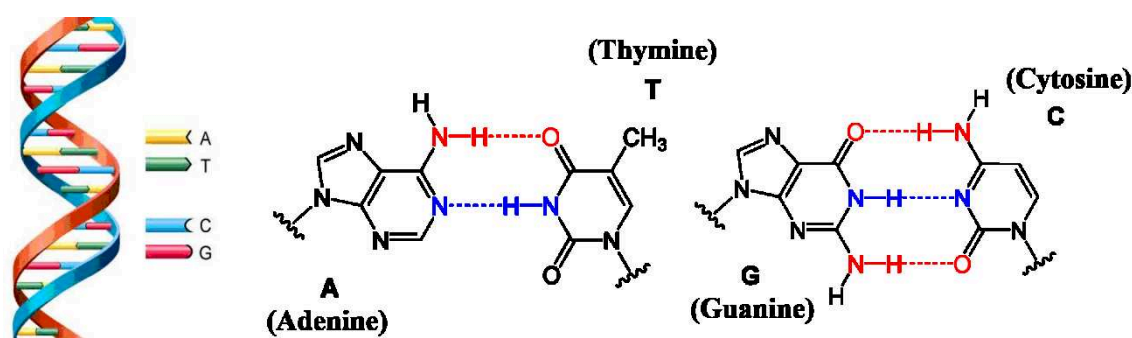


Figure 1.2. Left: Double helix structure of DNA; Right: illustration of hydrogen bonds in DNA.

Solids in the ammonia-water system are the simplest hydrogen bonded solids known. And yet there is a richness of bond types and polymorphism belied by that apparent simplicity. In the end member phases, one finds homonuclear hydrogen bonds (i.e., O-H \cdots O and N-H \cdots N) of differing strengths; in water ice they are strong (~ 20 kJ mol $^{-1}$), in ammonia they are weak (< 10 kJ mol $^{-1}$). In the ammonia hydrates, one finds both homo- and heteronuclear hydrogen bonds (O-H \cdots N and/or N-H \cdots O). Furthermore, in the polymorphs of water and ammonia, one encounters a range of hydrogen bond geometries, from almost perfectly linear (ice VIII: O-H \cdots O $\approx 180^\circ$) to highly strained (ice II: O-H \cdots O = $166^\circ - 178^\circ$).

Under high pressures, hydrogen bonds change their character, usually becoming stronger, such that the bridging hydrogen moves further away from the donor. This process can lead to the symmetrization of the H-bond, where the proton is located midway between the donor and acceptor atoms, as is the case in pure water ice^[4]. Due to the low mass of the hydrogen atom, this process is controlled by quantum phenomena such as tunneling, and so the observation of hydrogen bond centering is a sensitive test of the quantum mechanical theory. More generally, high pressure studies have proven to be a valuable tool in the understanding of H-bonds as it allows one to study them in a single compound as a function of density, and thus variable bond length, while the other parameters remain fixed, avoiding the complexity introduced by the change of chemistry.

1.3 The ammonia-water system in icy bodies of our solar system

1.3.1 The evidence of ammonia-water system in icy bodies of our solar system

The gas giant planets of the outer solar system, Jupiter, Saturn, Uranus and Neptune, are each accompanied by a cortege of satellites that contain a significant component of condensed volatiles, dominantly water ice. We know this because the spectroscopic signature of water ice dominates their surfaces^[5], and because of their low bulk density ($\sim 1000\text{-}1500 \text{ kg m}^{-3}$) as determined from observations of their orbital motions (e.g., Jacobson, 2003^[6,7]). These icy moons range in diameter from a few kilometers across to over 5200 km (larger than the planet Mercury). In addition, icy bodies of varying sizes dominate the outer reaches of the solar system beyond Neptune.

Models of the protosolar nebula (PSN) which gave birth to the solar system^[8,9] indicate that nitrogen in the form of ammonia would be an important condensate in the outer PSN, becoming incorporated into icy planet mantles and leading to low temperature melting and cryovolcanism. For carbon and nitrogen, the two gas phases reaction which govern the oxidation state of the most abundant species in a medium dominated by hydrogen gas are:



Under conditions of equilibrium in the outer PSN, the stable compounds will be the products of reactions (1.1) and (1.2), CH_4 , H_2O and NH_3 .

The model predicts a large inventory of ammonia in Titan's interior, $18 \pm 6 \text{ wt}\% NH_3$ ^[10]. A proportion of this NH_3 will have been outgassed during the latter stages of Titan's accretion and during differentiation of the interior. The outgassed NH_3 is thought to have been converted to N_2 by photolysis, radiolysis and thermolytic destruction in meteorite impacts^[11-14]. This is the ultimate source of Titan's present N_2 atmosphere.

Although ammonia hydrates have not been directly observed, there is some circumstantial evidence for their presence. Most of the icy satellites show signs of endogenic activity that are not consistent with the pure water ice mantle and the expected thermal history^[15]. However, it is worth noting that the lowering of the solidus by incorporation of ammonia can reduce the

heat flow required and increase the time available for endogenous activity. The potential for continuous cryovolcanic activity on Enceladus seems to require the presence of a cosmically sufficient antifreeze, such as ammonia^[16]. Ammonia was indeed detected in the water-rich plumes of Enceladus by the Cassini mission^[17,18]. In addition, there are lobate units on several icy bodies which are interpreted as cryovolcanic lava flows of high viscosity which have a morphology consistent with the known rheological properties of ammonia-water slurries^[19,20]. Although other candidate components (like methanol or formaldehyde) produce viscous solutions, they may be not sufficiently abundant enough. Only ammonia is cosmically abundant enough to explain the observed flow morphologies^[21].

These circumstantial shreds of evidence suggest that a significant amount of ammonia (circa 5-15 wt%) exists on giant icy planets and their satellites. Therefore, undertaking the models of the internal structure of giant icy planets and their satellites requires detailed knowledge of the physical properties of the ammonia-water system.

1.3.2 Interior models of Uranus and Neptune

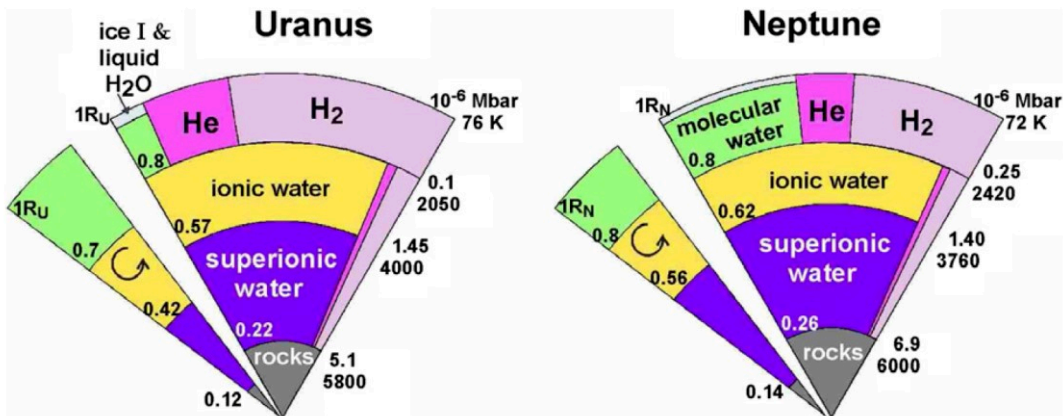


Figure 1.3. Interior models of Uranus and Neptune after Redmer et al^[22].

Although the interior structures of Uranus and Neptune are still poorly constrained, different models of the interior structure have been proposed based on their masses, radii, magnetic and gravitational fields measured by Voyager 2^[23]. The most widespread model assumes a three-layer structure^[18], schematically represented in Figure 1.3, composed of a rocky core, an icy mantle mostly composed of water with some addition of ammonia, methane and heavier hydrocarbons, and a light atmosphere mostly composed of hydrogen and helium. Based on computer simulations and experimental results, the thick intermediate layer of ices is expected to undergo a series of changes with increasing pressure and temperature. Going down from the surface to the core, water would be found as a molecular solid, a molecular liquid, an ionic liquid and finally a superionic solid^[22].

One of the most intriguing observations made by Voyager 2 is the very different magnetic field of Uranus and Neptune compared to the other planets of the solar system, including the gas giants Jupiter and Saturn. Indeed, Neptune and Uranus are the only planets for which the

magnetic field present large non-dipolar contributions. Moreover, the magnetic axis of these planets exhibits a large tilt from the rotation axis (by 59° in Uranus and 47° in Neptune) and does not pass through the center of the planets. As shown by Stanley & Boxham^[24], the origin of these unusual non-dipolar, non-axisymmetric magnetic fields may come from the convection of a thin shell of conductive material surrounding a non-convective but conductive layer. Comparing with the interior structure shown in Figure 1.3, it may be assumed that the convective and conductive thin shell is composed of ionic water, while the non-convective and conductive shell is superionic ice.

1.4 Water ice

1.4.1 The water molecule

The water molecule (H_2O) consists of one oxygen atom and two hydrogen atoms with an O-H covalent bond length of 0.97 \AA and a $\angle\text{H-O-H}$ bond angle of 104.5° . The free molecule is of symmetry C_{2v} and has three modes of vibration shown in Figure 1.4. The frequencies of these vibrations and their activities are listed in Table 1.1. The heterogeneous distribution of electrons in the H_2O molecule causes polarization of the molecule with a large dipole moment (1.85 D) which promotes water molecules to combine with each other to form hydrogen bonds. In the crystal structure, it is these hydrogen bonds that allow the water molecules to be arranged into a tetrahedron. These tetrahedra follow the Bernal-Fowler ice rules^[25]: each oxygen is bonded to two hydrogens via a covalent bond (O-H) and to another two hydrogens of the other two water molecules by a hydrogen bond (O \cdots H). Each hydrogen bond must have only one proton and there is one water molecule in the center of the tetrahedron.

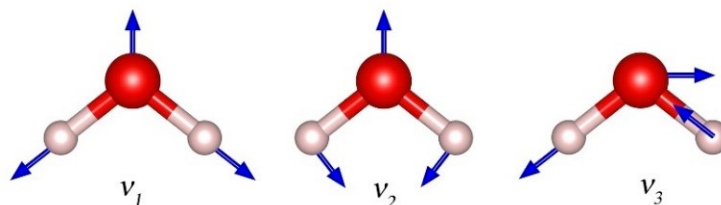


Figure 1.4. The three vibration modes of water. v_1 represents the symmetrical stretching vibration; v_2 represents the torsional vibration; v_3 represents the asymmetric stretching vibration.

Table 1.1. Activities and frequencies of the vibration modes of the free water molecule from Shimanouchi (1980)^[26]. R for Raman and IR for infrared.

Model	Frequency(cm ⁻¹)	Activity
v ₁	3652	R and IR
v ₂	1595	R and IR
v ₃	3756	R and IR

There may be several arrangements of water molecules fulfilling these rules, which is at the origin of the many ice polymorphs, as seen in the phase diagram of water presented in Figure 1.5. When these rules are not obeyed, for example, due to thermal agitation, localized ionic defects appear, called Bjerrum defects^[27]. These may be of two types: L-type, when no proton lies along the H-bond, or D-type, when there are two protons along the H-Bond^[28].

1.4.2 The phase diagram of water

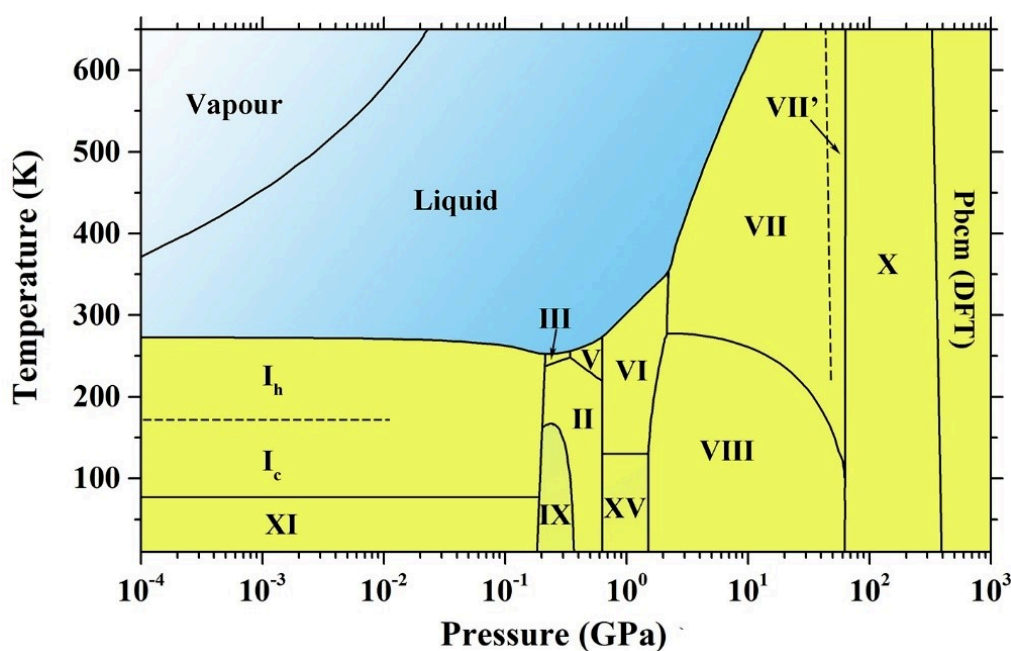


Figure 1.5. The phase diagram of water.

Water is present in more than seventeen crystalline and several amorphous ice structures which have been the subject of extensive research for decades^[29-31], as shown in Figure 1.5. The different solid phases can be divided into four major groups:

- The first group comprises structures with ordered hydrogen atoms. These include ices II, VIII, IX, XI, XIII and XIV. All these forms are found at low temperatures;
- The second group comprises structures with disordered proton positions. These include ices I_h, I_c, III, IV, V, VI, VII, VII' and XII;

-
- (c) The third group is composed of amorphous forms of ice, found at low temperature. There is no long-range order in these phases, which differ from each other by their density and local molecular arrangement.
 - (d) The fourth group is formed by non-molecular structures of ice. This group contains ice X and superionic ice, for which the description in terms of water molecules is no longer relevant.

Among these phases, some are metastable, like Ic, IV, IX and XIII. We will not elaborate on every phase here, but only on phases VII, X and superionic which are relevant to this thesis work.

1.4.2.1 Ice VII and VII'

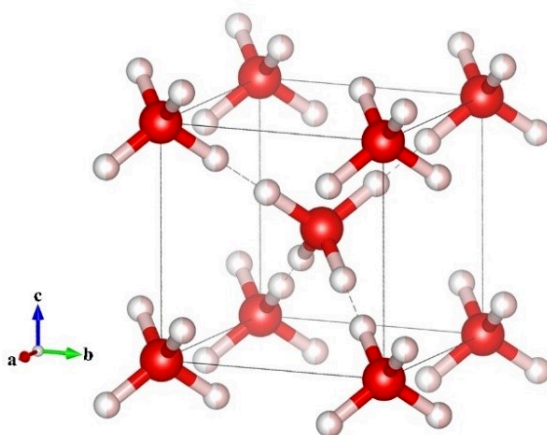


Figure 1.6. The schematic representation of ice VII. Red and light pink spheres designate oxygen and hydrogen atoms respectively and the dashed lines correspond to the hydrogen bonds. Ice VII is hydrogen disordered with oxygen on a bcc lattice and only 50% of H sites are occupied.

Ice VII was discovered by Bridgman in 1937^[32] by compressing ice VI above 2.2 GPa at ambient temperature. Ice VII also directly crystallizes from the liquid at temperatures above the L-VI-VII triple point (2.17 GPa, 355 K). Ice VII is a proton disordered phase, it crystallizes in the cubic space group $Pn-3m$ with O at $(1/4, 1/4, 1/4)$, and H at $(0.41, 0.41, 0.41)$ with site occupancy 0.5^[33]. The structure representation of ice VII is shown in Figure 1.6. The average structure has oxygen atoms on the body-centered cubic (*bcc*) lattice and twice as many H sites as hydrogen atoms available. It consists of two interpenetrating cubic ice lattices with hydrogen bonds passing through the center of the water hexamers and no connecting hydrogen bonds between the interpenetrating lattices. H-bond orientations are thought to be random but subject to the ice rules.

The evolution of the O-H \cdots O hydrogen bond in ice VII as a function of pressure has been extensively studied, in particular by spectroscopic methods. When the pressure is increased, the vibration frequency of the stretching mode O-H in ice VII decreases significantly^[34-36]. This indicates that the covalent bond elongates due to the displacement of the protons along the H junction. The potential seen by the proton can be modeled by a double Morse potential, as

represented in Figure 1.7^[4]. At low pressure, the proton is localized in one of the wells of the potential and the energy barrier separating the two wells is large. With increasing pressure, the energy barrier lowers and beyond ca. 60 GPa, becomes of the same order of magnitude as the zero-point energy of the proton so that the proton can tunnel from one well to the other. Ice VII then enters a state of translational dynamic disorder denoted ice VII'^[34-36].

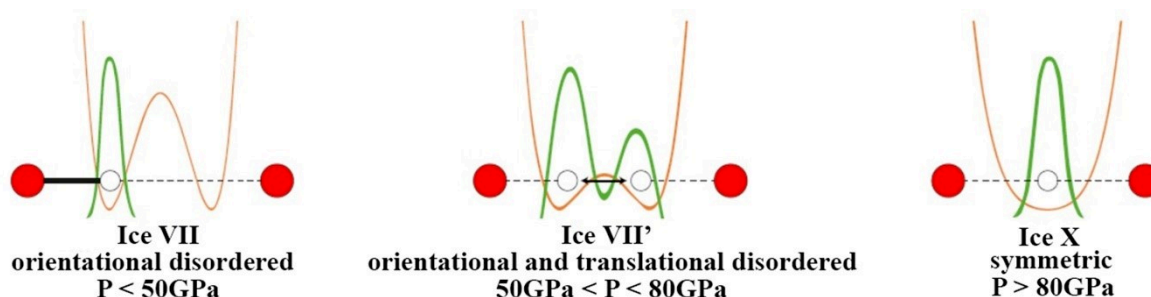


Figure 1.7. Double Morse potential for the proton in ice VII (left), VII' (middle) and X (right).

1.4.2.2 Ice X

Ice X, the so-called symmetric ice, is formed above 80 GPa, when the energy barrier of the double-Morse potential vanishes and the latter only presents a single well located in the middle of the O \cdots O link. The space group of ice X is the same as ice VII, $Pn-3m$, but the molecular character is lost and the structure (depicted in Figure 1.8) can be described as a lattice of O²⁻ and H⁺ ions. DFT calculations predict that ice X is stable up to about 400 GPa^[37], and then transits into another symmetric structure of orthorhombic symmetry^[38,39].

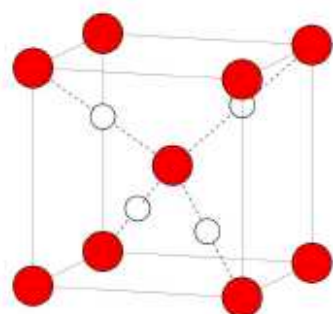


Figure 1.8. Representation of the ice X structure. Red and white balls are oxygen and hydrogen atoms, respectively.

1.4.2.3 Plastic ice VII

Recent theoretical calculations on water have predicted that a plastic form of ice VII exists in the vicinity of the melting line of ice-VII^[36-39]. Plastic solids are molecular crystals where the molecules have a dynamic orientational disorder. In plastic ice VII, the center of mass of the water molecules are located on a bcc lattice-like ice-VII, but the molecules may easily rotate around their center of mass. This phase was initially predicted by classical molecular dynamics (MD) simulations^[40-42] but was also recently observed in a study using *ab initio* MD simulations^[43]. The stability field determined in the latter work is shown in green color in the phase diagram of Figure 1.9. This plastic form of ice still awaits experimental confirmation.

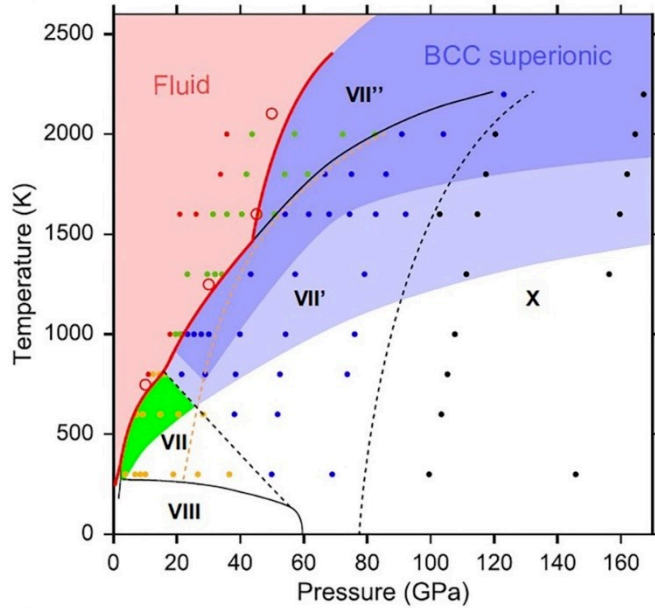


Figure 1.9. The phase diagram of water at high pressure and temperature after Ref. [44].

1.4.2.4 Superionic ice

Superionic solids are solids which present a very high ionic conductivity, in the same range as ionic liquids (the minimal value for ionic conductivity in a superionic solid is arbitrarily set at 0.1 S/cm). This ionic conductivity originates from the rapid diffusion of one ionic species through the crystal lattice. The historical examples are AgI and PbF₂, which transits at high T and ambient P to a superionic phase, where Ag and F are the diffusive species, respectively.

Superionic conduction was largely unexpected in molecular solids. However, the pioneer *ab-initio* simulations of Cavazzoni *et al* in 1999^[45] predicted that water (and, as we will see later on, also ammonia) underwent a transition to a superionic phase at high pressures (P~60 GPa) and high temperatures (T~1500 K), with large ionic conductivity values (in the range of 10-100 S/cm). In this case, the diffusive species is hydrogen and the network of O remains *bcc* as in ice VII.

This prediction attracted great interest and was confirmed in several other theoretical studies. The more recent, and probably more complete theoretical work on this subject is that of Hernandez & Caracas^[44,46], whose phase diagram is shown in Figure 1.9. As a matter of fact, these authors observed different regimes of superionic conduction, labeled superionic ice VI', VII'' and X. They all have in common the *bcc* lattice of oxygen atoms and mostly differ in the dynamics and average position of the hydrogen atoms.

There have also been several experimental attempts to find evidence of this superionic phase, using either static or dynamic compression and various experimental probes., Goncharov *et al.* (2005)^[47] reported the onset of superionicity beyond 60 GPa and 1000 K, using Raman spectroscopy. Sugimura *et al.* (2012)^[48] measured the conductivity of ice samples and obtained values above 0.1 S.cm⁻¹ at 56 GPa, 739 K and 62 GPa, 749 K. Recent laser-shock compression

studies also reported evidence of superionicity in the 100-200 GPa and ~2000-3000 K range^[49,50].

The existence of this superionic phase and its precise location in the P-T diagram of water is important for planetary sciences as theoretical studies^[45,51] indicated that superionic ice might exist in the mantle of Uranus and Neptune, and may play a crucial role to sustain the unusual non-dipolar, non-axisymmetric, magnetic fields on those planets (see section 1.2.3).

1.5 Ammonia ice

1.5.1 The ammonia molecule

The ammonia molecule (NH₃) consists of one nitrogen atom and three hydrogen atoms with an N-H bond length of 1.017 Å and a bond angle H-N-H of 106.7°. The free molecule NH₃ is of symmetry C_{3v} and has six modes of vibration shown in Figure 1.10. The frequencies of these vibrations and their activities are listed in Table 1.2. The nitrogen atom in the molecule has a lone electron pair which repels more strongly than bond pairs, wherefore the bond angle is not 109.5° (as in an ideal tetrahedron), but 106.7°. Ammonia, like water, is a polar hydrogenous molecule. However, it has weaker hydrogen bonds than water.

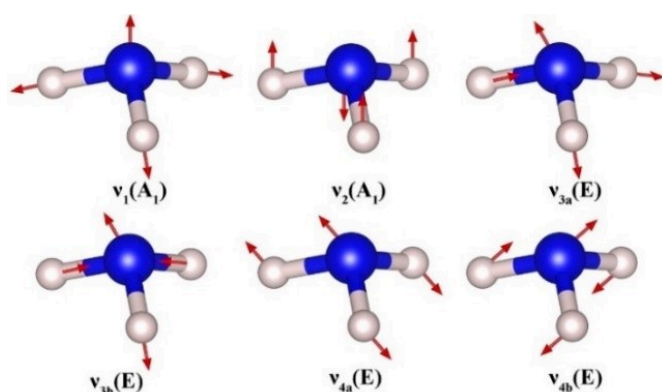


Figure 1.10. Schematic representation of the 6 vibrations of the ammonia molecule. v_1 and v_2 are stretching and symmetric torsion modes, respectively; $v_{3a,b}$ are asymmetric modes of stretching; $v_{4a,b}$ are asymmetric modes of torsion.

Table 1.2. Activities and frequencies of the vibration modes of the free ammonia molecule. R for activity in Raman and IR for infrared.

Vibration	Frequency(cm ⁻¹)	Activity
v_1 (A ₁)	3337	R
v_2 (A ₁)	950	R
v_{3a} (E), v_{3b} (E)	3444	R and IR
v_{4a} (E), v_{4b} (E)	1627	R and IR

1.5.2 The phase diagram of ammonia

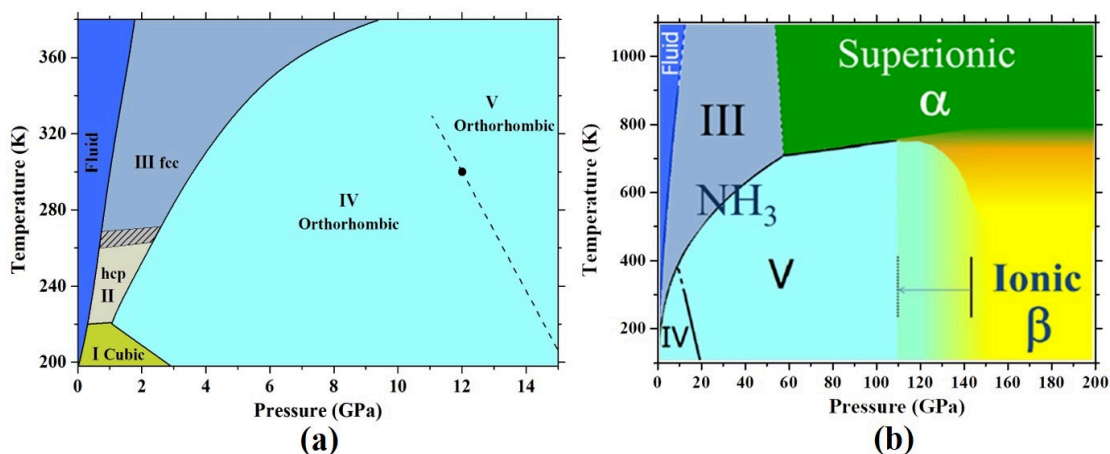


Figure 1.11. The phase diagram of ammonia. (a) at low temperature and pressure; (b). at high temperature and pressure.

The phase diagram of ammonia is shown in Figure 1.11. It can be seen that there are 5 molecular phases up to 100 GPa and 700 K. The molecular phases of ammonia can be classified into two groups: the first group comprises ordered phases and includes phases I, IV and V; the second group is composed of orientationally proton disordered phases and includes phases II and III. At higher pressures and temperatures, two non-molecular phases have been observed: the ionic β phase^[52,53], composed of NH_4^+ and NH_2^- ions, and the superionic α phase^[54] characterized by a fast diffusion of protons through the nitrogen lattice.

1.5.2.1 Phase I

Phase I is the stable solid phase at ambient pressure at temperatures below 220 K, as shown in Figure 1.11 (a). Its structure is cubic with space group $P2_13$ and with four molecules per unit cell^[55,56]. In this fully ordered structure, each ammonia molecule is bound to 6 others by hydrogen bonds, 3 as donor and 3 as acceptor (see Figure 1.12 left). These bonds are weaker than in ice Ih and are non-linear ($\angle\text{NHN}=160^\circ$) but have all the same lengths ($d_{\text{H}\dots\text{N}}=2.357 \text{ \AA}$).

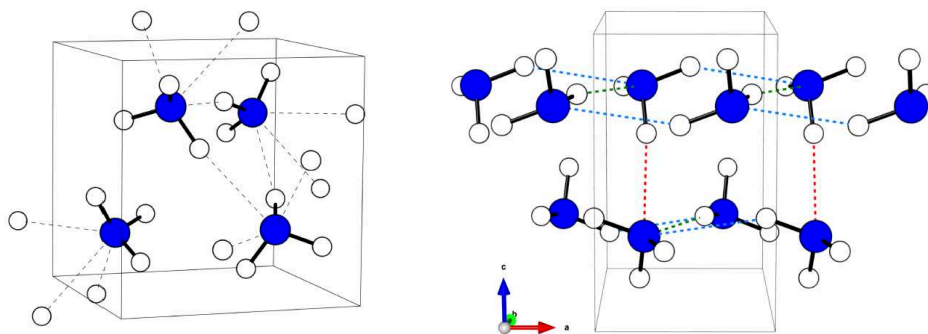


Figure 1.12. Structures of the ordered phases I (left) and IV (right) of ammonia.

1.5.2.2 Phase II

Phase I transits to phase II at 0.5 GPa and 230 K. The molecules in phase II are located on a hexagonal close-packed lattice^[57] and the space group is $P6_3/mmc$, with 2 molecules per unit cell. This structure is proton disordered and NMR measurements^[58] proved that this crystal is actually a plastic solid, i.e. present a dynamic orientational disorder. This is also supported by the observation of very broad Raman lattice and internal peaks^[59,60].

1.5.2.3 Phase III

Phase III was first observed by Hanson *et al.*^[61] by compressing liquid ammonia at room temperature in a diamond anvil cell. As seen in Figure 1.11 (b), phase III borders the melting line over a wide range of temperature and pressure. Its cubic structure of space group $Fm-3m$ was determined by Von Dreele & Hanson^[62]. It has 4 molecules per unit cell with N atoms at the 4a Wyckoff position. As in phase II, H atoms are disordered and the multiple positions that they may occupy are schematically represented in Figure 1.13. There are no Raman active lattice modes, but only broad N-H stretching Raman peaks, similar to those observed in phase II. The similitudes between phases II and III suggests that the latter is also a plastic phase.

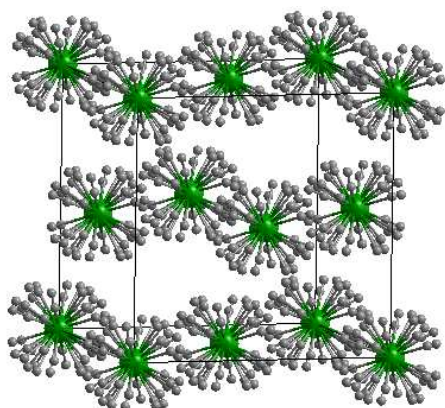


Figure 1.13. Structure representation of NH_3 -phase III. The nitrogen atoms are represented with green spheres and some of the possible sites for hydrogen atoms with grey spheres.

1.5.2.4 Phase IV and V

Phase IV can be obtained by compressing phases I, II or III, and is the first stable ordered structure at room temperature. The transition between phase III and Phase IV occurs at 3.8 GPa at 300 K. Neutron powder diffraction experiments^[63] have shown that phase IV is proton-ordered in an orthorhombic structure (space group: $P2_12_12_1$). The nitrogen lattice is close to a hexagonal close-packed (*hcp*), the position of N atoms being displaced by 0.11 Å from the ideal *hcp* positions. In this phase, each molecule is bound to 6 others by H-bonds, but unlike phase I, these bonds are non-equivalent: there are 3 different $N\cdots H$ bond lengths (from 2.196 Å to 2.256 Å) and $N-H\cdots N$ angles (from 149° to 168.9°). Its structure representation is depicted in Figure 1.12 (right).

Compressing phase IV at room temperature above 12 GPa in NH_3 and 18 GPa in ND_3 , an isostructural phase transition to phase V^[64] occurs. This phase transition was first reported by x-ray diffraction^[64] from an abrupt change in compressibility along the c -axis direction, but no volume discontinuity could be detected. Neutron studies have shown that this transition is induced by the movement of one of the deuterium atom^[65] leading to one linear H-bond, and a distortion of the molecule. Phase V is stable to about 150 GPa at room temperature.

1.5.2.5 The ionic β phase

The occurrence of non-molecular, ionic forms of ammonia at high pressure was first predicted by Pickard *et al.*^[66] using *ab initio* structure search methods. These authors found that molecular ammonia transforms above 90 GPa, via a proton transfer mechanism, into an ammonium amide ionic solid, with a $Pma2$ structure, composed of alternating layers of NH_4^+ and NH_2^- ions. This molecular to ionic transition was later observed in two independent experimental studies. On one hand, Palasyuk *et al.*^[53] reported a phase transition above 120 GPa using Raman spectroscopy and x-ray diffraction. Their observations are consistent with the presence of the $Pma2$ phase in the high pressure solid, but not alone, and these authors conclude that the molecular $P2_12_12_1$ (phase V) phase and the $Pma2$ ionic phase coexist up to 203 GPa. On the other hand, Ninet *et al.*^[52], using IR and Raman spectroscopy and XRD, also observed the transition to a new phase (denoted β) at 150 GPa. Here again, the $Pma2$ structure alone neither a coexistence of $Pma2$ with the $P2_12_12_1$ phase V could explain the experimental data. Instead, the authors proposed the coexistence of two ionic phases, the $Pma2$ and $Pca2_1$ ionic structures, which fit all the observations. The $Pca2_1$ structure was found stable in DFT calculations above 176 GPa and close in energy to the $Pma2$ phase up to 200 GPa, which would explain their coexistence. These structures are indeed very close: considering only the N atoms, $Pma2$ and $Pca2_1$ only differ by the plane stacking as can be seen in Figure 1.14. The back transition to the molecular solid V was observed at 110 GPa on decompression^[52].

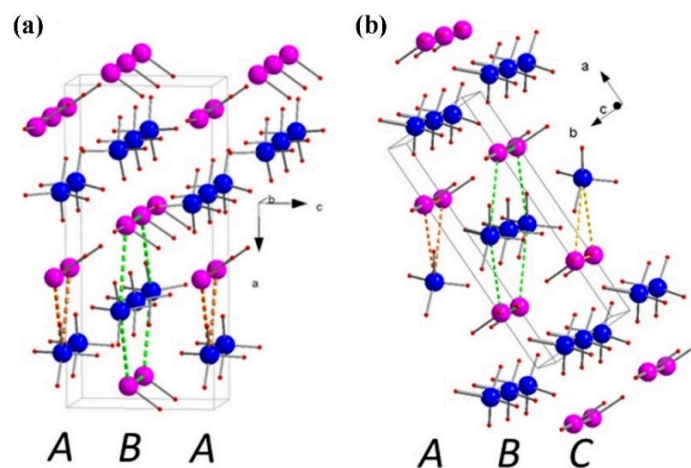


Figure 1.14. Structure representation of ionic ammonium amide phases of structure (a) $Pca2_1$ (pseudo-hcp) and (b) $Pma2$ (pseudo-fcc). Red, blue, and pink balls are, respectively, H atoms and the N atoms of the NH_2^- and NH_4^+ species. The pseudo-hcp (ABAB \cdots) or fcc (ABCABC \cdots) stacking of the nitrogen lattices are emphasized.

1.5.2.6 Superionic ammonia

Like water, Cavazzoni *et al.* predicted that ammonia becomes superionic above 60 GPa and 1200 K by *ab initio* molecular dynamics simulations^[45]. In superionic ammonia, the N atoms form a fixed crystalline lattice while hydrogen ions diffuse quickly through the lattice. By coupling Raman spectroscopy, X-ray diffraction combined and *ab initio* molecular dynamics simulations, Ninet *et al.* located the transition to the superionic phase at pressures above 57 GPa and temperatures above 700 K^[54], as shown in Figure 1.11 (b). They found that the transition was either of first-order or second-order, depending on whether the superionic phase was entered from the ordered phase V or the plastic phase III. Note that the temperature at which superionicity is detected (around 700 K) is lower than in the early simulations (1200 K) and than in water (~1000 K).

1.6 The ammonia-water system

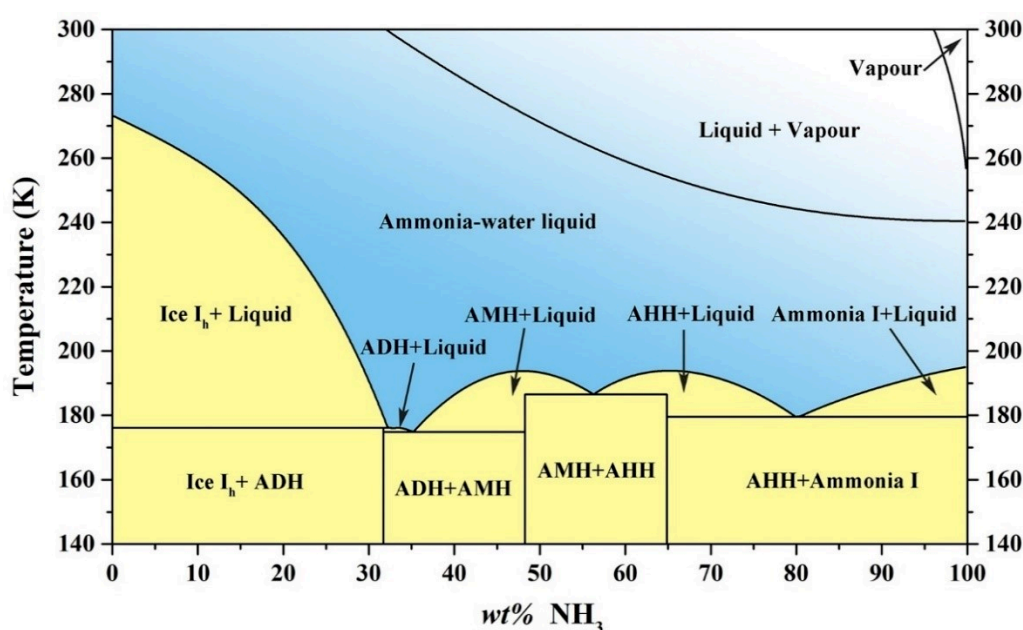


Figure 1.15. The binary phase diagram for the ammonia-water system at atmospheric pressure (Pickering 1893^[67]; Rupert 1909^[68], 1910^[69]; Smits and Postma 1910^[70]; Postma 1914^[71]; Elliott 1924^[72]; Clifford and Hunter 1933^[73]; Mironov 1955^[74]; Rollet and Vuillard 1956^[75]; Van Kasteren 1973^[76]; Kargel 1990^[77]; Yarger *et al.*, 1993^[78]).

The ammonia-water system has been studied at low temperature and ambient pressure over the last century. The results of these studies are compiled in Figure 1.15 showing the binary phase diagram of NH₃·H₂O at 1 bar. As can be seen in this diagram, water and ammonia are miscible at any concentration in the ambient pressure liquid, although the liquid phase with concentrations above ~32% is only stable at temperatures below 300 K. At temperatures below 273 K, five stoichiometric solids have been observed: pure water (H₂O), pure ammonia (NH₃), ammonia monohydrate (NH₃·H₂O, noted AMH), ammonia hemihydrate (2NH₃·H₂O, noted AHH), ammonia dihydrate (NH₃·2H₂O, noted ADH). No solid alloy has been observed at

ambient pressure. At the beginning of this thesis, high pressure studies on ammonia hydrates were mostly limited to pressures below 10 GPa. In the following, we give a summary of what was known on the phase diagrams of the three hydrates.

1.6.1 The phase diagram of ammonia monohydrate

The phase diagram of AMH known before this work is presented in Figure 1.16. Six different solid phases (noted AMH-I to VI) have been reported below 10 GPa and temperatures lower than 300 K. The structures of AMH-III and AMH-IV are still unknown^[79], while that of the other phases have been determined, mostly by neutron diffraction.

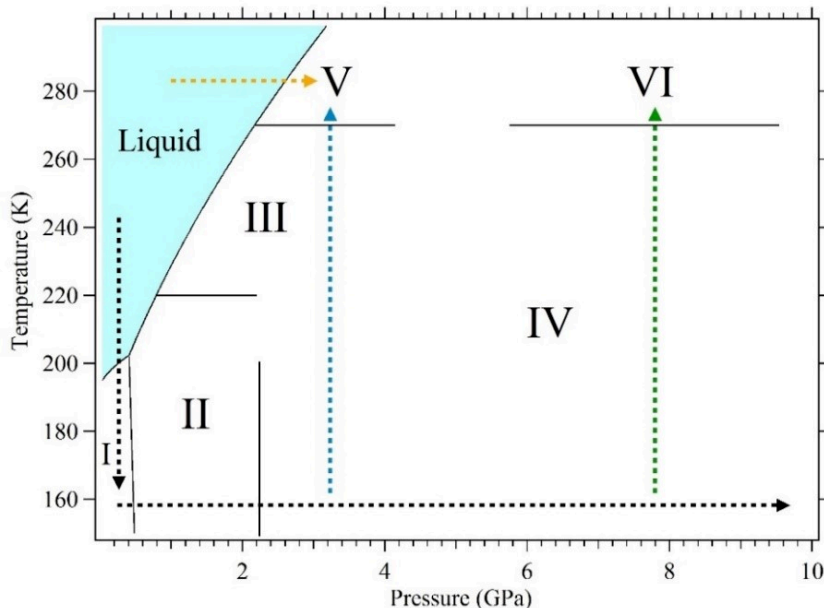


Figure 1.16. Experimental phase diagram of ammonia monohydrate below 10 GPa. The colored arrows represent different P - T paths followed during the neutron diffraction experiments of Loveday *et al.*^[80].

1.6.1.1 AMH I

AMH-I is the stable solid phase at ambient pressure and below 194.15 K. Early structural work by Olovsson *et al.*^[81] showed that phase I has an orthorhombic structure with 8 molecules per unit cell, space group $P2_12_12_1$ and lattice parameters $a=4.51(1)$ Å, $b=5.587(3)$ Å, $c=9.700(5)$ Å. As shown in Figure 1.17(left), the structure is fully proton-ordered and consists of H-bonded chains of water molecules extending along the a -axis and cross-linked by weaker H-bonded ammonia molecules, the ensemble forming a 3-dimensional network. Each ammonia molecule is tetrahedrally coordinated by four water molecules, donating three weak hydrogen bonds, and accepting a single stronger hydrogen bond. Each water molecule is 6-coordinated, bonding to four ammonia molecules and two other water molecules. In 2004, the neutron diffraction measurements of Loveday *et al.*^[82] confirmed the crystalline symmetry of phase I at 110 K and ambient pressure. The lattice parameters and atomic positions were determined more precisely: $a=4.51108(14)$ Å, $b=5.58691(20)$ Å, $c=9.71452(34)$ Å. Loveday *et al.*^[82] also

determined the equation of state of AMH-I at 130 K, and a fit to the third-order Birch-Murnaghan equation of state (EOS) gave a bulk modulus $B_0 = 8.9(4)$ GPa and first-pressure derivative $B_0' = 4.2(3)$. Using the same EOS relation, the neutron diffraction measurements at 180 K of Fortes *et al.*^[83] yielded $B_0=7.33(3)$ GPa and $B_0'=5.3$ (Fortes fixed B_0' to the value obtained in DFT calculations).

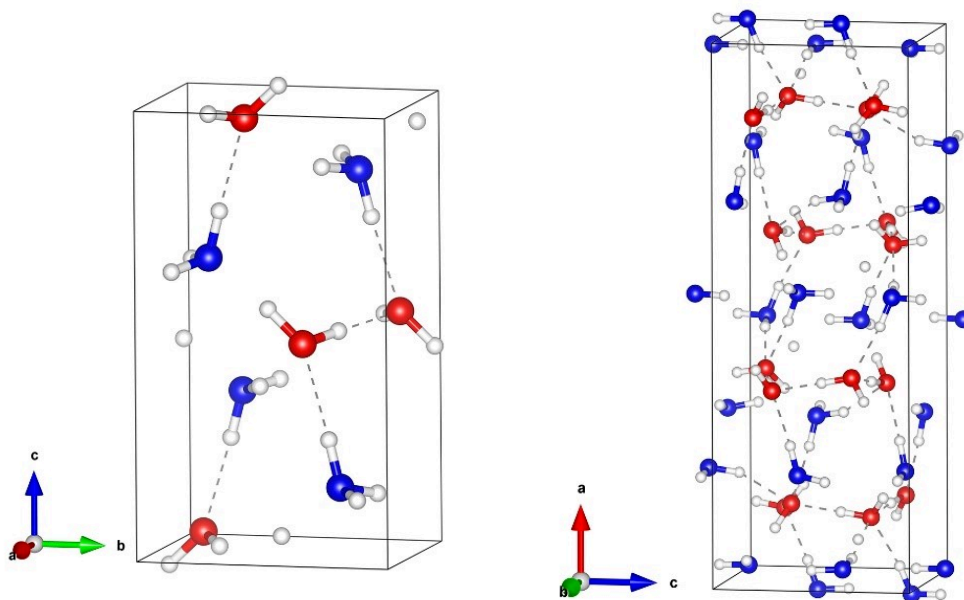


Figure 1.17. Representation of the structures of AMH-I (left) and AMH-II (right). The oxygen and nitrogen atoms are represented with the red and blue spheres, respectively. The hydrogen bonds are shown with dashed lines.

1.6.1.2 AMH-II

Hogenboom *et al.* discovered the first high-pressure polymorph of AMH, AMH-II^[84,85], which is stable above 340 MPa at 195 K. Fortes *et al.* determined the crystal structure of AMH-II by combining neutron powder diffraction measurements and *ab initio* structure search predictions^[83,86]. AMH-II crystallizes in an orthorhombic structure with space group *Pbca*: the lattice parameters are $a=18.8285(4)$ Å, $b=6.9415(2)$ Å, $c=6.8449(2)$ Å at 502 MPa and 180 K. This structure is depicted in Figure 1.17 (right): it is more complex than AMH-I, with 16 formula units per unit cell, and is characterized by sheets of pentagons formed by orientationally ordered O-D \cdots O, O-D \cdots N and N-D \cdots O hydrogen bonds. These sheets are stacked along the *a*-axis and connected by N-D \cdots O hydrogen bonds alone. The volume change from AMH-I to AMH-II is -4.6 % at 351 MPa, 180 K^[83].

1.6.1.3 AMH-V

Using neutron diffraction to investigate the high-pressure phase diagram of AMH, Loveday *et al.*^[82] discovered five other high-pressure polymorphs of AMH: phases III, IV, Va, Vb and VI. For a long time, it was believed that two different phases, called Va and Vb, were stable in the same (P, T) range but obtained by following different P-T paths as indicated in

Figure 1.16. AMH-Va was synthesized by warming AMH-IV above 270 K at 3.5 GPa (blue arrow) and observed stable up to ambient temperature, while the compression of liquid AMH at 280 K leads to AMH-Vb (yellow arrow). AMH-Vb can also be produced from warming phase III at 2.7 GPa and 270 K. As can be seen in Figure 1.18, the diffraction patterns of these two phases are very close and only differ by the relative intensity of two Bragg peaks.

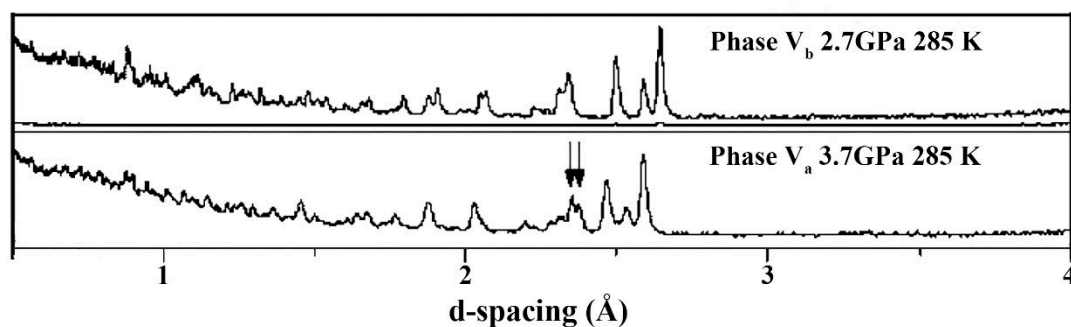


Figure 1.18. Neutron diffraction patterns of phases Va and Vb. The arrows mark the two peaks, which are the most significant difference between phases Va and Vb^[82].

In 2012, Wilson *et al.* determined the structure of the so-called AMH Vb, formed when the AMH liquid is compressed to 3.5(1) GPa at ambient temperature, using a combination of x-ray single-crystal and neutron powder diffraction experiments^[87]. Their results reveal that AMH Vb is not a homogeneous phase but that partial dehydration of AMH occurs. They demonstrated that their data are compatible with a mixture of solid ammonia hemihydrate-II (AHH-II) and water ice VII. The description of AHH-II and its high-pressure evolution will be done later in the section on AHH.

1.6.1.4 AMH-VI

As seen in the previous paragraph, it is not possible to produce a crystal of AMH by the compression of liquid AMH at ambient T as it leads to dehydration in ice VII + AHH-II. The formation of an ammonia monohydrate solid at high pressure and ambient T is however possible by following a particular thermodynamic pathway. Indeed Loveday *et al.*^[80] showed that upon heating an AMH sample compressed at ~140 K up to 6.5 GPa, a phase transition occurs at 270 K towards a new structure called AMH-VI. The followed P-T path is illustrated by the green arrow in the phase diagram of Figure 1.16.

The neutron diffraction of deuterated AMH-VI was indexed by a body-centered cubic structure (*bcc*) with lattice parameter $a=3.2727(2)$ Å at $P=6.5$ GPa and $T=300$ K. The extinctions were compatible with space groups *I-43m* and *Im-3m* but the structural refinement clearly favored the second one. The body centering requires that all molecular centers are identical and thus imply substitutional disorder of water and ammonia molecules. This substitutional disorder also implies orientational disorder of the molecules, hence the name of Disordered Molecular Alloy (DMA).

To explore the detailed nature of the orientational disorder, Loveday *et al.* refined a model with the O(N)-D bonds directed along the $\langle 111 \rangle$, $\langle 110 \rangle$ and $\langle 100 \rangle$ directions. The site

occupancies of the D atoms refined to show that the largest proportion, 82(16)%, of the O(N)-D bonds point along $\langle 111 \rangle$ and the remaining 18(5)% along $\langle 110 \rangle$, with a total occupancy of 5.1(9) D atoms in the average unit cell (if the total occupancy is constrained to 5, the site occupancies slightly change to 87(5)% along $\langle 111 \rangle$ and 13(5)% along $\langle 110 \rangle$). The refined average O(N)-D bond length was 0.976(4) Å, and the thermal parameters were $U_{\text{iso}}(\text{O/N})=0.0032(8)$ Å² and $U_{\text{iso}}(\text{D})=0.0035(11)$ Å², which are all in a reasonable range. The corresponding atom positions and unit cell parameters are given in Table 1.3, and a structural representation is shown in Figure 1.19, omitting the D atoms along $\langle 110 \rangle$ for clarity.

According to Loveday *et al.*, the fact that O(N)-D bonds are largely directed along $\langle 111 \rangle$ towards nearest neighbor atoms suggests that the structure is H-bonded. The N(O)···N(O) distance is 2.921 Å, giving a D···N(O) distance of 1.9 Å, which is comparable to the D···O distance in ice VII at this pressure^[80] and thus implies strong H bonding. The *bcc* arrangement of molecular centers also supports the case for H bonding: it provides the densest packing consistent with tetrahedral coordination, which is the most favorable for H bonding.

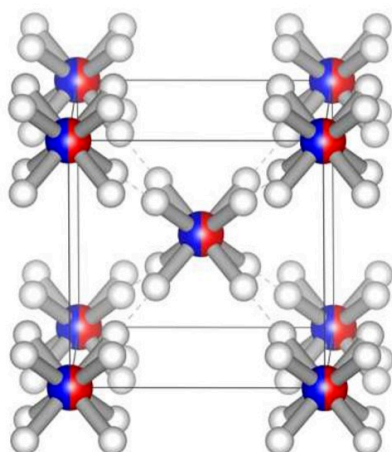


Figure 1.19. The structure of AMH-VI (DMA phase). The oxygen and nitrogen atoms are represented with the red and blue spheres, respectively. The water and ammonia molecules occupy the same sites with a 50% probability. The white spheres show the 16 possible positions along the $\langle 111 \rangle$ direction for the five hydrogen atoms in the unit cell. The other possible sites for H atoms along $\langle 110 \rangle$ are less probable and not represented for clarity.

Table 1.3. The lattice parameters and atomic positions of AMH-VI (DMA phase) at 6.5 GPa and 300 K (space group *Im-3m*, $a=3.2727(2)$ Å). Data from Loveday *et al.* ^[80].

Atom	Wyckoff symbol	atomic coordinates
N/O	2a	0.0000 0.0000 0.0000
D	24h	0.2109 0.2109 0.0000
D	16f	0.1722 0.1722 0.1722

This DMA phase is assumed to have a wide range of stability in pressure. As we will see in the next sections, this DMA phase was also found in the other hydrates.

1.6.1.5 Theoretical ionic and superionic structures

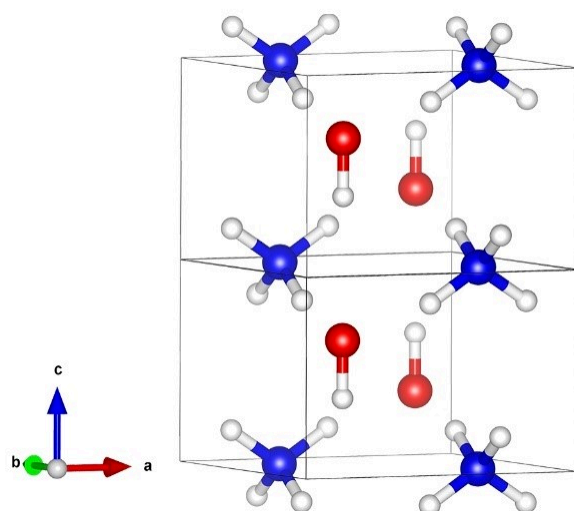


Figure 1.20. The structure of $P4/nmm$ ^[88]. The oxygen and nitrogen atoms are represented with the red and blue spheres, respectively.

As seen above, all the known structures of AMH below 10 GPa have been described as molecular phases. On the theoretical side, Fortes *et al.* investigated by DFT simulations the virtual compression of the AMH-I structure up to several GPa, that is, above the AMH-I to AMH-II transition, and found that AMH transforms into an ammonium hydroxide (NH_4OH) solid at 5 GPa, via proton transfers from water molecules to ammonia^[89]. In 2012, Griffiths *et al.*⁷⁶, using *ab initio* structure search, report another ammonium hydroxide phase, which this time is found more stable than AMH-II above a critical pressure ranging from 2.8 to 10 GPa, depending on the function used in the calculation. This structure, shown in Figure 1.20, is of tetragonal symmetry, space group $P4/nmm$, and is a fully ionic and ordered solid composed of 2 NH_4^+ and 2 OH^- per unit cell. N-H \cdots O hydrogen bonds link the ammonium ions to the hydroxyl ions but there is no O-H \cdots O nor O-H \cdots N hydrogen bonds in this structure. The structural parameters are given in Table 1.4. Before this work, no evidence of this phase had been seen in experiments.

Table 1.4. Lattice parameters and atomic positions of the predicted ionic phase $P4/nmm$ at (3 GPa, 175 K). Data from Griffiths *et al.*^[88].

Space group $P4/nmm$: $a=5.006 \text{ \AA}$, $b=5.006 \text{ \AA}$, $c=3.385 \text{ \AA}$		
Atom	Wyckoff symbol	Fractional atomic coordinates
N	2a	0.2500 0.7500 0.0000
O	2c	0.2500 0.2500 0.6562
H1	2c	0.7500 0.7500 0.6308
H2	8i	0.2500 0.5727 0.8262

In 2015, the phase diagram of AMH has been further investigated up to 800 GPa and 7000 K by Bethkenhagen *et al.* using *ab initio* structure search and molecular dynamics simulations^[90]. The results are summarized in the phase diagram of Figure 1.21. These authors found four ionic solid phases at high pressures. In addition to the previously predicted phase $P4/nmm$, a series of ionic-ionic phase transitions is predicted under pressure at 0 K: $P4/nmm$ to $Ima2$ at 38.3 GPa, then to $Pma2$ at 149 GPa, and finally to Pm at 527 GPa. These structures are all ammonium hydroxide solids, and in addition, $Pma2$ and Pm present symmetric O-H \cdots O hydrogen bonds.

At high temperature, like in the pure ices, a superionic phase of AMH with highly mobile hydrogen ions as well as a fixed lattice of alternating layers of nitrogen and oxygen is predicted by heating the 0 K stable structure from 750 to 6000 K at pressures between 26 and 800 GPa. Compared to the temperature and pressure ranges of the superionic states of pure water and ammonia, the superionic phase occurs at lower pressure in AMH. However, these theoretical results have not been confirmed by experiments so far.

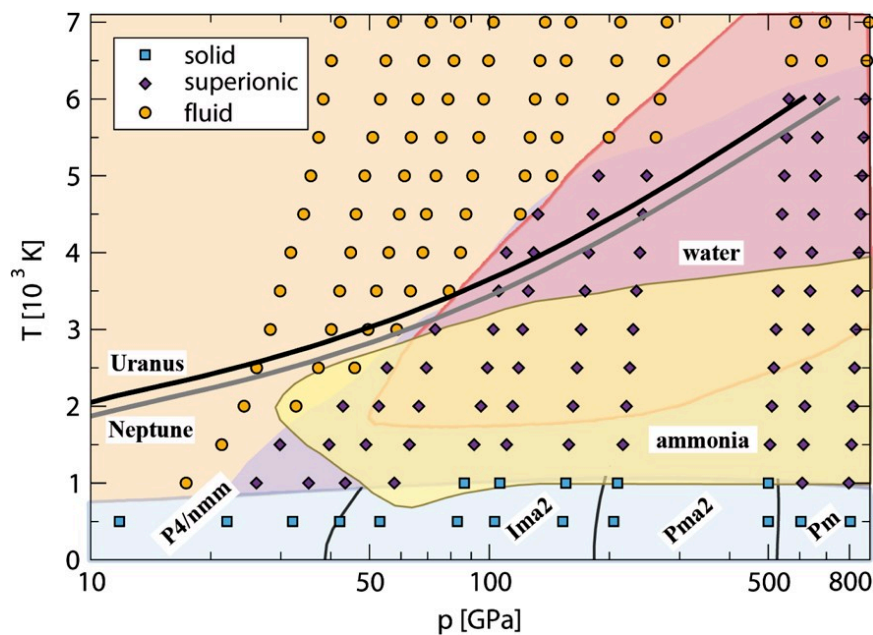


Figure 1.21. Phase diagram of AMH from the work of Bethkenhagen *et al.*^[90] (blue, purple, and orange shaded areas with symbols). The pink and yellow shaded areas represent the superionic phase for water^[22,91] and ammonia.^[92] The black and gray curves indicate the isentropes of Uranus and Neptune, respectively.^[91]

1.6.1.6 Melting curve of ammonia monohydrate

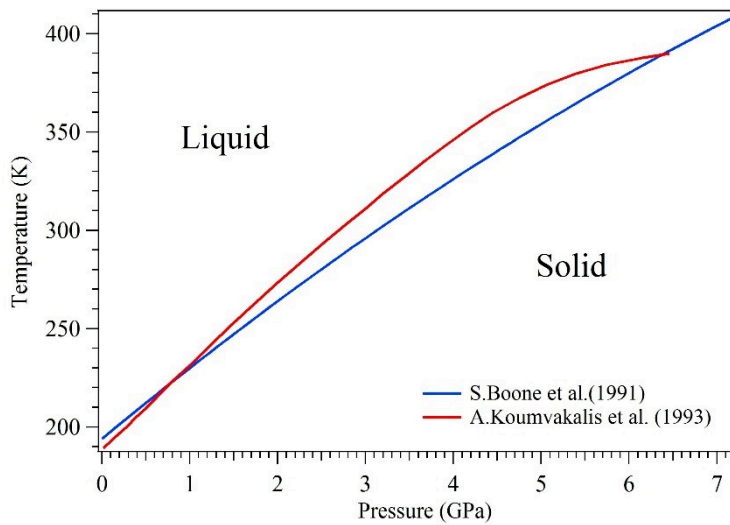


Figure 1.22. Melting curve of AMH determined by S.Boone *et al.*^[93] (blue line) and A.Koumvakalis *et al.*^[94] (red line), respectively.

The melting curve of AMH has been investigated in two studies, by Boone *et al.*^[93] in 1991, and by Koumvakalis *et al.*^[94] in 1993. In both experiments, samples were compressed in a diamond anvil cell and a vacuum cryostat (where the DAC could be heated or cooled by a reservoir of refrigerant) was used to control the sample temperature. Boone *et al.* determined the melting curve of AMH from 0 to 6 GPa and for temperatures ranging from 190 to 400 K, as shown in Figure 1.22 (the blue line). Phases were identified by optical microscopy under normal and polarized light. The melting line was drawn based on the points at which liquid and solid were found to coexist. Koumvakalis *et al.*^[94] measured the melting line of AMH to about 400 K at 6 GPa using Raman spectroscopy and optical microscopy. As seen in Figure 1.22, the two melting lines are not in good agreement, in particular, they greatly differ in the slope above 4 GPa. The melting line of AMH will be re-investigated in the present work (see Chapter 4).

1.6.2 The phase diagram of ammonia dihydrate

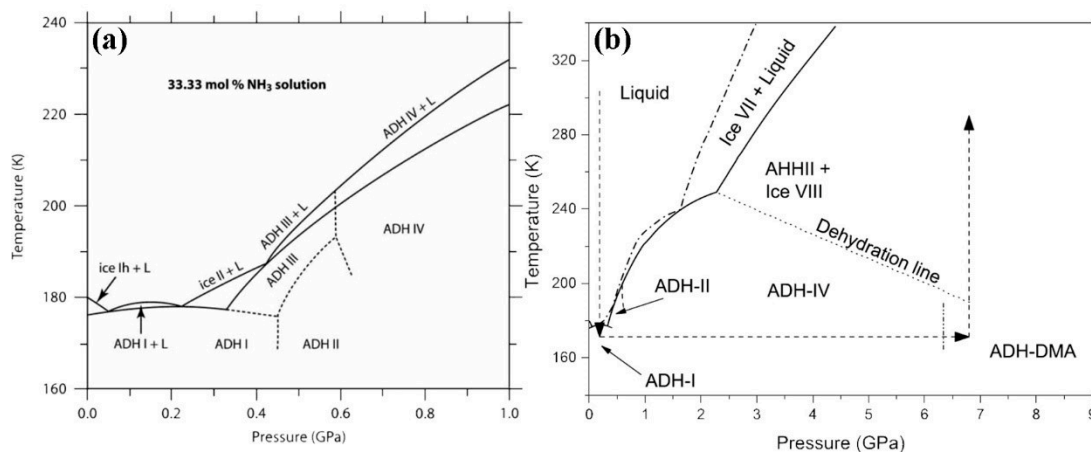


Figure 1.23. The phase diagram of ADH at low temperature (a) below 1.0 GPa^[95]; (b) above 1.0 GPa^[95].

1.6.2.1 Experimental phase diagram

As shown in Figure 1.23 (a) and (b), the phase diagram of ADH has so far been investigated below 7 GPa and $T < 300$ K. It is fairly complex, and some questions about the nature and structure of the high P phases remain. Powder neutron diffraction at 150K^[82] showed that the ambient pressure **ADH I** solid is a fully ordered structure of cubic symmetry with space group $P2_13$, $a = 7.1278(8)$ Å at 150 K, and 4 molecules per unit cell. Hogenboom *et al.*^[85] were the first to detect a new high-pressure phase ammonia dihydrate II (**ADH II**), which their dilatometry measurements showed to be stable above ~ 400 MPa at 170 K. Shortly afterward, a powder neutron diffraction pattern of ADH II was reported by Nelmes *et al.*^[82] with data acquired at 530MPa and 170 K. Three more high-pressure phases (III, IV and ADH-DMA) have been reported by Fortes *et al.* using powder neutron diffraction experiments^[95]. Also, the dehydration boundary was confirmed through the decomposition of ADH samples into a mixture of AMH V or VI and ice VII or VIII, depending on pressure and temperature. **ADH III** was later found to be a mixture of AMH II and ice II^[86].

In the domain of **ADH II**, two variants have been observed, noted IIa and IIb. These phases were found to have very similar unit cell parameters, and this was hypothesized to be due to a very similar heavy atom (N and O) arrangement while the deuterium positions varied greatly between the structures. These different variants of the ADH-II structure were suggested to arise for different rates of compression of the samples^[96]. The unit cell parameters of phase IIa from Fortes *et al.*^[96] and potential space groups deduced from systematic absences were used by Griffiths *et al.*^[97], as constraints for running AIRSS. The IIa structure that was preferred had a monoclinic space group of $P21/n$ and was fully ordered, and found to agree very well upon Rietveld refinement to the data collected by Fortes *et al.*^[28].

ADH IV was found to form consistently from the melt between 0.6 and 2.4 GPa, although the II-IV transition has never been observed^[86,95]. Its powder neutron diffraction pattern has been indexed by an orthorhombic unit cell but the complete structure is not determined.

A body-centered cubic phase was observed in one sample by Fortes *et al.*^[95] which was determined to have a structure very similar to the **DMA** phase of AMH (AMH-VI, see above), with ADH composition. Fortes *et al.* were only able to observe this phase once, but another study by Loveday *et al.*^[98] also managed to form this phase of ADH from a low temperature amorphous sample of ADH. Their ADH sample was rapidly frozen to prevent decomposition to a mixture of ammonia monohydrate and ice, as had been observed by Bertie and Shehata^[99]. This formed an amorphous solid which then transformed into a *bcc* phase on warming without decomposing into AMH VI plus Ice VII as was seen by Fortes *et al.*^[95]. The room temperature ADH DMA was observed in the presence of other phases^[98] thought to correspond to a small amount of Ice VII and a variant of the AMH-Vb structure.

1.6.2.2 Theoretical predictions

In 2017, A DFT theoretical study of ADH by Jiang *et al.* has predicted an ionic phase of tetragonal structure (space group $I4_1cd$) consisting of three alternating layers of H_2O , NH_4^+ , and

OH^- above 11.81 GPa^[100] as shown in Figure 1.24(b). The high temperature evolution has also been studied and, as seen previously in AMH^[92], this ionic phase would turn into a superionic phase at high temperature, along the phase transition line shown in Figure 1.24 (a). Robinson *et al.* have later predicted that the partial ionic phase $I4_1cd$ remains stable only up to 10 GPa, where a new orthorhombic partial ionic $Ama2$ phase is found to become more stable until 60 GPa^[43]. Similarly, as $I4_1cd$, $Ama2$ is composed of alternate layers of H_2O , NH_4^+ , and OH^- (Figure 1.24 (b)).

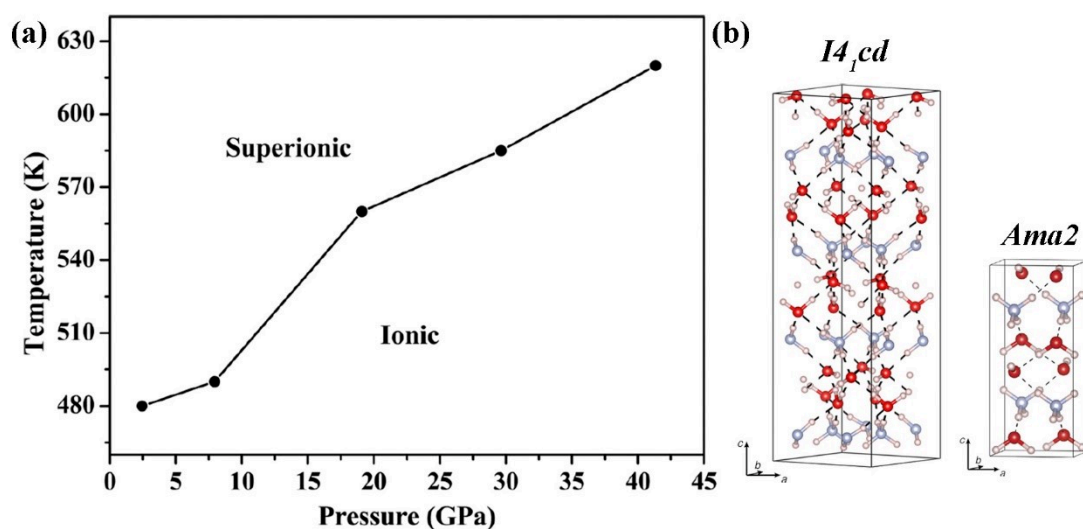


Figure 1.24. (a) Theoretical HP-HT phase diagram of $\text{ADH}^{[100]}$; (b) Structure representation of $I4_1cd$ ^[98] and $Ama2$ ^[39] phases. The oxygen and nitrogen atoms are represented with the red and blue spheres, respectively.

1.6.3 The phase diagram of ammonia hemihydrate

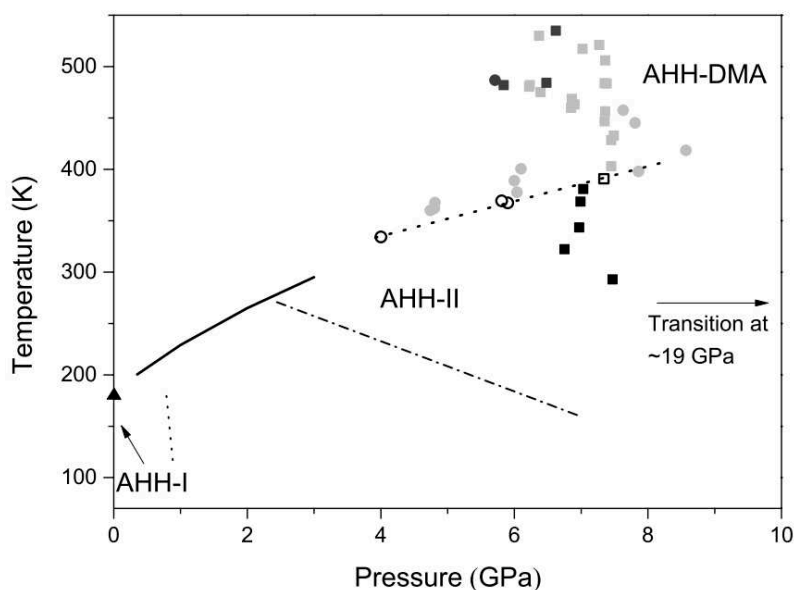


Figure 1.25. The phase diagram of AHH after Ref. ^[101]. The black and light grey symbols represent P - T points where the AHH-II and AHH-DMA phases are observed, respectively, and the dark grey symbols show where the sample is fully molten. The open symbols represent the mixture of AHH-II and AHH-DMA phase. The dashed-dotted line represents the dehydration line where water-rich samples break down into AHH-II and ice VII/VIII. The dotted line is the phase transition line based on the open symbols and the solid line represents the melting curve of AMH. The triangle denotes the P and T where the deuterated AHH sample started to freeze in solid AHH-I phase at ambient pressure.

1.6.3.1 Experimental phase diagram

Probably because of the high content of ammonia in AHH ($2\text{NH}_3 \cdot \text{H}_2\text{O}$), there are less reported researches on AHH than on AMH and ADH. However, since both AMH and ADH decompose into AHH and ice VII, around 3 GPa and at 250 K and 280 K, respectively ^[82,95], the abundance of AHH could be more important than previously thought.

The known phase diagram of AHH is reported in Figure 1.25. The ambient pressure solid **AHH-I** is obtained below 190 K. Its structure was determined by powder neutron diffraction at 110 K^[82]. It is orthorhombic (space group $Pbnm$), with 12 molecules per unit cell and lattice parameters $a=8.3220(3)$ Å, $b=8.3526(3)$ Å, $c=5.2799(2)$ Å.

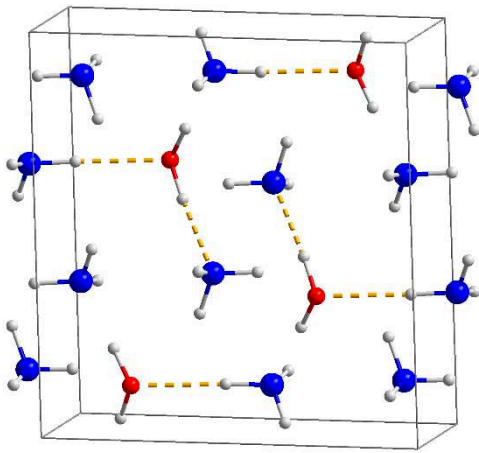


Figure 1.26. Structure representation of AHH-II. The oxygen and nitrogen atoms are represented with the red and blue spheres, respectively. Yellow dashed lines show hydrogen bonds.

Three high-pressure crystalline phases have been experimentally reported^[101] for $T < 500$ K and $P < 26$ GPa (Figure 1.25). The solid phase obtained on compressing the liquid at room temperature is **AHH-II**. It has a monoclinic structure (space group $P2_1/c$), with 12 molecules per unit cell and lattice parameters $a=3.3584(5)$ Å, $b=9.215(1)$ Å, $c=8.933(1)$ Å and $\beta=94.331(8)^\circ$ at 3.5(1) GPa, 300 K^{[73][87]}. As seen in Figure 1.26, the molecules in this structure are fully orientationally ordered and are bound by O—H \cdots N, N—H \cdots O, and N—H \cdots N hydrogen bonds. Although the hydrogen bonding of AHH-II is significantly different from that of ice VII, the packing of the molecules (crowned hexagonal hydrogen-bonded layers) is similar. The 300 K equation of state of AHH-II was measured by Wilson *et al.*^[102] up to 26 GPa, and the fit to the data by a third-order Birch Murnaghan equation gave $B_0=18(2)$ GPa, $B'_0=3.7(2)$ and $V_0=323(4)$ Å³.

Ma *et al.*^[87] compressed an AHH II sample at 300 K and observed that it remains stable to 19 GPa, pressure at which a solid-solid phase transition occurs to an unidentified phase. Later, Wilson *et al.*^[101] studied an AHH II deuterated sample produced by compressing 2:1 NH₃:H₂O liquid sample. They observed the AHH-II phase up to 26.5 GPa, after which it transformed to another solid phase at 27.0 GPa, whose x-ray diffraction pattern was found similar to the *bcc* **DMA** observed in AMH (AMH-VI)^[101]. A similar evolution was observed in a neutron diffraction experiment starting from an AHH-II+ice VII sample produced from an equimolar mixture. The origin of the differences between the Ma *et al.*^[87] and Wilson *et al.*^[101] experiments remains unclear. More importantly, Wilson *et al.*'s experiment showed that the DMA phase also exists in AHH, after having been uncovered in AMH and ADH. However, the DMA phase could not be obtained in AHH by the same P-T path as the two other compositions, that is, compression at low temperature to ~ 6 GPa and warming above 270 K^[101].

The **AHH-DMA** phase was also observed by Wilson *et al.*^[101] when heating AHH-II at different pressures between 4 and 8 GPa. The transition line is drawn from this dataset in Figure 1.25 and has a positive slope. To be consistent with the observed room-temperature AHH-II \rightarrow DMA transition, Wilson *et al.*^[101] suggested that the transition line has a dome shape with a negative slope above a certain pressure.

1.6.3.2 Theoretical predictions

As in AMH and ADH, theoretical calculations on the high-pressure solid phases of AHH have been reported recently (2017). Using *ab initio* structural searches, Robinson *et al.*^[103] have predicted that AHH first transforms at low temperature from AHH-II to, a partially ionized phase of monoclinic ($A2/m$) symmetry composed of NH_3 , NH_4^+ and OH^- at 20 GPa, and second, to a fully ionic $\text{O}^{2-}(\text{NH}_4^+)_2$ solid above 65 GPa, where the water molecules are completely depleted from their protons. These structures of space group $Amma$ and $P-3m1$ symmetry are represented in Figure 1.27. No experiment has confirmed these predictions yet.

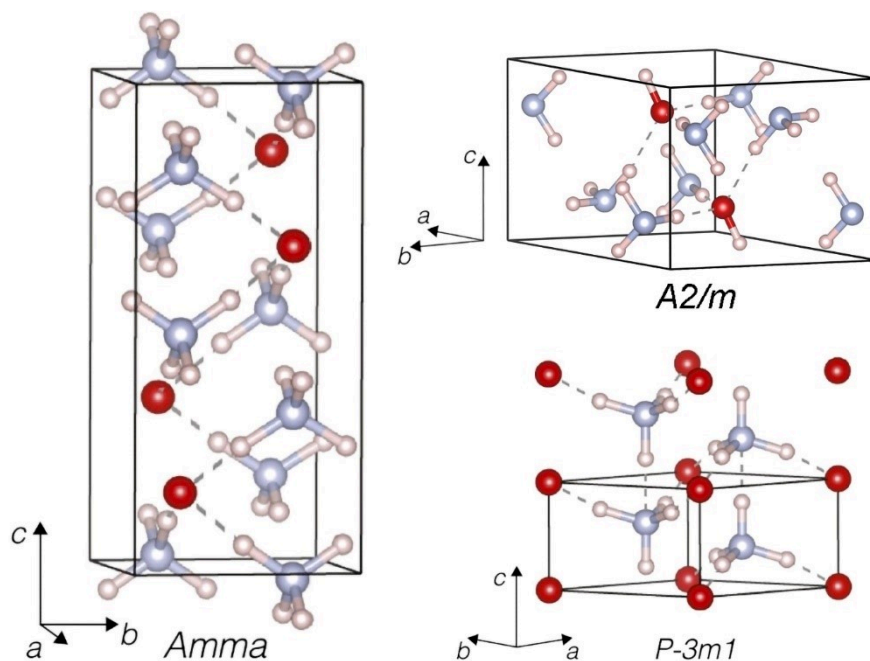


Figure 1.27. Structure representation of partially ionized phase $A2/m$, fully ionic phases $Amma$ and $P-3m1$ after Ref.^[103]. The oxygen and nitrogen atoms are represented with the red and blue spheres, respectively.

1.7 Conclusions and aims of the thesis work

In this chapter, we have reviewed the main scientific motivations to study water, ammonia and their mixtures. First, these systems form the simplest solids bound by the four $\text{O-H}\cdots\text{O}$, $\text{N-H}\cdots\text{N}$, $\text{O-H}\cdots\text{N}$ and $\text{N-H}\cdots\text{O}$ hydrogen bonds. These H-bonds have a large influence on the properties of these substances and their study under high pressure will help to understand the effect of varying the bond lengths and bond angles on the properties of these materials, which can be transferred to other important substances, such as proteins, where these interactions play an important role. Second, we have seen that there are several pieces of evidence that water and ammonia have condensed in the outer region of the solar systems where the giant planets have formed, and are thus major components of the interiors of these planets and their satellites. The phases formed by their mixtures under the temperature and pressure conditions of these giant

planets are therefore relevant for understanding observable properties like the magnetic field, gravitational moments and atmospheric composition.

In the second part, we have reviewed the present state-of-the-art knowledge about the high-pressure phase diagram of water, ammonia and the three experimentally observed ammonia hydrates, AHH, AMH and ADH. The present thesis work is focused on AMH, but we have seen that in some region of its phase diagram, AMH may dehydrate to AHH and ice, so it is also important to understand the solid phases of the other hydrates, as well as those of pure water and ammonia ices.

By analyzing the previous experimental and theoretical results, it is clear that there remain many questions about the phase diagram of AMH. First, all the solid phases experimentally observed so far have been described as molecular, while DFT calculations predict that AMH will ionize and become an ammonium hydroxide solid in the pressure range 5-10 GPa. We note in this respect that the large disorder, both substitutional and orientational, in the structure of AMH-VI (DMA) phase may have “hidden” the effects of ionization in the neutron structural studies. It thus appears important to study this phase in more detail and by using other experimental techniques such as Raman and infrared spectroscopies, since the latter will be sensitive to the presence of ionic species. Furthermore, the predicted transition to the fully ionic and ordered phase of $P4/nmm$ space group should be tested by extending the pressure range of investigation above 9 GPa.

Second, the phase diagram of AMH at high pressure and temperatures above 300 K, of high relevance for planetary modeling, has almost never been explored. An important question relates to the stability of the DMA structure at high temperature, since it has been observed in the same pressure range as the demixed AHH-II+ice mixture. Is the DMA structure more stable and in which P-T range? A second important question is whether a superionic phase of AMH may exist at high P-T, as observed in the pure ices. Can we trust the theoretical predictions that this superionic phase appears at lower temperature and pressure than in the pure ices?

The aim of this thesis is thus to explore the phase diagram of AMH over a much-extended pressure-temperature domain than done so far, using various experimental methods to answer the above questions.

References

- [1] Arunan, E., Desiraju, G. R., Klein, R. A. *et al.* Definition of the hydrogen bond (IUPAC Recommendations 2011). **83**, 1637-1641, (2011).
- [2] Fortes, A. *Computational and experimental studies of solids in the ammonia-water system*, University of London, (2004).
- [3] Steiner, T. The hydrogen bond in the solid state. *Angewandte Chemie International Edition* **41**, 48-76, (2002).
- [4] Holzapfel, W. On the symmetry of the hydrogen bonds in ice VII. *The Journal of Chemical Physics* **56**, 712-715, (1972).
- [5] Brown, R. H. & Cruikshank, D. P. Determination of the composition and state of icy surfaces in the outer solar system. *Annual Review of Earth Planetary Sciences* **25**, 243-277, (1997).
- [6] Jacobson, R. in *Bulletin of the American Astronomical Society*. 1037.
- [7] Jacobson, R. A. The orbits of the major saturnian satellites and the gravity field of Saturn from spacecraft and Earth-based observations. *The Astronomical Journal* **128**, 492, (2004).
- [8] Lewis, J. S. Satellites of the outer planets: Their physical and chemical nature. *Icarus* **15**, 174-185, (1971).
- [9] Lewis, J. S. Chemistry of the outer solar system. *Space Science Reviews* **14**, 401-411, (1973).
- [10] Hunten, D., Tomasko, M., Flasar, F. *et al.* Titan. *Saturn*, 671-759, (1984).
- [11] Atreya, S. K., Donahue, T. M. & Kuhn, W. R. Evolution of a nitrogen atmosphere on Titan. *Science* **201**, 611-613, (1978).
- [12] Lunine, J. I. & Stevenson, D. J. Clathrate and ammonia hydrates at high pressure: Application to the origin of methane on Titan. *Icarus* **70**, 61-77, (1987).
- [13] McKay, C. P., Scattergood, T. W., Pollack, J. B. *et al.* High-temperature shock formation of N₂ and organics on primordial Titan. *Nature* **332**, 520, (1988).
- [14] Zahnle, K. & Dones, L. in *Symposium on Titan*.
- [15] Burns, J. A. & Matthews, M. S. *Satellites*. (University of Arizona Press, 1986).
- [16] Kargel, J. S. & Pozio, S. The volcanic and tectonic history of Enceladus. *Icarus* **119**, 385-404, (1996).
- [17] Porco, C. C., Helfenstein, P., Thomas, P. *et al.* Cassini observes the active south pole of Enceladus. *science* **311**, 1393-1401, (2006).
- [18] Waite Jr, J. H., Lewis, W., Magee, B. *et al.* Liquid water on Enceladus from observations of ammonia and 40 Ar in the plume. *Nature* **460**, 487, (2009).
- [19] Kargel, J. & Hogenboom, D. in *Lunar and Planetary Science Conference*.
- [20] Arakawa, M. & Maeno, N. Effective viscosity of partially melted ice in the ammonia-water system. *Geophysical research letters* **21**, 1515-1518, (1994).
- [21] Schenk, P. M. Fluid volcanism on Miranda and Ariel: Flow morphology and composition. *Journal of Geophysical Research: Solid Earth* **96**, 1887-1906, (1991).
- [22] Redmer, R., Mattsson, T. R., Nettelmann, N. *et al.* The phase diagram of water and the magnetic fields of Uranus and Neptune. *Icarus* **211**, 798-803, (2011).
- [23] Smith, B. A., Soderblom, L. A., Banfield, D. *et al.* Voyager 2 at Neptune: Imaging science results. *Science* **246**, 1422-1449, (1989).
- [24] Stanley, S. & Bloxham, J. Numerical dynamo models of Uranus' and Neptune's magnetic fields. *Icarus* **184**, 556-572, (2006).

-
- [25]Bernal, J. D. & Fowler, R. H. A theory of water and ionic solution, with particular reference to hydrogen and hydroxyl ions. *The Journal of Chemical Physics* **1**, 515-548, (1933).
- [26]Shimanouchi, T. *Tables of molecular vibrational frequencies*. (National Bureau of Standards 1980).
- [27]Bjerrum, N. Structure and properties of ice. *Science* **115**, 385-390, (1952).
- [28]Fortes, A., Wood, I., Brodholt, J. *et al.* The structure, ordering and equation of state of ammonia dihydrate ($\text{NH}_3 \cdot 2\text{H}_2\text{O}$). *Icarus* **162**, 59-73, (2003).
- [29]Bridgman, P. W. in *Proceedings of the American Academy of Arts and Sciences*. 441-558 (JSTOR).
- [30]Bartels-Rausch, T., Bergeron, V., Cartwright, J. H. *et al.* Ice structures, patterns, and processes: A view across the icefields. *Reviews of Modern Physics* **84**, 885, (2012).
- [31]Malenkov, G. Liquid water and ices: understanding the structure and physical properties. *Journal of Physics: Condensed Matter* **21**, 283101, (2009).
- [32]Bridgman, P. The phase diagram of water to 45,000 kg/cm². *The Journal of Chemical Physics* **5**, 964-966, (1937).
- [33]Jorgensen, J. D. & Worlton, T. G. Disordered structure of D₂O ice vii from insitu neutron powder diffraction. *The Journal of chemical physics* **83**, 329-333, (1985).
- [34]Song, M., Yamawaki, H., Fujihisa, H. *et al.* Infrared absorption study of Fermi resonance and hydrogen-bond symmetrization of ice up to 141 GPa. *Physical Review B* **60**, 12644, (1999).
- [35]Goncharov, A. F., Struzhkin, V. V., Mao, H.-k. *et al.* Raman spectroscopy of dense H₂O and the transition to symmetric hydrogen bonds. *Physical Review Letters* **83**, 1998, (1999).
- [36]Pruzan, P., Chervin, J., Wolanin, E. *et al.* Phase diagram of ice in the VII–VIII–X domain. Vibrational and structural data for strongly compressed ice VIII. *Journal of Raman Spectroscopy* **34**, 591-610, (2003).
- [37]Hirsch, K. & Holzappel, W. Symmetric hydrogen bonds in ice X. *Physics Letters A* **101**, 142-144, (1984).
- [38]Caracas, R. Dynamical instabilities of ice X. *Physical review letters* **101**, 085502, (2008).
- [39]Benoit, M., Bernasconi, M., Focher, P. *et al.* New high-pressure phase of ice. *Physical Review Letters* **76**, 2934, (1996).
- [40]Takii, Y., Koga, K. & Tanaka, H. A plastic phase of water from computer simulation. *The Journal of chemical physics* **128**, 204501, (2008).
- [41]Aragones, J. & Vega, C. Plastic crystal phases of simple water models. *The Journal of chemical physics* **130**, 244504, (2009).
- [42]Himoto, K., Matsumoto, M. & Tanaka, H. Yet another criticality of water. *Physical Chemistry Chemical Physics* **16**, 5081-5087, (2014).
- [43]Naden Robinson, V., Marqués, M., Wang, Y. *et al.* Novel phases in ammonia-water mixtures under pressure. *The Journal of chemical physics* **149**, 234501, (2018).
- [44]Hernandez, J.-A. & Caracas, R. Proton dynamics and the phase diagram of dense water ice. *The Journal of chemical physics* **148**, 214501, (2018).
- [45]Cavazzoni, C., Chiarotti, G., Scandolo, S. *et al.* Superionic and metallic states of water and ammonia at giant planet conditions. *Science* **283**, 44-46, (1999).
- [46]Hernandez, J.-A. & Caracas, R. Superionic-superionic phase transitions in body-centered cubic H₂O ice. *Physical review letters* **117**, 135503, (2016).
- [47]Goncharov, A. F., Goldman, N., Fried, L. E. *et al.* Dynamic ionization of water under extreme conditions. *Physical review letters* **94**, 125508, (2005).

-
- [48]Sugimura, E., Komabayashi, T., Ohta, K. *et al.* Experimental evidence of superionic conduction in H₂O ice. *The Journal of chemical physics* **137**, 194505, (2012).
- [49]Millot, M., Coppari, F., Rygg, J. R. *et al.* Nanosecond X-ray diffraction of shock-compressed superionic water ice. *Nature* **569**, 251, (2019).
- [50]Millot, M., Hamel, S., Rygg, J. R. *et al.* Experimental evidence for superionic water ice using shock compression. *Nature Physics* **14**, 297, (2018).
- [51]Wilson, H. F., Wong, M. L. & Militzer, B. Superionic to superionic phase change in water: Consequences for the interiors of Uranus and Neptune. *Physical review letters* **110**, 151102, (2013).
- [52]Ninet, S., Datchi, F., Dumas, P. *et al.* Experimental and theoretical evidence for an ionic crystal of ammonia at high pressure. *Physical Review B* **89**, 174103, (2014).
- [53]Palasyuk, T., Troyan, I., Eremets, M. *et al.* Ammonia as a case study for the spontaneous ionization of a simple hydrogen-bonded compound. *Nature communications* **5**, 3460, (2014).
- [54]Ninet, S., Datchi, F. & Saitta, A. Proton disorder and superionicity in hot dense ammonia ice. *Physical review letters* **108**, 165702, (2012).
- [55]Reed, J. W. & Harris, P. Neutron diffraction study of solid deuterioammonia. *The Journal of Chemical Physics* **35**, 1730-1737, (1961).
- [56]Hewat A W, R. C. The crystal structure of deuterioammonia between 2 and 180 K by neutron powder profile refinement. *Acta Crystallographica Section A: Crystal Physics, Diffraction, Theoretical and General Crystallography* **35**, 569-571, (1979).
- [57]Eckert, J., Mills, R. L. & Satija, S. K. Structure of ND₃ solids I and II at high pressure by neutron diffraction. *The Journal of Chemical Physics* **81**, 6034-6038, (1984).
- [58]Doverspike, M. A., Liu, S.-B., Ennis, P. *et al.* NMR in high-pressure phases of solid NH₃ and ND₃. *Physical Review B* **33**, 14, (1986).
- [59]Luo, R., Nye, C. & Medina, F. Raman spectrum of ammonia solid II. *The Journal of chemical physics* **85**, 4903-4904, (1986).
- [60]Gauthier, M., Pruzan, P., Besson, J. *et al.* Investigation of the phase diagram of ammonia by Raman scattering. *Physica B+ C* **139**, 218-220, (1986).
- [61]Hanson, R. & Jordan, M. Ultrahigh-pressure studies of ammonia. *The Journal of Physical Chemistry* **84**, 1173-1175, (1980).
- [62]Von Dreele, R. & Hanson, R. Structure of NH₃-III at 1.28 GPa and room temperature. *Acta Crystallographica Section C: Crystal Structure Communications* **40**, 1635-1638, (1984).
- [63]Loveday, J., Nelmes, R., Marshall, W. *et al.* Structure of deuterated ammonia IV. *Physical review letters* **76**, 74, (1996).
- [64]Datchi, F., Ninet, S., Gauthier, M. *et al.* Solid ammonia at high pressure: A single-crystal x-ray diffraction study to 123 GPa. *Physical Review B* **73**, 174111, (2006).
- [65]Ninet, S., Datchi, F., Klotz, S. *et al.* Hydrogen bonding in ND₃ probed by neutron diffraction to 24 GPa. *Physical Review B* **79**, 100101, (2009).
- [66]Pickard, C. J. & Needs, R. Highly compressed ammonia forms an ionic crystal. *Nature materials* **7**, 775, (2008).
- [67]Pickering, S. Chem. Soc. London. *Trans* **63**, 141, (1893).
- [68]Rupert, F. F. THE SOLID HYDRATES OF AMMONIA. *Journal of the American Chemical Society* **31**, 866-868, (1909).

-
- [69]Rupert, F. F. THE SOLID HYDRATES OF AMMONIA. II. *Journal of the American Chemical Society* **32**, 748-749, (1910).
- [70]Smits, A. & Postma, S. Het stelsel ammoniak-water. *Versl. Akad. Wet. Ams-terdam* **12**, 110-118, (1910).
- [71]Postma, S. & Smits, A. The system ammonia-water. *Koninklijke Nederlandse Akademie van Wetenschappen Proceedings Series B Physical Sciences* **17**, 182-191, (1914).
- [72]Elliott, L. D. The freezing point curve of the system water-ammonia. *The Journal of Physical Chemistry* **28**, 887-888, (1924).
- [73]Clifford, I. & Hunter, E. The System Ammonia–Water at Temperatures up to 150° C. and at Pressures up to Twenty Atmospheres. *The Journal of Physical Chemistry* **37**, 101-118, (1933).
- [74]Mironov, K. The phase diagram of the system H₂O-NH₃ (translated from Russian). *Zh. Obshch. Khim* **25**, 1081-1086, (1955).
- [75]Rollet, A. & Vuillard, G. Sur un nouvel hydrate de l'ammoniac. *Comptes rendus hebdomadaires des seances de l'academie des sciences* **243**, 383-386, (1956).
- [76]Van Kasteren, P. The crystallization behavior and caloric properties of water/ammonia mixtures between 70 and 300 K. *Bull. Inst. Froid. Annexe* **4**, 81-87, (1973).
- [77]Kargel, J. S. *Cryomagmatism in the outer solar system* PHD thesis, University of Arizona, (1990).
- [78]Yarger, J., Lunine, J. I. & Burke, M. Calorimetric studies of the ammonia - water SYSTEM with application to the outer solar SYSTEM. *Journal of Geophysical Research: Planets* **98**, 13109-13117, (1993).
- [79]Sclater, G., Fortes, A., Norman, L. *et al.* High pressure study of ammonia monohydrate from 0-3.0 GPa. (2011).
- [80]Loveday, J. & Nelmes, R. Ammonia monohydrate VI: A hydrogen-bonded molecular alloy. *Physical review letters* **83**, 4329, (1999).
- [81]Olovsson, I. & Templeton, D. H. The crystal structure of ammonia monohydrate. *Acta Crystallographica* **12**, 827-832, (1959).
- [82]Loveday, J. & Nelmes, R. The ammonia hydrates—Model mixed-hydrogen-bonded systems. *High Pressure Research* **24**, 45-55, (2004).
- [83]Fortes, A. D., Suard, E., Lemée-Cailleau, M. H. *et al.* Equation of state and phase transition of deuterated ammonia monohydrate (ND₃ · D₂O) measured by high-resolution neutron powder diffraction up to 500 MPa. *The Journal of chemical physics* **131**, 154503, (2009).
- [84]Hogenboom, D., Kargel, J., Holden, T. *et al.* in *Lunar and Planetary Science Conference*.
- [85]Hogenboom, D., Kargel, J., Consolmagno, G. *et al.* The ammonia–water system and the chemical differentiation of icy satellites. *Icarus* **128**, 171-180, (1997).
- [86]Fortes, A. D., Suard, E., Lemée-Cailleau, M.-H. *et al.* Crystal structure of ammonia monohydrate phase II. *Journal of the American Chemical Society* **131**, 13508-13515, (2009).
- [87]Wilson, C., Bull, C., Stinton, G. *et al.* Pressure-induced dehydration and the structure of ammonia hemihydrate-II. *The Journal of chemical physics* **136**, 094506, (2012).
- [88]Griffiths, G. I., Misquitta, A. J., Fortes, A. D. *et al.* High pressure ionic and molecular crystals of ammonia monohydrate within density functional theory. *The Journal of chemical physics* **137**, 064506, (2012).
- [89]Fortes, A. D., Brodholt, J. P., Wood, I. G. *et al.* Ab initio simulation of ammonia monohydrate (NH₃ · H₂O) and ammonium hydroxide (NH₄OH). *The Journal of Chemical Physics* **115**, 7006-7014, (2001).
- [90]Bethkenhagen, M., Cebulla, D., Redmer, R. *et al.* Superionic phases of the 1: 1 water–ammonia mixture. *The Journal of Physical Chemistry A* **119**, 10582-10588, (2015).

-
- [91]French, M., Mattsson, T. R., Nettelmann, N. *et al.* Equation of state and phase diagram of water at ultrahigh pressures as in planetary interiors. *Physical Review B* **79**, 054107, (2009).
- [92]Bethkenhagen, M., French, M. & Redmer, R. Equation of state and phase diagram of ammonia at high pressures from ab initio simulations. *The Journal of chemical physics* **138**, 234504, (2013).
- [93]Boone, S. & Nicol, M. in *Lunar and Planetary Science Conference Proceedings*. 603-610.
- [94]Koumvakalis, A. & Nicol, M. in *High Pressure Chemistry, Biochemistry and Materials Science Raman Spectroscopy of Ammonia Monohydrate to 13.5 GPa* 265-274 (Springer, 1993).
- [95]Fortes, A. D., Wood, I. G., Alfredsson, M. *et al.* The high-pressure phase diagram of ammonia dihydrate. *High Pressure Research* **27**, 201-212, (2007).
- [96]Fortes, A., Wood, I., Vočadlo, L. *et al.* Phase behaviour and thermoelastic properties of perdeuterated ammonia hydrate and ice polymorphs from 0 to 2 GPa. *Journal of Applied Crystallography* **42**, 846-866, (2009).
- [97]Griffiths, G. I., Fortes, A. D., Pickard, C. J. *et al.* Crystal structure of ammonia dihydrate II. *The Journal of chemical physics* **136**, 174512, (2012).
- [98]Loveday, J., Nelmes, R., Bull, C. *et al.* Observation of ammonia dihydrate in the AMH-VI structure at room temperature—possible implications for the outer solar system. *High Pressure Research* **29**, 396-404, (2009).
- [99]Bertie, J. E. & Shehata, M. R. Ammonia dihydrate: Preparation, x-ray powder diffraction pattern and infrared spectrum of $\text{NH}_3 \cdot 2\text{H}_2\text{O}$ at 100 K. *The Journal of chemical physics* **81**, 27-30, (1984).
- [100]Jiang, X., Wu, X., Zheng, Z. *et al.* Ionic and superionic phases in ammonia dihydrate $\text{NH}_3 \cdot 2\text{H}_2\text{O}$ under high pressure. *Physical Review B* **95**, 144104, (2017).
- [101]Wilson, C., Bull, C., Stinton, G. *et al.* On the stability of the disordered molecular alloy phase of ammonia hemihydrate. *The Journal of chemical physics* **142**, 094707, (2015).
- [102]Wilson, C. W. *High-pressure studies of ammonia hydrates* Ph.D. thesis, The University of Edinburgh, (2014).
- [103]Robinson, V. N., Wang, Y., Ma, Y. *et al.* Stabilization of ammonia-rich hydrate inside icy planets. *Proceedings of the National Academy of Sciences* **114**, 9003-9008, (2017).

Chapter 2: Experimental methods

Contents

2.1 Introduction.....	38
2.2 High-pressure and high-temperature device	38
2.2.1 The diamond anvil cell.....	38
2.2.2 High temperature experiments in the DAC.....	39
2.3 Measuring the sample pressure in the DAC.....	40
2.3.1 Luminescent sensors	40
2.3.1.1 Ruby	40
2.3.1.2 Samarium-doped strontium tetraborate.....	42
2.3.2 The diamond Raman gauge.....	43
2.3.3 Pressure measurement by x-ray diffraction.....	44
2.4 Sample preparation and loading.....	45
2.4.1 Sample preparation.....	45
2.4.2 Loading the sample	46
2.5 Analytical techniques	47
2.5.1 X-ray diffraction.....	47
2.5.1.1 Principle of powder x-ray diffraction.....	47
2.5.1.2 X-ray diffraction setups.....	48
2.5.2 Optical vibrational spectroscopies	49
2.5.2.1 Principle of Raman spectroscopy.....	49
2.5.2.2 Raman spectroscopy setup	51
2.5.2.3 Principle of infrared spectroscopy.....	51
2.5.2.4 Infrared spectroscopy setups	52
2.5.3 Quasi-elastic incoherent neutron scattering	52
2.5.3.1 Basic principles	53
2.5.3.2 Experimental methods for high-pressure QENS experiments	59
References.....	62

2.1 Introduction

This chapter presents the high pressure and high temperature experimental methods used in this thesis work. The first part is devoted to the description of the devices used to generate high pressure and high temperature. The second part introduces the means of measuring pressure under high temperature and high pressure. The third part is dedicated to the presentation of sample preparation and loading methods. The last part presents the techniques used to characterize the sample during our work, and includes Raman and infrared spectroscopies, x-ray diffraction and quasielastic incoherent neutron scattering.

2.2 High-pressure and high-temperature device

2.2.1 The diamond anvil cell

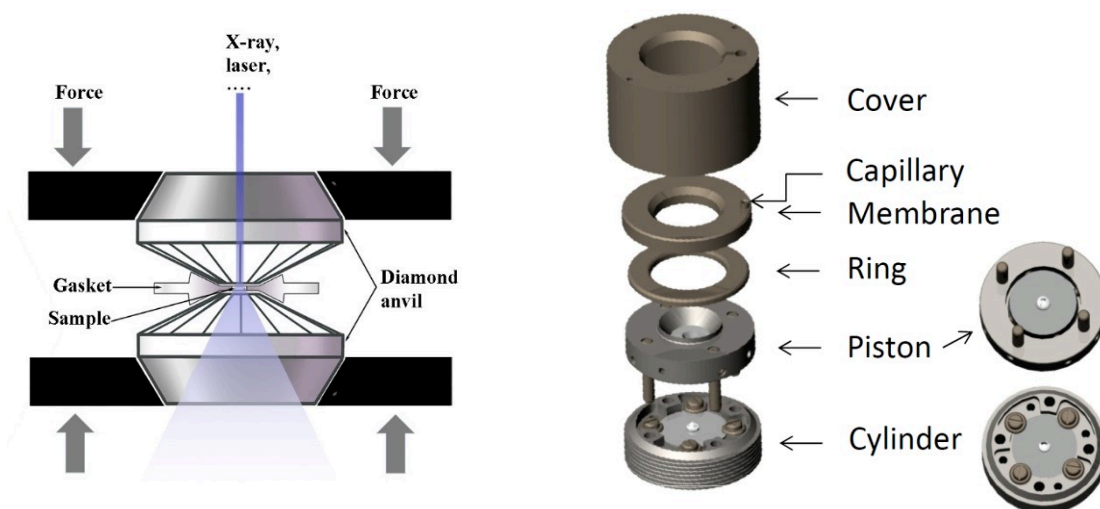


Figure 2.1. (Left) Schematic of the principle of a diamond anvil cell. (Right) The membrane diamond anvil cell used in our experiments.

The diamond anvil cell (DAC) was invented by Weir *et al.*^[1] in 1959. Since then, the DAC has become a very popular tool for research at high pressure. The principle of the DAC is simple: the sample, usually confined in a metallic gasket, is compressed in between the flat parallel tips of two diamond single-crystals facing each other as seen in Figure 2.1(left). The pressure being defined as the ratio of the force F exerted on a surface S ($P=F/S$), the higher the force and the smaller the surfaces are, the higher the pressure is. Diamond is the hardest material known, thus, it can sustain a very high force before rupture. Diamonds culets of 500 μm are used to achieve about 30 GPa, while 50 μm culets are necessary to reach ~ 200 GPa. The maximum pressure generated in a conventional DAC is about 400 GPa, but recently new developments enabled to generate pressures up to the Terapascal range^[2,3].

There exist several designs of the DAC, some of which are shown in Figure 2.2. The schematic representation of the DAC we have used is shown in Figure 2.1 (right). It consists of

four main parts: a cover, an inflatable membrane, a moveable piston, and a cylinder fixed to the cover. The cell works according to the piston-cylinder scheme. The piston has four rectified guide pins which are inserted in the corresponding holes in the bottom half-cylinder to ensure the alignment of the two parts. The movement of the piston is controlled by a membrane which pushes the piston from the top when inflated with pressurized helium gas^[4]. This allows remote and fine control of the sample pressure.

The two diamond anvils are mounted on each part, facing each other. The diamonds are single-crystals with a girdle 3.3 mm large. The tip is polished perpendicular to the [100] direction, resulting in an 8 or 16-sided polygonal face (the culet). The back part of the anvil is shaped like a cone, according to the Boehler-Almax design^[5]. One diamond is glued on a tungsten carbide hemisphere, to allow for parallelism adjustment, while the other one is glued on a platen support which can be moved to adjust the concentricity of the diamond culets. The whole system has to be well aligned to ensure uniaxial compression and to avoid any damage to the diamonds.

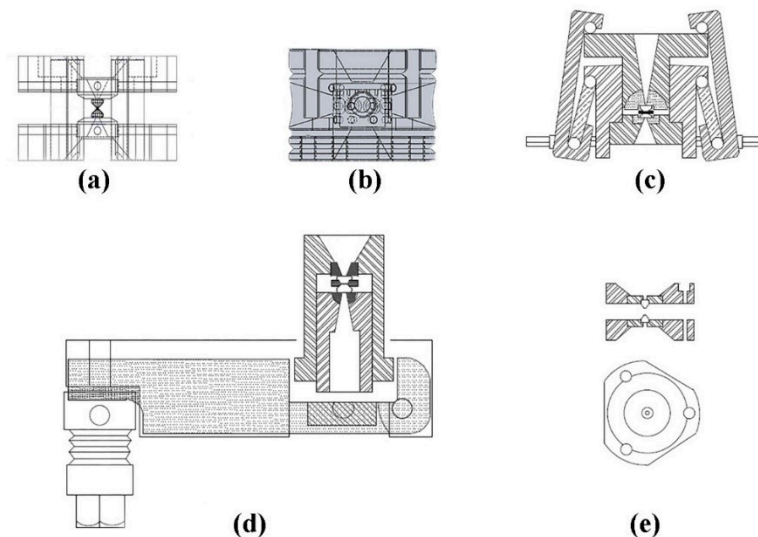


Figure 2.2. Schematic design of commonly employed diamond anvil cells: (a) Four-pin cell; (b) Mao-type cell; (c) Syassen–Holzapfel; (d) Mao–Bell; (e) Merrill–Bassett.

An important part of the DAC is the gasket which acts as a sample chamber. It allows using a pressure transmitting medium to provide quasi-hydrostatic conditions. The gasket is a thin metallic foil of thickness $\sim 200 \mu\text{m}$. Different kinds of materials are used depending upon the requirement. Hard stainless steel is mostly used, but for high temperatures or very high pressure applications rhenium is preferred. The metallic foil is first compressed in between the two diamonds to form an imprint of $40\text{--}80 \mu\text{m}$ thickness (depending on the diamond culet size) and then a circular hole is drilled at the center of the indentation using a laser drilling apparatus. The circular shape is necessary in order to ensure a radially homogeneous pressure field. Typical hole diameters used in our experiments are $100 \mu\text{m}$ for $300 \mu\text{m}$ diamond culets.

2.2.2 High temperature experiments in the DAC

There are two main techniques to heat a sample in a DAC, either by resistive or by laser

heating. Laser heating is used to reach temperatures in excess of 1500 K, while resistive heating is used below ~ 1000 K. In the present work, only resistive heating has been used. Since the whole DAC is heated, temperature gradients are very small (unlike in laser heating) and the sample temperature can be considered as homogeneous. Furthermore, the sample temperature can be precisely controlled and measured using a thermocouple.

Resistive heating has been done by using an external heater. It is a cylindrical resistive heater whose internal diameter and length fit the external dimensions of the cell. It envelops the cell, ensuring homogeneous heating. The heater is connected to a power unit and a temperature controller using a feedback loop. A K-type thermocouple is connected to the cell to measure the sample temperature. The accuracy of temperature measurement, in this case, is about 5 K. It is possible to reach 750 K using this type of resistive heater.

2.3 Measuring the sample pressure in the DAC

An important element in high-pressure research is the pressure gauge which should allow accurate measurements of the sample pressure. It is usually inserted in the sample chamber, experiencing the same pressure as the sample. The gauge is a substance for which the behavior of a certain physical property with pressure is well known so that its measurement gives an indirect measurement of the pressure. Gauges must be small compared to the sample and preferably placed in its center, where the pressure field is more homogeneous. The small size is required not to disturb any measurement on the sample, to experience a strong pressure gradient, and to avoid contact with the diamonds and gasket. In addition, the material of the gauge must be structurally stable and not chemically react with the sample within the experimental P-T range.

Below we describe three means to measure the pressure in the DAC used in the present work, based on, respectively, the gauge luminescence, Raman spectra or equation of state.

2.3.1 Luminescent sensors

A rapid, easy and effective means of in situ pressure measurements in the DAC is provided by the use of a luminescent compound placed in the sample chamber. This technique is advantageous because it requires only a low-power visible laser and a compact spectrometer. The compactness and low cost of this measurement system make it one of the most common methods of measuring pressure. Here we will present the two compounds that were used in our works, namely the ruby ($\text{Al}_2\text{O}_3: \text{Cr}^{3+}$) and samarium-doped strontium tetraborate ($\text{SrB}_4\text{O}_7: \text{Sm}^{2+}$).

2.3.1.1 Ruby

Since Forman et al. first proposed to use ruby as a pressure sensor in 1972^[6], this technique has become more and more popular in the application of DACs. The ruby pressure sensor uses the pressure-dependent shift to longer wavelengths of the R_1 and R_2 fluorescence emission lines. Examples of ruby spectra in the area of interest are shown in Figure 2.3. The shift of the most intense line, R_1 , was prone to many calibrations. Barnett et al.^[7] and Piermarini et al.^[8]

calibrated the ruby with the state equation of NaCl from Decker^[9] up to 19.5 GPa. Mao et al.^[10] resume the ruby calibration up to 80 GPa and get a relationship between the displacement of the wavelength R_1 and the pressure, as shown in Eq. 2.1.

$$P = \frac{A}{B} \left[\left(\frac{\lambda_{R_1}(P) - \lambda_{R_1}(P=0)}{\lambda_{R_1}(P=0)} \right)^B - 1 \right] \quad (2.1)$$

Table 2.1. The parameters A , B , and C of Equations 2.1, 2.2 and 2.3 according to various authors.

Equation	A (GPa)	B	C	reference
(2.1)	1904	7.665		Mao et al. (1986) ^[10]
(2.1)	1871	10.06		Dorogokupets et al. (2003) ^[11]
(2.3)	1860	15.5		Kunc, K et al. (2004) ^[12,13]
(2.2)	1845	14.7	7.5	Holzappel et al.(2005) ^[14]
(2.1)	1873	10.82		Chijioke et al. (2005) ^[15]
(2.1)	1920	9.61		Dewaele, A et al. (2008) ^[16]

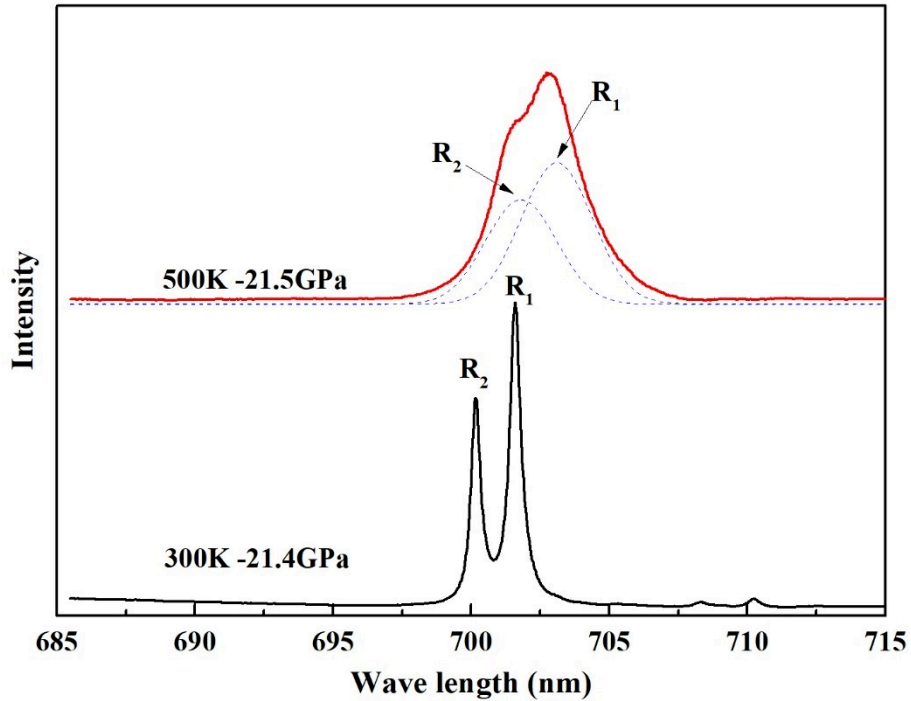


Figure 2.3. Luminescence spectrum of ruby under different temperatures.

The ruby scale has been revisited by several authors in the last ~10 years, based on a new

analysis of shock compression data^[11], and extensive Raman and XRD data for diamond^[17] and metals under hydrostatic conditions^[18]. Other expressions for the pressure as a function of the wavelength have also been proposed:

$$P = \frac{A}{B+C} \left\{ \exp \left[\frac{B+C}{C} \left[1 - \left(\frac{\lambda_{R1}(P)}{\lambda_{R1}(P=0)} \right)^{-C} \right] \right] - 1 \right\} \quad (2.2)$$

$$P = A \left(\frac{\lambda_{R1}(P) - \lambda_{R1}(P=0)}{\lambda_{R1}(P=0)} \right) \left[1 + \frac{B}{2} \left(\frac{\lambda_{R1}(P) - \lambda_{R1}(P=0)}{\lambda_{R1}(P=0)} \right) \right] \quad (2.3)$$

In all cases, P is expressed in GPa, λ_{R1} is the wavelength of the R₁ ruby fluorescence line. The parameters A, B and C according to different authors are reported in Table 2.1. In the present work, we used the calibration proposed by Dewaele *et al.*^[16], which is based on measurements of the equation of state of 12 metals.

The ruby R lines also shift with temperature. Datchi *et al.*^[19] measured the displacement of R₁ over a range of 296 to 900 K, and reported the following result:

$$\Delta\lambda_{R1}(296K < T < 900K) = 0.00746(4)\Delta T - 3.01(25) \times 10^{-6}\Delta T^2 + 8.76(33) \times 10^{-9}\Delta T^3 \quad (2.4)$$

where $\Delta\lambda_{R1} = \lambda(T) - \lambda(T=296 K)$ is in nm and $\Delta T = T - T(296 K)$ in K.

With increasing temperature above 300 K, the ruby lines broaden, overlap and diminish in intensity, as shown in Figure 2.3. The two R lines are no more resolved above 600 K, which reduces the measurement accuracy. In addition, a 5 K variation is equivalent to 0.1 GPa in terms of ruby fluorescence shift^[20-22], such that the temperature of the sample must be known with accuracy in order to reduce the uncertainty on pressure.

2.3.1.2 Samarium-doped strontium tetraborate

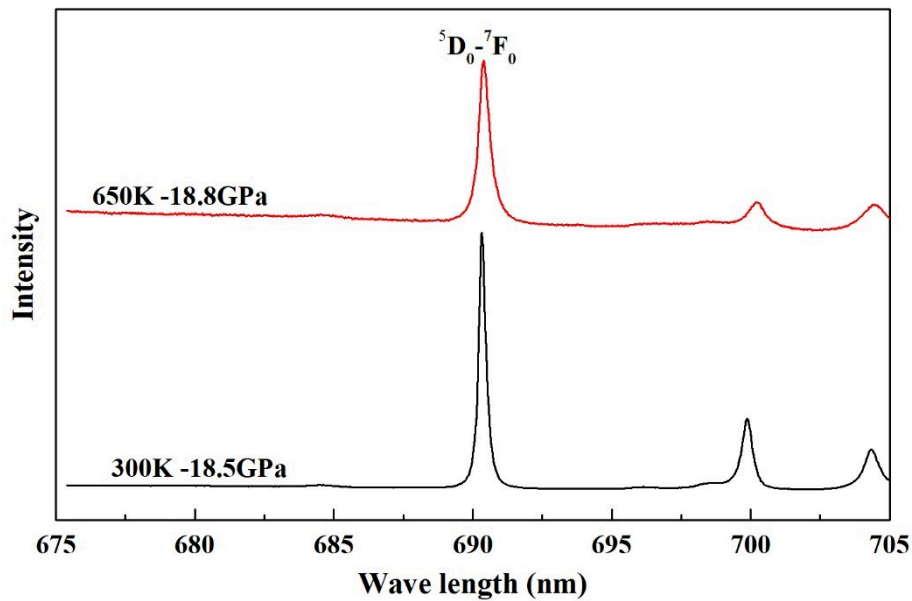


Figure 2.4. Luminescence spectrum of $SrB_4O_7: Sm^{2+}$ at different temperatures around 18.5 GPa.

For the reasons listed above, ruby is not the ideal pressure sensor at high temperatures. Another luminescence sensor was found more adequate for high-temperature DAC experiments: samarium-doped strontium tetraborate ($\text{SrB}_4\text{O}_7: \text{Sm}^{2+}$). This compound has a luminescence line that is a non-degenerate ${}^5\text{D}_0\text{-}{}^7\text{F}_0$ singlet (denoted 0-0) at 685.41 nm at ambient pressure. The first calibration of $\text{SrB}_4\text{O}_7: \text{Sm}^{2+}$ with pressure was reported by Lacam & Chateau^[23] and Leger et al.^[24]. They demonstrated large advantages over ruby: first, the effect of temperature on wavelength shift of $\text{SrB}_4\text{O}_7: \text{Sm}^{2+}$ is almost negligible; second, the bandwidth of $\text{SrB}_4\text{O}_7: \text{Sm}^{2+}$ is narrow, and it varies very slowly with pressure and temperature. Thence, the position of the peak is well distinguished even at high temperatures and pressures, as shown in Figure 2.4. Datchi *et al.*^[19] calibrated this gauge in helium, which provides quasi-hydrostatic conditions up to 124 GPa. Ruby and gold were used as a reference for the pressure and the data were adjusted with the following function:

$$P = A\Delta\lambda \left(\frac{1+B\Delta\lambda}{1+C\Delta\lambda} \right) \quad (2.5)$$

where $A=3.9096$ GPa/nm, $B=3.378 \times 10^{-3}$ nm⁻¹, $C=1.05 \times 10^2$ nm⁻¹ and $\Delta\lambda = \lambda_{0-0}(P) - \lambda_{0-0}(P=0)$. The small non-linear variation of the wavelength with the temperature at ambient P is given by equation 2.6:

$$\Delta\lambda_{0-0}(T) = -8.7(12) \times 10^{-5} \Delta T^2 \Delta T + 4.62(60) \times 10^{-6} \Delta T^2 - 2.38(70) \times 10^{-9} \Delta T^3 \quad (2.6)$$

In fact, the shift with temperature is very small, it is only 0.06 nm in total from 300 to 900 K^[25] which is two orders of magnitude lower than the ruby R_1 line. Therefore, $\text{SrB}_4\text{O}_7: \text{Sm}^{2+}$ is more suitable for high temperature studies than ruby. However, compared to the ruby ball, $\text{SrB}_4\text{O}_7: \text{Sm}^{2+}$ is easily dissolved in supercritical water, or decomposed into small particles in a liquid sample. During our work, we thus combined $\text{Al}_2\text{O}_3: \text{Cr}^{3+}$ (ruby) and $\text{SrB}_4\text{O}_7: \text{Sm}^{2+}$ to measure the pressure in the sample chamber at high temperature and pressure.

2.3.2 The diamond Raman gauge

During the compression of the sample, a pressure gradient exists in the loaded diamond anvil and causes the broadening of the Raman bands of the diamond. The high-frequency edge of the first-order T_{2g} Raman band measured at the center of the diamond tip face exhibits a dependence on the pressure in the sample chamber. This frequency shift can thus be used as a pressure gauge. The optical method was first proposed by Hanfland & Syassen^[26]. One of the calibrations reported on measurements up to 410 GPa^[27] gives

$$P = A \frac{\Delta\omega}{\omega_0} \left[1 + \frac{1}{2} (B - 1) \frac{\Delta\omega}{\omega_0} \right] \quad (2.7)$$

where $\omega_0 = 1333$ cm⁻¹ is the diamond wavenumber at ambient pressure, $A=547$ GPa and $B=3.75$. This method for pressure measurement can effectively avoid chemical contamination of the sample since no calibrant is needed inside the sample. However, it does not give an accurate pressure measurement, especially at low pressure, as it depends on the stress inside the anvil which differs for different anvil culet size^[28]. In our Raman experiments, we only used this method to cross-check the pressure obtained with luminescence sensors.

2.3.3 Pressure measurement by x-ray diffraction

The use of the equation of state (EOS) of some materials to determine pressure is a common method in DAC research, especially during XRD experiments. Indeed, if the EOS of some certain substances are known, the pressure can be determined by measuring its volume using X-ray diffraction techniques. The most common EOS relations which relate the pressure to the volume are the 3-order Birch-Murnaghan (2.8) and Vinet (2.9) equations:

$$P_{B-M} = \frac{3}{2}B_0 \left[\left(\frac{V}{V_0} \right)^{-\frac{7}{3}} - \left(\frac{V}{V_0} \right)^{-\frac{5}{3}} \right] \left[1 + \frac{3}{4}(K'_0 - 4) \left[\left(\frac{V}{V_0} \right)^{-\frac{2}{3}} - 1 \right] \right] \quad (2.8)$$

$$P_{Vinet}(V) = 3B_0 \frac{\left(1 - \left(\frac{V}{V_0} \right)^{\frac{1}{3}} \right)}{\left(\frac{V}{V_0} \right)^{\frac{2}{3}}} \exp \left[\frac{3}{2}(B'_0 - 1) \left(1 - \left(\frac{V}{V_0} \right)^{\frac{1}{3}} \right) \right] \quad (2.9)$$

where V_0 is the volume at zero pressure, $B_0 = -V(\partial P/\partial V)_{P=0}$ is the bulk modulus and $B'_0 = (\partial B_0/\partial P)_{P=0}$ is the first pressure-derivative of the bulk modulus at $P=0$.

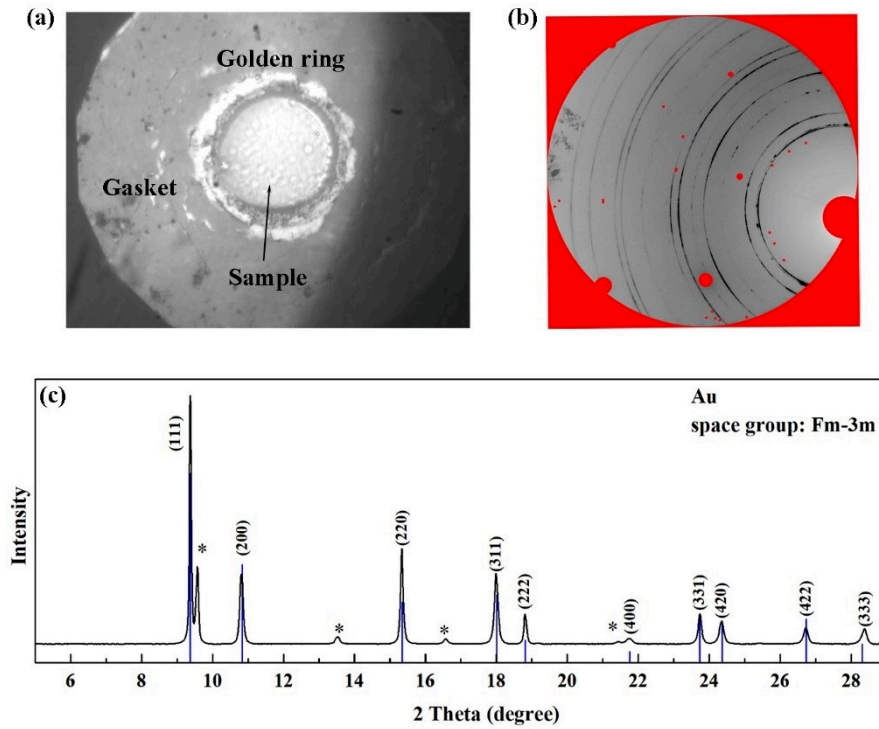


Figure 2.5. (a) Photograph of a loaded sample in a gasket hole lined by a gold ring; (b) and (c) are the XRD diffraction image and diffraction pattern obtained when the x-ray beam is close to the gasket edge. Asterisks in (c) mark the sample diffraction peaks.

The most commonly used standard materials are Au, Pt, MgO and NaCl. Since our samples have strong chemical activity at high temperatures, the chemically inert gold is a good choice to measure the pressure. In addition, it has many other advantages:

- 1) The bulk modulus of gold is rather low, 167 GPa^[29];
- 2) There is no structural phase transition up to 640 GPa^[30] at room temperature;

- 3) It has a strong x-ray diffraction signal;
- 4) The EOS of gold is very well constrained by numerous works, ensuring its accuracy.

Figure 2.5(a) shows the photograph of a typical sample chamber used in this work during synchrotron x-ray diffraction experiments. The rhenium gasket hole is lined by a gold ring, which acts both as a chemically inert barrier between the sample and Re, and as the pressure sensor. The diffraction image and pattern collected in one of our experiments at ESRF ID27 with the x-ray beam ($2 \times 3 \mu\text{m}^2$ FWHM spot size) close to the gold ring at 18.75 GPa and 300 K are shown in Figure 2.5(b,c).

2.4 Sample preparation and loading

2.4.1 Sample preparation

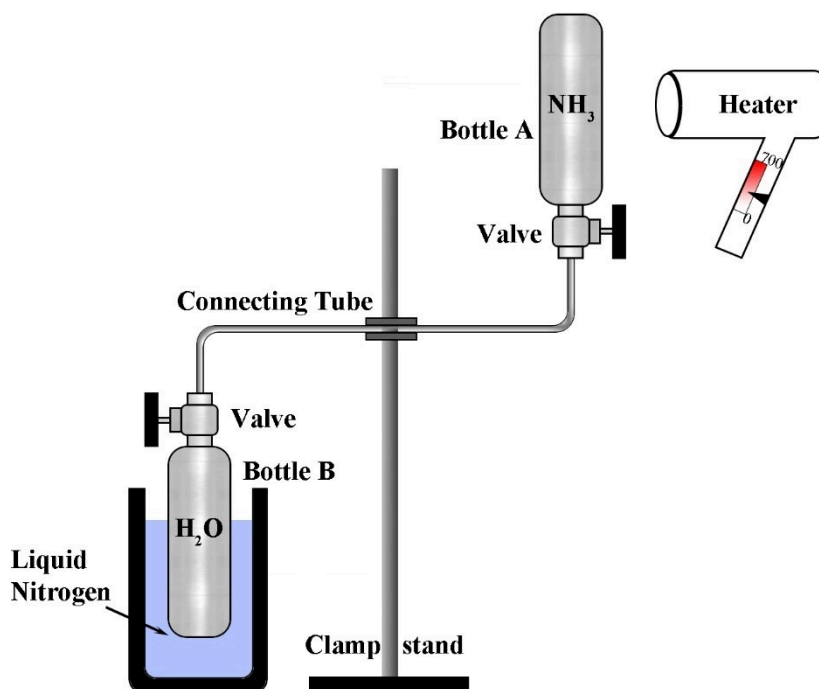


Figure 2.6. Schematic diagram representing the experimental set up used to prepare the mixtures of water and ammonia as described in the text.

Although liquid water and ammonia are fully miscible at low temperature, only $\sim 30\%$ of ammonia can be dissolved in liquid water at ambient conditions. Therefore, the preparation of equimolar mixtures needs to be carried out in a low temperature and sealed environment. Equimolar mixtures of water and ammonia were prepared in a stainless steel cylinder. Ammonia gas (99.99% purity) obtained from Air Liquide and deionized water were used. Ammonia was condensed at the liquid–nitrogen temperature into a preweighed stainless steel bottle. The bottle was sealed, warmed and the amount of ammonia condensed measured by weighing the bottle again. The correct mass of water to create a 1:1 molar mixture was put into a second steel bottle, which was again sealed and the two bottles were connected together, as displayed in Figure 2.6. The bottle containing the water was cooled in liquid nitrogen while the other, containing the

ammonia, was held at room temperature. The valves sealing the bottles were opened and the ammonia condensed into the cold bottle containing the water ice. In order to promote the condensation of all the ammonia into the water bottle, a heat gun was used to heat the ammonia bottle (below 450 K). The valves were then closed and the mixture was allowed to warm to room temperature and homogenize for over 24 h. The final composition was checked by weighing the mixed solution and comparing to the sum of the masses of the two components. The difference was in the range of 0.08–1.74%, and whenever it was larger than 1%, the mixture was discarded and prepared again.

2.4.2 Loading the sample

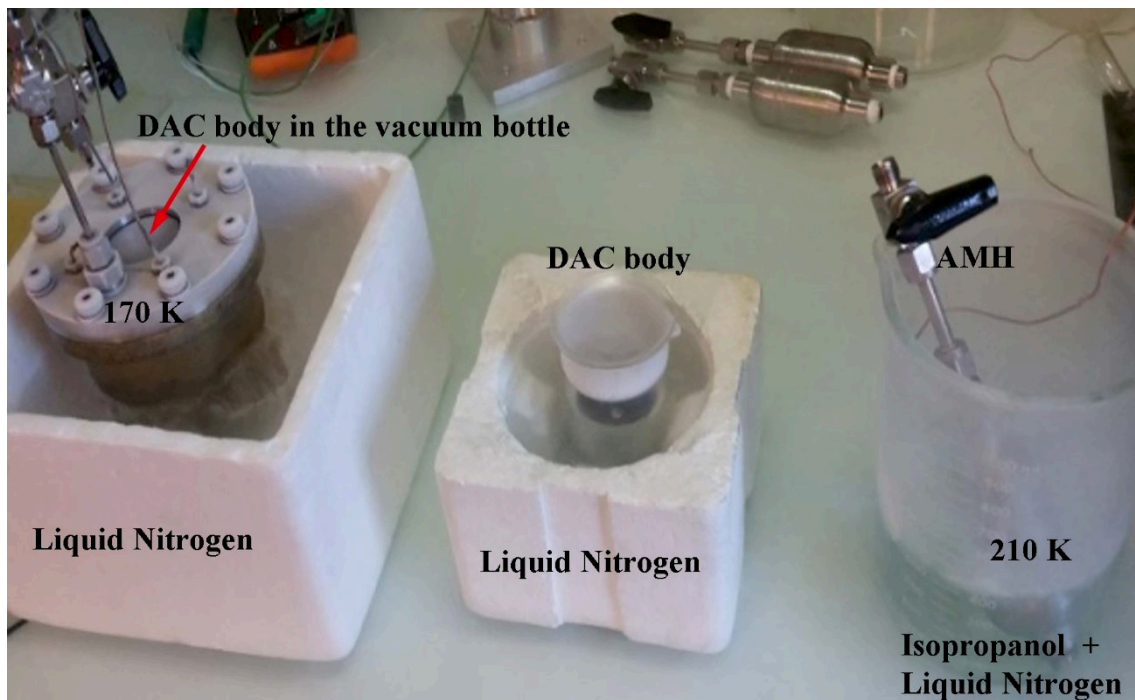


Figure 2.7. Photograph showing the equipment used during the loading of AMH samples into the DAC.

Figure 2.7 shows the equipment used for loading the equimolar ammonia-water mixture into the DAC. The DAC bottom half, to which the gasket is attached, is placed inside a leak-tight cylinder from which air is pumped out and dry helium gas is flushed to prevent the condensation of water vapor inside the gasket hole. The cylinder is cooled to ~ 170 K using liquid N_2 . The other half of the DAC body is cooled separately in a beaker under the atmosphere of the N_2 gas generated by the vaporization of liquid N_2 . The equimolar mixture (AMH) (right part in the photo) is also cooled to ~ 210 K using a mixture of isopropanol and liquid N_2 , in order to bring the mixture in the stable liquid domain at 1 bar, and thus prevent ammonia to evaporate. The sample bottle and cylinder are then opened and a drop of the liquid is rapidly poured onto the gasket hole, which freezes upon contact with the DAC body. The separate DAC body parts are then quickly assembled, put back above the liquid N_2 bath, and compressed to a pressure between 10 and 25 GPa (estimated from the membrane pressure) before letting the DAC warm to room temperature. The compression and warming rates, as well as the pressure at which the sample is warmed up, are not precisely controlled and varied

between loadings. According to ref.^[31], the stable solid phase recovered using this procedure is AMH VI, whereas the direct room temperature compression of the liquid results in a mixed AHH II + ice VII sample^[32].

2.5 Analytical techniques

2.5.1 X-ray diffraction

Understanding the structure of a material and how the latter evolves with pressure and temperature is essential for multiple scientific questions of fundamental or applied interest. Nowadays, the x-ray diffraction method is the most used technique to determine the structure of samples under extreme P-T conditions. The use of synchrotron sources, in particular of the third generation such as the European Synchrotron Radiation Facility (ESRF, Grenoble, France) and the SOLEIL synchrotron (Saint Aubin, France), has revolutionized the domain by providing a highly focused and extremely brilliant x-ray beam, enabling the study of very small samples and/or composed of light elements. Most x-ray diffraction experiments performed during this thesis have been made at ESRF (ID27 beamline) or SOLEIL (PSICHE Beamline). Below we describe the principles of this method and give some relevant information on these beamlines.

2.5.1.1 Principle of powder x-ray diffraction

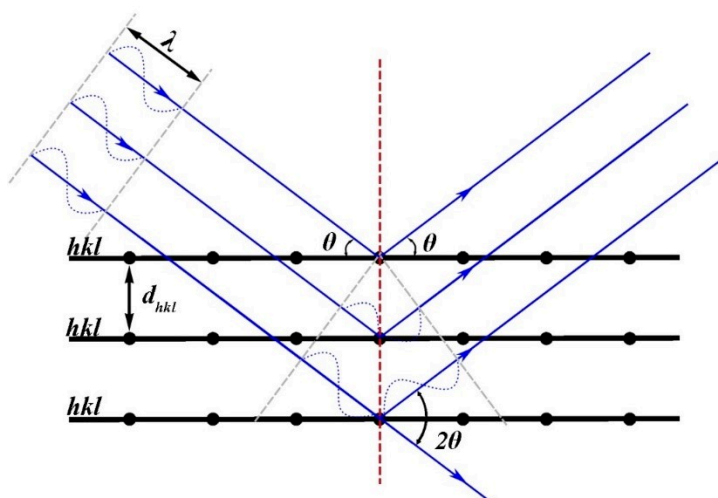


Figure 2.8. Schematic of Bragg's formalism: the incident X-ray is elastically scattered by a set of parallel and equidistant planes separated by the interreticular distance d_{hkl} where h , k and l are the Miller indices.

The diffraction of x-rays by matter results from the direct interaction of x-rays with the electronic density of the material and has thus been early recognized as a powerful technique to obtain an atomic description of its structure. Figure 2.8 displays a simplified view of the diffusion of an x-ray beam of wavelength λ with incident angle θ by a network of atoms in a crystal. The latter can be described as an ensemble of equidistant lattice (reticular) planes of atoms indexed by the Miller indices (hkl) . Constructive interference between the scattered x-ray waves by the atomic electronic clouds from all the lattice planes will be obtained if the

Bragg conditions are satisfied:

$$2d_{hkl}\sin(\theta) = n\lambda \quad (2.10)$$

where d_{hkl} is the interreticular distance between the lattice planes of the index (hkl) and n is a positive integer. Thus, for a given x-ray wavelength, the (hkl) lattice planes will diffract the x-rays at a given angle (called a Bragg reflection), which enables to determine d_{hkl} . The knowledge of all interreticular distances will enable to determine the metrics and elements of the symmetry of the atomic crystalline lattice.

The sum of the complex amplitudes diffused by the atoms of the lattice is called the structure factor F_{hkl} for the (hkl) reflection:

$$F_{hkl} = \sum_{j=1}^n N_j f_j e^{2\pi i(hx_j + ky_j + lz_j)} e^{-T} \quad (2.11)$$

where N_j is the occupancy rate of the atom j , f_j is the atomic diffusion factor of the atom j and x_j , y_j and z_j are the coordinates of the atom j in the lattice. T takes into account the influence of the atomic displacements with respect to equilibrium positions due to the thermal agitation:

$$T = B_j \frac{\sin^2 \theta_{hkl}}{\lambda^2} \quad (2.12)$$

where B_j the Debye-Waller coefficient of isotropic thermal agitation of the atom j .

The diffracted intensity for the (hkl) reflection is given by

$$I_{hkl} = |F_{hkl} \cdot F_{hkl}^*| \quad (2.13)$$

Thus, the measurement of I_{hkl} enables to obtain further information on the crystalline symmetry and the position of the atoms, from which the complete crystalline structure may be obtained. We note though that the information contained in the phase of F_{hkl} is not present in I_{hkl} , and the “art” of crystallography consists of retrieving these phases from the measured intensities, from which the F_{hkl} and eventually the crystal structure can be deduced.

In the case of the diffraction from a powder sample, the sample is ideally composed of a large number of randomly oriented crystallites. The diffracted diagram will thus consist of all the (hkl) reflections at the same time. Moreover, due to the random orientation, the diagram will have a revolution symmetry with respect to the x-ray beam axis, and the diffracted image seen by a flat bidimensional detector positioned ahead of the sample and perpendicular to the beam will show diffracted intensities along the so-called Debye-Scherrer angles 2θ from the position of the incident beam. The integration of the intensity along with the rings for each 2θ position gives an integrated 1D pattern that is analyzed in order to solve and/or refine the structure.

2.5.1.2 X-ray diffraction setups

In this thesis, all XRD experiments were done in the angular dispersive mode using monochromatic x-rays. Most experiments were done using the synchrotron sources of the European Radiation Synchrotron Facility (ESRF), beamline ID27 or of SOLEIL, beamline PSICHÉ. These two beamlines are specialized in x-ray diffraction experiments under extreme conditions. In both cases, the x-ray wavelength λ was 0.3738 Å. The focused x-ray beam has a

spot size of 2.5x3 μm (FWHM) at ID27, and about 10 μm FWHM at PSICHE. Note that in addition to providing highly focused and brilliant x-ray beams, the availability of small wavelengths at synchrotron sources is advantageous for high pressure experiments due to the limited angular aperture of 74° of the DAC. Since the diffracted angle of a given reflection (2θ) depends on the x-ray wavelength according to the Bragg law (the smaller λ is, the smaller θ is), the use of a small wavelength enables us to collect more Bragg reflection in a given angular aperture.

Diffraction images were recorded on 2D detectors (MarResearch mar345 IP or marCCD at ESRF, marCCD and Dectris Pilatus 2M CdTe at SOLEIL). The acquisition times varied from a few seconds to a few minutes depending on the sample. At the ESRF, the scattered x-rays were in some cases filtered by a multichannel collimator to reduce the large contribution originating from the Compton scattering of the diamond anvils^[33].

Additional diffraction patterns collected during this work were obtained using XRD facility at IMPMC, where the source is a Rigaku Mo rotating anode ($\lambda=0.71 \text{ \AA}$), focused by mirror optics to a size of 70 μm , and the detector is a Rigaku RAXIS-IV image plate.

In all cases, the detector distance and tilt, and the position of the x-ray beam are calibrated using x-ray standards from NIST (Si, LaB₆ or CeO₂). The integration of the x-ray images was performed with the fit2D^[34] or Dioptas^[35] software programs. Le Bail or Rietveld refinement of the diffraction patterns was performed with the Fullprof software suite^[36].

2.5.2 Optical vibrational spectroscopies

Optical vibrational spectroscopies, such as Raman scattering and infrared (IR) absorption spectroscopy, have been major tools for studying the physical and chemical properties of molecular materials under high pressure for many years. Raman and infrared spectroscopies detect the molecular dynamics through the measurements of the molecular vibrations, providing information on the interatomic (molecular) interactions and the microstructure of the material, they are often used to study the high pressure phase diagrams in a DAC, due to their facile implementation and the sensitivity of the frequency, intensity and linewidth of optical vibration peaks to solid-liquid and solid-solid phase transitions.

2.5.2.1 Principle of Raman spectroscopy

Raman spectroscopy is a technique which enables to probe the vibrational modes (or phonons) of a material in the range of optical frequencies (THz). It is broadly used to obtain information on the chemical content, bond properties, crystalline symmetry of material, etc...

The Raman effect was discovered in 1928 by the Indian physicist C.V. Raman, for which he was awarded the Nobel Prize in Physics in 1930. It originates from the interaction of an electromagnetic (EM) wave with the vibrations of a material (molecular vibrations or optical phonons in solids). This interaction can give rise to scattered radiation at the same frequency (ν_0) of the incident EM wave (elastic or Mie-Rayleigh scattering) and to radiation at a different frequency ν (inelastic scattering). The latter process is called Brillouin or Raman scattering, depending on whether the frequency shift $\Delta\nu = \nu_0 - \nu$ is in the range of acoustic (GHz) or optic

(THz) vibrations. An inelastic scattering event is 10^{-3} to 10^{-6} less probable than an elastic scattering one, thus the Brillouin or Raman scattered light will be much less intense than the elastically scattered one.

A full understanding of the Raman effect requires a quantum description of the electric field and of the atomic vibrations. The theory is however complex and beyond the scope of this introductory text. We will thus discuss the Raman effect as described by the classical formalism.

An electromagnetic wave of electric field E interacts with the material through the dipole moment μ of the latter. At first order, μ can be written as:

$$\mu = \mu_0 + \tilde{\alpha}E \quad (2.14)$$

where μ_0 is the permanent (field-free) dipole moment and α is the polarizability of the material. The first term will give rise to the infrared absorption effect, while the second one is responsible for the Raman effect. α quantifies the deformation of the electron clouds induced by the presence of the EM wave. In general, α depends on the orientation of E and is thus a second-rank tensor. The induced dipole moment is, at first order:

$$P = \tilde{\alpha}E \quad (2.15)$$

Classically, the emission of a scattered radiation is explained by the periodic variations of the induced dipole moment P . The elastic part of this scattered radiation comes from the static value of the polarizability (α_0), while the inelastic part (Raman) comes from the oscillations of the polarizability due to the molecular or lattice vibrations.

Let's consider the simplest case of a homo-diatomic molecule (e.g., H_2 or N_2): this molecule has a unique vibration type (stretching) of frequency ν_1 or pulsation $\omega_1 = 2\pi\nu_1$. Since the molecular electronic orbitals are nearly spherical, at first order α is a diagonal tensor $\tilde{\alpha} = \alpha\tilde{1}$, where α is a scalar. The displacement of the atoms along the molecular axis due to the vibration can be expressed as:

$$q = q_0 \cos 2\pi\nu_1 t \quad (2.16)$$

where q_0 is the maximum displacement about the equilibrium position. Typically, this displacement is small, such that the polarizability may be expressed as a Taylor expansion, namely:

$$\alpha = \alpha_0 + \left(\frac{\partial\alpha}{\partial q}\right)_0 q \quad (2.17)$$

If we express the incident electric field of frequency ν as:

$$E = E_0 \cos 2\pi\nu t \quad (2.18)$$

Then P can be expressed as:

$$P = \alpha E = \alpha E_0 \cos 2\pi\nu t \quad (2.19)$$

By combining Eq. 2.16-2.18, we get:

$$\begin{aligned}
P &= \alpha E_0 \cos 2\pi \nu t \\
&= \alpha_0 E_0 \cos 2\pi \nu t + \left(\frac{\partial \alpha}{\partial q}\right)_0 q_0 E_0 \cos 2\pi \nu t \cdot q_0 \cos 2\pi \nu_1 t \\
&= \alpha_0 E_0 \cos 2\pi \nu t + \frac{1}{2} \left(\frac{\partial \alpha}{\partial q}\right)_0 q_0 E_0 \{ \cos [2\pi(\nu + \nu_1)t] + \cos [2\pi(\nu - \nu_1)t] \} \quad (2.20)
\end{aligned}$$

The first term represents the elastic or Mie-Rayleigh scattering (the dipole oscillates at the same frequency as the EM wave) while the second and third term respectively represents the inelastic anti-Stokes and Stokes Raman scattering. If $(\partial\alpha/\partial q)_0$ is equal to zero, both the second and third terms are absent, and the vibration does not have Raman activity. Figure 2.9 displays a schematic Raman spectrum.

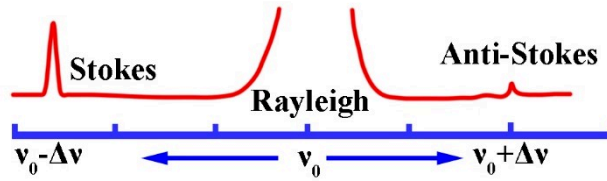


Figure 2.9. Schematic of a typical Raman spectrum.

2.5.2.2 Raman spectroscopy setup

The Raman experiments of this work were carried out at IMPMC with an in-house spectrometer. The excitation source is a continuous laser Ar⁺ at 514.5 nm. The backscattered light was filtered by razor edge filters from Semrock and dispersed by an HR450 spectrograph from Horiba coupled to a CCD camera from Andor. The spectrum obtained represents the Raman intensity as a function of the Raman inelastic shift in cm⁻¹. The optics of the microscope allow focusing on a diameter of about 2 μm.

2.5.2.3 Principle of infrared spectroscopy

As mentioned above, the optical-type molecular or lattice vibrations of a crystal have frequencies in the THz range, which is the range of infrared light. These vibrations are said to be polar if the atomic displacements induce a change in the permanent dipole moment, i.e. $(\partial\mu/\partial q)_0 \neq 0$. In this case, the sample may directly absorb infrared light at the frequency of the vibration. The infrared spectrum is the line spectrum produced by the absorption of a broadband infrared source by the sample. The infrared spectrum can be subdivided according to its wavelength: near-infrared (NIR, 0.75–1.4 μm, 13300–4000 cm⁻¹), mid-wavelength infrared (mid-IR, 2.5–25 μm, 4000–400 cm⁻¹) and far-infrared (far-IR, 25–1000 μm, 400–40 cm⁻¹)^[37]. Among them, the mid-infrared region is the one in which occurs the fundamental vibrations (stretching and bending normal modes of vibration) of most organic and inorganic compounds.

When infrared light illuminates the sample, the radiation can be absorbed by a molecule to cause a transition of vibrational and rotational energy levels. The molecular absorption of infrared radiation and the generation of the vibrational level transition must meet two conditions:

1) *The energy of the radiated photons should satisfy the energy required for molecular transitions.*

Assuming that the frequency of the photon is ν_a , the energy E_a is expressed as $E_a = h\nu_a$. According to the theory of quantum mechanics, the molecular vibrational energy E_V is quantized,

$$E_V = (V + 1/2)h\nu \quad (2.21)$$

where ν is the molecular vibration frequency, V is the vibration quantum number, and its value is 0,1,2, The difference in vibrational energy levels in the molecule is:

$$\Delta E_V = (V_1 + 1/2)h\nu - (V_0 + 1/2)h\nu = \Delta V h\nu \quad (2.22)$$

The vibration level transition is only possible when $\Delta E_V = E_a$ or $\nu_a = \Delta V \nu$. For example, when a molecule transitions from a ground state ($V=0$) to a first excited state ($V=1$), $\Delta V=1$, that is, $\nu_a = \nu$. The amount of energy required to generate a vibrational level transition depends on the reduced mass of the atoms at both ends of the bond and the force constant of the bond, ie, depends on the structural characteristics of the molecule.

2) *In order to satisfy the conditions of generating the infrared absorption spectrum, the molecular vibration must be accompanied by dipole moment changes.*

The mechanism of energy transfer occurs through the variation of the dipole moment caused by the vibration process and the alternating electromagnetic field (infrared) interaction. When the infrared radiation frequency is matched with the dipole frequency, the molecules interact with the radiation (vibration coupling); otherwise, they do not have infrared activity.

2.5.2.4 Infrared spectroscopy setups

There are two main types of infrared spectrometers, including dispersive and Fourier Transform Infrared (FTIR) spectrometers^[38]. Currently, most infrared spectrometers are FTIR-type. The core of the Fourier transform infrared spectrometer is the Michelson interferometer. The time-dependent optical path difference is obtained by moving the mirror to obtain an interference spectrum, which is then converted into an infrared absorption spectrum by Fourier transform.

In our works, FTIR absorption experiments were performed either on the SMIS beamline of the SOLEIL synchrotron facility (Saint-Aubin, France), which provides a 25 μm beam in the mid-IR, or with an in-house interferometer, with a 120 μm beam in the mid-IR. IR spectra were collected in the range 600–8000 cm^{-1} . Synthetic type IIa diamond anvils (Almax industries) with flat culets of 300 or 400 μm diameter were used. In order not to saturate the absorption, the sample was loaded on top of KBr pellet to produce a thin sample film of 1 μm or less. The reference spectra were obtained with the DAC loaded with pure KBr.

2.5.3 Quasi-elastic incoherent neutron scattering

The availability of intense thermal neutron sources since the 1950s has enabled the study of their interaction with matter, from which information on the material static and dynamic properties can be accessed, in a way similar to x-rays. If the thermal neutron beam provides a wavelength range on the order of the distance between the atoms, then the interaction of the neutron beam with the material causes a scattering phenomenon, and the structure of the sample

can be known by analysis. The energy of a thermal neutron, around 25 meV, is of the order of magnitude of many excitations in condensed matter. Therefore, the analysis of the energy exchanged between neutrons and samples also allows access to the dynamics of the system.

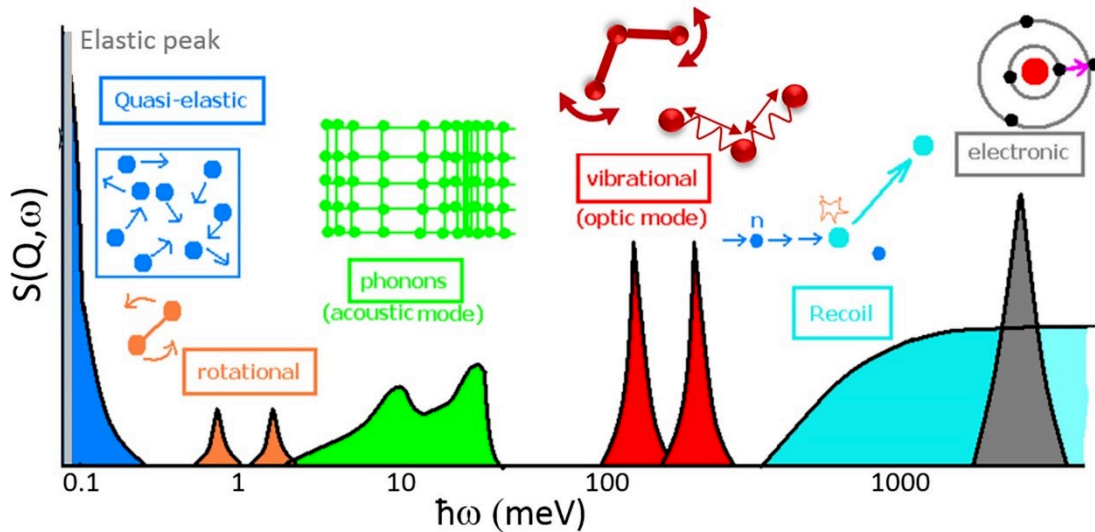


Figure 2.10. Schematics of the dynamical structure factors, $S(Q, \omega)$, of a selection of phenomena accessible by quasi-elastic and inelastic neutron scattering. After ref.^[39]

As shown in Figure 2.10, the signal can correspond to the exchange of quanta of energy between the neutron and the sample over the entire energy range from 0 to several hundred meV. The quasi-elastic region is extended up to a few meV around the elastic peak (zero energy transfer point, 0 meV), which is characteristic of the phenomenon and/or relaxation process in the system. The energy transfer range above 1 meV is commonly referred to as neutron spectroscopy.

2.5.3.1 Basic principles

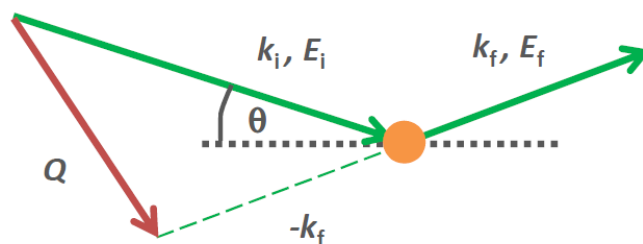


Figure 2.11. Principle of a neutron scattering experiment.

As a result of the neutron interacting with the sample (Figure 2.11), incident neutrons (\vec{k}_i) undergo a wave vector and energy changes which can be expressed as:

$$E = \hbar\omega = \frac{\hbar^2 |\vec{k}|^2}{2m_n}, \quad k = \frac{2\pi}{\lambda} \quad (2.23a)$$

$$\vec{Q} = \vec{k}_i - \vec{k}_f \quad (2.23b)$$

$$\Delta E = \hbar\omega = E_i - E_f \quad (2.23c)$$

where m_n is the neutron mass, \hbar is the Planck constant divided by 2π and \vec{Q} is a diffusion vector.

The diffusion vector $Q = |\vec{Q}|$, the diffusion angle 2θ and the energy transfer $\hbar\omega$ are linked by the relation (the conservation law of momentum and energy imposes the kinematic condition):

$$Q^2 = k_i^2 + k_f^2 - 2k_i k_f \cos 2\theta \quad (2.24a)$$

$$Q^2 = 2 \left(\frac{2\pi}{\lambda_i} \right)^2 \left(1 - \frac{\hbar\omega}{2E_i} - \sqrt{1 - \frac{\hbar\omega}{E_i}} \cos(2\theta) \right) \quad (2.24b)$$

From Eq. 2.24, the maximum energy transfer is defined by the incident energy, here $\hbar\omega_{MAX} = E_i$, as shown in Figure 2.12.

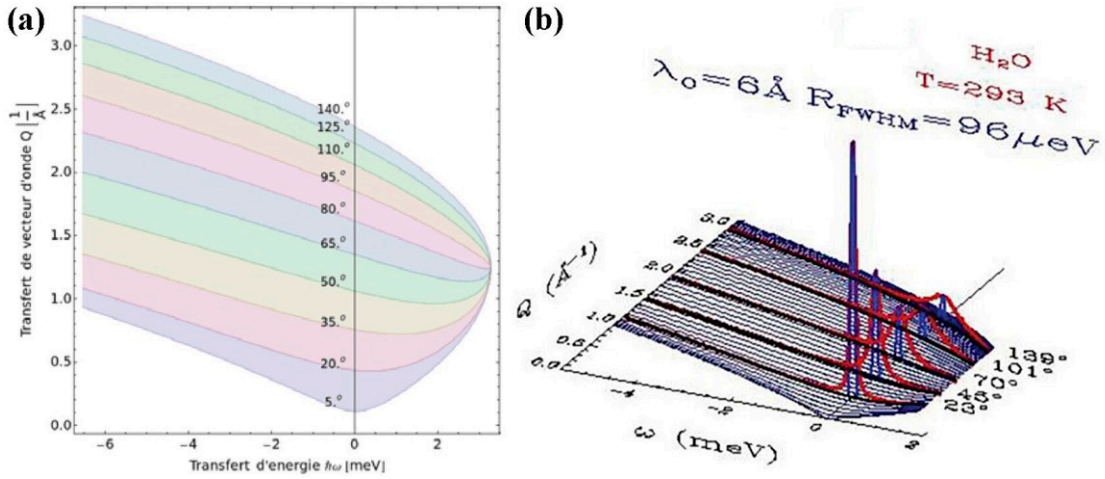


Figure 2.12. (a). Representation of constant-angle lines in space (Q , $\hbar\omega$) from Equation 2.24 form ref.^[39]; (b). The spectrum of water measured on Mibemol (LLB)^[39].

The neutron scattering process is the result of nuclear interactions, depending on the spin of the neutron and of the target nucleus. This process can be taken into account by a single quantity, the scattering length b_i . Experimentally, one measures the differential scattering cross-section $\frac{d^2\sigma}{d\Omega d\omega}$, the number of neutrons scattered over a solid-angle $d\Omega$ and by energy transfer $d\omega$ ^[40]. This quantity is ruled by the time dependence of the positions $\mathbf{r}_i(\mathbf{t})$ of the atoms of the system^[41]:

$$\left(\frac{d^2\sigma}{d\Omega d\omega} \right) = \frac{1}{2\pi} \frac{k_1}{k_0} \sum_{i,j} \langle b_i b_j \rangle \int_{-\infty}^{+\infty} \langle e^{i\vec{Q}\cdot\mathbf{r}_i(0)} e^{-i\vec{Q}\cdot\mathbf{r}_j(t)} \rangle e^{-i\omega t} dt \quad (2.25a)$$

The development of the $\langle b_i b_j \rangle$ term of Eq. 2.25a leads to an expression where the scattered intensity is expressed in terms of coherent and incoherent contributions:

$$\left(\frac{d^2\sigma}{d\Omega d\omega}\right) = \left(\frac{d^2\sigma}{d\Omega d\omega}\right)_{coh} + \left(\frac{d^2\sigma}{d\Omega d\omega}\right)_{inc} \quad (2.25b)$$

The terms of Eq. 2.25b are weighted by the neutron scattering σ_{coh} et σ_{incoh} cross-sections:

$$\left(\frac{d^2\sigma}{d\Omega d\omega}\right)_{coh} = \frac{k_1}{k_0} \frac{\sigma_{coh}}{4\pi} S(Q, \omega) \quad (2.26a)$$

$$\left(\frac{d^2\sigma}{d\Omega d\omega}\right)_{inc} = \frac{k_1}{k_0} \frac{\sigma_{inc}}{4\pi} S_{inc}(Q, \omega) \quad (2.26b)$$

where $S(Q, \omega)$ and $S_{inc}(Q, \omega)$ are the coherent and incoherent dynamical structure factors respectively. The latter obey the so-called summation rules:

$$\int_{-\infty}^{+\infty} S(Q, \omega) d\omega = S(Q) \quad (2.27)$$

$$\int_{-\infty}^{+\infty} S_{inc}(Q, \omega) d\omega = 1 \quad (2.28)$$

The coherent structure factor $S(Q)$ (Eq. 2.27) is usually a Q dependent quantity showing for example Bragg peaks for crystalline materials or halos for liquids. After integration over ω , the incoherent dynamical structure factor is a Q -independent signal (Eq. 2.28). In Small Angle Neutron Scattering (SANS) or diffraction experiments, it is therefore often labeled as a "background" and one tends to minimize its contribution. In what follows, we will show that this incoherent contribution is much more than a background: its dependence on energy carries key information on the dynamics of the system. This feature is made crystal-clear by the use of the van Hove formalism.

Let's consider a particle assembly and a correlation function $G(r, t)$ which indicate the probability of observing a particle at position r at time t , provided that a particle P is at position $r=0$ at time $t=0$. One can split $G(r, t)$ in a *self*, $G_s(r, t)$, and a *distinct*, $G_d(r, t)$ contributions:

$$G(r, t) = G_s(r, t) + G_d(r, t) \quad (2.29)$$

$G_s(r, t)$ is the probability of the initial particle P stands at r at time t , and $G_d(r, t)$ the probability that it is a different particle. The van Hove formalism^[42] establishes a direct connection between the correlation functions above and the scattered intensity:

$$S(Q, \omega) = \frac{1}{2\pi} \int G(r, t) e^{i(Qr - \omega t)} dr dt \quad (2.30)$$

$$S_{inc}(Q, \omega) = \frac{1}{2\pi} \int G_s(r, t) e^{i(Qr - \omega t)} dr dt \quad (2.31)$$

The **coherent intensity** is partly related to the "distinct" $G_d(r, t)$ term. It, therefore, accounts for the collective information. As it appears from Eq. 2.27, for a coherent system, after integration in energy, the analysis of the scattered intensity provides information on the structure of the system. One should note that the "self" term also contributes to Eq. 2.30 (terms $i = j$ of the array Eq. 2.25a). This so-called "self-coherent" contribution is a Q independent signal, adding up to the incoherent scattering to define the high Q limit of diffracted signals. If one now considers the dependence in the energy of the coherent intensity, it is possible to assess

collective dynamical processes like phonons for example.

The **incoherent intensity** is only connected to the self contribution "self" $G_S(r, t)$. As this signal only carries an individual information, it does not give access to any direct information regarding the structure of the system. Depending on the energy associated with the incoherent process, one defines:

- the elastic (i.e. $\hbar\omega = 0$) incoherent scattering: it can be used to access indirect dynamical information (mean-square displacements, confinement volume of a particle).
- the quasi-elastic (i.e. energy exchange of few meV) incoherent scattering: it can be used to measure self-diffusion coefficients, residence times in jump diffusion processes.
- the inelastic incoherent scattering: It can be used to extract the vibrational density of states i.e. the distribution in the energy of the vibrational modes of the system.

In this work, we are only concerned about the quasi-elastic incoherent scattering. We detail below the expected theoretical form of the incoherent structure factor relative to different microscopic processes.

Random walk diffusion (Fick's law)

The isotropic diffusion mechanism of a particle can be described as a cyclic phenomenon: following an interaction, with another particle by example, the particle is set in motion and travels a path r_{elem} in space over time τ . Then, a new event changes the speed and direction of the particle so that the initial history of the particle (position, speed, direction) is lost. One can show that^[43], if we observe the system at a scale larger than r_{elem} and a long time compared to τ , the probability of finding the particle at a position r at time t obeys the relation:

$$\frac{\partial G_S(r, t)}{\partial t} = D_t \nabla^2 G_S(r, t) \quad (2.32)$$

where D_t is the long range diffusion coefficient. With the boundary conditions $G_S(r, 0) = \delta(r)$ and $G_S(r, \infty) = 0$, the solution of this differential equation is:

$$G_S(r, t) = \frac{1}{(4\pi D_t t)^{3/2}} e^{-\frac{r^2}{4D_t t}} \quad (2.33)$$

The corresponding incoherent dynamic structure factor is obtained by time Fourier transform:

$$S_{inc}(Q, \omega) = \frac{1}{\pi} \frac{D_T Q^2}{(D_T Q^2)^2 + \omega^2} \quad (2.34)$$

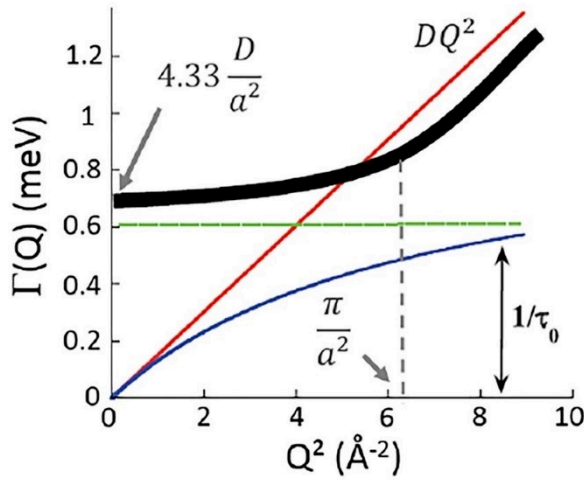


Figure 2.13. Q -dependence of the quasi-elastic HWHM of selected dynamical processes. In red: long-range translational diffusion (Fick's law or DQ^2 law). Blue: jump-diffusion. Green: reorientational diffusion. Black: diffusion within a confinement volume^[43,44].

As can be seen from Eq. 2.34, $S_{inc}(Q, \omega)$ is a Lorentzian line in energy with integrated intensity 1 (as shown in Eq. 2.28). The half-width at half maximum (HWHM) is $\Gamma = D_T Q^2$ which shows a linear dependence with Q^2 and the slope is D_T , as shown in Figure 2.13.

Jump diffusion

In the situation where the (Q, ω) range used allows to access phenomena with spatial and temporal characteristics of the same order of magnitude than those of the elementary process leading to the diffusion, the conditions that led us to write Eq. 2.32 is no longer valid. It is the case when working at a large vector of diffusion. In the model of jump diffusion^[43], it is assumed that between two events leading to diffusion, the particle remains on a given site for a time τ_0 , very long in front of the jump duration τ . In this case, the dynamic structure factor writes:

$$S_{inc}(Q, \omega) = \frac{1}{\pi} \frac{\Gamma(Q)^2}{\Gamma(Q)^2 + \omega^2} \quad (2.35)$$

$S_{inc}(Q, \omega)$ is thus still a Lorentzian line with an HWHM $\Gamma(Q)$:

$$\Gamma(Q) = \frac{D_T Q^2}{1 + D_T Q^2 \tau_0} \quad (2.36)$$

At small Q , Eq. 2.36 is similar to the free diffusion model $D_T Q^2$. At large Q , Eq. 2.36 makes the linear behavior tend to an asymptotic value of the reverse of the residence time τ_0 , as the blue line shown in Figure 2.13.

Rotational diffusion

In the case of a particle diffusing freely over a sphere of radius b , with a good approximation^[45], the incoherent dynamical structure factor writes

$$S_{inc}(Q, \omega) = B_0(Q) \delta(\omega) + [1 - B_0(Q)] L(\omega, \Gamma_R) \quad (2.37)$$

where $B_0(Q) = j_0(bQ)^2$ and $j_l(x)$ is the 1st-order spherical Bessel function. $\delta(\omega)$ represents the elastic peak. $L(\omega, \Gamma_R)$ represents a Lorentzian line with the HWHM $\Gamma_R = 2D_R$ where D_R is the rotational diffusion coefficient, which is the inverse of the rotational relaxation time.

At the opposite of the free (non-confined) diffusion: *i*) the particle is confined in a restricted

portion of the space induces the presence of an elastic peak in the expression of the dynamical structure factor [first term in $\delta(\omega)$], *ii*) I_R is Q independent. This is a property common to all the reorientational processes.

The elastic and quasi-elastic incoherent structure factor (EISF and QISF, respectively) are defined by the following equations:

$$\text{EISF}(Q) = \frac{I^{el}(Q)}{I^{el}(Q)+I^{qe}(Q)} \quad (2.38a)$$

$$\text{QISF}(Q) = \frac{I^{qe}(Q)}{I^{el}(Q)+I^{qe}(Q)} \quad (2.38b)$$

where $I^{el}(Q)$ and $I^{qe}(Q)$ are the elastic and quasi-elastic intensity, respectively, ie:

$$I^{el}(Q) = \int S_{inc}^{el}(Q, \omega) d\omega \quad (2.39a)$$

$$I^{qe}(Q) = \int S_{inc}^{qe}(Q, \omega) d\omega \quad (2.39b)$$

The Q dependence of the EISF or QISF provides information about the geometry of the motion.

Vibrational dynamics

The intensity excitations strongly depend on the temperature (T) of the system. The state vibration density (VDOS), $g(\omega)$ is actually the frequency distribution function of the vibrations of the system. At a temperature T, the intensity of elastic scattering is proportional to^[46]:

$$S(Q, \omega = 0) = e^{-Q^2 \langle u^2 \rangle / 3} \delta(\omega) \quad (2.40)$$

where $\langle u^2 \rangle = \frac{\hbar}{6MN} \int \frac{g(\omega)}{\omega} \coth\left(\frac{\hbar\omega}{2k_B T}\right) d\omega$ represents the single-proton vibrational amplitude and $g(\omega)$ is the density of states which is controlled by the temperature of the sample via the Bose population factor. This term is analogous to the Debye-Waller factor of solids.

The total dynamical structure factor

In general, the total dynamic structural factor (DSF) is the convolution of the structure factors described in previous sections (in its simplest case we can consider vibrations, rotations and translations):

$$S_{inc}(Q, \omega) = S_{inc}^{trans}(Q, \omega) \otimes S_{inc}^{rot}(Q, \omega) \otimes S_{inc}^{vib}(Q, \omega) \quad (2.41)$$

It is worth noting that for the sake of simplicity, we assume that they are independent motions. The specific formula used in our experiment will be described in detail in the QENS section of Chapter 5.6. Of course, in the experiment, the signal $S(Q, \omega)_{exp}$ is the convolution product of the DSF, $S(Q, \omega)$ by the instrumental resolution $R(Q, \omega)$:

$$S(Q, \omega)_{exp} = S(Q, \omega) \otimes R(Q, \omega) \quad (2.42)$$

2.5.3.2 Experimental methods for high-pressure QENS experiments

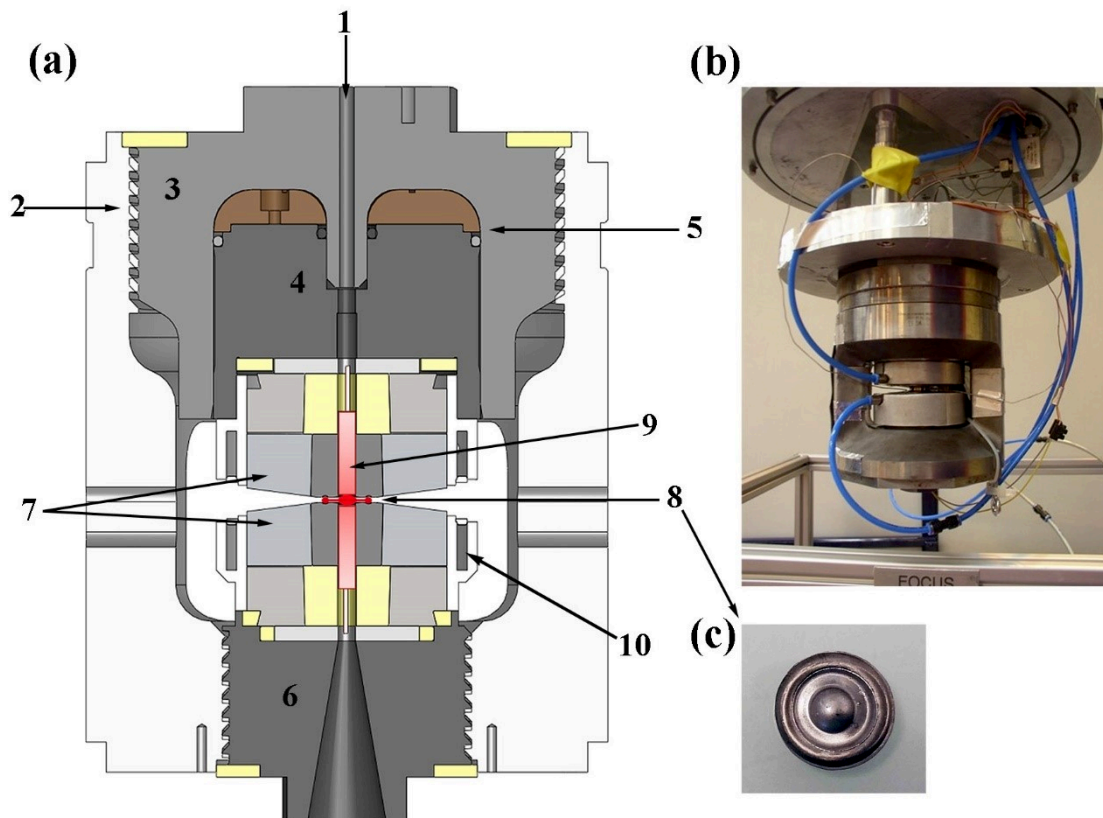


Figure 2.14. (a). Paris-Edinburgh high pressure hydraulic cell for QENS measurements: (1) oil inlet, (2) load frame, (3) cylinder, (4) piston, (5) O-ring seal, (6) breach, (7) anvils, (8) gaskets and sample (red), (9) cartridge heater, (10) cooling rings; (b). the photo of Paris-Edinburgh high pressure hydraulic cell; (c) Inconel gasket. Diameter: 16.4 mm.

The high-pressure QENS experiments were performed using the Paris-Edinburgh (PE) press, which allows measurements to be carried out in the multi GPa range and specially conceived for QENS measurements^[47,48]. As seen in Figure 2.14, the PE press is an opposed-anvil apparatus. The sample is loaded inside a toroidal gasket which is located in the center of the anvil culet.

The gasket (Figure 2.14 (c)) consists of two symmetrical parts with a 16.4 mm diameter. The most suitable material for this gasket is Inconel which is suited for high temperature and meets the requirements for high strength and low incoherent and absorption cross-sections. Anvils were made of sintered diamond which has a central bore of 6 mm diameter to insert two 80 W cartridge heaters. At the same time, the external water cooling setup ensures anvils cooling. Two K-type thermocouples were attached to each anvil to measure temperature, and the distance from the gasket was approximately 5 mm. The temperature gradient between the sample position and the edge of the gasket is almost zero, as demonstrated by finite-element calculations^[48].

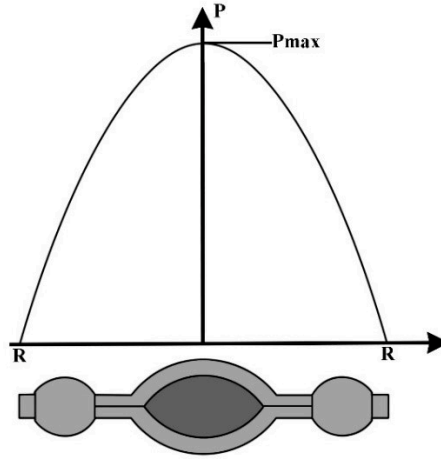


Figure 2.15. Simple model of the pressure distribution across the sample-gasket assembly in toroidal anvils.

Since the anvil is opaque, it is inconvenient to determine the pressure. However, there is an easy method to determine approximately the maximum achieved pressure after unloading. From this, intermediate pressure can be determined according to the force on the anvils and the appropriate interpolation scheme. As shown in Figure 2.15, the premise of this method is to assume that the pressure distribution across the gasket and sample is parabolic^[48]:

$$P(r) = P_{max} \left(1 - \frac{r^2}{R^2}\right) \quad (2.43)$$

where P_{max} is the maximal pressure at the center of the sample chamber, R is the radius of the gasket where the pressure is necessarily zero. The total force F applied to the anvil is the surface below the parabola, so the integral of Eq. (2.43) between 0 and R can be expressed as^[48]:

$$P_{max} = \frac{2F}{A} \quad (2.44)$$

where $A = \pi R^2$ is the cross-section of the gasket (in our experiment $R = 8.2$ mm). After multiple measurements^[48], for "standard" samples, the pressures obtained by Eq. 2.44 is close to the pressures measured by *in situ* methods, the error is about ± 10 -20 %. Typically 80 tonnes are needed to deform the gasket assembly and generate pressures in the multi-GPa range which were generated by a VX Paris-Edinburgh press (the capacity is 130 tonnes)^[49]. Hydraulic pressure was supplied by the manual oil pump and maintained at the desired value.

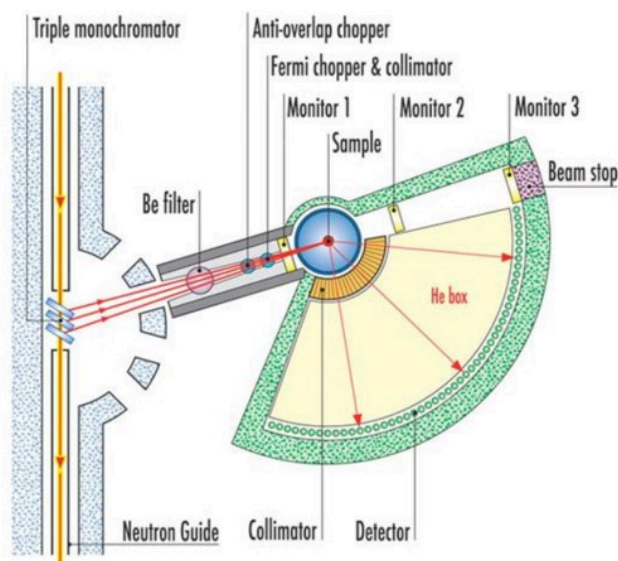


Figure 2.16. *The instrument layout of IN6-Sharp.*

QENS experiments were performed at Institut Laue Langevin (ILL), beamline IN6-Sharp (as shown in Figure 2.16) which is a time-focussing time-of-flight spectrometer designed for quasielastic and inelastic scattering for incident wavelengths in the range of 4 to 6 Å. In our measurements, the incident wavelength is 5.1 Å, with an energy resolution of 70 μeV. The elastic momentum transfer Q covered the range of 0.45 to 1.95 Å⁻¹ corresponding to the angular range of 10° to 115° of the detector banks. In order to improve the counting statistics, the signals of all the 60 available detectors were grouped in 6 groups of 10 detectors each, corresponding to the following average wave vectors $Q = 0.45, 0.75, 1.05, 1.35, 1.65$ and 1.95 Å⁻¹. Similar scans were collected for the empty cell, empty gasket and a vanadium standard to properly account for all background contributions, experimental resolution and detector efficiency. The background signal from the gasket is mainly elastic and can be clearly distinguished from the quasi-elastic signal of the sample and extracted at each Q vector. The data were thus corrected for background and cell scattering, sample self-absorption, and for the multiple scattering (MS) processes occurring within both the sample and the gasket.

Due to the high volatility of our sample, it is necessary to load the sample into the two symmetrical gaskets at low temperatures. First, the sample was cooled to ~210 K using the mixture of isopropanol and liquid N₂, the two gaskets were cooled to ~170 K using liquid N₂. Second, a big drop of the liquid was then poured on one half of the gasket, which froze in contact with the gasket, and then the second gasket half was rapidly added on top. Finally, the gasket-sample assembly is quickly transferred into the center of the toroidal anvils and put under sufficient load to ensure a tight confinement of the sample.

References

- [1]Weir, C., Lippincott, E., Van Valkenburg, A. *et al.* Infrared studies in the 1-to 15-micron region to 30,000 atmospheres. *Journal of Research of the National Bureau of Standards. Section A, Physics Chemistry* **63**, 55, (1959).
- [2]Dubrovinskaia, N., Dubrovinsky, L., Solopova, N. A. *et al.* Terapascal static pressure generation with ultrahigh yield strength nanodiamond. *Science advances* **2**, e1600341, (2016).
- [3]Dewaele, A., Loubeyre, P., Occelli, F. *et al.* Toroidal diamond anvil cell for detailed measurements under extreme static pressures. *Nature communications* **9**, (2018).
- [4]Letoullec, R., Pinceaux, J. & Loubeyre, P. The membrane diamond anvil cell: a new device for generating continuous pressure and temperature variations. *International Journal of High Pressure Research* **1**, 77-90, (1988).
- [5]Boehler, R. & De Hantsetters, K. New anvil designs in diamond-cells. *High Pressure Research* **24**, 391-396, (2004).
- [6]Forman, R. A., Piermarini, G. J., Barnett, J. D. *et al.* Pressure measurement made by the utilization of ruby sharp-line luminescence. *Science* **176**, 284-285, (1972).
- [7]Barnett, J., Block, S. & Piermarini, G. An optical fluorescence system for quantitative pressure measurement in the diamond-anvil cell. *Review of scientific instruments* **44**, 1-9, (1973).
- [8]Piermarini, G. & Block, S. Ultrahigh pressure diamond-anvil cell and several semiconductor phase transition pressures in relation to the fixed point pressure scale. *Review of Scientific Instruments* **46**, 973-979, (1975).
- [9]Decker, D. L. High-pressure equation of state for NaCl, KCl, and CsCl. *Journal of Applied Physics* **42**, 3239-3244, (1971).
- [10]Mao, H., Xu, J.-A. & Bell, P. Calibration of the ruby pressure gauge to 800 kbar under quasi-hydrostatic conditions. *Journal of Geophysical Research: Solid Earth* **91**, 4673-4676, (1986).
- [11]Dorogokupets, P. & Oganov, A. in *DOKLADY EARTH SCIENCES C/C OF DOKLADY-AKADEMIIA NAUK*. 854-857 (INTERPERIODICA PUBLISHING).
- [12]Kunc, K., Loa, I. & Syassen, K. Equation of state and phonon frequency calculations of diamond at high pressures. *Physical Review B* **68**, 094107, (2003).
- [13]Kunc, K., Loa, I. & Syassen, K. Diamond under pressure: Ab-initio calculations of the equation of state and optical phonon frequency revisited. *High Pressure Research* **24**, 101-110, (2004).
- [14]Holzapfel, W. B. Progress in the realization of a practical pressure scale for the range 1–300 GPa. *High Pressure Research* **25**, 87-99, (2005).
- [15]Chijioke, A. D., Nellis, W., Soldatov, A. *et al.* The ruby pressure standard to 150 GPa. *Journal of Applied Physics* **98**, 114905, (2005).
- [16]Dewaele, A., Torrent, M., Loubeyre, P. *et al.* Compression curves of transition metals in the Mbar range: Experiments and projector augmented-wave calculations. *Physical Review B* **78**, 104102, (2008).
- [17]Occelli, F., Loubeyre, P. & LeToullec, R. Properties of diamond under hydrostatic pressures up to 140 GPa. *Nature materials* **2**, 151, (2003).
- [18]Dewaele, A., Loubeyre, P. & Mezouar, M. Equations of state of six metals above 94 GPa. *Physical Review B* **70**, 094112, (2004).
- [19]Datchi, F., Dewaele, A., Loubeyre, P. *et al.* Optical pressure sensors for high-pressure–high-temperature studies in a diamond anvil cell. *High Pressure Research* **27**, 447-463, (2007).

-
- [20]Ragan, D. D., Gustavsen, R. & Schiferl, D. Calibration of the ruby R 1 and R 2 fluorescence shifts as a function of temperature from 0 to 600 K. *Journal of applied physics* **72**, 5539-5544, (1992).
- [21]Vos, W. L. & Schouten, J. A. On the temperature correction to the ruby pressure scale. *Journal of applied physics* **69**, 6744-6746, (1991).
- [22]Rekhi, S., Dubrovinsky, L. S. & Saxena, S. K. Temperature-induced ruby fluorescence shifts up to a pressure of 15 GPa in an externally heated diamond anvil cell. *High Temperatures-High Pressures* **31**, 299-305, (1999).
- [23]Lacam, A. & Chateau, C. High-pressure measurements at moderate temperatures in a diamond anvil cell with a new optical sensor: SrB₄O₇: Sm²⁺. *Journal of Applied Physics* **66**, 366-372, (1989).
- [24]Leger, J., Chateau, C. & Lacam, A. SrB₄O₇: Sm²⁺ pressure optical sensor: Investigations in the megabar range. *Journal of Applied Physics* **68**, 2351-2354, (1990).
- [25]Datchi, F., LeToullec, R. & Loubeyre, P. Improved calibration of the SrB₄O₇: Sm²⁺ optical pressure gauge: advantages at very high pressures and high temperatures. *Journal of Applied Physics* **81**, 3333-3339, (1997).
- [26]Hanfland, M. & Syassen. A Raman study of diamond anvils under stress. *Journal of applied physics* **57**, 2752-2756, (1985).
- [27]Akahama, Y. & Kawamura, H. in *Journal of Physics: Conference Series*. 012195 (IOP Publishing).
- [28]Baer, B. J., Chang, M. E. & Evans, W. J. Raman shift of stressed diamond anvils: Pressure calibration and culet geometry dependence. *Journal of Applied Physics* **104**, 034504, (2008).
- [29]Dorogokupets, P. & Dewaele, A. Equations of state of MgO, Au, Pt, NaCl-B1, and NaCl-B2: Internally consistent high-temperature pressure scales. *High Pressure Research* **27**, 431-446, (2007).
- [30]Dubrovinsky, L., Dubrovinskaia, N., Prakapenka, V. B. *et al.* Implementation of micro-ball nanodiamond anvils for high-pressure studies above 6 Mbar. *Nature communications* **3**, 1163, (2012).
- [31]Loveday, J. & Nelmes, R. Ammonia monohydrate VI: A hydrogen-bonded molecular alloy. *Physical review letters* **83**, 4329, (1999).
- [32]Wilson, C., Bull, C., Stinton, G. *et al.* Pressure-induced dehydration and the structure of ammonia hemihydrate-II. *The Journal of chemical physics* **136**, 094506, (2012).
- [33]Weck, G., Garbarino, G., Ninet, S. *et al.* Use of a multichannel collimator for structural investigation of low-Z dense liquids in a diamond anvil cell: Validation on fluid H₂ up to 5 GPa. *Review of Scientific Instruments* **84**, 063901, (2013).
- [34]Hammersley, A., Svensson, S., Hanfland, M. *et al.* Two-dimensional detector software: from real detector to idealised image or two-theta scan. *International Journal of High Pressure Research* **14**, 235-248, (1996).
- [35]Prescher, C. & Prakapenka, V. B. DIOPTAS: a program for reduction of two-dimensional X-ray diffraction data and data exploration. *High Pressure Research* **35**, 223-230, (2015).
- [36]Rodríguez-Carvajal, J. Recent advances in magnetic structure determination by neutron powder diffraction. *Physica B: Condensed Matter* **192**, 55-69, (1993).
- [37]Staurt, B. *Infrared spectroscopy: fundamentals and applications*. (John Wiley and Sons, Ltd, 2004).
- [38]Griffiths, P. R. & De Haseth, J. A. *Fourier transform infrared spectrometry*. Vol. 171 (John Wiley & Sons, 2007).
- [39]Ollivier, J. & Zanotti, J.-M. Diffusion inélastique de neutrons par temps de vol. *École thématique de la Société Française de la Neutronique* **10**, 379-423, (2010).
- [40]Squires, G. L. *Introduction to the theory of thermal neutron scattering*. (Cambridge university press, 2012).
- [41]Leclercq-Hugeux, F., Coulet, M.-V., Gaspard, J.-P. *et al.* Neutrons probing the structure and dynamics of liquids. *Comptes Rendus Physique* **8**, 884-908, (2007).

-
- [42]Van Hove, L. Correlations in space and time and Born approximation scattering in systems of interacting particles. *Physical Review* **95**, 249, (1954).
- [43]Bée, M. Quasielastic neutron scattering. (1988).
- [44]Volino, F. & Dianoux, A. Neutron incoherent scattering law for diffusion in a potential of spherical symmetry: general formalism and application to diffusion inside a sphere. *Molecular Physics* **41**, 271-279, (1980).
- [45]Sears, V. Theory of cold neutron scattering by homonuclear diatomic liquids: I. Free rotation. *Canadian Journal of Physics* **44**, 1279-1297, (1966).
- [46]Berrod, Q., Lagrené, K., Ollivier, J. *et al.* in *EPJ Web of Conferences*. 05001 (EDP Sciences).
- [47]Klotz, S., Strässle, T. & Bove, L. Quasi-elastic neutron scattering in the multi-GPa range and its application to liquid water. *Applied Physics Letters* **103**, 193504, (2013).
- [48]Klotz, S. *Techniques in high pressure neutron scattering*. (CRC press, 2012).
- [49]Klotz, S., Strässle, T., Rouse, G. *et al.* Angle-dispersive neutron diffraction under high pressure to 10 GPa. *Applied Physics Letters* **86**, 031917, (2005).

Chapter 3: Observation of a disordered ionico-molecular alloy in ammonia monohydrate

Contents

3.1 Introduction.....	66
3.2 Experimental methods.....	66
3.3 Results.....	66
3.3.1 Ionisation at mild pressure	66
3.3.2 Evolution of the IR spectra with pressure	68
3.3.3 X-ray and neutron diffraction results	71
3.3.3.1 Equation of state of AMH at 300 K.....	74
3.3.3.2 Ionico-molecular transition on decompression	75
3.3.4 The disordered ionico-molecular crystal.....	76
3.4 Conclusions.....	80
References.....	82

3.1 Introduction

In this chapter, we present the results of our investigations of AMH up to 80 GPa at low temperatures from 50 to 300 K by experiments and first-principles computer simulations. Spectroscopic measurements reveal the presence of NH_4^+ and OH^- species above 7.4 GPa but, at variance with the density functional theory (DFT) predictions of refs.^[1,2], AMH does not fully ionize up to 80 GPa, as we observe the persistent signature of NH_3 and H_2O molecules. Our diffraction data show evidence of the presence of a dominant *bcc* phase, similar to DMA, with a minor addition of a second phase which can be assigned to the ionic *P4/nmm* structure. Our computational study reveals that the DMA phase, at 10 GPa, spontaneously but partially ionize, to form a mixed ionic-molecular alloy. Complete ionization is topologically hindered by the substitutional disorder which makes the proton transfer from a water to an ammonia molecule dependent on the near-neighbor environment. This ionic-molecular state of AMH, which we baptize disordered ionic-molecular alloy (DIMA), adds to the list of unconventional forms of ice.

3.2 Experimental methods

In all our experiments, AMH samples were prepared using an equimolar (at 1% precision) liquid mixture rapidly frozen to liquid nitrogen temperature and cold compressed to pressures between 10 and 25 GPa before warming up to room temperature (RT) (see Chapter 2 for experimental details). The low-temperature (LT) compression prevents the dehydration of the AMH solid, which occurs at the liquid-solid transition at RT^[3]. About 30 different samples were studied, either by XRD, Raman and IR experiments.

3.3 Results

3.3.1 Ionisation at mild pressure

Figure 3.1 shows the Raman and infrared (IR) absorbance spectra collected at 10 and 12 GPa, respectively. A striking feature of both spectra is the presence of a well-separated and sharp band at 3700 cm^{-1} . This band has not previously been observed in the ambient pressure, low-T IR spectra of any of the hydrates^[4,5]. To determine whether this results from the predicted pressure-induced ionization of AMH, we compared the experimental spectra to the theoretical ones computed for the *P4/nmm* ionic structure (see Chapter 2 for computational details). As seen in Figure 3.1, the calculations predict a Raman and IR active band at 3745 cm^{-1} in the *P4/nmm* structure, i.e., within 1.2% of the observed one, which originates from the stretching of the OH^- ions. In addition, the experimental spectra present Raman and IR activity near all the predicted frequencies for the *P4/nmm* structure, which include the lattice bands in between 200 and 800 cm^{-1} , the NH_4^+ bending (1460 and 1540 cm^{-1}), twisting (1840 cm^{-1}) and stretching (2715 and 2970 cm^{-1}) vibrations.

This correspondence would suggest that AMH at 10 GPa has indeed transformed into the $P4/nmm$ ionic structure. However, the experimental spectra also show spectral bands in frequency ranges where none is predicted for $P4/nmm$: the Raman bands peaked at 1630, 2040 and 3300 cm^{-1} , and the IR bands at 980 and 1150 cm^{-1} . The broad IR band extending from ~ 2300 to ~ 3500 cm^{-1} can also hardly be assigned to the mere stretching modes of NH_4^+ predicted at 2715 and 2900 cm^{-1} . The frequencies of these “extra” bands are in turn characteristic of the vibrations of the H_2O and NH_3 molecules, which are observed in the ambient pressure hydrates^[4,6]. The Raman stretching band at 3300 cm^{-1} is broad with little features, which is more typical of the disordered solid phases in the pure ices^[7,8]. The Raman and IR spectra thus suggest that the sample is a mixture of ionic and molecular species.

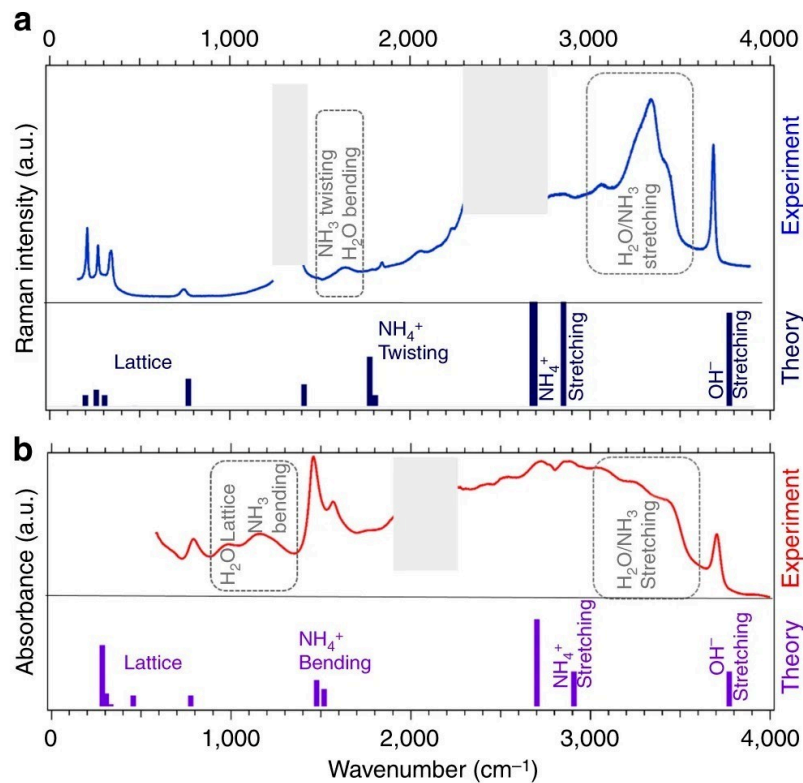


Figure 3.1. Vibrational spectra of AMH. *a.* Raman, and *b.* IR absorption spectra of AMH, at room temperature and respective P of 10 and 12 GPa. The experimental spectra (collected at room temperature) is shown in the upper panels and the theoretical ones (at 0 K) for the fully ionic $P4/nmm$ structure are shown in the lower panels. In the experimental Raman spectra, the frequency regions from 1300-1400 cm^{-1} to 2200-2600 cm^{-1} are greyed as they are dominated by the first- and second-order Raman signal from the diamond anvils, respectively, and in the experimental IR absorption spectrum, the frequency region from 2000 to 2300 cm^{-1} is obscured by the strong IR absorption band of the diamond anvils. For visibility, Raman (respectively, IR) simulated intensities have been divided by 30 (respectively, 5) for NH_4^+ and OH^- stretching modes.

As shown in Figure 3.2, we also observed that the intensities of the Raman peaks assigned to the $P4/nmm$ ionic structure depend on the position of the laser spot (of size 2–3 μm) on the sample and are anti-correlated to those assigned to the molecular species, suggesting that the

distribution of ionic species is not homogeneous over the size of the sample. Moreover, these peaks varied in intensity between different loadings and could not be observed at all in some samples.

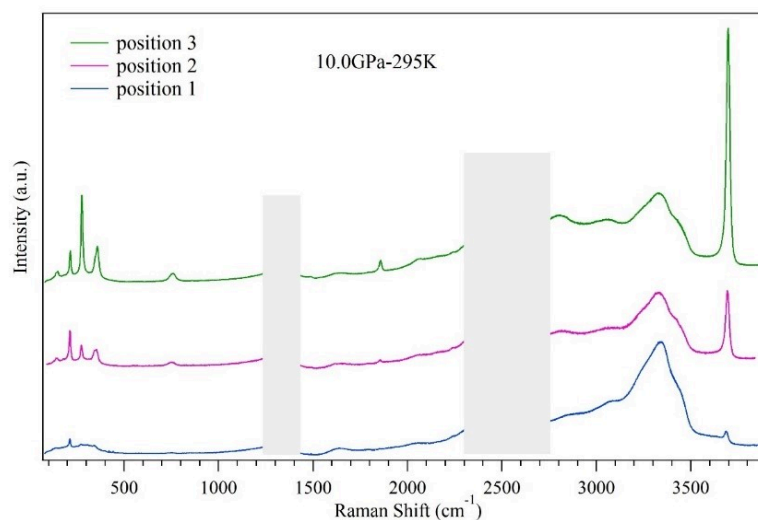


Figure 3.2. Raman spectra of AMH at 10.0 GPa and room temperature. Different colors represent different positions of the laser spot (of size 2-3 μm) on the sample. The frequency regions from 1300-1400 cm^{-1} to 2200-2600 cm^{-1} are greyed as they are dominated by the first- and second-order Raman signal from the diamond anvils.

3.3.2 Evolution of the IR spectra with pressure

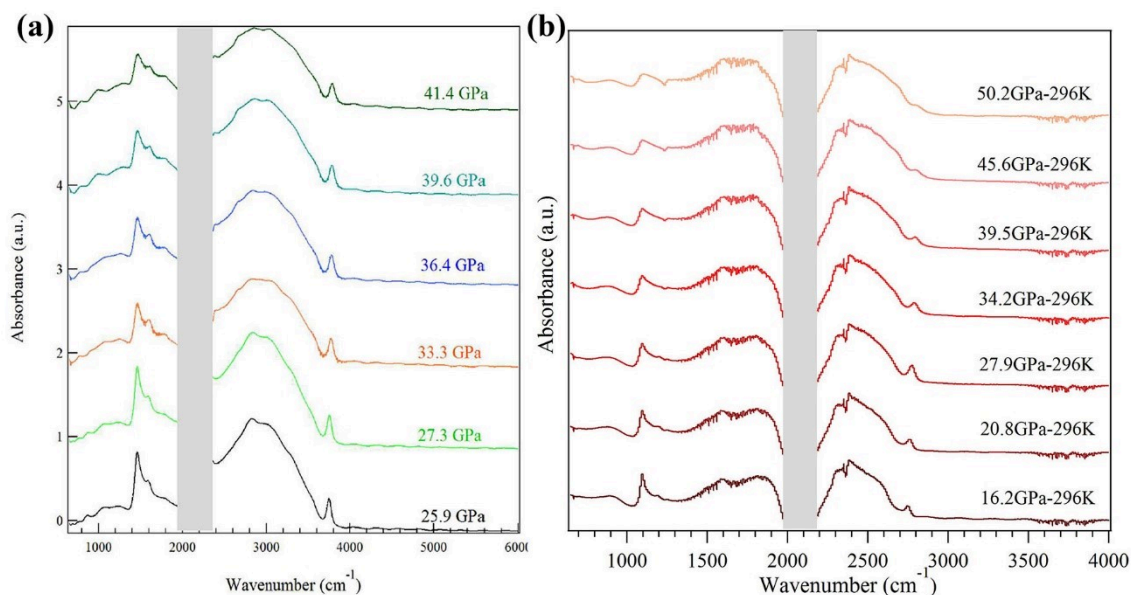


Figure 3.3. Evolution of the infrared absorption spectra of AMH with pressure at room temperature. (a). $\text{NH}_3\cdot\text{H}_2\text{O}$; (b). $\text{ND}_3\cdot\text{D}_2\text{O}$. The frequency region from 2000 to 2300 cm^{-1} is obscured by the strong IR absorption band of the diamond anvils.

The evolution of the IR spectra with pressure was followed during compression at room temperature, examples of collected IR spectra are shown in Figure 3.3. Whether the sample is

$\text{NH}_3 \cdot \text{H}_2\text{O}$ or $\text{ND}_3 \cdot \text{D}_2\text{O}$, the IR spectra remain qualitatively the same until the maximum pressure (56.9 GPa) in the experiments, indicating the absence of phase transition.

The room-temperature pressure evolution of the infrared band wavenumbers assigned to the stretching of the OH^- and OD^- ions (for the hydrogenous and deuterated samples respectively) are shown in Figure 3.4 (a) and (b). For a harmonic, isolated vibration, the ratio $\nu_{\text{OH}^-} / \nu_{\text{OD}^-} = \sqrt{\mu_{\text{OH}} / \mu_{\text{OD}}} = 1.374$, where μ is the reduced mass. As seen in Figure 3.4 (c), the experimental ratio is, within error bars, approximately constant within error bars at 1.355. This value is close to the ratio found for O-H \cdots O and O-H \cdots N infrared-active vibrations (1.32-1.34) in the molecular AMH-phase I at ambient pressure and 100 K^[9]. This result thus confirms that the band at $\sim 3700 \text{ cm}^{-1}$ originates from OH(D) vibrations.

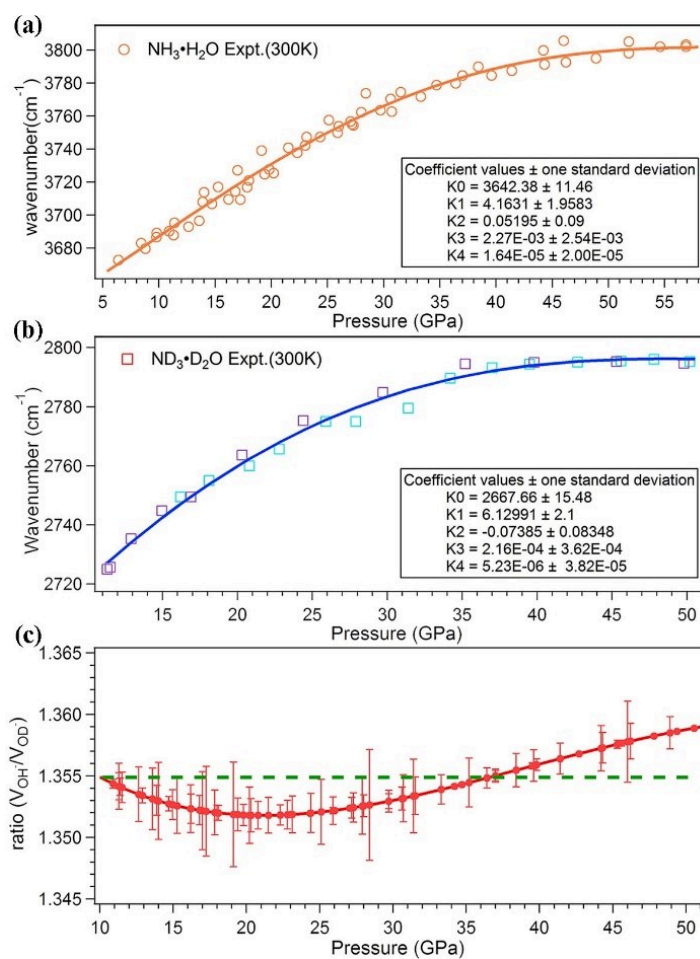


Figure 3.4. Pressure evolution of infrared band wavenumbers of the stretching of the OH^- and OD^- ions at room temperature. (a) $\text{NH}_3 \cdot \text{H}_2\text{O}$; (b) $\text{ND}_3 \cdot \text{D}_2\text{O}$; (c) the ratio of $\nu_{\text{OH}^-} / \nu_{\text{OD}^-}$. The red line is a guide through experimental data and the green dashed line is the average ratio over the full pressure range.

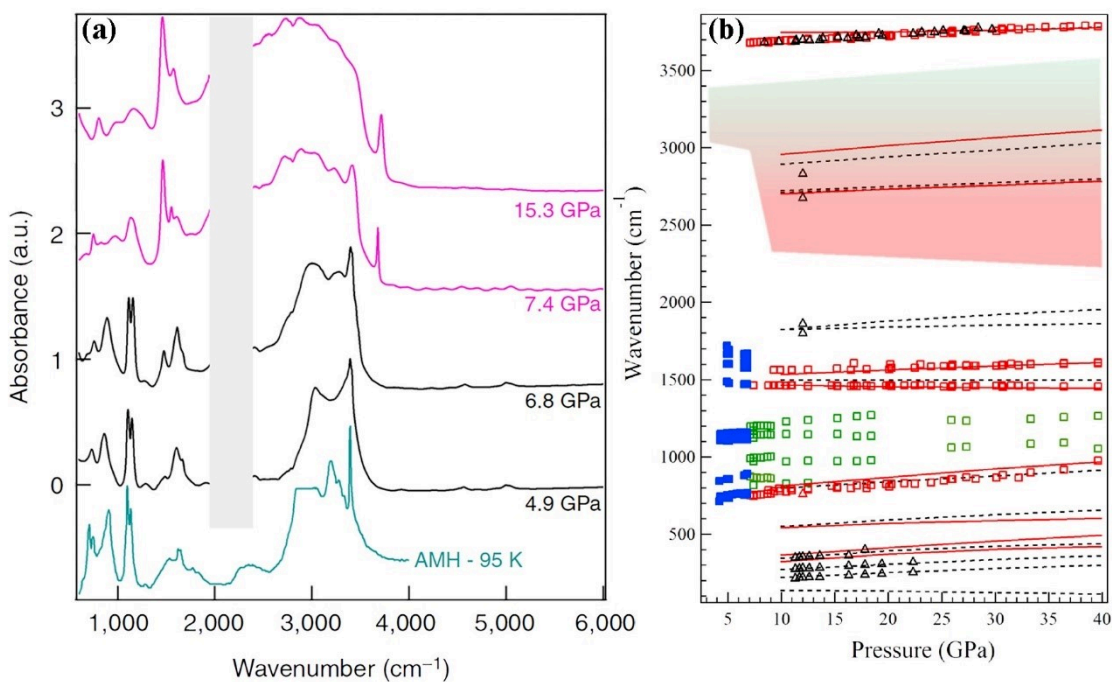


Figure 3.5. (a) Evolution with the pressure of the experimental IR absorption spectra of AMH. The spectra were collected upon decompression at RT. Pink and black curves are spectra collected above and below the ionic-molecular phase transition, respectively. The frequency window from 2000 to 2300 cm^{-1} is obscured by the strong absorption band of the diamond anvils. Pressures are indicated on the right. The blue curve is the experimental spectrum of the molecular AMH-I phase at ambient pressure and 95 K from ref.^[4]. (b) Pressure evolution of the Raman and infrared band wavenumbers of AMH at ambient temperature. Experimental data are represented with symbols. The continuous and discontinuous lines respectively represent the calculated wavenumbers of the infrared and Raman modes in the $P4/nmm$ structure. Red open squares indicate IR modes compatible with the predicted ionic $P4/nmm$ structure while green open squares correspond to the molecular NH_3 and H_2O IR modes above 7.4 GPa. The red/green shaded region corresponds to the broad IR absorption in the stretching region of NH_4^+ , OH^- and NH_3 . Solid blue squares show IR modes below the phase transition at 7.4 GPa, where modes from the ionic species disappear. The Raman experimental data are shown by open triangles.

The evolution of the IR spectra with pressure was followed during decompression at RT, examples of collected IR spectra are shown in Figure 3.5 (a). From 40 GPa down to 7.4 GPa, the spectra are all similar to that of Figure 3.3 (a). The frequency of the modes assigned to the $P4/nmm$ structure correlates very well with the predicted ones over the full pressure range, as displayed in Figure 3.5 (b). The ratio between molecular and ionic species appears not to be much affected by pressure as the relative intensity of the respective IR bands does not change with pressure. Below 7.4 GPa, large modifications of the IR absorbance occur. Notably, all the spectral features correlated with the ionic species, in particular, the OH^- stretching band at $\sim 3700 \text{ cm}^{-1}$ and the NH_4^+ bending at 1460 cm^{-1} , disappear below this pressure, and only those assigned to the neutral H_2O and NH_3 molecules remain. Moreover, the widths of most spectral bands decrease below 7.4 GPa, and previously unresolved features appear. This is strongly

indicative of a phase transition to a purely molecular phase. We also note that the IR spectrum at 7.4 GPa contains both features from the high-pressure and low-pressure spectra, suggesting a coexistence of the two phases and thus a first-order transition. IR spectra were also collected from 10 to 30 GPa at 100 K, showing no appreciable change of the IR absorbance with temperature between 300 and 100 K.

The high-pressure phase is thus stable over a large range of P-T conditions, which is confirmed by our X-ray diffraction experiments as discussed hereafter. Our spectroscopic observations thus point to a partial ionization of AMH above 7.4 GPa. Although several spectral bands match those expected for the $P4/nmm$ structure, the latter is a fully ionic structure and does not explain the presence of the spectral bands originating from H_2O and NH_3 molecules. To understand the structure of the high-pressure phase, we conducted X-ray and neutron diffraction experiments as described below.

3.3.3 X-ray and neutron diffraction results

Angular dispersive X-ray diffraction (XRD) experiments were conducted either at beamline ID27 of the European Radiation Synchrotron Facility or using an in-house diffractometer (for details, see chapter 2). We first present the results obtained at 10.6 GPa and RT on the sample whose Raman spectra is shown in Figure 3.1 (a). This sample of diameter 100 μm was mapped by XRD in steps of 10 μm , taking advantage of the small X-ray beam ($3 \times 3 \mu m$ FWHM) of the ESRF-ID27 beamline. The XRD images show that the sample is a textured powder. Five to six Bragg reflections are observed at all sample positions, which can be indexed by a bcc unit cell with lattice parameter $a = 3.322 \text{ \AA}$. This is the same unit cell as that found for the AMH-VI (DMA) phase in ref.^[10]. A second set of reflections is also present with variable intensities depending on the sample position. These reflections can be indexed by the $P4/nmm$ ionic structure with $a = 4.821 \text{ \AA}$ and $c = 3.08 \text{ \AA}$, which is close to the predicted cell parameters for this structure at the same pressure, $a = 4.875 \text{ \AA}$ and $c = 3.047 \text{ \AA}$, as shown in Table 3.1. Figure 3.6 shows the integrated XRD pattern of one image and the Le Bail fit using a mixture of $Im-3m$ and $P4/nmm$.

Table 3.1: Atomic coordinates and Wyckoff positions of the calculated $P4/nmm$ structure at 10 GPa.

Lattice parameter	Atom	x	y	z	Site
$a = 4.875 \text{ \AA}$, $c = 3.047 \text{ \AA}$	N	0.7500	0.2500	0.0000	2a
$\alpha = \beta = \gamma = 90^\circ$	O	0.2500	0.2500	0.6013	2c
	H1	0.2500	0.5687	0.8029	8i
	H2	0.2500	0.2500	0.2775	2c

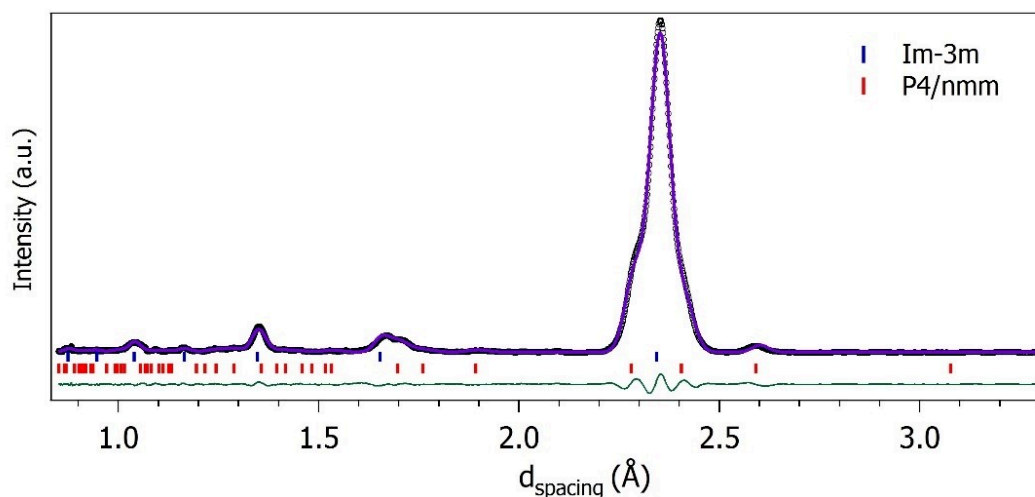


Figure 3.6. XRD diffraction pattern of AMH at 10.3 GPa and room temperature. The symbols are experimental data after subtraction of background, the solid purple lines are Le Bail refinement using a mixture of $Im-3m$ ^[10] and $P4/nmm$ ^[1] structures. Sticks show the positions of Bragg reflections. The green line represents the difference between observed and calculated profiles.

In several other samples, the Bragg peaks from $P4/nmm$ were more difficult to detect, an example of which is shown in Figure 3.7. This suggests that the high-pressure solid is mainly composed of the DMA phase, with a variable but minor addition of $P4/nmm$. The P–T phase diagram of AMH was further mapped using XRD. Consistently with our IR spectroscopy measurements, we did not observe any phase transition on cooling the sample from 300 to 50 K at 12–13 GPa, or on compressing the sample up to 80 GPa at RT.

Additional information on the structure of high-pressure AMH was sought using time-of-flight powder neutron diffraction (ND) at the PEARL station of the ISIS facility (see Chapter 2 for details). A deuterated sample was used in this case, since hydrogen has a strong incoherent neutron cross-section. The sample was loaded and compressed to 6.5 GPa at 150 K in order to obtain the AMH-VI phase as described in ref.^[10], and then compressed from 6 to 12 GPa at room temperature. No obvious change of the diffraction pattern was detected and the structural model of the DMA phase gives a good fit of the data in the whole pressure range. No evidence of the $P4/nmm$ structure was found in this experiment, as seen in Figure 3.7 D. In a second loading though, non-*bcc* peaks were observed around the (110) peak of $Im-3m$ at 8.6 GPa, which can be interpreted as the (200) and (111) peaks of $P4/nmm$, as shown in Figure 3.8.

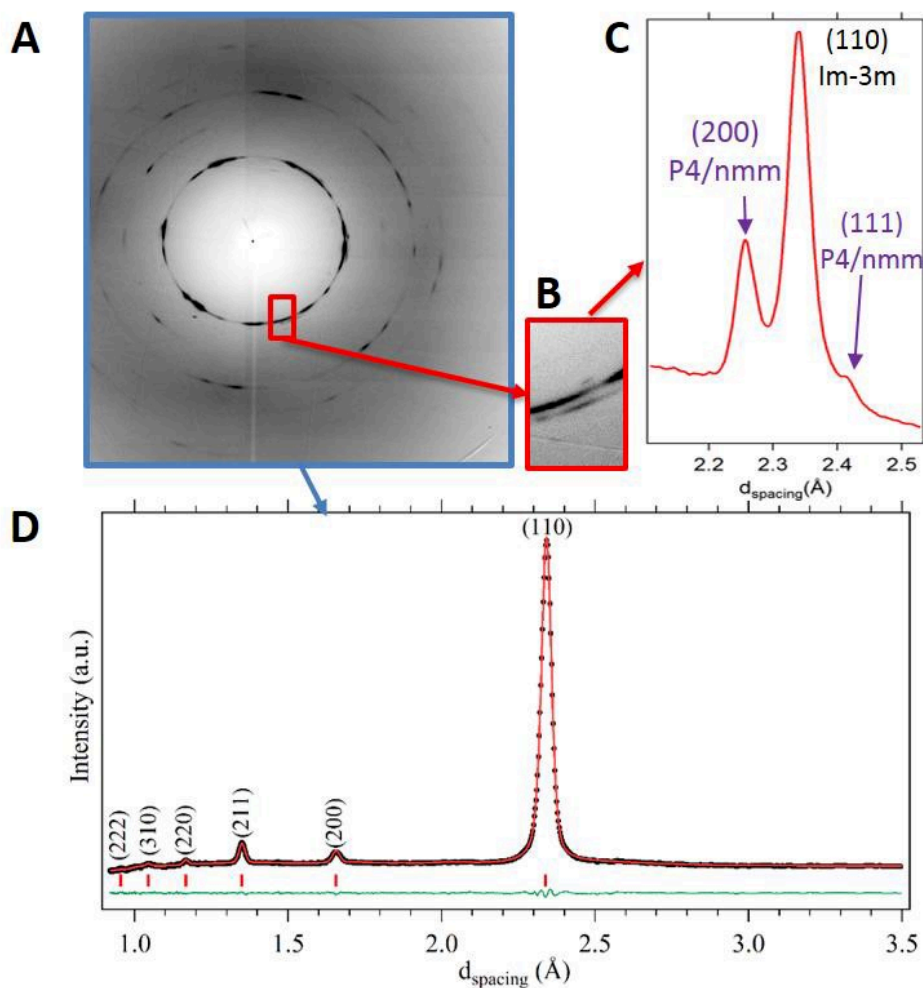


Figure 3.7. Panel A shows the x-ray diffraction bi-dimensional image collected at 12 GPa and 300 K from a sample showing less intense Raman peaks of the P4/nmm structure. Consistently, the Bragg peaks from the P4/nmm structure are less intense in this sample, and the diffraction pattern is dominated by the Im-3m phase. Panel B shows an enlarged view of the red box to show the two additional partial rings on each side of the (110) ring of Im-3m and indexed as the (200) and (111) peaks of the P4/nmm structure. Panel C shows the one-dimensional patterns obtained by integrating the zoomed region. The pattern obtained by the integration of the complete image is shown in panel D. The two peaks of P4/nmm barely stand out from the background in this integration. In D, the symbols are experimental data, the red solid line is a full profile Rietveld refinements using the Im-3m model of Loveday et al.^[10]. The green line shows the difference between observed and calculated profiles. Sticks show the positions of Bragg reflections of Im-3m.

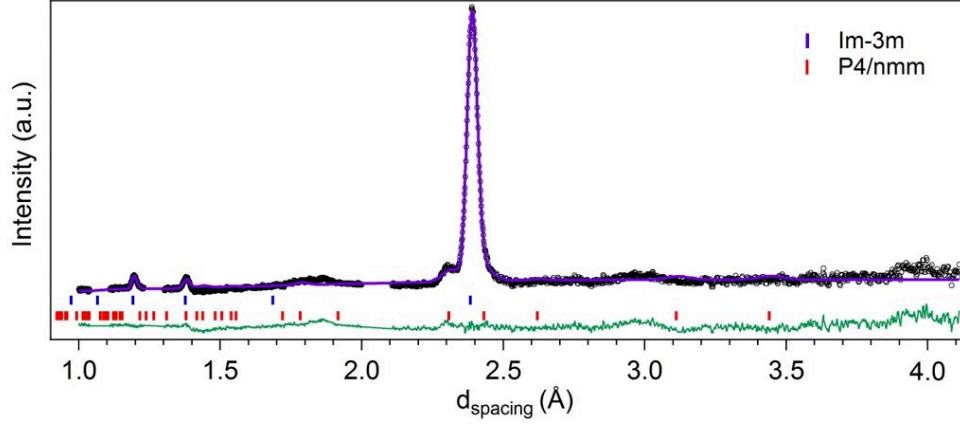


Figure 3.8. Neutron diffraction pattern of AMH at 8.6 GPa and room temperature. The symbols are experimental data after subtraction of background and removal of the reflections from the diamond anvils in the neutron pattern. The solid purple lines are Le Bail refinement using a mixture of $Im-3m$ ^[10] and $P4/nmm$ ^[1] structures. Sticks show the positions of Bragg reflections. The green line represents the difference between observed and calculated profiles.

3.3.3.1 Equation of state of AMH at 300 K

The measured volume of the $Im-3m$ phase over the 8-80 GPa pressure range at 300 K is represented in Figure 3.9. The experimental P-V data are well fitted by a third-order Birch-Murnaghan equation of state^[11] (in the following abbreviated as “BM”):

$$P(V) = \frac{3}{2}B_0 \left[\left(\frac{V}{V_0} \right)^{-\frac{7}{3}} - \left(\frac{V}{V_0} \right)^{-\frac{5}{3}} \right] \left\{ 1 - \frac{3}{4}(4 - B'_0) \left[\left(\frac{V}{V_0} \right)^{-\frac{2}{3}} - 1 \right] \right\} \quad (3.1)$$

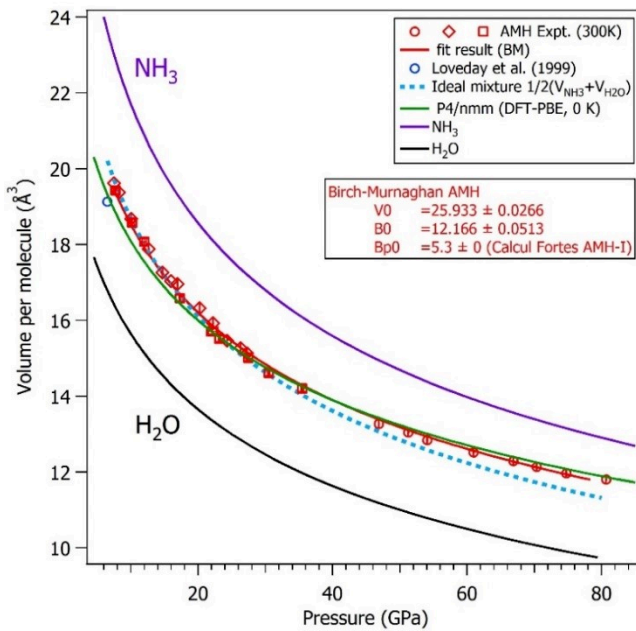


Figure 3.9. Pressure dependence of unit cell volume of AMH. The symbols are the experimental volume of the $Im-3m$ structure at room temperature. The red line is the fit to our experimental data using a third-order BM equation of state. The green line represents the equation of state of the theoretical $P4/nmm$ ionic phase obtained by DFT calculations (with PBE functional) at 0 K^[12]. The purple and black lines represent the fits of the BM equation of state to NH_3 ^[13] and H_2O ^[14], respectively. The blue dashed line is the equation of state to the ideal equimolar mixture of NH_3 and H_2O : $V_{AMH} = (V_{H_2O} + V_{NH_3})/2$.

where the three parameters V_0 , B_0 and B'_0 represent the unit cell volume, the bulk modulus and the first derivative of the bulk modulus at zero pressure, respectively. Since the $Im-3m$ phase is unstable at zero pressure, there is no constraint on either of these parameters, and large correlations between them exist if they are all left free to vary. We thus chose to fix B'_0 to the value 5.3 which well fits experimental^[15] and theoretical P-V data of AMH-I^[16]. We then obtain $V_0=25.93(3) \text{ \AA}^3$ and $B_0 =12.16(5) \text{ GPa}$. This value of B_0 is typical of H-bonded solids: it is close to that of ice VII, $13.8(2) \text{ GPa}$ ^[17] and slightly above those of $\text{NH}_3\text{-IV}$, $7(1) \text{ GPa}$ ^[13] and AMH-I, $7.3(3) \text{ GPa}$ ^[15]. The EOS of the $P4/nmm$ ionic phase calculated by DFT using the PBE functional at 0 K^[12] is also shown in Figure 3.9 as a red line for comparison. An unconstrained BM fit to the theoretical data from 2 to 60 GPa gives $V_0=23.7(3) \text{ \AA}^3$, $B_0 =18(1) \text{ GPa}$ and $B'_0 =5.4(2)$. It can be seen that the EOS of the $Im-3m$ and $P4/nmm$ structures are very close. This could indicate that their Gibbs free energy themselves are similar and explain why they are observed to coexist. Below 35 GPa, the EOS of the $Im-3m$ structure is also close to the one calculated assuming an ideal mixture of NH_3 and H_2O , but the two EOS gradually deviate at higher pressure, which could be linked to the ionization of the molecules.

3.3.3.2 Ionico-molecular transition on decompression

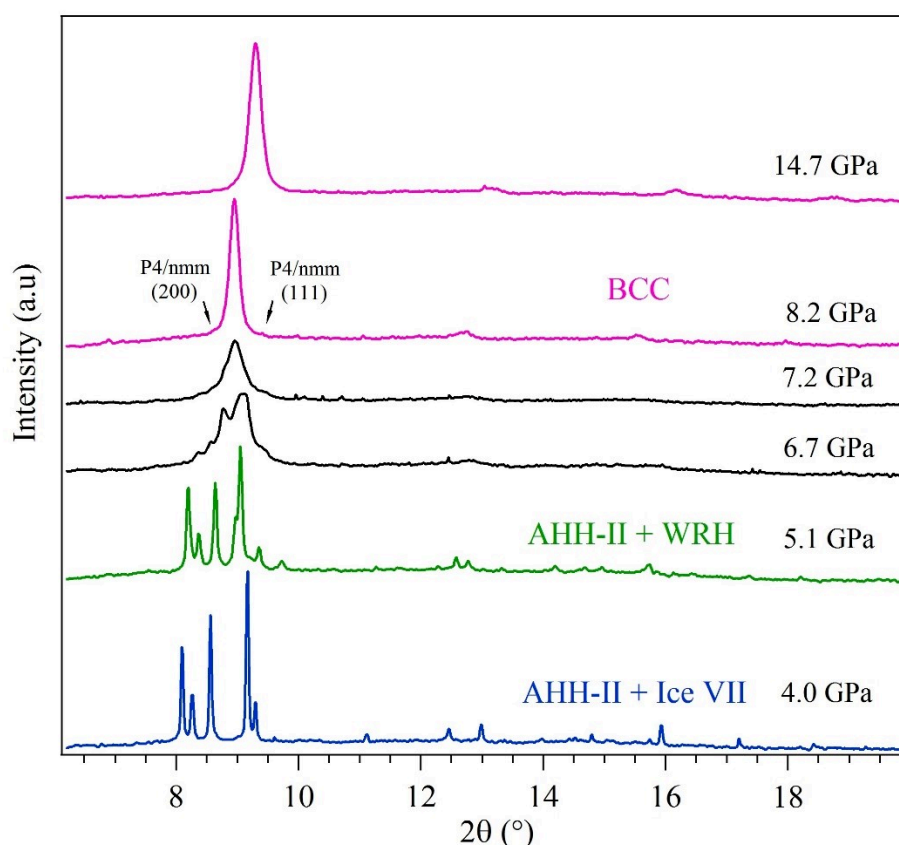


Figure 3.10. Evolution with the pressure of XRD patterns of AMH at room temperature. The spectra were collected upon decompression.

On decompression at RT, as shown in Figure 3.10, the Bragg reflections of the cubic ($Im-3m$) phase suddenly broadened and took the appearance of unresolved multiplets at 7.2 GPa. The sample became homogeneous again at 5.1 GPa, both visually and by XRD. The new Bragg

reflections appearing below 7.2 GPa are much sharper than those of AMH-VI. Most of them can be indexed by the AHH-II structure reported by Ref.^[3] but not all. The extra peaks cannot be indexed by ice-VII as well, and are thus assigned to an unidentified hydrate. Since this hydrate coexists with AHH, its composition must be richer in water than in ammonia to comply with the initial equimolar composition of the sample. We thus named it water-rich hydrate (WRH). At 4 GPa, the XRD pattern changes again and is the same as that observed by Wilson *et al.*^[3] on freezing the 1:1 liquid at room temperature and interpreted as a mixture of AHH-II and ice VII. Accordingly, we performed a Le Bail fit of this pattern using a mixture of AHH-II and ice VII. The result is displayed in Figure 3.11, and the lattice parameters obtained for AHH-II (space group $P2_1/c$ with $a= 3.3754 \text{ \AA}$, $b= 9.2285 \text{ \AA}$, $c=8.9690 \text{ \AA}$ and $\beta= 94.4135^\circ$) and for ice-VII (space group $Pn-3m$ with $a= 3.3088 \text{ \AA}$)^[3] are in good agreement with literature.

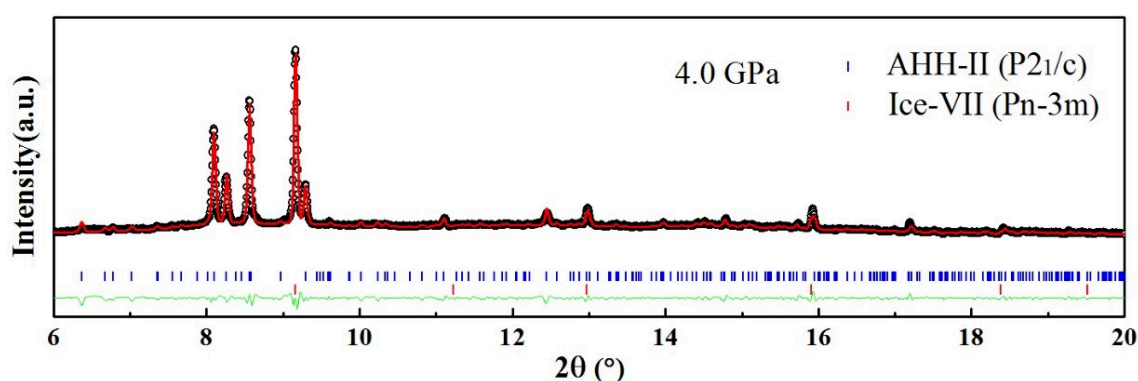


Figure 3.11. Le Bail fits of the XRD data at 4 GPa using a mixture of AHH-II and ice VII. The symbols are experimental data and the red lines are Le Bail refinement. Sticks show the positions of Bragg reflections. The green line represents the difference between observed and calculated profiles. structure^[3].

To sum up, both XRD and ND show that samples of AMH above 7.4 GPa are mainly composed of the *bcc* phase previously observed by ref.^[10], but also contain the $P4/nmm$ phase as a minor addition. The observed variability in the amount of $P4/nmm$ phase between different samples is consistent with the variations in Raman and IR peak intensities noted above. It is likely due to differences between loadings in the compression and warming rates, the pressure at which the sample is warmed up to RT, and/or a small deviations (below 1%) from the 1:1 composition. Indeed, as seen hereafter, the creation of ionic species is strongly dependent on the local environment, and the final state is controlled by kinetics. No other phases are observed on compression up to 80 GPa, at temperatures from 50 to 300 K. On decompression below 7.4 GPa at 300 K, the signature of the ionic species is lost concomitantly with the dehydration of AMH into AHH + WRH at 5 GPa, evolving to AHH + ice VII below 4 GPa.

3.3.4 The disordered ionico-molecular crystal

Our experimental results confirm the predicted existence of a $P4/nmm$ ionic structure of AMH above 7.4 GPa at RT, as its signature is observed in both spectroscopic and diffraction data. However, the dominant phase in our samples is always the $Im-3m$ structure found earlier by Loveday *et al.*. This coexistence of a fully ordered ionic crystal, on one hand, and of a

disordered molecular alloy, on the other hand, is highly intriguing and raises the following questions: first, if $P4/nmm$ really is the thermodynamically stable state, why is it only present at best as a minor phase in all our samples? Second, is the $Im-3m$ phase purely molecular?

We recall that $P4/nmm$ emerged as the lowest enthalpy structure at 10 GPa–0 K in theoretical calculations using the *ab initio* random structure search (AIRSS) code^[18], where searches spanned unit cells with up to 8 $NH_3 \cdot H_2O$ formula units^[1]. We used the same code to perform new searches in a larger pressure range, from 10 to 40 GPa, with up to 4 f.u. per unit cell (see Chapter 2 for details on the search strategy). The result is that $P4/nmm$ is indeed the lowest enthalpy structure coming out from all searches in this pressure range, which also agrees with the recent report of ref.^[2] who used a different search strategy and code. It is clear, however, that these searches are not able to find the $Im-3m$ structure, which fits present and previous^[10] diffraction data for the *bcc* phase, because the large disorder of this structure cannot be described with the small numbers of f.u. to which the searches are limited. As a matter of fact, this disorder precludes a direct description of the $Im-3m$ structure in theoretical calculations, and thus to discuss its stability with respect to $P4/nmm$.

Griffiths *et al.*^[1] noted that an ionic equivalent of Loveday *et al.*'s $Im-3m$ phase could be constructed from the $P4/nmm$ structure by (1) slightly contracting the *a* and *b* axes to make the unit cell cubic, (2) sliding the O atom along *z* by $0.1562c$ to bring it to the center of the cube and (3) mixing the occupancies of the two *bcc* sites with ammonium and hydroxyl ions to obtain the substitutional disorder imposed by the $Im-3m$ structure. If we assume that these operations would present a gain in energy with respect to $P4/nmm$, this could explain why the $Im-3m$ phase is dominant, but the latter would then not be molecular as previously assumed by Loveday *et al.*^[10], but fully ionic. We confronted this structural model¹ to the neutron diffraction data at 6 GPa and found that it fits almost equally well the diffraction pattern than the original molecular $Im-3m$ structure (the respective weighted R-factors are 2.63 and 2.61%). This disordered ionic structure, however, presents a major flaw: the substitutional disorder implies that two ammonium ions have a 25% probability to be first neighbours, i.e., distant by ~ 2.85 Å. The corresponding Coulomb repulsion would have a large energetic cost, which makes it very unlikely that such a structure would be stable. This reasoning leads us to think that the *bcc* phase cannot be fully composed of ionic species and thus remains partly molecular, which also complies with the observed signature of both ionic and molecular species in the vibrational Raman and IR spectra.

¹The resulting structure, of space group $Im-3m$; has N and O atoms positioned at (0, 0, 0) with 50% probability, and H (or D) atoms on (x, x, x) and (0, 0, z) (where x and z are chosen to have N-H(D) and O-H (D) distances of 1.04 and 0.97 Å, respectively) with occupancy factors of 1/4 and 1/12, respectively.

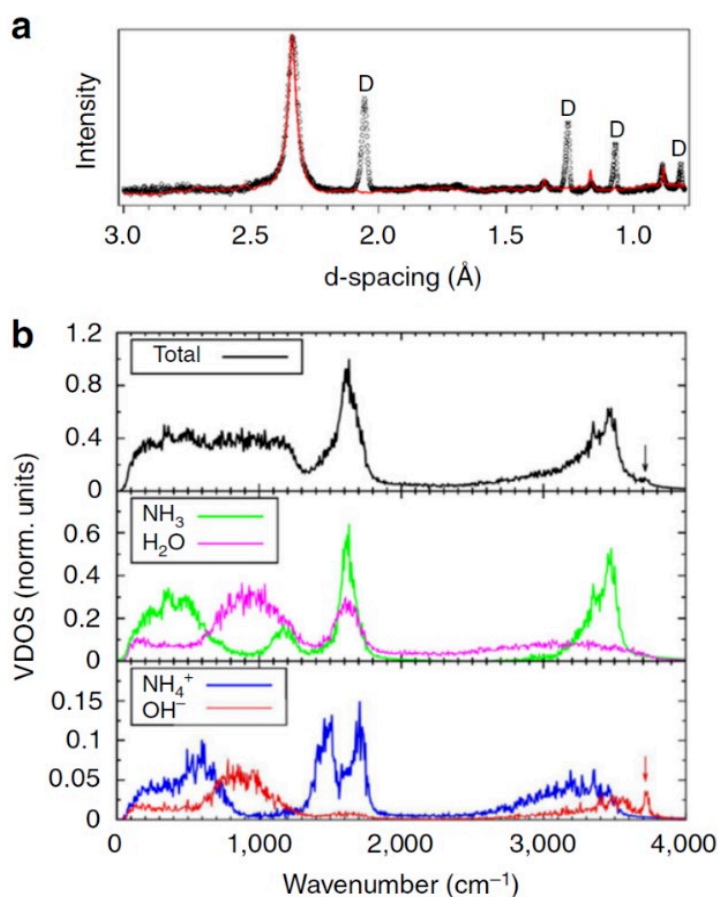


Figure 3.12. Structural and vibrational properties of the disordered ionic-molecular alloy. In (a), we compare the simulated neutron pattern for the $6 \times 6 \times 6$ simulation box (red line) to the experimental neutron pattern collected at 10 GPa, 295 K (symbols). The x scale of the simulated pattern has been multiplied by 0.994 to account for the density difference, and the intensity adjusted to scale with the main (110) peak. The Bragg peaks were modelled by pseudo-Voigt profiles of constant width. “D” indicates the reflections from the diamond anvils. (b) shows the vibrational density of states obtained from the AIMD trajectories. The arrows indicate the OH^- stretching mode.

To go further and achieve a better understanding, I collaborated with Adrien Mafey (PhD student under the supervision of A.M. Saitta) who performed an extensive theoretical study^[12] of the $Im\text{-}3m$ phase using classical and *ab initio* molecular dynamics, whose results are presented below. First, an approximate model of this structure was constructed, compatible with computational capabilities, by generating a few tens of supercells containing $4 \times 4 \times 4$ *bcc* units, where 64 water and 64 ammonia molecules were distributed at random over the crystal sites according to the $Im\text{-}3m$ structure of ref.^[10]. One $6 \times 6 \times 6$ supercell containing 432 molecules was also studied to check for size effects. Those cells were annealed using classical force fields, in order for the molecules to achieve the most stable orientational configuration. The 10 most stable $4 \times 4 \times 4$ cells and the $6 \times 6 \times 6$ cell were then selected, and optimized by DFT relaxation at 0 K. All those structures displayed some ionization, characterized by a proton relaxation from one donor water molecule to an acceptor ammonia one to which it is H-bonded, and thus resulting in a disordered crystal where NH_4^+ and OH^- ions coexist with NH_3 and H_2O neutral

molecules. This ionization concerned 12–17% of the molecules in the $4 \times 4 \times 4$ cells, and 13% in the $6 \times 6 \times 6$ one, showing that the concentration of ionic pairs does not depend much on the cell size. Figure 3.12 (a) compares the neutron pattern computed from the atomic positions of the $6 \times 6 \times 6$ supercell to the experimental one at 10 GPa. The excellent agreement shows that, despite the additional disorder induced by ionization, the average structure remains of $Im-3m$ symmetry and that our model is compatible with the experiment.

For comparison, another supercell with an ordered version of the structure was built, i.e., where one of the two “*bcc*” sites were systematically occupied by a water molecule, and the other one by an ammonia one. In this case, the $T = 0$ K relaxation immediately resulted in a full ionization of the system in the $P4/nmm$ structure. These results strongly suggest that the ionization process in the substitutionally disordered structure depends on the local arrangement of species and topology, which will be further analyzed below.

In order to understand the effects of temperature, *ab initio* molecular dynamics simulations (AIMD) were performed at 300 K at a pressure of 10 GPa on one supercell from the above set, which contained 12% ionic species after 0 K optimization. These simulations show that the sample undergoes a further, dynamically induced ionization: after ~ 8 ps, the number of ionic species reached the maximum values of 36% f.u. of NH_4^+OH^- , a ratio which remained stable up to ~ 20 ps. The vibrational density of states (VDOS) obtained from these simulations are shown in Figure 3.12 (b). As expected, vibrational modes from both molecular and ionic species are present, and the decomposition of the full VDOS (top panel) into their respective contributions are shown in the middle and lower panel. Of particular interest is the higher energy mode at 3715 cm^{-1} : the projected VDOS clearly shows that it comes from the OH^- stretching, as in $P4/nmm$, however, its intensity in the total VDOS is much weaker in the disordered *bcc* phase than in $P4/nmm$ due to the relatively low concentration of about 7.5% OH^- vibrators. The same is true for the NH_4^+ vibrational bands around 1500 cm^{-1} . As a matter of fact, the vibrational bands of the ionic species in the *bcc* phase are barely discernible from those of molecular species, which confirms that the Raman and IR bands assigned to ionic species in the experimental spectra of Figure 3.1 mainly come from the occurrence of $P4/nmm$ in our samples.

We next try and explain why the ionization is only partial in the *bcc* structure. To illustrate the main result of our analysis, we show on one hand in Figure 3.13 (a) a local configuration where an OH^- - NH_4^+ pair has formed through a proton transfer from the water molecule at the corner to the ammonia molecule at the center of the cube to which it is H-bonded. On the other hand, Figure 3.13 (b) shows a configuration where no proton transfer has occurred between an equivalent pair of molecules. The main difference between these two configurations is that in the second case, other ammonium ions which formed at an earlier instant are first neighbors of the central ammonia molecule. In fact, the full substitutional disorder of ammonia and water units over the crystal sites implies homomolecular vicinity, i.e., that NH_3 molecules easily are nearest neighbors of other ammonia ones. If one of those molecules receives a proton from a nearby water molecule, Coulombic repulsion then hinders the formation of other ammonium cation in its first neighbor shell, which is the case illustrated in Figure 3.13 (b). At the end of our AIMD trajectory, we observe that nearly 90% of the neutral NH_3 molecules are surrounded by at least one NH_4^+ ion. Moreover, we find that Grotthuss-like water–hydroxide proton hopping is relatively common, in agreement with results in the literature^[19-21], whereas

ammonium–water and ammonium–ammonia proton hopping never occur. This last observation is consistent with the much more extreme thermodynamic conditions necessary to observe superionicity in pure ammonia ice^[22], and suggests that ammonium ions are, at our milder conditions, “topological proton wells”, which sequester Grotthuss-diffusing protons, thus hindering a more efficient charge distribution within the crystal, and, at last, to attain a full ionization as in $P4/nmm$.

To sum up, the observed $Im-3m$ phase is topologically frustrated by homomolecular vicinity and, as a result, cannot be fully composed of ionic species, thus remaining partly molecular. The experimental observation that $P4/nmm$ is only produced locally and as a minor phase likely results from the fact that the formation of $P4/nmm$ requires a local configuration, where ammonia molecules are exclusively surrounded by water, or vice versa, a situation which has a low probability. It is also likely that proton transfer between water and ammonia molecules precede and trigger the structural phase transition, and while the system tends towards the ordered ionic state, it is kinetically trapped into a lattice-topological frustrated state, dictated by the specific local arrangements, which permit, or not, proton transfer events from water to ammonia.

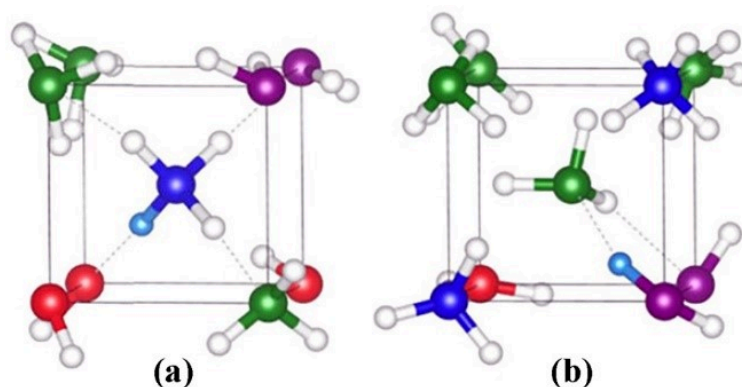


Figure 3.13. Representative simulation snapshots showing the nearest-neighbor environment of an ammonium ion (a) or an ammonia molecule (b). The H atom involved in the H-bond between the central ammonia and neighbor water molecule is rendered in cyan, white spheres represent the others. For NH_3 and NH_4^+ , N atoms are in green and blue respectively. For H_2O and OH^- , O atoms are in magenta and red, respectively. The solid line and dashed lines depict the cubic unit cell and the H bonds, respectively. For the sake of clarity, all species are in their respective average sites.

3.4 Conclusions

The present work shows that the ammonia monohydrate compound spontaneously converts into an unusual crystalline state at high pressure, where the standard molecular forms of water and ammonia coexist with hydroxyl and ammonium ions^[23]. The relatively low-pressure onset for static ionization (7.4 GPa) in AMH contrasts with the extreme pressures required in the pure ices (150 GPa in NH_3 ^[24], over 1.4 TPa in H_2O ^[25]) and can be understood by the lower energy cost for the proton transfer between water and ammonia.

Consistent with previous theoretical works^[1,2], the lowest enthalpy crystal for AMH is found to be the ordered and fully ionic $P4/nmm$ phase in the pressure range 10–60 GPa. However, this phase is only obtained at best as a minor phase in all our experiments. On the other hand, our X-ray and neutron diffraction data are consistent with the cubic, highly disordered structure of ref.^[10], which is moreover observed to persist on compression to at least 80 GPa. We solve this apparent riddle by showing that the cubic phase is not purely molecular, as described in ref.^[10], but is a mixed ionic-molecular one (called DIMA), and that the system is trapped in this state and cannot reach its global minimum energy one. Due to the highly disordered nature of this phase, the present experiments alone do not allow to discriminate between the purely molecular and mixed ionic-molecular state, which made the input of *ab initio* calculations essential to understand this system.

Besides the fundamental aspects, AMH might be present in the interiors of icy bodies of the solar system, and these ionization properties could be relevant in their modelling, in particular, to understand the unusual magnetic fields of the icy planets Neptune and Uranus. Superionicity with large proton conductivity has been predicted in AMH in different structures at significantly higher P/T conditions^[2], close to those of the respective pure ices^[22,26,27]; we speculate and leave that to future research, that proton mobility might set in at much milder conditions, and be significantly higher over the whole phase diagram.

References

- [1]Griffiths, G. I., Misquitta, A. J., Fortes, A. D. *et al.* High pressure ionic and molecular crystals of ammonia monohydrate within density functional theory. *The Journal of chemical physics* **137**, 064506, (2012).
- [2]Bethkenhagen, M., Cebulla, D., Redmer, R. *et al.* Superionic phases of the 1: 1 water–ammonia mixture. *The Journal of Physical Chemistry A* **119**, 10582-10588, (2015).
- [3]Wilson, C., Bull, C., Stinton, G. *et al.* Pressure-induced dehydration and the structure of ammonia hemihydrate-II. *The Journal of chemical physics* **136**, 094506, (2012).
- [4]Bertie, J. E. & Morrison, M. M. The infrared spectra of the hydrates of ammonia, $\text{NH}_3 \cdot \text{H}_2\text{O}$ and $2\text{NH}_3 \cdot \text{H}_2\text{O}$ at 95°K . *The Journal of Chemical Physics* **73**, 4832-4837, (1980).
- [5]Bertie, J. E. & Shehata, M. R. Ammonia dihydrate: Preparation, x-ray powder diffraction pattern and infrared spectrum of $\text{NH}_3 \cdot 2\text{H}_2\text{O}$ at 100 K. *The Journal of chemical physics* **81**, 27-30, (1984).
- [6]Moore, M. H., Ferrante, R., Hudson, R. *et al.* Ammonia–water ice laboratory studies relevant to outer Solar System surfaces. *Icarus* **190**, 260-273, (2007).
- [7]Pruzan, P., Chervin, J., Wolanin, E. *et al.* Phase diagram of ice in the VII–VIII–X domain. Vibrational and structural data for strongly compressed ice VIII. *Journal of Raman Spectroscopy* **34**, 591-610, (2003).
- [8]Ninet, S. & Datchi, F. High pressure–high temperature phase diagram of ammonia. *The Journal of chemical physics* **128**, 154508, (2008).
- [9]Bertie, J. E. & Shehata, M. R. The infrared spectra of $\text{NH}_3 \cdot \text{H}_2\text{O}$ and $\text{ND}_3 \cdot \text{D}_2\text{O}$ at 100 K. *The Journal of chemical physics* **83**, 1449-1456, (1985).
- [10]Loveday, J. & Nelmes, R. Ammonia monohydrate VI: A hydrogen-bonded molecular alloy. *Physical review letters* **83**, 4329, (1999).
- [11]Birch, F. The effect of pressure upon the elastic parameters of isotropic solids, according to Murnaghan's theory of finite strain. *Journal of Applied Physics* **9**, 279-288, (1938).
- [12]Mafety, A. *Etude ab initio des glaces d'ammoniac fluoré et hydraté sous conditions thermodynamiques extrêmes*, Université Pierre et Marie Curie-Paris VI, (2016).
- [13]Datchi, F., Ninet, S., Gauthier, M. *et al.* Solid ammonia at high pressure: A single-crystal x-ray diffraction study to 123 GPa. *Physical Review B* **73**, 174111, (2006).
- [14]Frank, M. R., Fei, Y. & Hu, J. Constraining the equation of state of fluid H_2O to 80 GPa using the melting curve, bulk modulus, and thermal expansivity of Ice VII. *Geochimica et cosmochimica acta* **68**, 2781-2790, (2004).
- [15]Fortes, A. D., Suard, E., Lemée-Cailleau, M. H. *et al.* Equation of state and phase transition of deuterated ammonia monohydrate ($\text{ND}_3 \cdot \text{D}_2\text{O}$) measured by high-resolution neutron powder diffraction up to 500 MPa. *The Journal of chemical physics* **131**, 154503, (2009).
- [16]Fortes, A. D., Brodholt, J. P., Wood, I. G. *et al.* Ab initio simulation of ammonia monohydrate ($\text{NH}_3 \cdot \text{H}_2\text{O}$) and ammonium hydroxide (NH_4OH). *The Journal of Chemical Physics* **115**, 7006-7014, (2001).
- [17]Klotz, S., Komatsu, K., Kagi, H. *et al.* Bulk moduli and equations of state of ice VII and ice VIII. *Physical Review B* **95**, 174111, (2017).
- [18]Pickard, C. J. & Needs, R. Ab initio random structure searching. *Journal of Physics: Condensed Matter* **23**, 053201, (2011).
- [19]Saitta, A. M., Saija, F. & Giaquinta, P. V. Ab initio molecular dynamics study of dissociation of water under an electric field. *Physical review letters* **108**, 207801, (2012).
- [20]Cassone, G., Giaquinta, P. V., Saija, F. *et al.* Proton conduction in water ices under an electric field. *The Journal of Physical Chemistry B* **118**, 4419-4424, (2014).

-
- [21]Cassone, G., Giaquinta, P. V., Saija, F. *et al.* Effect of electric field orientation on the mechanical and electrical properties of water ices: an Ab-initio study. *The Journal of Physical Chemistry B* **118**, 12717-12724, (2014).
- [22]Ninet, S., Datchi, F. & Saitta, A. Proton disorder and superionicity in hot dense ammonia ice. *Physical review letters* **108**, 165702, (2012).
- [23]Liu, C., Mafety, A., Queyroux, J. *et al.* Topologically frustrated ionisation in a water-ammonia ice mixture. *Nature communications* **8**, 1065, (2017).
- [24]Ninet, S., Datchi, F., Dumas, P. *et al.* Experimental and theoretical evidence for an ionic crystal of ammonia at high pressure. *Physical Review B* **89**, 174103, (2014).
- [25]Wang, Y., Liu, H., Lv, J. *et al.* High pressure partially ionic phase of water ice. *Nature communications* **2**, 563, (2011).
- [26]Goncharov, A. F., Goldman, N., Fried, L. E. *et al.* Dynamic ionization of water under extreme conditions. *Physical review letters* **94**, 125508, (2005).
- [27]Cavazzoni, C., Chiarotti, G., Scandolo, S. *et al.* Superionic and metallic states of water and ammonia at giant planet conditions. *Science* **283**, 44-46, (1999).

Chapter 4: Melting curve of ammonia monohydrate

Contents

4.1 Introduction.....	85
4.2 Experimental protocol.....	85
4.3 Results.....	86
4.3.1 Observation and characterization of the non-congruent melting line ($T < 324$ K).....	87
4.3.2 Observation and characterization of the congruent melting line ($T > 324$ K).....	89
4.4 Discussion.....	93
4.4.1 Comparison with literature.....	93
4.4.2 Comparison with pure water and ammonia.....	94
4.5 Conclusions.....	96
References.....	97

4.1 Introduction

The melting curve of a substance separates the respective stability fields of the solid and fluid phases in the P-T phase diagram. Its knowledge is particularly important in the case of planetary materials, as this allows us to determine whether this material is solid or fluid at a given depth inside the planet, with important consequences on dynamic properties on which depend macroscopic properties such as the magnetic field.

Up to now, there have been, to our knowledge, only two experimental studies^[1,2] of the melting curve of AMH, and these are limited to temperatures below 400 K. In 1991, Boone & Nicol determined the melting curve of AMH from 0 to 6 GPa and from 190 to 330 K by optical microscopy under normal and polarized light^[2]. Another melting line of AMH was reported by Koumvakalis & Nicol in 1993 up to about 400 K and 6 GPa by Raman spectroscopy and optical microscopy^[1]. The melting points reported in these two works present a rather large scatter and do not agree well with each other, calling for more experimental data.

In this chapter, we present our investigations of the melting properties of AMH from 300 K to 675 K. We find two different melting behavior, non-congruent and congruent, depending on whether the temperature is below or above 324 K. The congruent melting above 324 K is shown to be associated to the stability of a previously unknown solid phase of AMH, which we named AMH-VII. After presenting our experimental findings in detail, we discuss the results with respect to literature and compare the melting line of AMH to those of the pure water and ammonia ices.

4.2 Experimental protocol

Two samples were dedicated to the present experiments. The samples were loaded as described in Chapter 2. A cylindrical resistive heater (Watlow) surrounding the body of the cell was used for heating and a type-K thermocouple was placed in contact with the DAC, close to the diamond anvils to measure the temperature. A ruby ball was used to measure the pressure, as shown in Figure 4.1. We used ruby instead of $\text{SrB}_4\text{O}_7:\text{Sm}^{2+}$ despite the lower accuracy achieved with ruby at high temperatures because $\text{SrB}_4\text{O}_7:\text{Sm}^{2+}$ is chemically attacked by liquid water above 550 K, resulting in its total dissolution. The uncertainties on pressure have been estimated from the standard deviation of the fitted luminescence peaks versus wavelength and the worst uncertainty estimated at 675 K is about 0.37 GPa. The temperature uncertainties are about 5 K.

The melting line of AMH was determined by visual observations of the solid-fluid equilibrium as shown in Figure 4.1. This is possible because of the difference in refractive index between the fluid and solid phase. To determine the nature of the melting line (congruent or not), we have checked whether this solid/fluid equilibrium occurs only at a given (P, T) point (case of a congruent melting point) or if at fixed T, this equilibrium exists over a limited range of pressure $[P_1, P_2]$ with $P_1 \neq P_2$ (case of a non-congruent melting point).

In the temperature range where congruent melting was established, the measurement of

pressure and temperature when the solid/fluid equilibrium is stabilized defines a melting point. The coexistence was maintained during the slow heating of the sample by simultaneously increasing the load. This method enables precise and smooth measurement of the melting curve and prevents from the problems related to metastabilities such as undercooling or overpressurization.

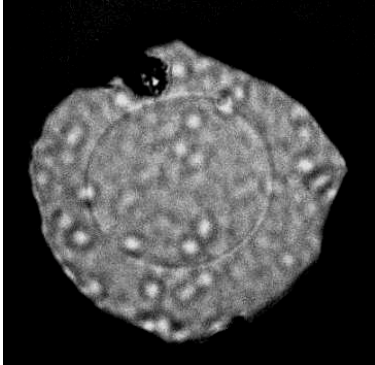


Figure 4.1. Photograph of the solid-fluid equilibrium at 8.34GPa, 675 K. The interface between the solid and fluid phases is visible thanks to the difference in the refractive index of the solid and fluid phases. The blur in the image comes from dust on the camera.

4.3 Results

The experimental melting points of AMH were determined from 300 to 675 K and from 2 to 8.3 GPa. The data are gathered in Figure 4.2 and Table 4.1.

Two domains of the melting line of AMH are observed:

- Below 3.59 GPa and $T < 324$ K, the solid-fluid equilibrium is observed in a finite range of pressure along an isotherm. In this domain, the melting is thus not congruent. The associated solidus and liquidus curves are respectively depicted in blue and brown dashed line in Figure 4.2.
- Above 3.59 GPa and $T > 324$ K, the solid/fluid equilibrium is observed only at definite (P, T) data as for a pure compound. The melting line is congruent and depicted in red in Figure 4.2.

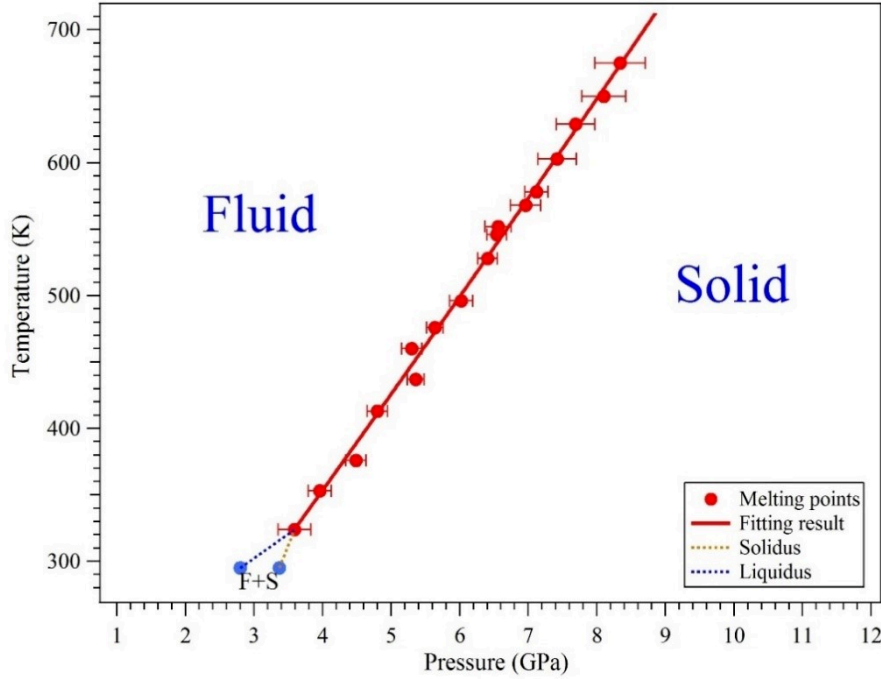


Figure 4.2. Experimental melting curve of AMH determined in this work. The symbols are the experimental melting points. Above 324 K, the melting line is congruent and is presented with red symbols. The red line represents the fit to the data with a Simon-Glatzel equation. Below 324 K, the melting line is not congruent and the blue symbols represent respectively the solidus and liquidus. Between these two lines, solid and fluid phases coexist (F+S).

4.3.1 Observation and characterization of the non-congruent melting line (T<324 K)

Figure 4.3 shows several photographs of the sample taken during decompression from 4.8 GPa to 2.76 GPa at room temperature. The Raman spectra collected during the experiment are shown in Fig. 4.4(a). The sample was initially (after loading) in the AMH-VI phase, which as shown in the previous chapter is actually a mixture of the DIMA and *P4/nmm* phases, as confirmed by the measured Raman spectrum. Upon decompression, the same sequence of phase transitions as described in Chapter 3 is observed: first, AMH-VI transits into a mixture of AHH-II and the unknown, water-rich hydrate phase (WRH) at 4.8 GPa, which then transits into a mixture of AHH-II and ice VII at 3.41 GPa. The latter transition is visually detected by changes in the sample texture, as seen by comparing Figures 4.3(a) and 4.3(b): the initially transparent sample develops a granular aspect at the transition. Slight differences are also detected in the O-H and N-H stretching modes at the transition, as seen in Figure 4.4(a). We note however that it is difficult to distinguish the Raman spectra in the stretching mode region of the AHH-II + ice VII mixture from that of pure AHH-II, since the weak O-H stretch Raman modes of ice VII occur in the same frequency range as the strong N-H stretch modes of AHH-II. This is illustrated in Figure 4.4(b).

We observed the sample starting to melt as the pressure reached 3.33 GPa, which thus corresponds to the pressure of the solidus at 300 K. This observation is mostly based on the change of the sample aspect at this pressure: the crystal grains in the sample grow larger and

start to move [Figures 4.3(c) to 4.3(e)]. Meanwhile, the amount of fluid is too small at this pressure to be detectable by Raman, and the Raman spectra taken at different positions resemble that of the AHH-II+ice VII mixture.

Upon further decrease of pressure, the amount of fluid phase increases (Figure 4.3(f)) and Raman spectra may be collected from the two phases (note that the Raman spectra of the solid may contain a contribution from the liquid not visible in the 2D image). This is illustrated in Figure 4.4 at 3.09 GPa, which shows that (1) the Raman spectra of the (mostly) solid phase closely resembles that of AHH-II and (2) the Raman spectra of the liquid is very different from that of AHH-II and consistent with the literature. At 2.76 GPa, the sample becomes a completely homogeneous and transparent fluid, which was confirmed by its Raman spectra.

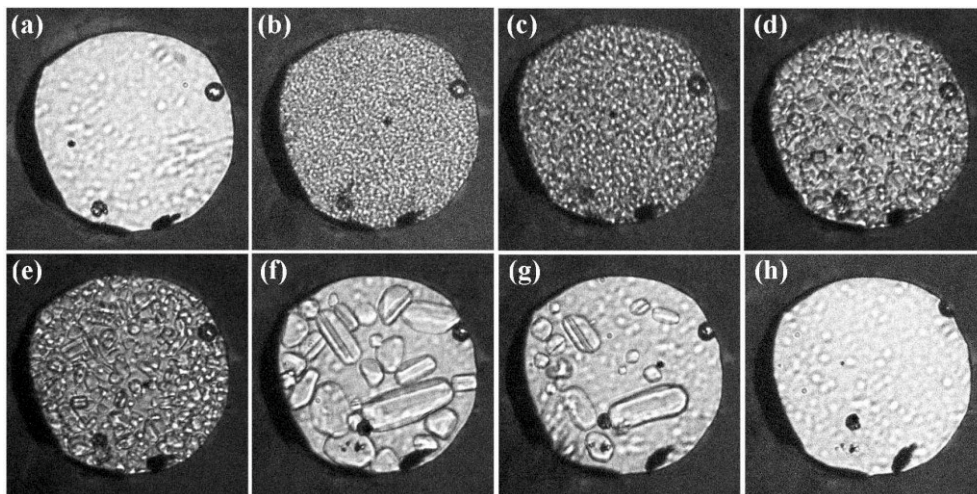


Figure 4.3. Photographs of AMH sample during decompression from 4.80 GPa to 2.76 GPa at room temperature. (a) 4.80 GPa: the sample is solid and corresponds to a mixture of AHH-II+hydrate (the visible white domains are due to dust particles on the camera) ; (b) 3.41 GPa: the sample is solid and is a mixture of AHH-II+ice-VII; (c), (d) and (e): the sample starts to melt – coexistence of solid and liquid and the pressure is stable at 3.33 GPa; (f) 3.09 GPa: several crystals (solid AHH-II) in coexistence with the fluid. When the pressure decreases down to 2.84 GPa (g), the volume of the solid phase decreases and the amount of liquid increases; (k) at 2.76 GPa, the sample becomes homogeneous, transparent and corresponds to the fluid.

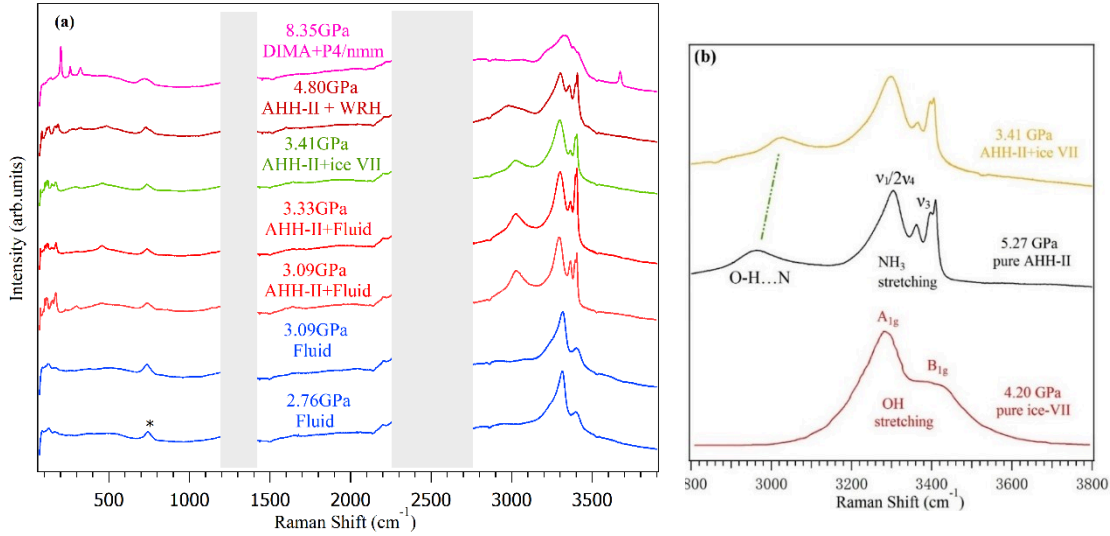


Figure 4.4. (a) Evolution of the Raman spectra of AMH during the decompression from 8.35 GPa to 2.76 GPa at ambient temperature. The frequency windows from 1200–1400 cm^{-1} to 2300–2700 cm^{-1} are greyed as they are dominated by, respectively, the first- and second-order Raman signal from the diamond anvils. The peak around 750 cm^{-1} marked by asterisk comes from impurities in the diamond anvils. (b) Comparison of Raman spectra of pure ice-VII^[3], pure AHH-II and the mixture of ice-VII+AHH-II. The Raman spectra of pure AHH-II and of its mixture with ice VII close to the melting point of AMH are hardly discernible.

In conclusion, at 300 K, the solid phase before melting is a mixture of AHH-II and ice VII, as reported in the literature^[4]. At the solidus pressure, ice VII melts first and AHH-II coexists with the fluid down to the liquidus pressure. Our best estimates for the solidus and liquidus pressures are 3.33 GPa and 2.76 GPa respectively. As seen below, for all temperatures above 300 K investigated in the present work, a different melting behavior was observed, indicative of a congruent melting.

4.3.2 Observation and characterization of the congruent melting line (T>324 K)

Table 4.1. Experimental melting points of AMH. P_m is in GPa and T_m is in K.

P_m	T_m	P_m	T_m	P_m	T_m
3.59(24)	324	5.64(12)	476	7.12(17)	578
3.96(17)	353	6.02(17)	496	7.42(28)	603
4.45(15)	376	6.41(14)	528	7.69(28)	629
4.80(15)	413	6.54(14)	546	8.10(32)	650
5.30(15)	460	6.56(19)	552	8.34(37)	675
5.36(12)	437	6.96(22)	568		

From 324 K to 700 K, we observe that the solid-fluid equilibrium occurs at a finite value of P along an isotherm (no data was collected between 300 and 324 K). The (P , T) conditions which define the congruent melting line are reported with red symbols in Figure 4.2 and presented in Table 4.1. In this P - T range, the melting pressure is a monotonously increasing function of temperature and no discontinuity is observed.

Figure 4.5 shows photographs of the sample taken during the decompression at 376 K, and Figure 4.6 presents the respective Raman spectra. At 6.7 GPa, the sample is a mixture of AHH-II and WRH, as revealed by its Raman spectra. The visual aspect of the sample is that of a polycrystal with some “cracks”. As the pressure is decreased to 5.83 GPa, the sample image suddenly becomes more transparent (Figures 4.5 (b)) and the Raman spectra change, signaling a phase transition to another solid phase which we called AMH-VII.

On further decompression, we detect the coexistence of a fluid and a solid phase at 4.45 GPa, as visible in Figures 4.5(d) and 4.5(e). The interface between them is however more difficult to observe than at ambient temperature, which indicates that the difference in refractive indices between the fluid and solid phase at high temperature is small. The Raman spectra of the solid phase are the same as that measured just above the melting pressure, thus we identify it as AMH-VII.

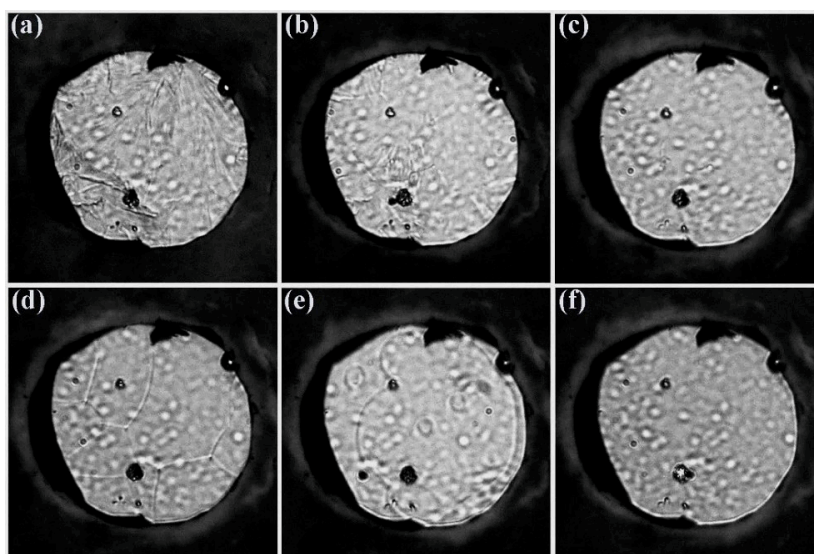


Figure 4.5. Photographs of AMH from solid to fluid at 376 K. (a) 6.7 GPa; (b) 5.83 GPa; (c) 4.98 GPa; (d) 4.45 GPa; (e) 4.45 GPa; (f) 4.34 GPa.

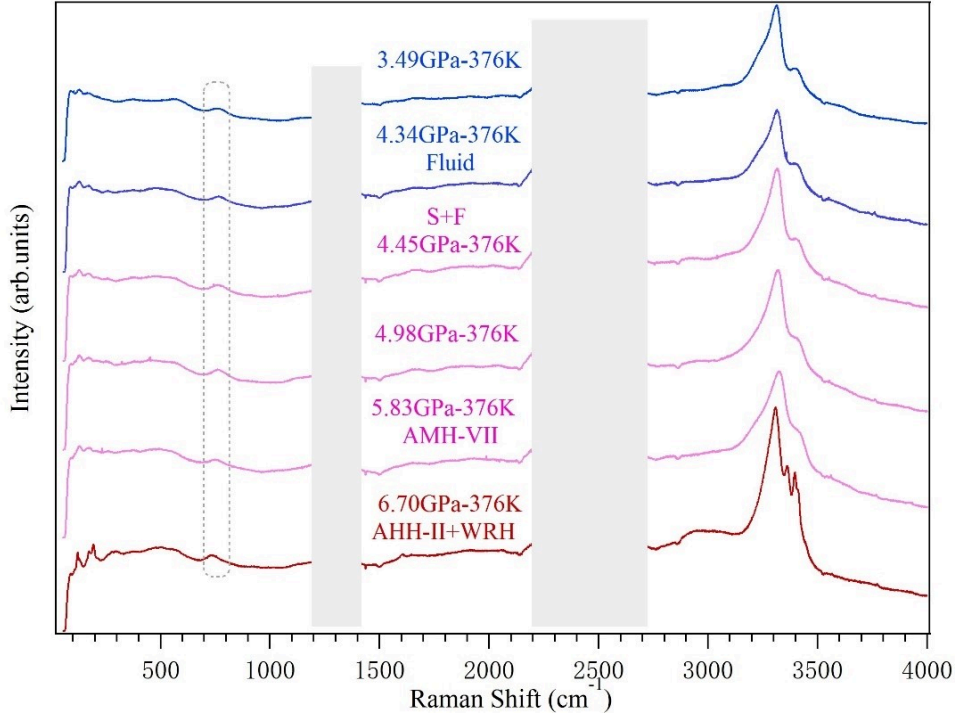


Figure 4.6. Evolution of the Raman spectra of AMH from solid (6.7 GPa) to fluid (3.49 GPa) at 376 K. The frequency windows from 1200–1400 cm^{-1} to 2300–2700 cm^{-1} are greyed as they are dominated by, respectively, the first- and second-order Raman signal from the diamond anvils. The peak around 750 cm^{-1} marked by the gray dotted frame comes from impurities in the diamond.

Contrary to the room temperature observations, the measured pressure does not change while varying the load at 4.45 GPa, only the respective amount of fluid and solid phase varies. This demonstrates that (1) melting is congruent at 376 K, and (2) the solid phase has the same composition as the fluid, i.e 1:1, and thus AMH-VII is a proper AMH solid phase.

It can also be observed from Figure 4.6 that the Raman spectra of AMH-VII is very similar to that of the fluid phase, and it is thus difficult to infer melting solely from the Raman measurements.

The lowest temperature at which the solid transition to AMH-VII before melting was detected is 324 K, as seen in Figure 4.7, and the AMH-VII/fluid equilibrium was observed up to at least 8.34 GPa – 675 K (maximum P-T conditions investigated in this work). These data allow us to fix a triple point between the solidus/liquidus and the congruent melting line of AMH-VII at 324 K and 3.59 GPa as illustrated in Figure 4.2.

Among the various relations proposed in the literature to reproduce the experimental melting line, the semi-empirical Simon-Glatzel equation^[5] has been found to well reproduce the melting curve of many substances, provided that they have a regular (i.e. monotonic) behavior. This is the case in particular for water^[6] and ammonia^[7]. This relation can be written as:

$$T_m = T_0 \left(1 + \frac{P_m - P_0}{a} \right)^{\frac{1}{b}} \quad 4.1$$

Where T_m and P_m are the melting pressure, respectively, a and b are fit parameters and T_0 , P_0 are the T - P condition of a reference point. We used the solidus/liquidus/congruent melting line triple point coordinates of AMH as the reference point, i.e. $T_0 = 324$ K and $P_0 = 3.59$ GPa. The fit values of a and b are $a = 4.9 \pm 0.8$ GPa and $b = 0.93 \pm 0.12$, and the fit curve is displayed in Figure 4.2.

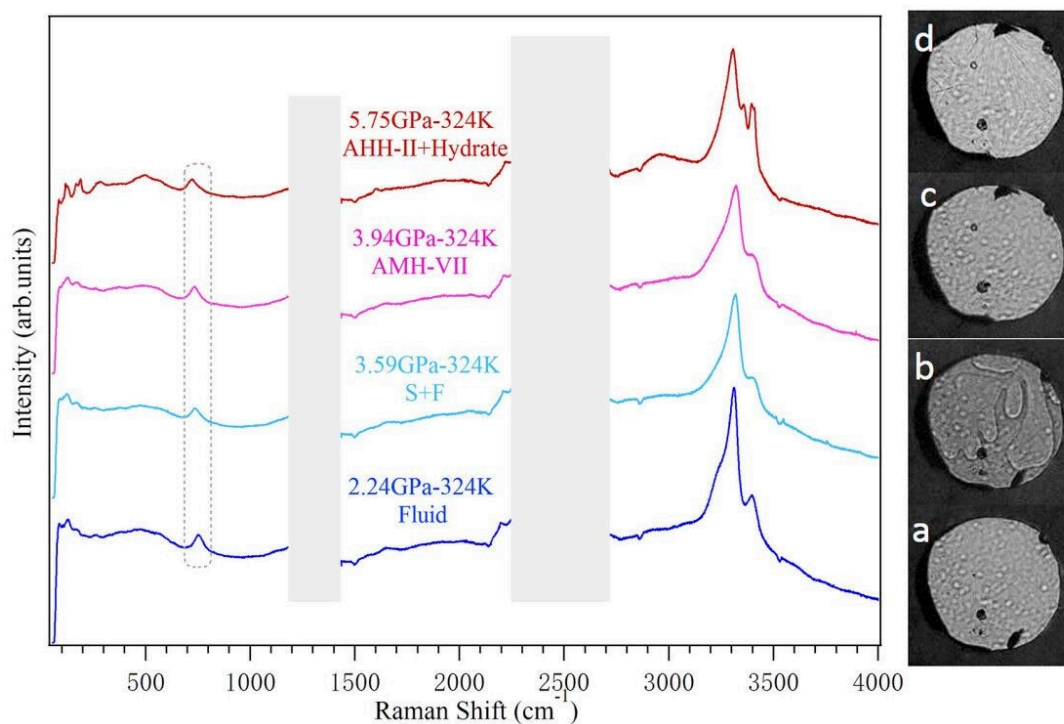


Figure 4.7. Raman spectrum and photographs of AMH from liquid to solid at 324 K. (a) 2.24 GPa; (b) 3.59 GPa.; (c) 3.94 GPa; (d) 5.75 GPa. The frequency windows from 1200–1400 cm^{-1} to 2300–2700 cm^{-1} are greyed as they are dominated by, respectively, the first- and second-order Raman signal from the diamond anvils. The peak around 750 cm^{-1} marked by the gray dotted frame is the impurities in the diamond.

4.4 Discussion

4.4.1 Comparison with literature

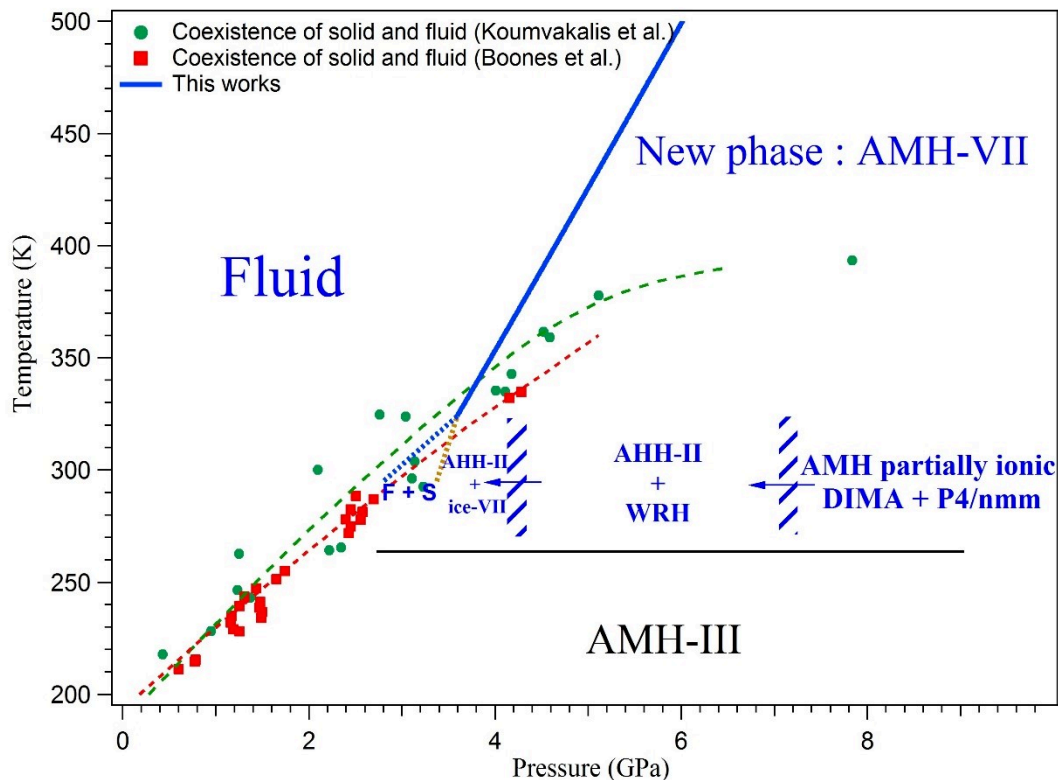


Figure 4.8. Comparison between the melting lines of AMH from our work with the literature^[1,2]. The dotted green and red lines respectively represent the “average” melting curves reported by Koumvakalis & Nicol. and Boone & Nicol. ^[1,2].

In Figure 4.8, our melting line of AMH is compared with the previous results reported by Boone & Nicol^[2] and Koumvakalis & Nicol^[1]. Our melting curve is clearly different from these previous references:

- Below 324 K: Previous works report a congruent melting whereas our work clearly shows a pressure range of solid-fluid coexistence at 300 K. We also note that the two melting lines of Boone & Nicol and Koumvakalis & Nicol differ from each other and are in closer agreement with the liquidus curve of this work.
- Above 324 K: the few melting points reported by Koumvakalis & Nicol are at higher pressure than in our work for a given temperature. Furthermore the slope dT/dP of their melting line decrease with pressure much faster than in the present work.

To explain the difference in the nature of the melting (congruent or not) below 324 K, there are several arguments associated with the difference of methods for measuring the melting line:

- In reference^[1], the melting line was determined by the observation of a sudden clearing of the textured and cracked samples when the sample was heated slowly (2 K/min) under a

constant load or when pressure was isothermally released. As the authors observed that the melting and crystallization were “rapid”, they conclude that the melting is “apparently congruent”. Nevertheless, Koumvakalis & Nicol mentioned that solid and fluid were also observed to coexist over a large range of pressure and temperature, and the individual melting observations were highly scattered^[1]. Actually, the plot of these coexistence data (green symbol in Figure 4.8) is more compatible with our non-congruent melting line: for example, at 300 K, they observe the coexistence of fluid and solid at 2.2 GPa and also at 3.2 GPa. The spread of their data also seems to decrease with temperature as observed in our experiments.

- Boone & Nicol^[2] used the same method that Koumvakalis & Nicol and also reported a congruent melting curve. As can be seen in Figure 4.8, their experimental data were mainly focused at $T < 300$ and 4 distinct zones of temperature have been studied: around 220 K, 240 K, 270 K and 330 K. They have fitted the whole of their data with a single curve whereas several solid/solid phase transitions [AMH-II/AMH-III and AMH-III/AMH-V (=AHH-II + ice-VII)] are observed in this range of temperature. It is also interesting to note that the dehydration of AMH was not reported in these papers whereas their Raman spectra are compatible with ice-VII + AHH-II.

In our opinion, the difference between the present and previous melting experiments can be explained if we suppose that the authors of Refs.^[1,2] confused melting with the transition to the high-temperature phase AMH-VII. Indeed the latter shows strong similarities with the liquid: the two phases are transparent, their refractive indexes are close and their Raman spectra are similar. We thus conjecture that the melting curves of Koumvakalis & Nicol and Boone & Nicol at high temperature corresponds in fact to a solid/solid phase transition between the low-pressure phase (Ice-VII or WRH+AHH-II) to the new HT AMH-VII phase. We will see in Chapter 5 that this conjecture is confirmed by our measurements of the AMH-VII stability domain.

4.4.2 Comparison with pure water and ammonia

We have compared the melting line of AMH with those of pure water^[6] and pure ammonia^[7]. This comparison is shown both on an absolute and reduced P-T scales in Figures 4.9 (a) and (b).

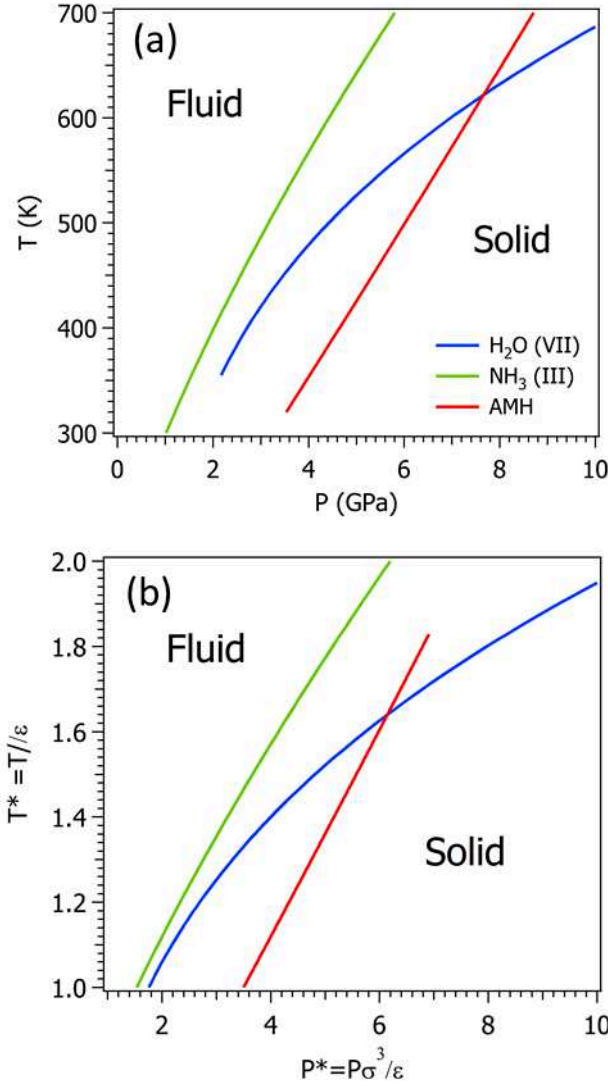


Figure 4.9. Comparison between the melting lines of the isoelectronic solids H₂O^[6], NH₃^[7] and AMH(a) in absolute (P, T) scale, (b) using reduced units.

In order to compare the melting lines on the same density map, we computed the reduced pressure (P) and temperature (T) using the following formulas^[8], derived from the law of corresponding states²:

$$P^* = P\sigma^3/\varepsilon \quad 4.2$$

$$T^* = T/\varepsilon \quad 4.3$$

where σ and ε are respectively the position and depth of the minimum of the effective pair potential. For pure species like H₂O and NH₃, parameters σ and ε have been determined for the Buckingham (exp-6) potential by Belonoshko and Saxena^[8]. To determine these parameters for AMH, we use the mixing rules given below ^[8,9]:

² The law of corresponding states assesses that classical (i.e. non quantum) systems interacting with the same interatomic pair potential which can be written in the form $\varphi(r) = \varepsilon f(r/\sigma)$ possess identical thermodynamic properties at a given reduced pressure and temperature expressed as in Eqs. 4.2 and 4.3.

$$\sigma_{ij} = \frac{(\sigma_i + \sigma_j)}{2}, \quad \varepsilon_{ij} = \sqrt{\varepsilon_i \varepsilon_j} \quad 4.4$$

The values of parameters σ and ε of AMH for H₂O, NH₃ and AMH are shown in Table 4.2.

Table 4.2. Values of the parameters σ and ε determined from the exp-6 potential by Belonoshko et al.^[8]. k is the Boltzmann constant

	ε/k (K)	σ (Å)
NH ₃	328.0	3.3970
H ₂ O	446.7	2.8431
AMH	382.8	3.1201

It can be seen that the slope dT_m/dP_m of the melting line of AMH is closer to that of NH₃ than to the one of H₂O at high P-T. This similarity in the melting curves of AMH and NH₃ indicates that the intermolecular interactions in the high temperature solid AMH-VII are closer to those in the pure NH₃ solid than in the pure H₂O solid. This suggests that the H-bond strength in AMH-VII is of the same order as in pure NH₃, and thus weaker than in pure H₂O.

4.5 Conclusions

In this chapter, the melting curve of AMH is determined up to 700 K by visual observation and Raman experiments. Below 324 K, we have observed that melting is non-congruent due to the fact that the solid phase bordering the fluid is not a proper AMH phase but a mixture of AHH-II and ice VII. The solidus and liquidus pressure have been determined at 300 K. Above 324 K, the solid-fluid equilibrium occurs at a unique (P, T) value and thus become congruent. This reveals that above 324 K, the solid in equilibrium with the fluid, which we named AMH-VII has the same stoichiometry as the latter, and thus is a proper AMH phase. This new high temperature phase has similar refractive index and Raman spectra as the fluid, making it more difficult to detect melting by visual and Raman observation. However, we obtained a precise determination of the melting line from our visual observations up to 675K and 8.3 GPa. Comparison of the melting line of AMH-VII with NH₃ and H₂O reveals that its slope is closer to that of NH₃, which suggests a stronger correspondence between AMH-VII and the plastic solid phase III of NH₃. The properties of AMH-VII are further explored in the next chapter.

References

- [1] Koumvakalis, A. & Nicol, M. in *High Pressure Chemistry, Biochemistry and Materials Science Raman Spectroscopy of Ammonia Monohydrate to 13.5 GPa* 265-274 (Springer, 1993).
- [2] Boone, S. & Nicol, M. in *Lunar and Planetary Science Conference Proceedings*. 603-610.
- [3] Lin, J.-F., Militzer, B., Struzhkin, V. V. *et al.* High pressure-temperature Raman measurements of H₂O melting to 22 GPa and 900 K. *The Journal of chemical physics* **121**, 8423-8427, (2004).
- [4] Wilson, C., Bull, C., Stinton, G. *et al.* Pressure-induced dehydration and the structure of ammonia hemihydrate-II. *The Journal of chemical physics* **136**, 094506, (2012).
- [5] Simon, F. & Glatzel, G. Bemerkungen zur schmelzdruckkurve. *Zeitschrift für anorganische und allgemeine Chemie* **178**, 309-316, (1929).
- [6] Datchi, F., Loubeyre, P. & LeToullec, R. Extended and accurate determination of the melting curves of argon, helium, ice (H₂O), and hydrogen (H₂). *Physical Review B* **61**, 6535, (2000).
- [7] Ninet, S. & Datchi, F. High pressure–high temperature phase diagram of ammonia. *The Journal of chemical physics* **128**, 154508, (2008).
- [8] Belonoshko, A. & Saxena, S. A unified equation of state for fluids of CHONS-Ar composition and their mixtures up to very high temperatures and pressures. *Geochimica et Cosmochimica Acta* **56**, 3611-3626, (1992).
- [9] Ross, M., Ree, F. & Young, D. The equation of state of molecular hydrogen at very high density. *The Journal of chemical physics* **79**, 1487-1494, (1983).

Chapter 5: A plastic solid phase of ammonia hydrate at high P-T

Contents

5.1 Introduction	99
5.2 Structure of AMH-phase VII.....	99
5.3 Stability field of AMH-VII below 10 GPa.....	103
5.4 Evidence for the plastic nature of AMH-VII.....	104
5.4.1 Similitudes with the plastic phases of NH ₃ and H ₂ O	104
5.4.2 QENS experiments.....	105
5.4.2.1 Experimental protocol.....	105
5.4.2.2 Results	107
A. Results for the liquid phase	108
B. Results for the solid phase.....	111
5.5 Conclusions	116
References	117

5.1 Introduction

As reported in the previous chapter, we have discovered a new high temperature solid phase of AMH called AMH-VII. We have shown that this phase is obtained by compression of liquid AMH or decompression of the solid above 324 K, and is thus the thermodynamically stable phase at melting above 324 K. In this chapter, we present our detailed study of the structural and vibrational properties of AMH-VII obtained by XRD and Raman scattering. We then present the stability domain of AMH-VII in the moderate pressure domain ($P < 10$ GPa). We will see that strong similarities exist between AMH-VII and the plastic phase III of pure ammonia, suggesting that AMH-VII is itself a plastic solid. This motivated us to perform quasi-elastic neutron experiments which provide the experimental proof that AMH-VII phase is a plastic solid.

5.2 Structure of AMH-phase VII

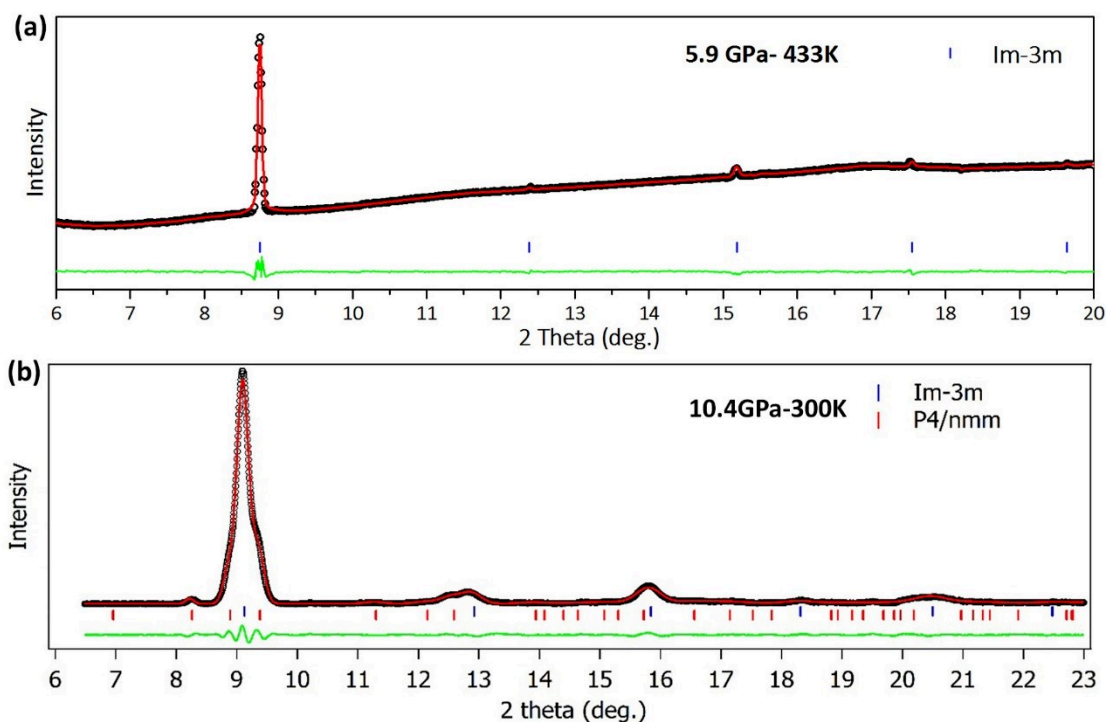


Figure 5.1. Le Bail fits of the XRD patterns of (a) AMH-VII and that of (b) AMH-VI (DIMA phase). The symbols are experimental data and the red line is Le Bail refinement using $Im-3m$ structure. Sticks show the positions of Bragg reflections. The green line represents the difference between observed and calculated profiles.

The structure of the AMH-VII phase was investigated by XRD experiments. The integrated pattern collected at 5.9 GPa and 433 K is shown in Figure 5.1(a). The Bragg peaks can all be indexed by a body-centered cubic (bcc) unit cell with $Im-3m$ space group. The Le Bail fit using this symmetry is reported in Figure 5.1(a), and agree very well with the experimental data. Figure 5.1(b) shows a diffraction pattern of AMH-VI measured at 10.4 GPa

and room temperature for comparison. As seen in Chapter 3, the latter can be interpreted as a mixture of an $Im-3m$ bcc structure and of the ionic $P4/nmm$ structure. According to our *ab initio* simulations, the bcc phase in AMH-VI is not purely molecular, as initially described by Loveday et al, but is partly ionic, and can be described as a disordered ionico-molecular (DIMA) phase. The comparison between the XRD patterns of AMH-VII and AMH-VI phases reveals that:

✧ In the XRD patterns of AMH-VII phase, the Bragg peaks which index as $P4/nmm$ phase are never observed, while they are usually present, with weak or strong intensities depending on the sample in the patterns of AMH-VI. This indicates that the AMH-VII phase is a pure phase. The volume per molecule of AMH-VII measured at 433 K is presented in Figure 5.2. This volume is close to the ambient temperature equation of state of AMH, the difference likely coming from the thermal expansion due to the higher temperature. This is another proof that AMH-VII is a proper AMH solid phase.

✧ The full width at half maximum (FWHM) of the Bragg peaks of AMH-VII phase is much smaller than in AMH-VI phase. The simulations of the DIMA phase described in Chapter 3 suggest that the large width of the Bragg peaks in AMH-VI are due to the local and fluctuating distortion of the cubic unit cell induced by the partial ionization of molecules through local proton transfer, and different H-bonding scheme between the ions and molecules. The small peak width in AMH-VII indicates that this microscopic strain is absent. There are at least two possible interpretations: either AMH-VII is purely molecular, and would thus correspond to the DMA phase described by Loveday et al^[1], or there exists a dynamic disorder that results in a more isotropic distribution of the protons.

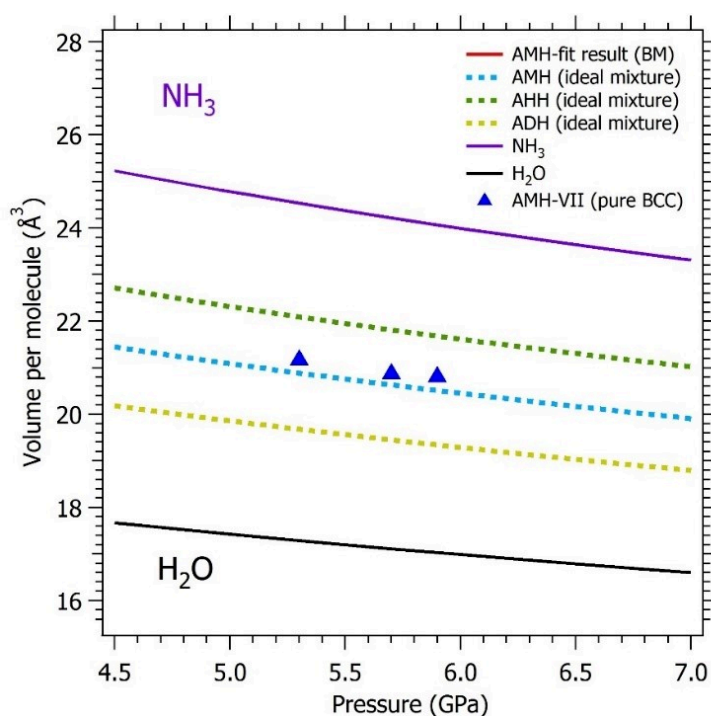


Figure 5.2. Pressure dependence of the molecular volume of AMH-VII measured at 433K (triangle symbols).

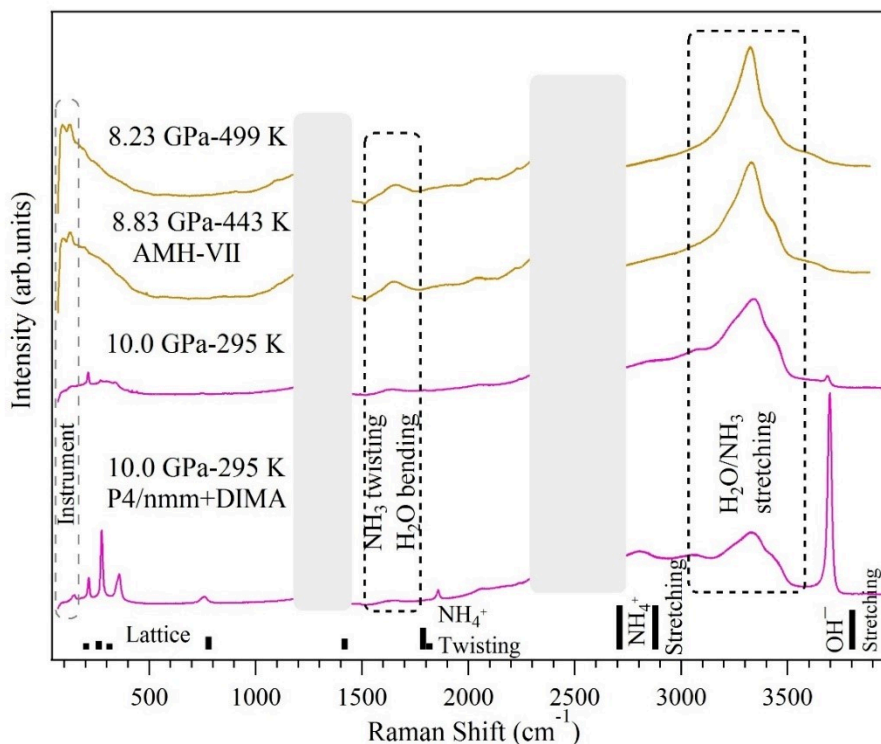


Figure 5.3. Comparison between the Raman spectra of AMH-VI and AMH-VII. The theoretical vibrational spectra (at 0 K) for the fully ionic $P4/nmm$ structure is shown in the lower panels. The black dashed lines represent the molecular vibration mode and the gray dashed line represents the signal from the instrument. The frequency windows from 1200–1400 cm^{-1} to 2300–2700 cm^{-1} are greyed as they are dominated by, respectively, the first- and second-order Raman signal from the diamond anvils.

To study the vibrational properties of AMH-VII, we compare the Raman spectra of AMH-VII and AMH-VI phases at near pressures as depicted in Figure 5.3. The Raman spectra of AMH-VI (the pink ones) were collected at different positions of the sample at room temperature. The most striking difference between the Raman spectra of AMH-VII and AMH-VI is the absence of the Raman peaks of the ionic $P4/nmm$ phase in AMH-VII, which confirms the absence of this phase noted above in the XRD pattern. By contrast, the modes assigned to the molecular species are more similar in the two phases: similar frequency range and shape in the OH/NH stretching and bending regions, broad peaks characteristic of a proton disordered phase.

The comparison of the stretching band is shown in more detail in Figure 5.4(a,b), where a tentative deconvolution of the broadband into individual Raman modes is presented. Their pressure dependence is shown in Figure 5.4(c). For AMH-VI, at least 7 modes are needed to reproduce the band shape. Two of them, the NH stretch of NH_4^+ at 2900 cm^{-1} and the OH stretch of OH^- at 3700 cm^{-1} , are assigned to the $P4/nmm$ phase and are not seen in AMH-VII. The five others are observed in the two phases with a slight difference in intensities. The one centered at 3100 cm^{-1} at 10 GPa has a negative frequency shift with pressure and is assigned to the ν_1 OH stretch of H_2O . The three modes in the region 3200–3400 cm^{-1} present slight positive shifts with pressure and are assigned to either the ν_1 – ν_3 stretching modes of NH_3 or the overtone $2\nu_4$ of the NH bending of NH_3 ^[2,3]. The band centered at 3600 cm^{-1} has a positive shift with pressure and

has not been observed in other solid phases of the hydrates so far. This band is present in both AMH-VI and VII but is more intense in AMH-VII. It is unlikely that it originates from an overtone or a combination band of H₂O or NH₃, as none has been observed at this frequency^[2], and the highest frequency bending mode has a frequency of ~ 1660 cm⁻¹, so its overtone should be near 3320 cm⁻¹. On the other hand, the frequency of this peak is close to that of the OH stretch of the OH⁻ ion in *P4/nmm*, which also has a positive variation with pressure, so this mode could indicate the presence of OH⁻. Its large bandwidth compared to that in *P4/nmm* could originate from the disorder of DIMA, leading to various possible environments for the ion, or from a short lifetime of this ion.

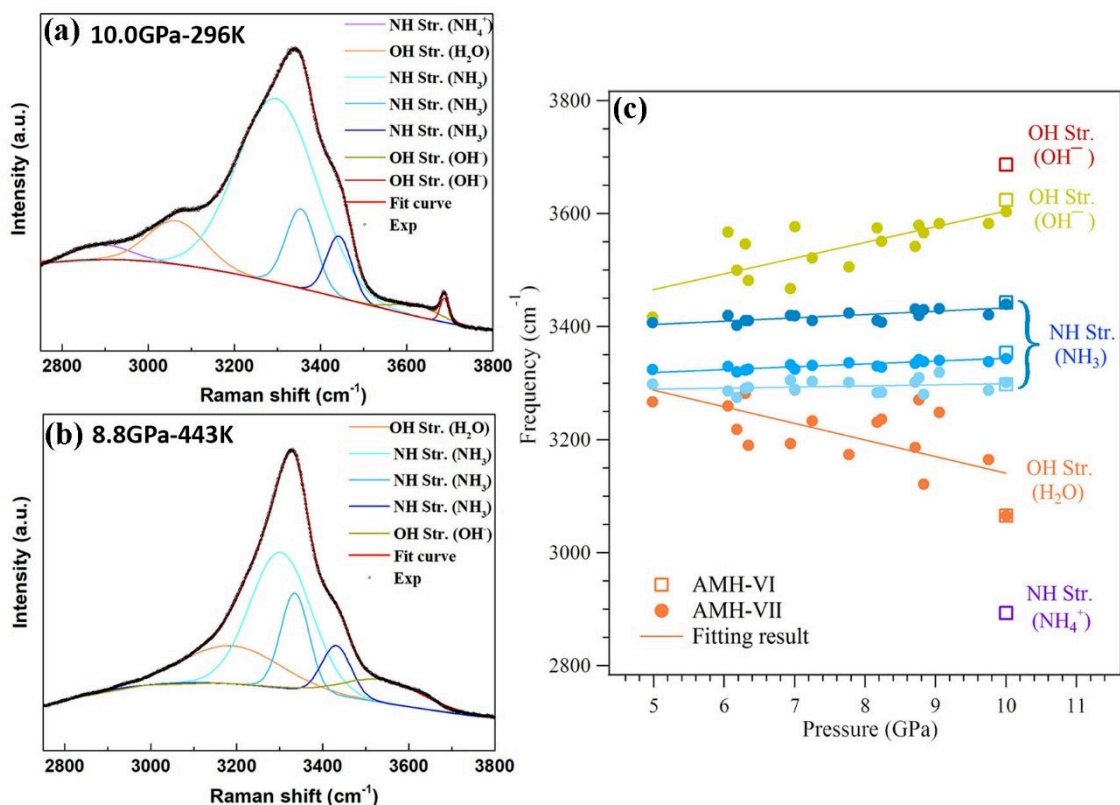


Figure 5.4. Stretching region of the Raman spectra of (a). AMH-VI phase at 10.0 GPa-295 K, (b). AMH-VII phase at 8.8 GPa-443 K. (c). Pressure evolution of the Raman band wavenumbers of AMH-VI and AMH-VII at varied temperatures. Hollow squares represent AMH-VI, solid circle represents AMH-VII. Different colors represent different vibration modes, and the lines represent the fitting results of our experimental data.

Finally, we note that AMH-VI and VII markedly differ in the low frequency part of the Raman spectra. As a matter of fact, AMH-VII presents a strong but featureless Raman activity extending from 500 cm⁻¹ down to the lowest measurable frequency (60 cm⁻¹), while AMH-VI only present broad and weak modes apart from those of the *P4/nmm* phase. This suggests a marked difference in the translational and/or rotational dynamics of the two phases.

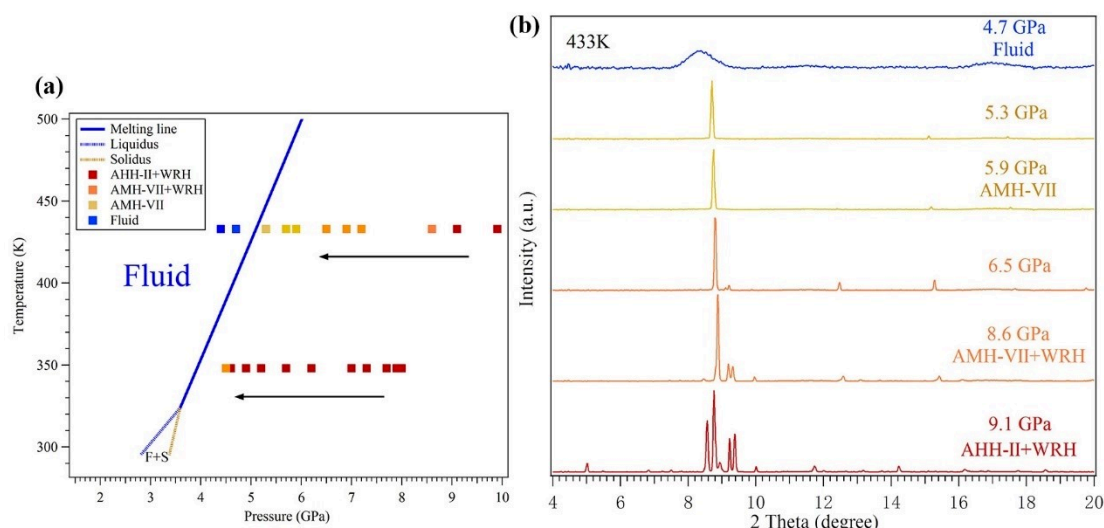


Figure 5.6 (a). Isothermal decompression paths followed during an XRD experiment on AMH at 348 K and 433 K. The different color symbols represent different phases; (b). X-ray diffraction patterns collected along the decompression path at 433 K. The color code is the same as in (a).

As seen in Figure 5.5(b), the P-T stability field of AMH-VII is delimited by the melting line at low pressure and the solid-solid transition line depicted in red at high pressure. The latter intersects the melting line at the same P-T point where the solidus, liquidus and melting line meet (324 K, 3.59 GPa – see Chapter 4). We note that in this pressure range, this solid-solid transition line coincides with the dehydration of AMH into AHH-II+WRH. The transition/dehydration temperature appears to linearly increase with pressure with a slope of 21 K/GPa. It is also interesting to note that this line is close to the melting curves reported in Refs.^[3,4] (see Chapter 4), substantiating our hypothesis that these authors confused melting with the presently determined solid-solid phase transition.

5.4 Evidence for the plastic nature of AMH-VII

5.4.1 Similitudes with the plastic phases of NH₃ and H₂O

As recalled in Chapter 1, the phase diagram of ammonia presents two solid phases, II (*hcp* structure) and III (*fcc* structure), which are plastic solids, that is to say, the molecules in these phases behave as free or nearly-free rotators. As a matter of fact, the plastic nature has only been demonstrated for phase II using NMR^[5], but several arguments support that phase III is also plastic: 1) the *fcc* structure (space group *Fm-3m*), as the *hcp* one, is not compatible with proton-ordered molecules, and thus phase III must be orientationally disordered; (2) the *fcc* and *hcp* structures have very close Gibbs free energy, as shown by the absence of kink in the melting line at the II-III-L triple point; and (3) plasticity is observed in *ab initio* molecular dynamics (MD) simulations of phase III^[6].

There are strong similarities between AMH-VII and phases II and III of pure ammonia: (1) they are orientationally disordered phases; (2) they are bordered by the melting line at low pressure and the slope of the melting lines of AMH-VII and NH₃-III have close values (see Chapter 4); (3) the Raman spectra of AMH-VII has strong resemblance with that of fluid AMH at the same temperature, which is also the case for NH₃ phases II and III (see Figure 5.7).

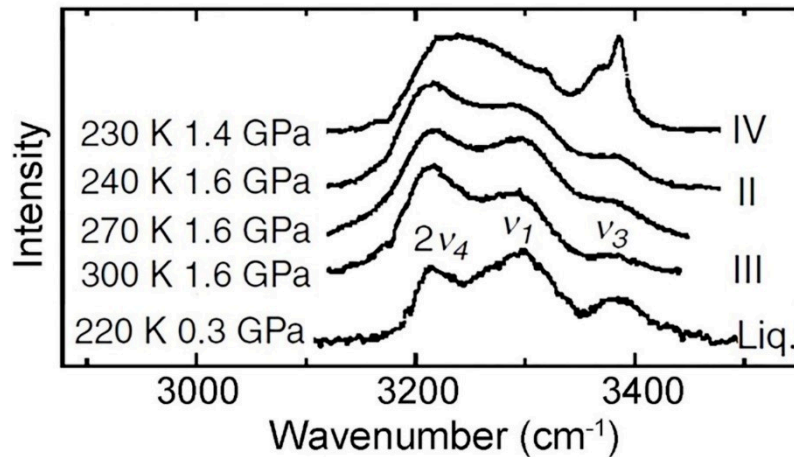


Figure 5.7. N-H stretch Raman spectra of different phases of ammonia from ref^[7]. Note the resemblance between the Raman spectra of the liquid phase and the plastic solid phases II and III.

In addition, we recall that classical^[8] and *ab initio* MD simulations^[9] have predicted the existence of a plastic phase of ice in the vicinity of the melting line (above 352 K, 6 GPa in ref^[8]), i.e. in a P-T range intersecting the P-T stability of AMH-VII (see Chapter 1). This phase has the same symmetry as ice VII (space group *Pm3m*), with orientationally disordered molecules on a *bcc* lattice, i.e. the same crystal lattice as AMH-VII. No experimental evidence of this plastic ice VII has been reported yet.

All these observations suggest that AMH-VII phase may also be a plastic solid. To check this hypothesis, we performed high pressure quasi-elastic neutron experiments as presented in the following.

5.4.2 QENS experiments

As described in Chapter 2, quasi-elastic incoherent neutron scattering (QENS) measurements can provide some information about the diffusion at a molecular scale and the motion of H/D atoms around the molecular center of mass. Therefore, QENS is an effective experimental method to judge whether AMH-VII is a plastic phase or not.

5.4.2.1 Experimental protocol

A distinct advantage of neutrons compared to X-rays is that they are very sensitive to light atoms such as H. Incoherent neutron scattering can detect the individual motions of atoms, and especially of H atom which has large incoherent scattering cross-section ($\sigma_{\text{inc}}=80.27$ barn, $\sigma_{\text{coh}}=1.7583$ barn)^[10]. Similarly, deuterium D is also special because its coherent and incoherent

sections ($\sigma_{\text{inc}}=2.05$ barn, $\sigma_{\text{coh}}=5.592$ barn) are of the same order of magnitude^[10]. In our experiments, in order to prevent multiple neutron scattering, D₂O was used instead of H₂O to reduce the total amount of H, so the content of H in the sample (NH₃·D₂O) is about 60%. Therefore, the QENS signal measured in present experiments mainly comes from the motion of H atoms in ammonia.

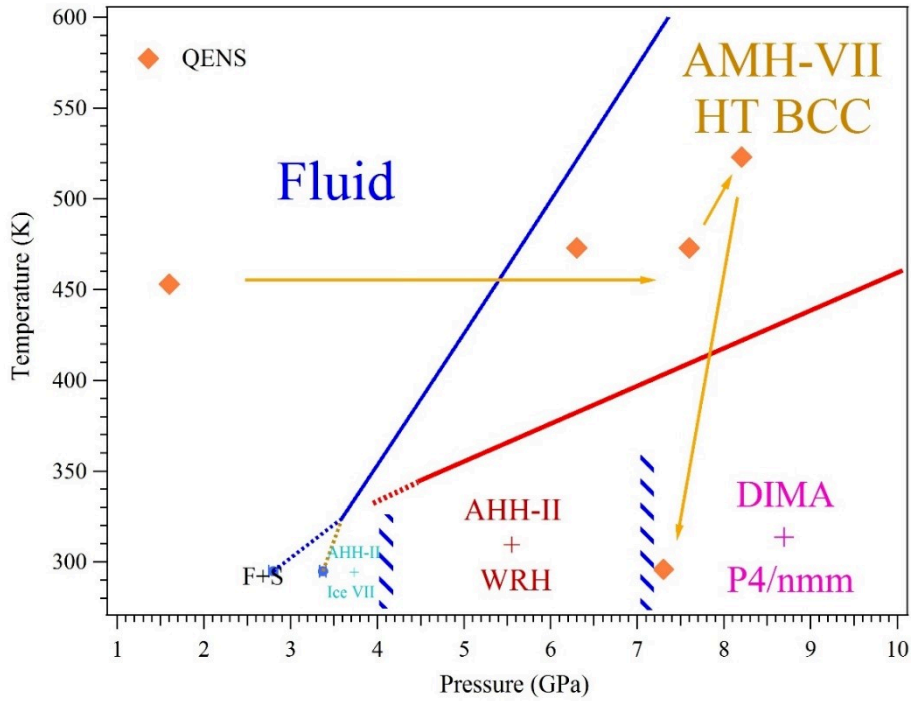


Figure 5.8. The P-T path diagram of QENS. The orange symbols represent the measured P-T points in the experiment.

The specific sample loading process has been described in detail in Chapter 2. The followed pressure-temperature (P-T) path is shown in Figure 5.8 and designed to measure the QENS signal from phase AMH-VII. First, the liquid sample was heated isobarically to 453K at 1.6 GPa and the data was collected for 8 hours. Second, the liquid sample was isothermally compressed to collect QENS spectra in the solid at 6.3 GPa (collection time: 8 hours) and 7.6 GPa (collection time: 24 hours) at 473 K. The acquisition time had to be increased in the solid phase as it became weaker than in the liquid. Then, the sample was heated to 523 K and the pressure was increased to 8.2 GPa (collection time: 30 hours). Finally, the sample was cooled to 300 K (7.3 GPa) and the data was collected for 32 hours. The latter spectra were used as the resolution for the other data sets, since we do not expect any QENS signal from the solid at these P-T conditions as the protons are fully ordered.

5.4.2.2 Results

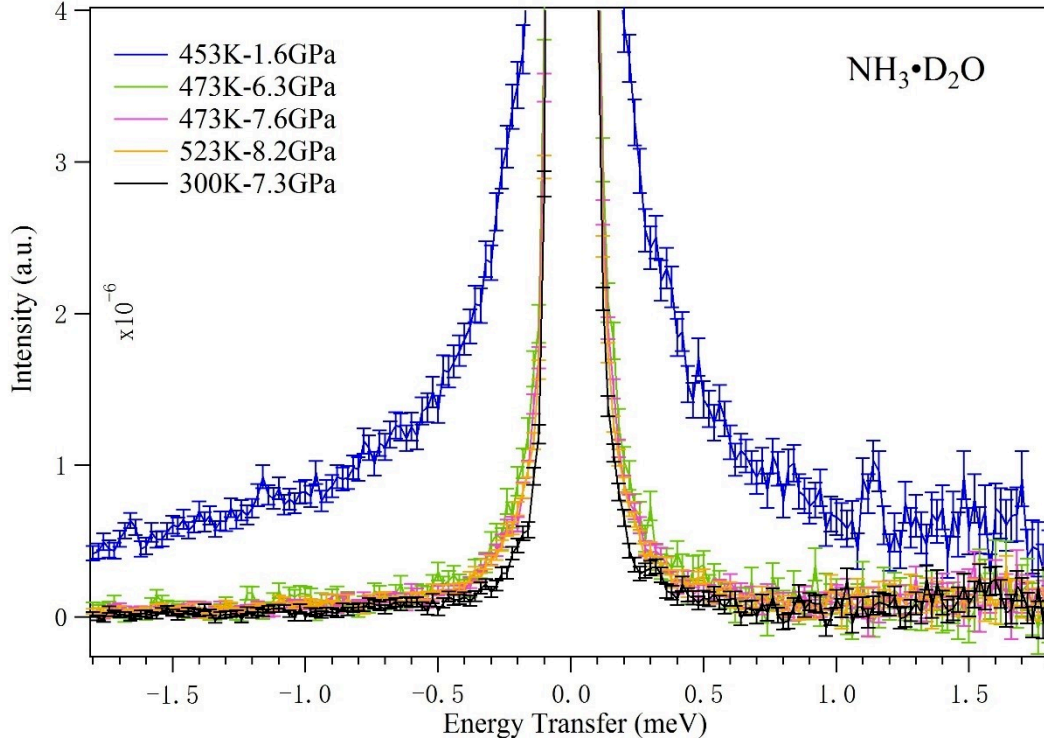


Figure 5.9. QENS spectra integrated overall Q of $\text{NH}_3 \cdot \text{D}_2\text{O}$ collected at varied pressure and temperature.

QENS spectra integrated overall Q of $\text{NH}_3 \cdot \text{D}_2\text{O}$ collected at varied pressure and temperature are shown in Figure 5.9. This figure illustrates the large reduction in diffusion intensity when the sample changed from liquid to solid. The intensity of the total $S(Q)$, on the other hand, didn't change significantly from 6.3 GPa (473 K), 7.6 GPa (473 K) and 8.2 GPa (523K).

A major advantage of the QENS experiment is that the energy spectrum of the dynamic structure factor $S(Q, \omega)$ is measured as a function of the wavevector Q which allows distinguishing translational and rotational relaxation phenomena in the system. In the quasielastic regime (Here we restrict this domain to $[-2.5$ to 2.5 meV]. As the signal of quasielastic was too weak in addition to this range.), within the assumption of a roto-translational decoupling and a multi-exponential time decay of the density–density correlation function, all spectra obtained in our experiment can be represented as a convolution of the incoherent dynamic structure factor (DSF), $S(Q, \omega)$, and the resolution function, $R(Q, \omega)$ ^[11-13]:

$$I(Q, \omega) = S(Q, \omega) \otimes R(Q, \omega) \quad 5.1$$

where the DSF is generally expressed as

$$S(Q, \omega) = e^{-\langle u^2 \rangle Q^2 / 3} \left[\frac{j_0^2(Qa)}{\pi} \frac{\Gamma_T(Q)}{\omega^2 + \Gamma_T^2(Q)} + \frac{1}{\pi} \sum_{l=1}^{\infty} (2l+1) \frac{j_l^2(Qa)}{\pi} \frac{l(l+1)D_R + \Gamma_T(Q)}{\omega^2 + (l(l+1)D_R + \Gamma_T(Q))^2} \right] \quad 5.2$$

The exponential term is analogous of the Debye-Waller factor of solids: $\langle u^2 \rangle$ represents the single-proton vibrational amplitude.

- $j_l(x)$ represents the l^{th} -order spherical Bessel function and $j_0^2(Qa)$ represents 0-order spherical Bessel function ($l=0$ for elastic incoherent structure factor).
- a is the radius of rotation (we use the distance of N-H in ammonia which is approximately 1.017 Å here).
- Γ_T (meV) is the translational half-width at half maximum and it represents the translational contribution.
- D_R (meV) represents the rotational diffusion coefficient which containing information about the motions of individual hydrogen atoms around the molecular center of mass.

This model of fit takes into account both translational and rotational motions. In practical, as we will see in the next section, Equation 5.2 is not suitable for all the data and another relatively simple Equation 5.4 which just contains rotational motion is more suitable for the fitting of solid samples.

A. Results for the liquid phase

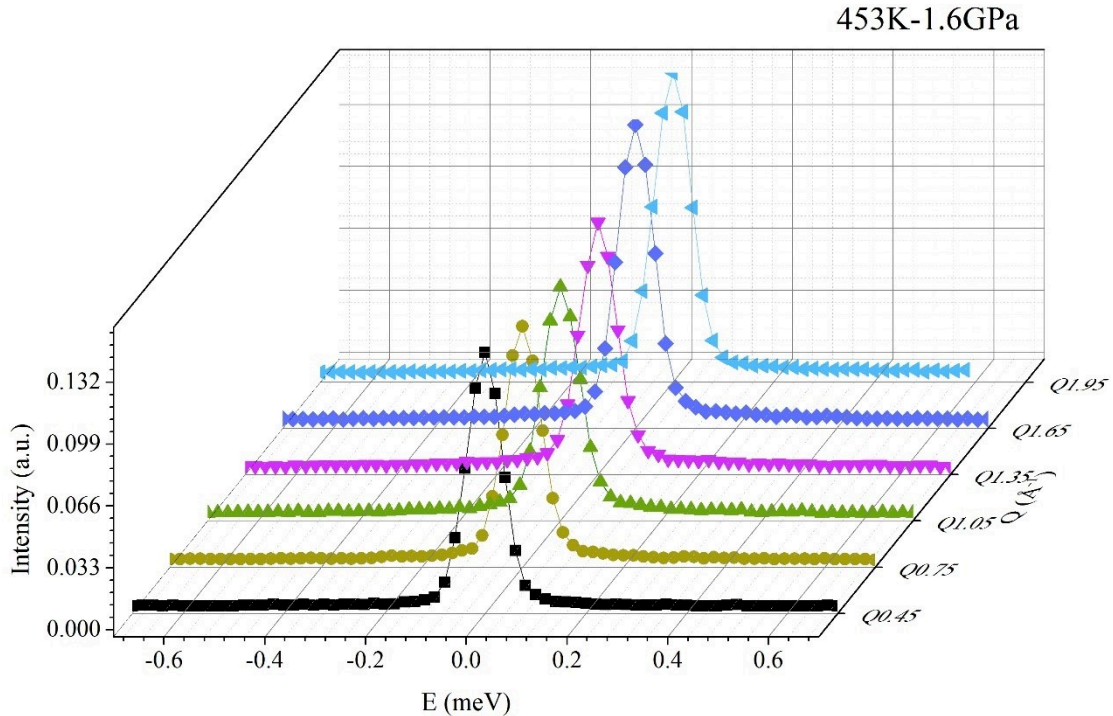


Figure 5.10. Normalized QENS spectra collected on liquid $\text{NH}_3\cdot\text{D}_2\text{O}$ at 1.6 GPa, 453 K. Different colors represent different Q cuts from 0.45 to 1.95 Å⁻¹.

The spectra of liquid $\text{NH}_3 \cdot \text{D}_2\text{O}$ collected at 1.6 GPa and 453 K, as a function of the exchanged energy (E), for different selected momentum transfers (Q) is shown in Figure 5.10. We have shown that equation 5.3 is the most suitable for liquid spectra. Compared to Equation 5.2, in Equation 5.3, the Bessel function $j_l(Qa)$ within the Q range covered in our experiments is negligible for $l > 1$ which means that QENS measures almost exclusively the relaxation time $\tau_1 = 1/2D_R$. This indicates that only the first spherical harmonic contributes significantly to the scattering intensity in our experiment. Therefore, Γ_T represents the translational contribution and $2D_R + \Gamma_T$ represents the rotational contribution. With this model, the expression of DSF is more simple and is the sum of the two Lorentzians (taking into account both translational and rotational motions)^[11-13]:

$$S(Q, \omega) = e^{-\langle u^2 \rangle Q^2/3} \left[A(Q) \frac{\Gamma_T(Q)}{\omega^2 + \Gamma_T^2(Q)} + B(Q) \frac{2D_R + \Gamma_T(Q)}{\omega^2 + (2D_R + \Gamma_T(Q))^2} \right] \quad 5.3$$

where $A(Q)$, $B(Q)$, $\Gamma_T(Q)$ and $D_R(Q)$ are taken to be free parameters. The fit results using Equation 5.3 compared to the experimental data are shown in Figure 5.11.

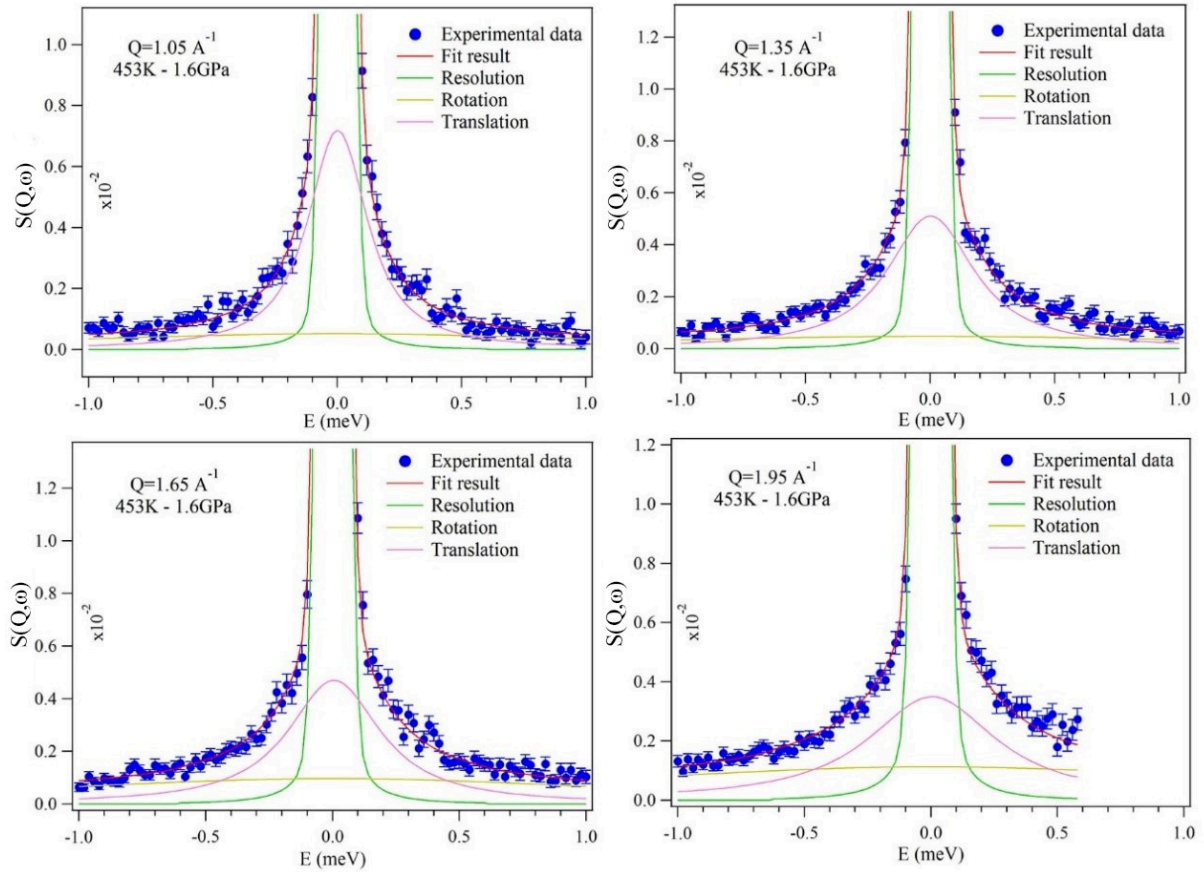


Figure 5.11. Normalized QENS spectra collected on liquid $\text{NH}_3 \cdot \text{D}_2\text{O}$ at 1.6 GPa, 453 K and $Q = 1.05, 1.35, 1.65$ and 1.95 \AA^{-1} . The blue symbols represent the experimental data and the red line represents the fit result. The translational (rotational) contribution is shown in pink (yellow). The green line is the resolution function.

Figure 5.11 shows the fit result at 1.6 GPa and 453 K. The red line is the fitted total DSF, convoluted with the resolution, while the contribution from the translational motion, rotational

motion and the resolution are shown with the pink, yellow and green lines respectively. This result shows that the H atoms of ammonia experience both translational and rotational motions in the liquid phase of AMH.

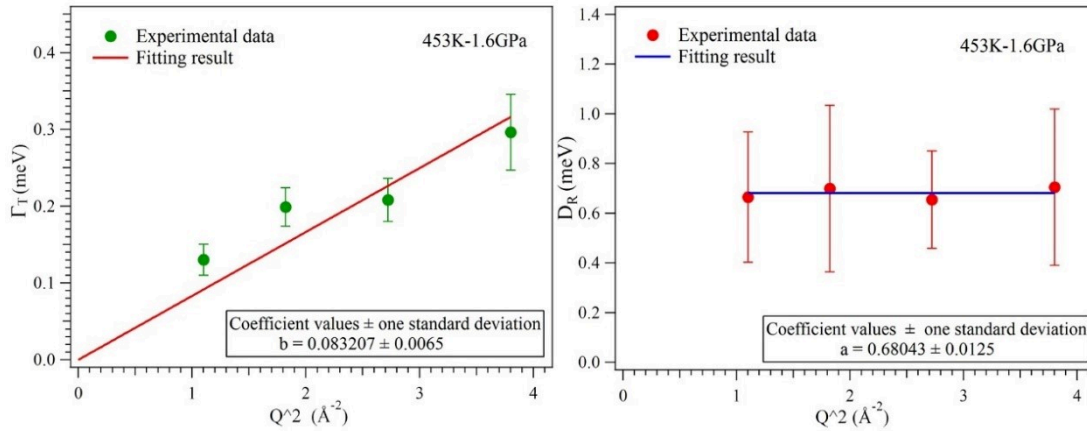


Figure 5.12. Q^2 dependence of the translational contribution Γ_T (the equation of fit: $\Gamma_T = D_T Q^2$) (left) and of the rotational diffusion coefficient D_R (the equation of fit: $D_R = a$) (right) at 1.6 GPa, 453 K. For these plots, we have limited the energy range from -1.3 to 1.3 meV. Although Q vectors ranging from 0.45 to 1.95 \AA^{-1} during the measurements, the rotational contributions which are too weak (small $Q = 0.45$ and 0.75 \AA^{-1}) are excluded in the process of fitting and not shown.

Figure 5.12(a) shows the variation of Γ_T as a function of Q^2 . Within uncertainties, $\Gamma_T(Q)$ is linearly related to Q^2 and can be fitted by the relation $\Gamma_T(Q) = D_T Q^2$ where D_T is Q -independent and defines the translational diffusion constant. The observed linearity proportionality between $\Gamma_T(Q)$ and Q^2 , indicates a free diffusion^[13-15]. The value of D_T measured at 1.6 GPa, 453 K is $1.26 \times 10^{-5} \text{ cm}^2 \cdot \text{s}^{-1}$, which is approximately 3.5 times smaller than that of water ($4.35 \times 10^{-5} \text{ cm}^2 \cdot \text{s}^{-1}$) at 400K, 1.5 GPa^[12], but is close to that of water at the ambient-pressure melting point ($1.1 \times 10^{-5} \text{ cm}^2 \cdot \text{s}^{-1}$)^[16] and methane at 200 K ($1.8 \times 10^{-5} \text{ cm}^2 \cdot \text{s}^{-1}$)^[17]. The translational diffusion of hydrogen in ammonia in liquid AMH is thus slower than that in pure water at the same P-T condition.

Figure 5.12(b) shows the variation of D_R as a function of Q^2 where it can be seen that D_R is independent of Q . We note that the rotational coefficient D_R is more affected by the choices of the energy range and the flat background, which results in greater uncertainties in the values of D_R . However, within the error bars, D_R is constant for the different Q values, as expected for a localized motion. The average value of D_R is 0.6804 meV from which we can obtain the relaxation time $\tau_1 = 1/2D_R = 0.48$ ps. In pure water, at 1.5 GPa and 400 K, the relaxation time τ_1 is also about 0.48 ps^[12], thus the molecular reorientation time of hydrogen atoms of ammonia molecules in liquid AMH coincides with that of water molecules in liquid water.

Our results thus show that translational and rotational diffusions exist simultaneously in liquid AMH. However, in our experimental measurements, only one point (1.6 GPa and 453 K) fits this fitting mode, starting from the next P-T point (6.3 GPa and 473 K), the molecular motion has changed.

B. Results for the solid phase

As shown in Figure 5.8, according to our melting curve, the second P-T point (6.3GPa, 473 K) is solid. At first, the same fit function used for the liquid phase, with two Lorentzian contributions (one for the translational and one for the rotational contributions, respectively) was used to fit the data for the solid phase, but the fitted parameters turned out to have very large error bars (larger than 100%), which made the fit insignificant. We thus used a fit function with a single Lorentzian function for the solid data. We observed that the linewidth Γ of this Lorentzian is independent of Q , which suggests that the QENS signal comes from rotational motion and that the translational dynamics have become too slow to be observed in the Q, ω window of the experiment. The fit function used for the solid data is thus:

$$S(Q, \omega) = e^{-\langle u^2 \rangle Q^2/3} [A(Q)\delta(\omega) + B(Q) \frac{\Gamma_R(Q)}{\omega^2 + \Gamma_R^2(Q)}] \quad 5.4$$

where $A(Q)$, $B(Q)$, $\Gamma_R(Q)$ are taken to be free parameters. As seen in Chapter 2, we expect from the theory that $A(Q)$ is proportional to the 0-order spherical Bessel function $j_0^2(Qa)$ and $B(Q)$ to the 1-order spherical Bessel function $j_1^2(Qa)$. As no translational contribution is considered in this model ($\Gamma_T=0$) and l is 1, therefore $\Gamma_R(Q)=2D_R$.

Figure 5.13 shows the fit results for the various Q wavevectors. The QENS signal intensity is much smaller in the solid phase, and can only be discerned from the noise for $Q > 1 \text{ \AA}^{-1}$. Therefore, the fit values for $\Gamma_R(Q)$ are only considered significant for $Q > 1 \text{ \AA}^{-1}$.

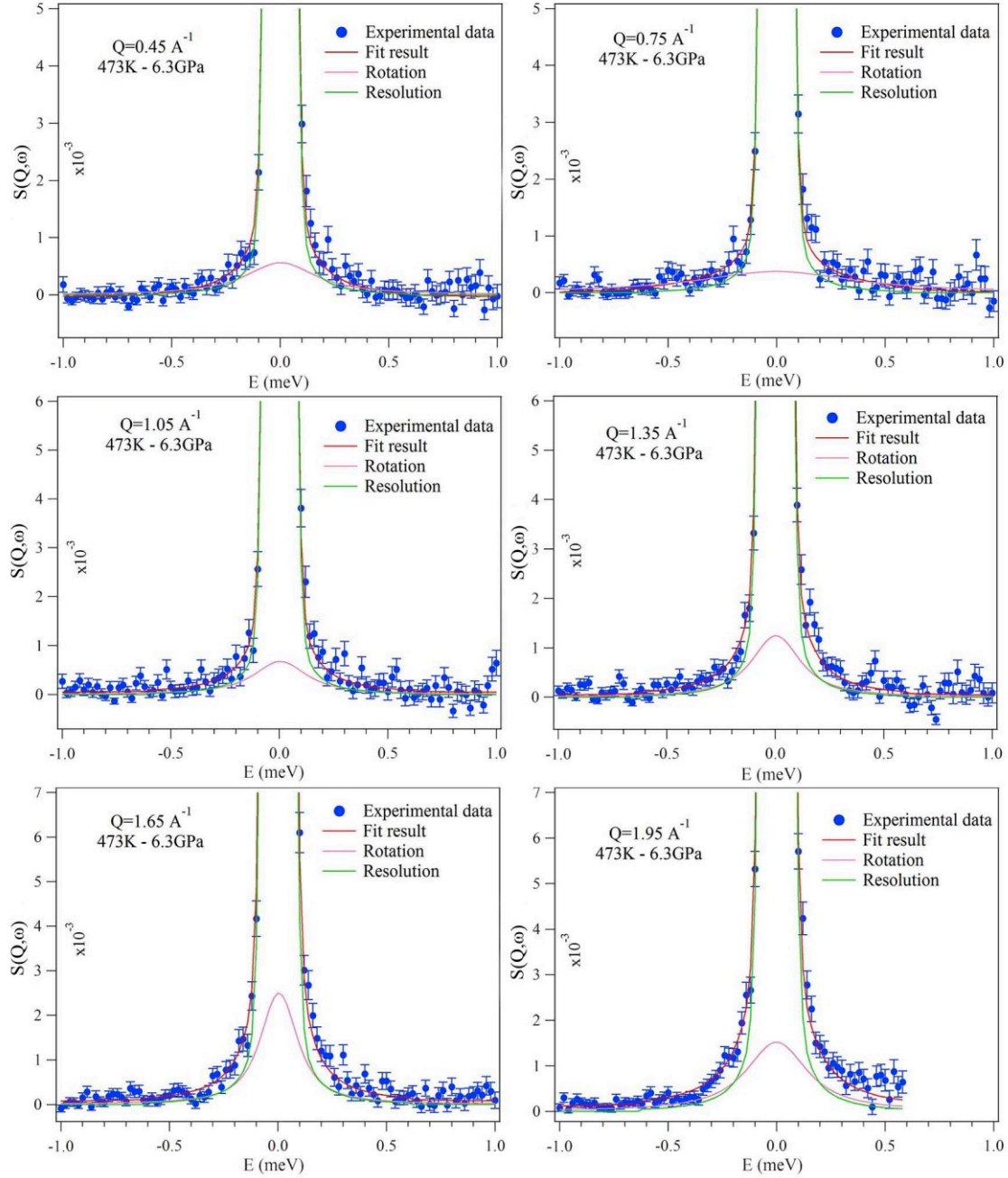


Figure 5.13. Normalized QENS spectra collected on $\text{NH}_3\cdot\text{D}_2\text{O}$ at 6.3 GPa, 473 K and $Q=0.45, 0.75, 1.05, 1.35, 1.65$ and 1.95 \AA^{-1} . The blue symbols represent the experimental data and the red line represents the fit result. The rotational contribution is shown in pink and the green line is the resolution function.

Figure 5.14 presents the evolution of the fitting parameter Γ_R as a function of Q^2 and shows that Γ_R is independent of Q within uncertainties, with the average value of $0.127(14) \text{ meV}$. This gives a rotational diffusion coefficient $D_R=0.063 \text{ meV}$ and a relaxation time $\tau_R=5.23 \text{ ps}$. τ_R is much larger than the one determined in the AMH liquid (0.48 ps). It is also larger than the orientation correlation time for deuteron ($\tau_R=1.00 \text{ ps}$) in plastic ND_3 -phase II at 0.4 GPa and 220 K determined by NMR^[5]. However, the present results show that the ammonia molecules may rotate in solid AMH-VII and that this solid phase is plastic at 6.3 GPa, 473 K.

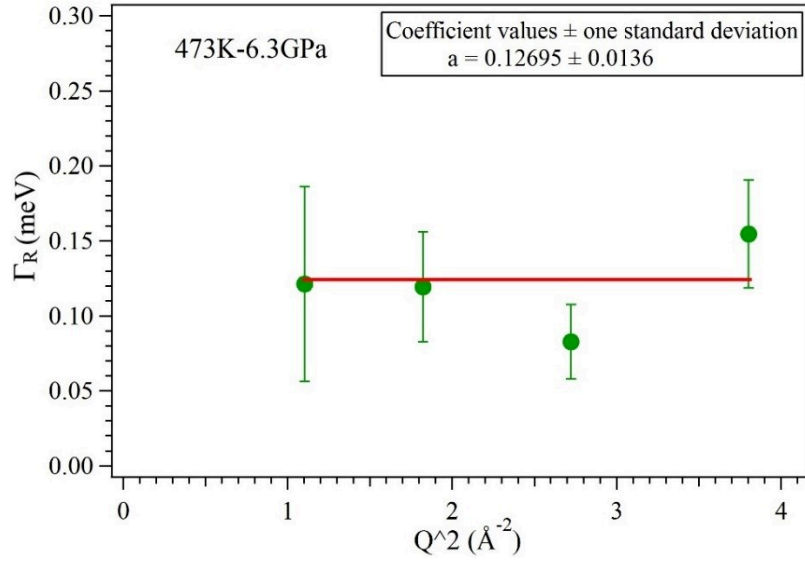


Figure 5.14. Q^2 dependence of the rotational contribution Γ_R at 6.3 GPa, 473 K. The green symbols represent the experimental data and the red line is the fitting result of the average value of Γ_R .

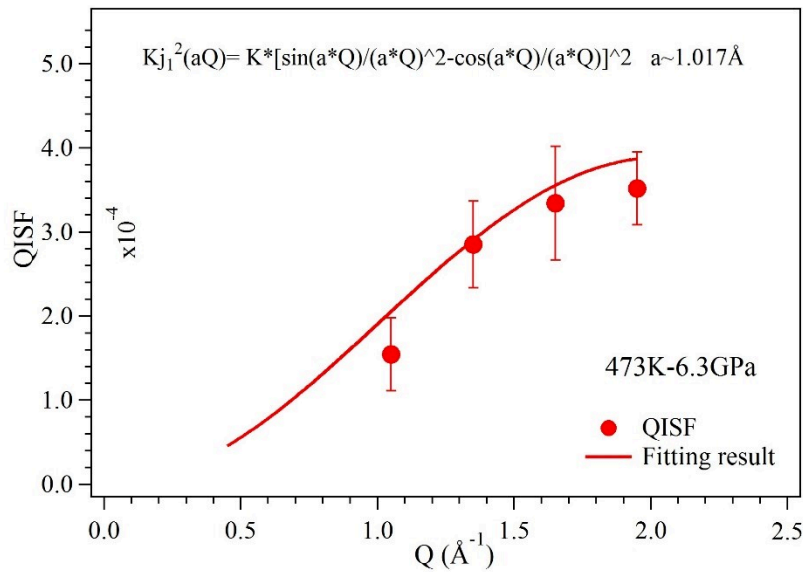


Figure 5.15. Wavevector dependence of the energy integrated QISF at 6.3 GPa, 473K. The red symbols represent experimental data and the red line is the fitted result of Equation 5.5. The coefficient K is 0.00205(42).

The Q dependence of the quasielastic incoherent structure factor ($\text{QISF} = \frac{B(Q)}{A(Q)+B(Q)}$, see Chapter 2), provides information about the geometry of the motion. Figure 5.15 represents the QISF as a function of Q ($A(Q)$ and $B(Q)$ come from the fit of $S(Q, \omega)$ with Equation 5.4). As can be seen in Figure 5.15, the QISF is well fitted with error bars by a function proportional to the square of the first-order Bessel equation [12,17]:

$$QISF(Q) = K \left[\frac{\sin(aQ)}{(aQ)^2} - \frac{\cos(aQ)}{aQ} \right]^2 \quad 5.5$$

In this Equation 5.5, a is the spherical surface of radius 1.017\AA (the distance of N-H in ammonia^[18]) and K is a free parameter. This confirms that only the first spherical harmonic contributes significantly to the scattering intensity (in agreement with the choice of Equation 5.4), i.e. the hydrogen motions in ammonia depend mainly on the first shell structured environment.

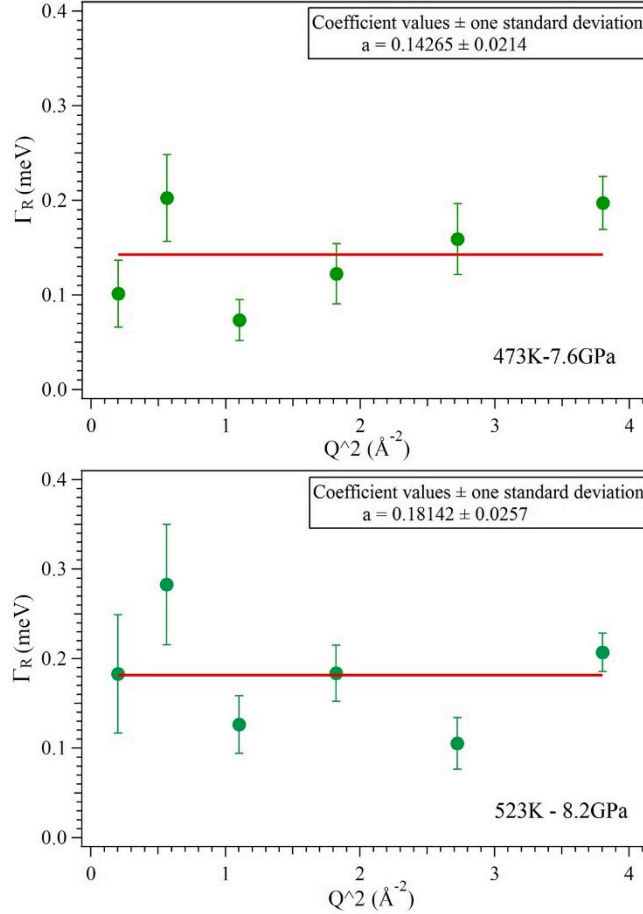


Figure 5.16. Q^2 dependence of the rotational contribution Γ_R at varied temperature and pressure. The green symbols represent the experimental data and the red lines are the fitting result of the average value of Γ_R . The corresponding relation of the fit is $\Gamma_R=a$. The different values of a are indicated in the legend of each figure.

We used the same model (Equation 5.4) and procedure to analyze our data recorded at higher pressure in the solid phase at (473 K, 7.6 GPa) and (8.2 GPa, 523 K).

The evolution of Γ_R as a function of Q^2 for these two (P, T) points are shown in Figure 5.16, and the QISF is shown in Figure 5.17. The same observations are made for these two P-T points than for the data collected at 6.3 GPa, 673 K.

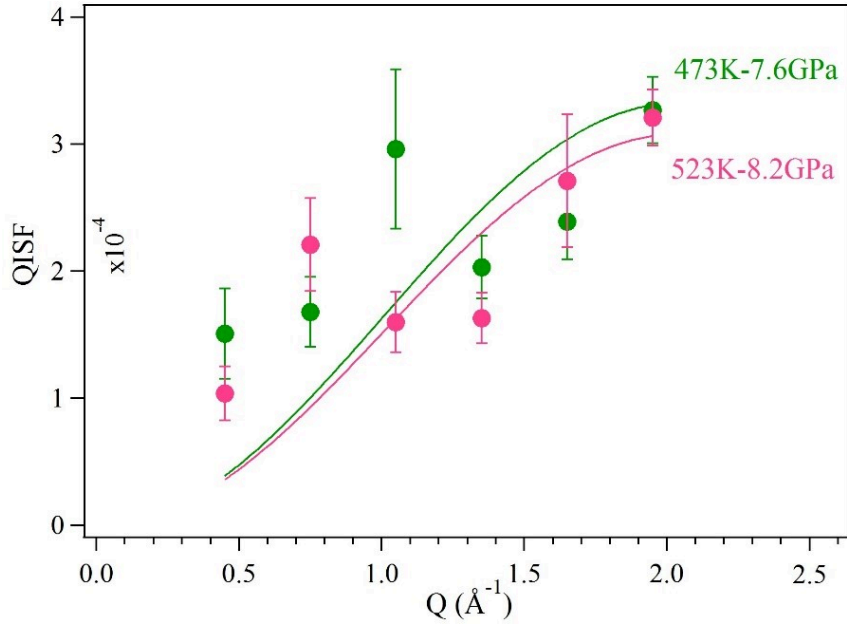


Figure 5.17. Wave vector dependence of the energy integrated $QISF$ for varied pressure and temperature. The symbols represent experimental results and the lines are the fitted results of Equation 5.5.

Table 5.1 summarize the values of D_R and τ_R determined in this work for the different (P, T) points and Figure 5.18 shows the evolution of the rotational diffusion coefficient D_R as a function of pressure. A clear decrease is observed for D_R between the liquid and the solid phase and within the error bars, D_R can be considered as insensitive to pressure variation (1.3 GPa of variation) along the 473 K isotherm.

We also note that D_R increased slightly at 8.2 GPa and 523 K which seems coherent, but within the error bars, it can still be regarded as unchanged. Further experiments are needed to confirm the dependence of D_R on pressure and temperature.

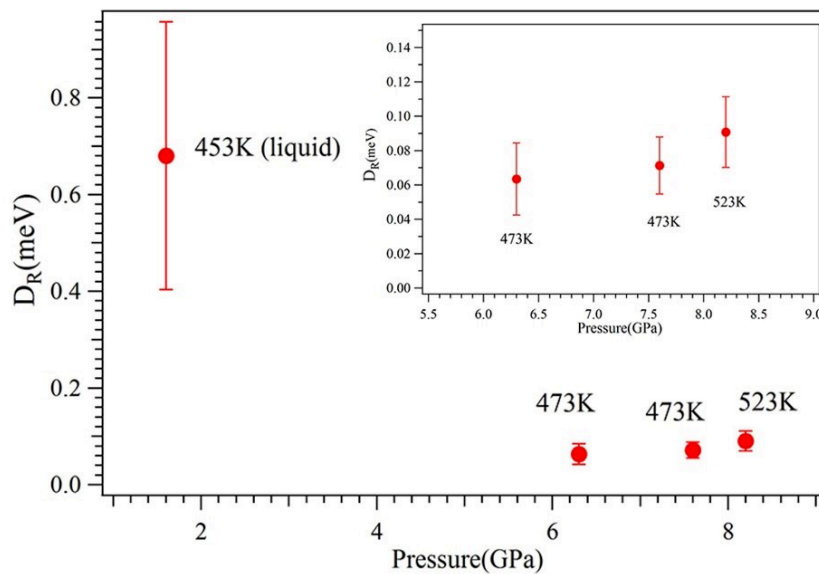


Figure 5.18. Pressure dependence of the rotational diffusion coefficient D_R at varied pressure and temperature measured by QENS. The inset shows a magnified view of the pressure dependence of solid's D_R .

Table 5.1 Pressure dependence of the rotational diffusion coefficient D_R and the relaxation time at varied pressure and temperature measured by QENS.

Pressure (GPa)	Temperature (K)	D_R (meV)	τ_R (ps)
1.6	453	0.680	0.48
6.3	473	0.063	5.23
7.6	473	0.071	4.64
8.2	523	0.091	3.62

5.5 Conclusions

In this chapter, we have presented the results of our XRD, Raman and QENS experiments on the solid AMH-VII phase. We demonstrated that AMH-VII has a *bcc* structure with *Im-3m* space group, as previously determined for AMH-VI. However, unlike AMH-VI, there is no evidence for the presence of the *P4/nmm* ionic solid in AMH-VII, and thus this phase is a pure and single AMH solid. The *Im-3m* structure of AMH-VII implies that it is substitutionally and rotationally disordered. The Raman spectra of AMH-VII reveals the presence of vibrational modes from molecular H_2O and NH_3 close to those observed in AMH-VI, but no modes from *P4/nmm*, consistent with the XRD results. A broad Raman band centered at 3600 cm^{-1} may indicate the presence of OH^- ions, thus AMH VII might also be partially ionic.

Our QENS experiments show that hydrogen atoms of the ammonia molecules display a rotational dynamic in AMH-VII, indicating that the ammonia molecules may rotate and that AMH-VII is a plastic solid. However, the QENS experiments need to be repeated with a deuterated ammonia/hydrogenous water sample to determine whether the hydrogen atoms in water molecules also display a rotational dynamic.

References

- [1] Loveday, J., Nelmes, R., Bull, C. *et al.* Observation of ammonia dihydrate in the AMH-VI structure at room temperature—possible implications for the outer solar system. *High Pressure Research* **29**, 396-404, (2009).
- [2] Bertie, J. E. & Shehata, M. R. The infrared spectra of $\text{NH}_3 \cdot \text{H}_2\text{O}$ and $\text{ND}_3 \cdot \text{D}_2\text{O}$ at 100 K. *The Journal of chemical physics* **83**, 1449-1456, (1985).
- [3] Koumvakalis, A. & Nicol, M. in *High Pressure Chemistry, Biochemistry and Materials Science – Raman Spectroscopy of Ammonia Monohydrate to 13.5 GPa* 265-274 (Springer, 1993).
- [4] Boone, S. & Nicol, M. in *Lunar and Planetary Science Conference Proceedings*. 603-610.
- [5] Doverspike, M. A., Liu, S.-B., Ennis, P. *et al.* NMR in high-pressure phases of solid NH_3 and ND_3 . *Physical Review B* **33**, 14, (1986).
- [6] Ninet, S., Datchi, F. & Saitta, A. Proton disorder and superionicity in hot dense ammonia ice. *Physical review letters* **108**, 165702, (2012).
- [7] Ninet, S. & Datchi, F. High pressure–high temperature phase diagram of ammonia. *The Journal of chemical physics* **128**, 154508, (2008).
- [8] Aragonés, J. & Vega, C. Plastic crystal phases of simple water models. *The Journal of chemical physics* **130**, 244504, (2009).
- [9] Hernandez, J.-A. & Caracas, R. Proton dynamics and the phase diagram of dense water ice. *The Journal of chemical physics* **148**, 214501, (2018).
- [10] Börner, H., Brown, J., Carlile, C. *et al.* (Old City Publishing: Philadelphia, PA, 2003).
- [11] Ranieri, U., Giura, P., Gorelli, F. A. *et al.* Dynamical crossover in hot dense water: the hydrogen bond role. *The Journal of Physical Chemistry B* **120**, 9051-9059, (2016).
- [12] Bove, L., Klotz, S., Strässle, T. *et al.* Translational and rotational diffusion in water in the gigapascal range. *Physical review letters* **111**, 185901, (2013).
- [13] Qvist, J., Schober, H. & Halle, B. Structural dynamics of supercooled water from quasielastic neutron scattering and molecular simulations. *The Journal of chemical physics* **134**, 144508, (2011).
- [14] Singwi, K. & Sjölander, A. Diffusive motions in water and cold neutron scattering. *Physical Review* **119**, 863, (1960).
- [15] Bée, M. Quasielastic neutron scattering. (1988).
- [16] Krynicki, K., Green, C. D. & Sawyer, D. W. Pressure and temperature dependence of self-diffusion in water. *Faraday Discussions of the Chemical Society* **66**, 199-208, (1978).
- [17] Jovic, H. & Theodorou, D. N. Quasi-elastic neutron scattering and molecular dynamics simulation as complementary techniques for studying diffusion in zeolites. *Microporous mesoporous materials* **102**, 21-50, (2007).
- [18] Bastiansen, O. & Beagley, B. A comparison of the molecular structures of ammonia and deuterio ammonia as determined by electron diffraction. *Acta Chem Scand* **18**, 2077-2080, (1964).

Chapter 6: High pressure-temperature phase diagram of AMH

Contents

Chapter 6: High pressure-temperature phase diagram of AMH..... 118

Contents	118
6.1 Introduction.....	119
6.2 Overview of the high P-T phase diagram	119
6.3 Evolution of AMH-VI (DIMA+P4/nmm) at high temperature	121
6.3.1 Evolution below 18 GPa	122
6.3.2 Evolution above 18 GPa	126
6.4 Cooling and compression of AMH-VII	128
6.4.1 Formation of AMH-VIII	129
6.4.2 Structure of AMH-VIII	131
6.4.3 Raman spectra of AMH-VIII	136
6.4.4 Transition line between AMH-VII and VIII	137
6.4.5 Stability range of AMH-VIII	138
6.5 Stability of the DIMA phase above 18 GPa.....	139
6.6 Stability of AMH-VII at high pressure and high temperature	142
6.7 Signature of superionicity in AMH-VII?.....	144
6.8 Conclusions.....	148
References.....	150

6.1 Introduction

In Chapter 3, we have reported that the DIMA phase (previously referred as AMH-VI or DMA) is synthesized on compression of the equimolar $\text{NH}_3:\text{H}_2\text{O}$ mixture above 7 GPa at low temperature (150 K) and warming to 300 K, while the compression of the liquid at ambient temperature leads to the dehydration of AMH into AHH-II + ice VII. The DIMA phase is generally mixed with a small amount of the pure ionic compound with space group $P4/nmm$ and the ratio of these two phases (DIMA/ $P4/nmm$) depends on the sample loading. We have also shown that the DIMA phase mixed with $P4/nmm$ is stable on compression at ambient temperature up to 80 GPa and on decompression down to 7 GPa.

In Chapter 4, we have presented our experimental studies of the phase diagram of AMH below 10 GPa and 600 K. In particular, we have shown the existence of a new high temperature phase with *bcc* structure which we called AMH-VII. The plastic nature of this phase has been demonstrated by QENS experiment.

In this chapter, we will present the results of our experimental investigations of the phase diagram of AMH in the range 7-70 GPa and 295-765 K, based on x-ray diffraction (XRD), Raman and infrared measurements. We will focus in particular on the evolution with the temperature of the DIMA + $P4/nmm$ mixed phase, and on the evolution with the pressure of AMH-VII up to 70 GPa. We will see that these studies have revealed the existence of a new phase of AMH called AMH-phase VIII. We will discuss the existence of the superionic phase which is predicted by Bethkenhagen et al^[1] at lower pressures and temperatures in AMH than in pure H_2O and NH_3 .

6.2 Overview of the high P-T phase diagram

We have explored the phase diagram of AMH by XRD and Raman scattering experiments over a wide range of pressure [0-52 GPa] and temperature [300-765 K]. The full set of explored (P, T) points are represented in Figure 6.1, where each phase is assigned a different color. In particular, these studies have revealed the existence of a new phase called AMH-VIII, which will be described in section 6.3. In the pressure range 7-18 GPa, and below the transition temperature to AMH-VII, different phases can be observed depending on the followed thermodynamic path, thus revealing large metastabilities.

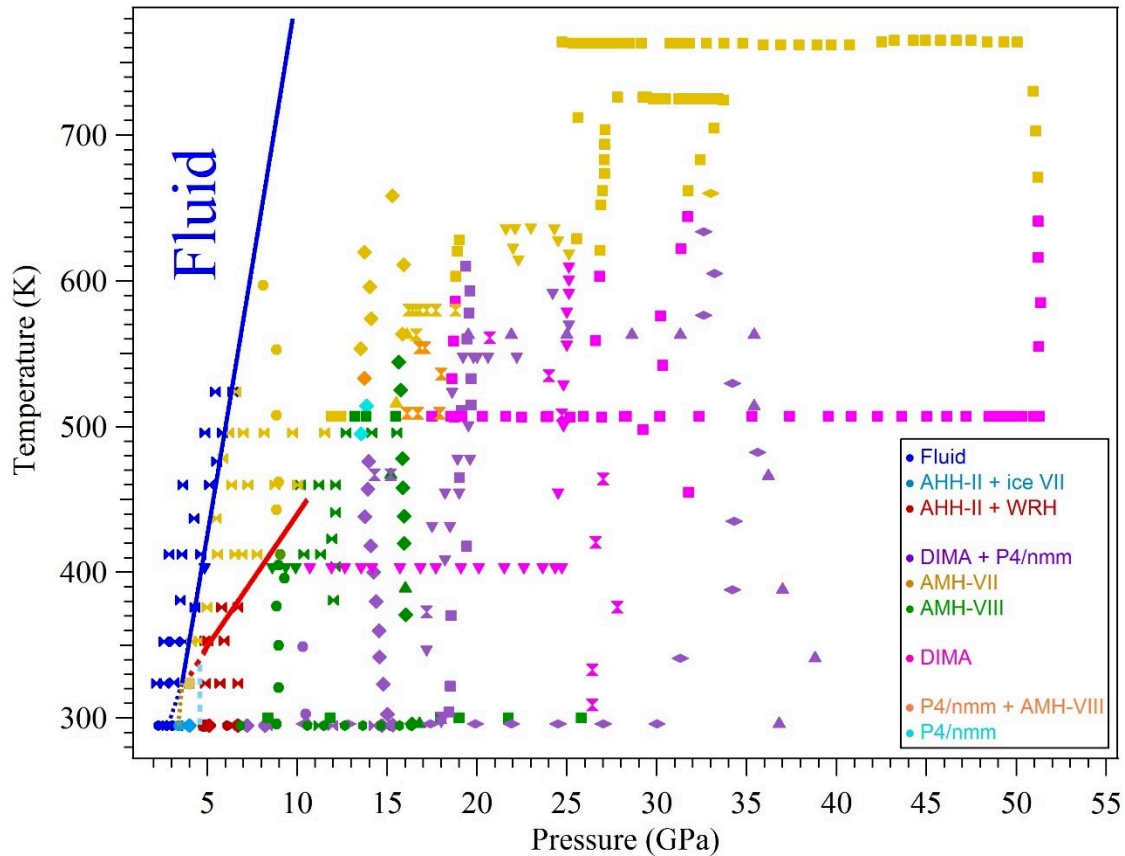


Figure 6.1. Full set of data points in the phase diagram of AMH explored in the present work by XRD or Raman experiments. The symbol colors refer to the observed phase or mixture of phases as indicated in the legend.

Based on the data set shown in Figure 6.1, we can distinguish four domains in the phase diagram:

- At pressures below 7 GPa and temperatures below 400 K, the dehydration of AMH into AHH-II and a water-rich hydrate (WRH) or pure water is observed, as previously seen in Chapters 3 and 5.
- At intermediate pressures, 7-18 GPa, and temperatures 300-600 K, three different phases, DIMA, *P4/nmm* and phase VIII, are observed depending on the followed thermodynamic path.
- For pressures above 18 GPa (below 30 GPa), the *bcc* DIMA phase occupies a large P-T domain.
- Above 30 GPa, the phase transition between AMH-VII and the low temperature phase (DIMA) becomes more difficult to observe. This may signal that the nature of the transition between the two phases changes from first-order to second-order above 30 GPa.

We will now describe the different observed phases and explain the construction of this complex phase diagram.

6.3 Evolution of AMH-VI (DIMA+P4/nmm) at high temperature

As said above, the initial sample phase in our experiments is a mixture of DIMA and $P4/nmm$. We reported in Chapter 3 that no phase transition is observed when compressing this sample to 80 GPa at room temperature, or lowering the temperature down to 50 K in the range 15-80 GPa. In the experiments described below, we used XRD to study the stability of this sample under heating above 10 GPa. Six samples have been studied, which were initially compressed at low temperature to different pressures. In each case, we observed upon heating a transition towards a pure bcc structure. We collected 5 transition points upon heating (13.8 GPa–543 K, 16.8 GPa–558.5 K, 19.5 GPa–601.5 K, 23.3 GPa–603.5 K and 33.2 GPa–646 K), and one point (17.8 GPa) upon an isothermal decompression of a sample first heated to 563 K at 35 GPa, as shown in Figure 6.2. The x-ray pattern of the high-temperature phase is the same as that of phase VII reported in the previous chapter. We thus conclude that phase VII remains the stable AMH phase at high temperature to at least 33 GPa.

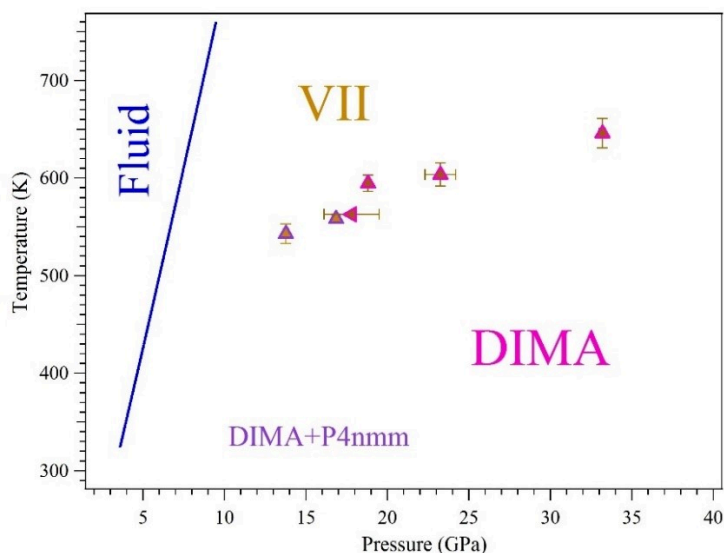


Figure 6.2. Phase diagram of AMH. The symbols represent the observed transition points. Below 18 GPa, the purple triangles represent the phase transition points during the heating of rich $P4/nmm + DIMA$ samples. Above 18 GPa, the pink triangles represent the direct transition from $DIMA+P4/nmm$ to AMH-VII. (The plain triangle: external color: initial phase $DIMA+(P4/nmm)$; internal color: final phase (VII).)

Although the high-temperature scan eventually resulted to the formation of AMH-VII in all studied samples, we observed two different phase transition sequences between the initial and AMH-VII phases, depending on the starting sample pressure and/or on the initial concentration of the $P4/nmm$ phase:

- Below 18 GPa, a complex sequence of phase transitions was observed for two initial samples containing a large amount of the $P4/nmm$ phase.
- Above 18 GPa, a direct transition from the $DIMA + P4/nmm$ phase to phase VII was observed for 4 samples.

We will discuss these two different cases in the following sections. We will start to describe the more complex case (a) and will then discuss the simpler case (b).

6.3.1 Evolution below 18 GPa

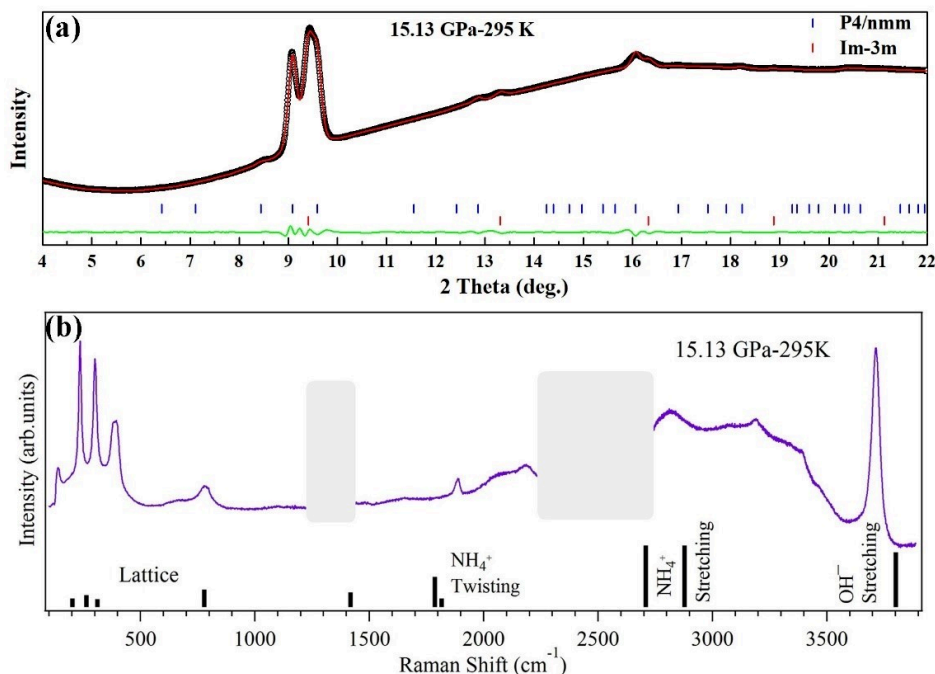


Figure 6.3. (a) *Le Bail* fit of the XRD pattern (with background) of AMH at 15.13 GPa, 295 K. The symbols are experimental data and the red lines are *Le Bail* refinement. Tick marks indicate the positions of the Bragg peaks as given in the legend. The green line is the fit residual. *Le Bail* refinement used a mixture of DIMA and *P4/nmm* structures^[2]; (b) Raman spectra of the same sample and same *P-T* conditions. The black histogram represents the theoretical Raman spectra, calculated at 10 GPa - 0 K, of the fully ionic *P4/nmm* structure. The frequency windows from 1200-1400 cm^{-1} to 2200-2700 cm^{-1} are greyed as they are dominated by, respectively, the first- and second-order Raman signal from the diamond anvils.

For the two samples studied below 18 GPa, the amount of the *P4/nmm* phase was large compared to all the others studied samples. In this section, we will describe the evolution of one sample but the observations are very similar for the other one. This sample was at 15.1 GPa and 295 K after loading. The XRD pattern and Raman spectrum of this sample are plotted in Figure 6.3(a) and (b). The *Le Bail* fit of the XRD pattern, shown in Figure 6.3(a), gives for the cell parameters $a=3.2238 \text{ \AA}$ for the *Im-3m* DIMA phase, and $a=b=4.7188 \text{ \AA}$, $c=3.0122 \text{ \AA}$ for the *P4/nmm* phase, respectively, which gives nearly identical volumes for the two phases: $V(\text{DIMA})=16.75 \text{ \AA}^3/\text{molecule}$ and $V(\text{P4/nmm})=16.77 \text{ \AA}^3/\text{molecule}$. As can be seen in Figure 6.3(a), the intensities of the reflections of the *P4/nmm* are strong in comparison to those observed in the pattern of Figure 6.9. The Rietveld fit of the XRD pattern was not satisfactory due to the strong sample texture; however, a rough estimate based on this fit gives a proportion of about two-third *P4/nmm* and one-third *Im-3m*. The large proportion of *P4/nmm* is also obvious in the Raman spectrum (Figure 6.3(b)).

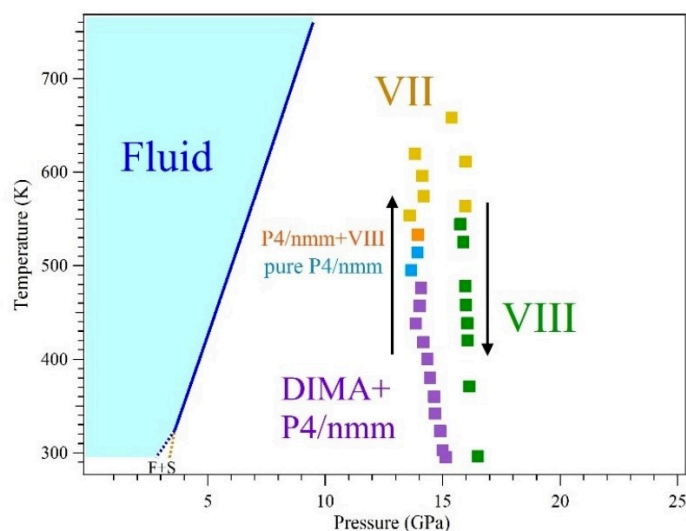


Figure 6.4. Heating and cooling paths in the phase diagram of AMH followed during the experiment with the P4/nmm-rich sample. Square symbols of different colors represent different phases.

This sample was heated along a quasi-isobar ($14 < P < 15$ GPa) by steps of 20 K from the room temperature to 658 K and then isobarically cooled down to room temperature. The (P, T) locations of the collected dataset are shown with square symbols in Figure 6.4, each observed phase being represented by a different color.

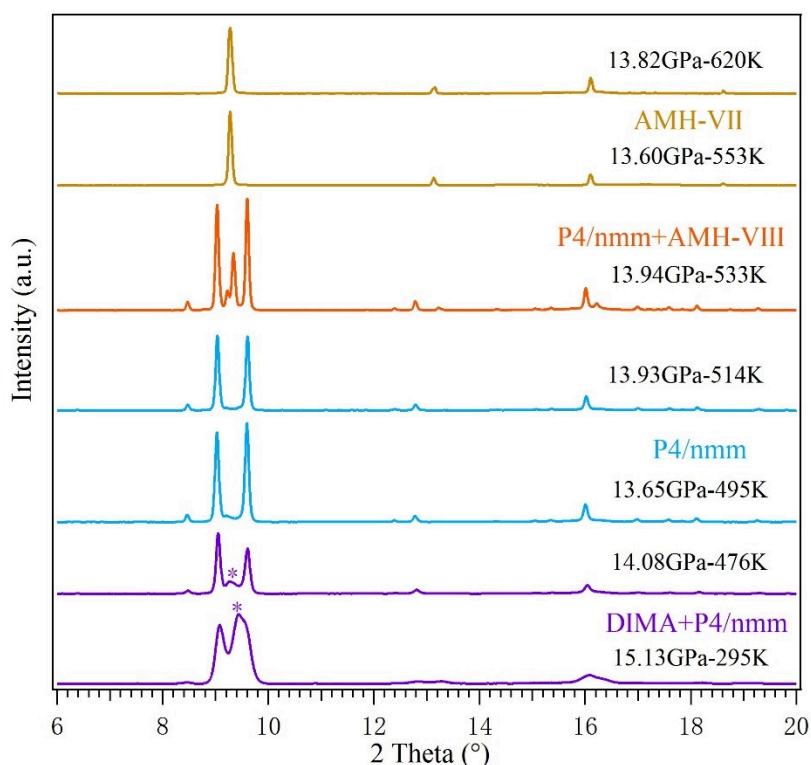


Figure 6.5. Evolution of the integrated XRD pattern of AMH during the heating of an initially AMH-sample rich in P4/nmm phase. The peaks indicated with * correspond to the (110) of the DIMA phase.

Figure 6.5 shows the evolution of the integrated XRD patterns collected during the quasi-isobaric [13.6 – 15.4 GPa] heating process. As can be seen, the transition from DIMA+ $P4/nmm$ to AMH-VII is not direct and is preceded by two other phase transitions. First, we observed that the intensity of the diffraction peaks of the DIMA ($Im-3m$, for example, (110) peak at around $2\theta=9.4^\circ$) gradually decreased as the temperature increased from 295 K to 476 K, while the diffraction peaks of the $P4/nmm$ phase remained (indicate below the first XRD pattern the main peaks of the DIMA and $P4/nmm$ phases). When the temperature increased to 495 K, the diffraction peaks of the DIMA phase mostly disappeared, which indicates that the sample transformed into the pure ionic $P4/nmm$ phase.

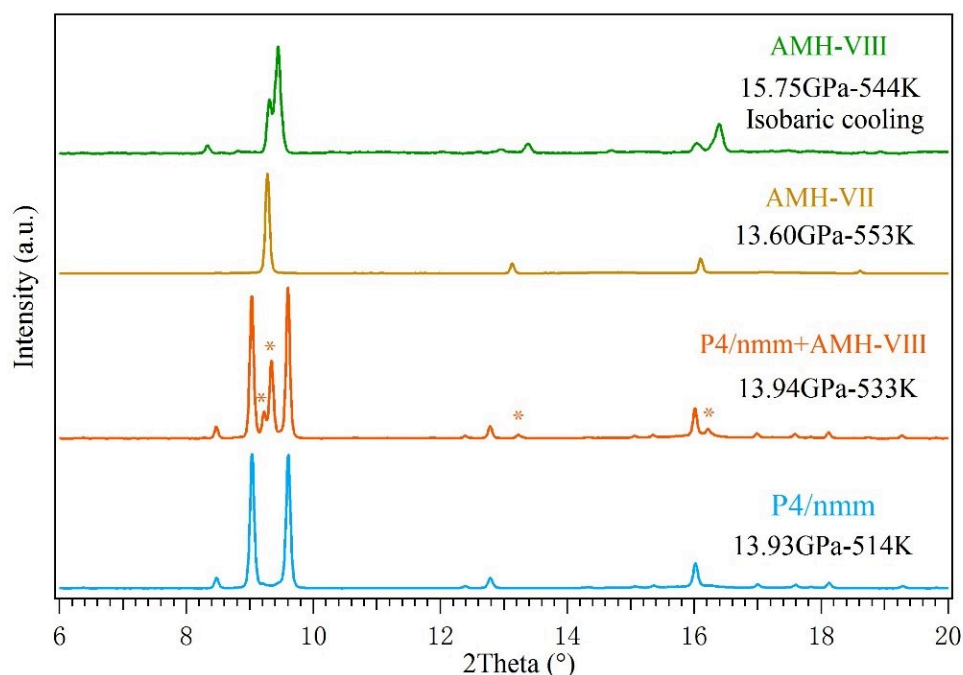


Figure 6.6. X-ray diffraction patterns of AMH by isobarically heating from 514 K to 553 K. The * indicates some new peaks which can be indexed to AMH-VIII phase.

Second, on heating to 533 K, new diffraction peaks appear which cannot be indexed by the $P4/nmm$ structure nor the DIMA phase (Figure 6.6). In particular, two new peaks appeared near $2\theta=9.3^\circ$, while those of the $P4/nmm$ phase remained. This reveals the coexistence of two phases: $P4/nmm$ and a new phase called AMH-VIII (the details of this new phase will be presented in the next section). Then, the temperature was increased to 553 K, the sample transformed into the pure bcc AMH-phase VII as shown in Figure 6.6 (the brown pattern). The diffraction pattern colored in “green” was measured during the isobaric cooling which is consistent with the new phase AMH-VIII.

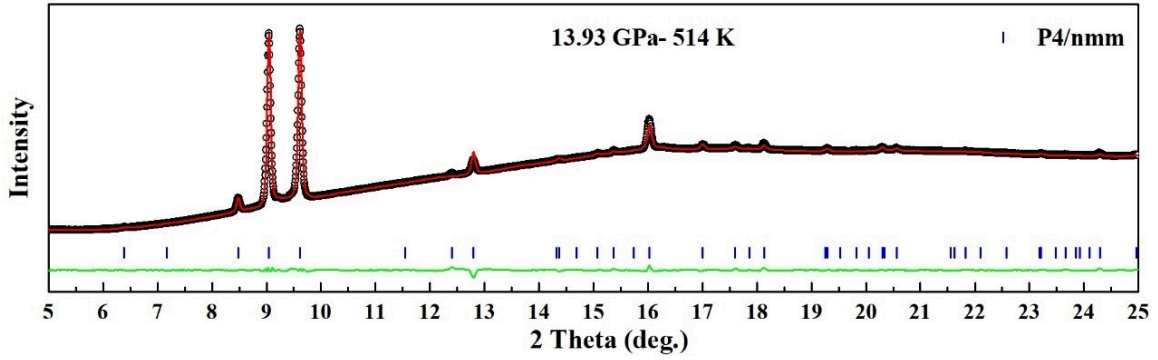


Figure 6.7. Rietveld profile refinement of the XRD pattern at 13.93 GPa and 514 K. The symbols are experimental data and the red line is the calculated pattern. Sticks show the positions of Bragg reflections. The green line shows the difference between observed and calculated profiles.

The quality of the powder pattern of the nearly pure $P4/nmm$ sample at 13.9 GPa and 514 K was suitable for Rietveld refinement. The atomic positions predicted by DFT at 10 GPa^[2] were used as the initial model. The O-H distance was constrained at 0.97 Å, and the thermal factors B of the H atoms were fixed at 3 Å², while those of O and N were left free to vary. Figure 6.7 shows that a good fit ($R_{wp}=0.31\%$) could be obtained by including a preferred orientation model along (200). The refined parameters are shown in Table 6.1. The lattice parameters are $a=b=4.743$ Å, $c=2.989$ Å, which gives a volume per molecule of 16.81 Å³/molecule, and consistent well with DFT predicted values ($a=b=4.805$ Å, $c=2.965$ Å). We note however that the isotropic thermal factor $B=3.44$ Å² of oxygen (O) atoms is larger than typical values, and about twice larger than that of nitrogen (N) atoms, which would indicate some disorder for the O atoms. In addition, the O atoms are closer to the center of the tetragonal unit cell ($z=0.56544$) than in the theoretical structure ($z=0.6562$). We have tested a substitutional disorder for the O sites but this does not improve the fit, nor reduce $B(O)$. The large thermal factor may thus signal a rotational or translational disorder for the OH⁻ ions.

Table 6.1. Refined parameters of ionic $P4/nmm$ at 13.9 GPa and 514 K.

Lattice parameter	Atom	x	y	z	B	Site
$a=b=4.743$ Å	N	0.75000	0.25000	0.00000	1.30	2a
$c=2.989$ Å	O	0.25000	0.25000	0.56544	3.44	2c
$\alpha=\beta=\gamma=90^\circ$	H1	0.25000	0.25000	0.24121	3.0	2c
	H2	0.25000	0.56870	0.80290	3.0	8i

These results thus suggest that there could be a P-T range of stability for the pure $P4/nmm$ phase around 15 GPa-500 K. However, this P-T domain would be rather small since the $P4/nmm$ transits into the newly observed phase VIII above 530 K. Moreover, as seen below, the $P4/nmm$ phase is never observed on cooling the high temperature phase VII. This tends to show that $P4/nmm$ is never thermodynamically stable but only becomes more stable than the DIMA phase at $P\sim 15$ GPa and $T\sim 500$ K.

6.3.2 Evolution above 18 GPa

The direct phase transition from the DIMA+ $P4/nmm$ phase to the AMH-VII phase was observed in four different samples initially compressed above 18 GPa and where the $P4/nmm$ phase was clearly in minor proportion compared to the DIMA phase.

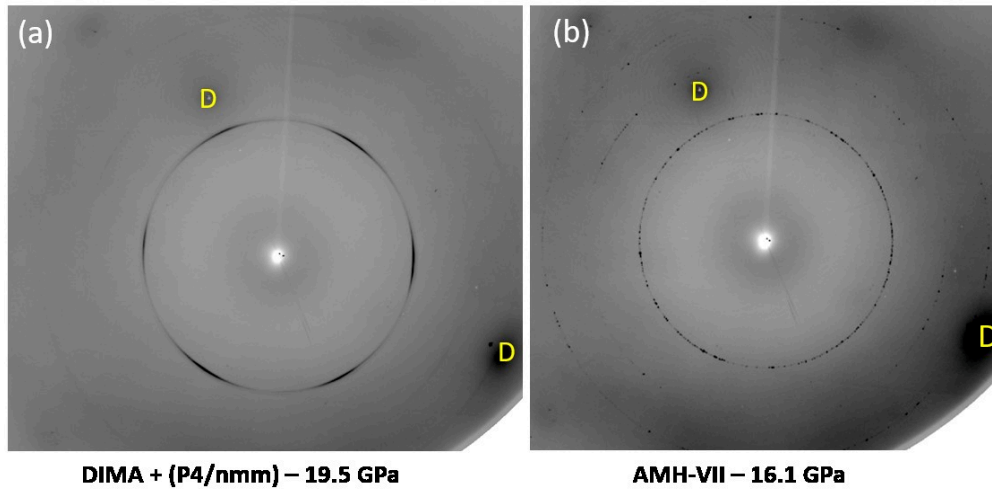


Figure 6.8. (a) Diffraction image of the DIMA+ $P4/nmm$ at 19.5 GPa and 563 K; (b) Diffraction image of the AMH-VII at 16.1 GPa and 563 K. The symbols D corresponds to diamond diffraction peaks.

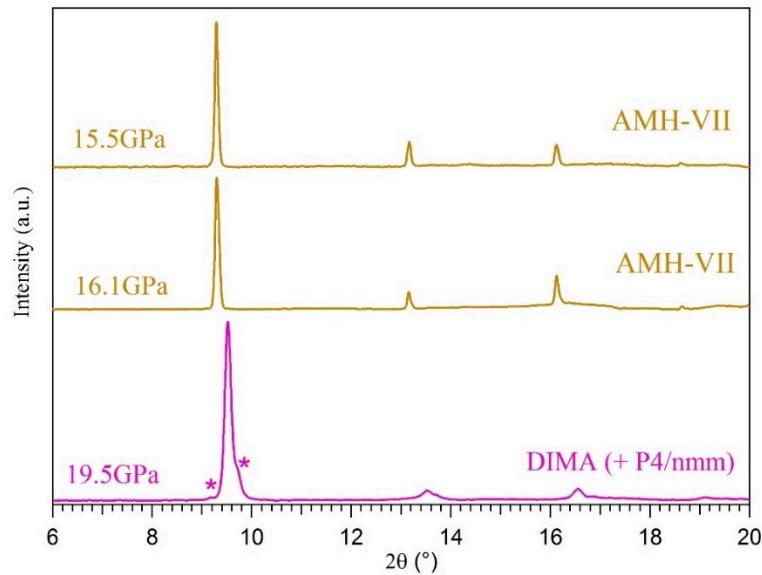


Figure 6.9. Evolution of the integrated XRD pattern of AMH during the decompression of the DIMA (+ $P4/nmm$) phase along an isotherm at 563 K showing the phase transition from DIMA + ($P4/nmm$) to AMH-VII. The small reflections peaks (indicated with *) around the main reflections of the $Im-3m$ DIMA phase are due to the presence of the $P4/nmm$ ionic phase.

This phase transition is easily detected by XRD using the following criteria:

- First, as seen in Figure 6.8 (a) and (b) showing respectively two typical XRD images

before and after the phase transition, the powder texture of the two phases are very different: the DIMA (+ $P4/nmm$) corresponds to an oriented powder with continuous and relatively broad diffraction rings, whereas AMH-VII presents thin and spotty diffraction rings.

- Second, as seen in the integrated X-ray patterns of Figure 6.9, the phase transition is associated with the complete disappearance of the $P4/nmm$ diffraction peaks, which appear as shoulders of the Bragg peaks of the $Im-3m$ DIMA phase (as the pink symbols shown in Figure 6.9).

- Third, we have observed a strong and discontinuous sharpening of the diffraction peaks across the isostructural DIMA-VII phase transition. This effect is illustrated in Figure 6.10(b), which gives the evolution of the linewidth of the (110) peak on decompression at 563 K. The reduction of the linewidth is thus also a sign of the phase transition between DIMA and AMH-VII.

Along a decompression isotherm at 563 K, we did observe a volume jump of around 3% (see Figure 6.10(a)) which seems to indicate that the phase transition is first order. However, as we discussed before, we suspected that along this path, the sample first transitioned to the new phase VIII, which we failed to observe because of a too large pressure step before the observed transition to phase VII. We may thus not determine whether the volume discontinuity occurs at the transition to phase VIII or phase VII.

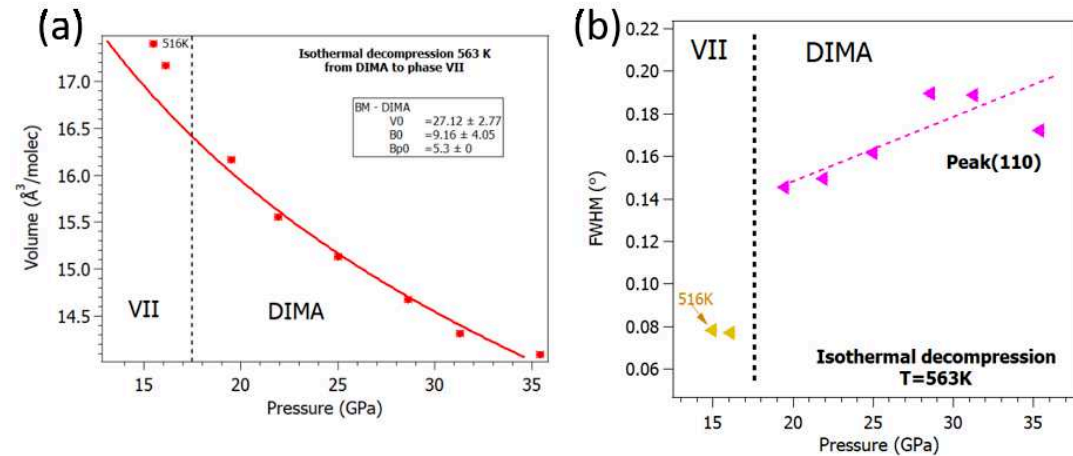


Figure 6.10. (a) Equation of state of AMH on decompression of the DIMA-AMH along an isotherm at 563 K. (b) Evolution of the linewidth of the (110) peak measured during the isostructural phase transition DIMA-VII along an isotherm at 563 K.

For samples where only the $Im-3m$ DIMA phase could be detected by x-ray diffraction, the sharpening of the bcc diffraction peaks of the DIMA, associated with the changes in the powder texture, was used as the main criteria to detect the isostructural DIMA→AMH-VII phase transition (Figure 6.11). We were not able to detect any volume discontinuity at the transition along heating paths because the variations of pressure at each temperature increase make it difficult to separate the temperature-induced from the pressure-induced volume changes.

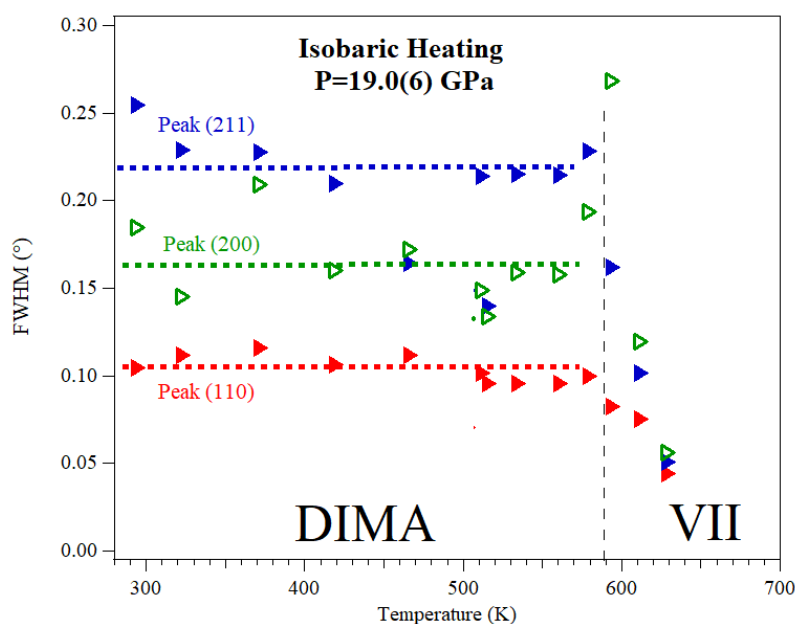


Figure 6.11. Evolution of the FWHM of the first three peaks of the $Im\text{-}3m$ structure along with the isostructural DIMA→AMH-VII phase transition.

In conclusion, we have shown that the phase sequence observed on heating the DIMA+ $P4/nmm$ samples depends on pressure, and that the final phase obtained at high temperature is always AMH-VII, whatever the starting pressure. Moreover, we have detected a new phase (AMH-VIII) on cooling AMH-VII below 18 GPa which is described in the following section.

6.4 Cooling and compression of AMH-VII

The cooling of AMH-VII below 7 GPa has already been discussed in Chapter 5: it results, below a critical temperature, in the dehydration of AMH into AHH and either a water-rich hydrate (WRH) or ice VII. The same process was also observed on the decompression of the DIMA+ $P4/nmm$ samples at 300 K, as discussed in Chapter 3. We note that the demixed sample can be compressed at ambient temperature up to at least 20 GPa without transformation, which indicates a large kinetic barrier between the demixed sample and what we think is the stable phase above 7 GPa, AMH-VIII. The transition line between AMH-VIII and the “dehydrated AMH” domain below 7 GPa was drawn from decompression experiments, and represent either the dehydration from the DIMA or the VIII phase.

In the pressure range [7-18 GPa], AMH-VII transits upon cooling to the new phase called AMH-phase VIII. This phase was also observed during high-temperature compression of phase VII or decompression of the DIMA phase in the same pressure range. Moreover, phase VIII can be quenched to ambient temperature.

We emphasize that the initial phase obtained after the low-temperature sample loading, which is always a mixture of the DIMA + $P4/nmm$ phases with varying ratio, is never recovered on cooling from the high temperature phase VII. $P4/nmm$ is never recovered as a single phase either. We thus conclude that the DIMA+ $P4/nmm$ and $P4/nmm$ are metastable. By contrast, the new phase VIII, in 7-18 GPa range is stable upon cooling down to ambient temperature, or on compression from phase VII, thus we indicate it as the stable AMH phase in the phase diagram.

In the following, we described the conditions of the formation, the stability domain, the structural and the vibrational properties of AMH-VIII phase.

6.4.1 Formation of AMH-VIII

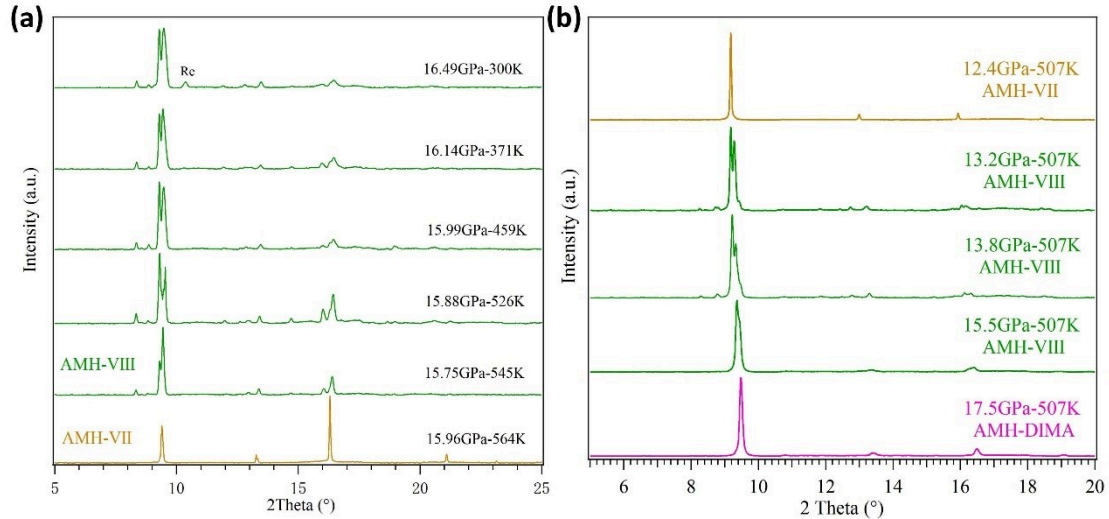


Figure 6.12. Integrated XRD patterns of AMH (a) by isobarically cooling from 658 K to 300 K. Starting from AMH-VII, the phase transition to phase VIII is observed and then this phase is recovered at ambient temperature; (b) by isothermally decompression from 17.5 GPa to 12.4 GPa at 507 K. Starting from AMH-DIMA, the phase transitions to AMH-VIII and then from phase VIII to phase VII are detected.

Our studies show that the formation of phase VIII requires high temperature (at least 400 K) and that it can be recovered down to ambient temperature (as shown in Figure 6.12(a)) and is then stable on compression up to at least 25 GPa. Not only does AMH-VII transform into AMH-VIII during the cooling process and stabilize to room temperature, but also AMH-VIII can transform into the AMH-VII phase during decompression at 507 K, as shown in Figure 6.12(b). Therefore, the phase transition between AMH-VII and AMH-VIII is reversible.

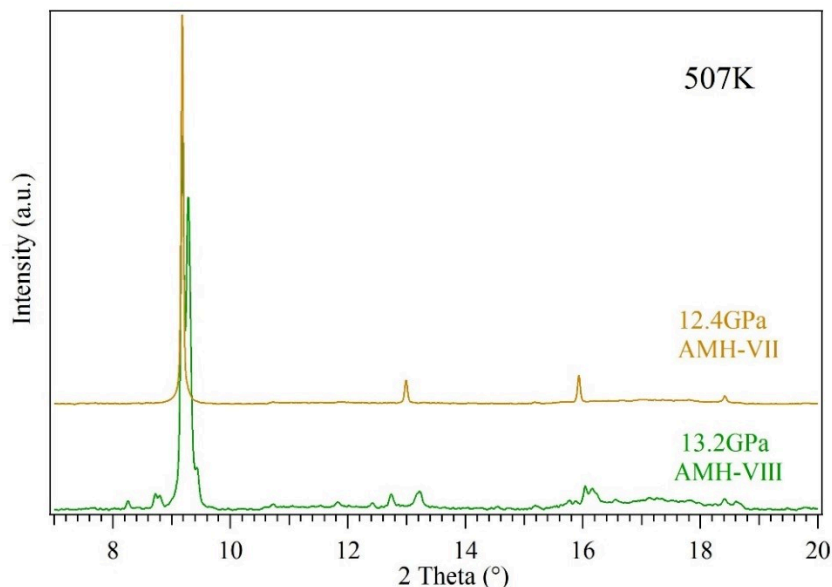


Figure 6.13. Comparison of the XRD pattern of AMH-VII and AMH-VIII. These data are recorded on decompression along the isotherm at 507 K.

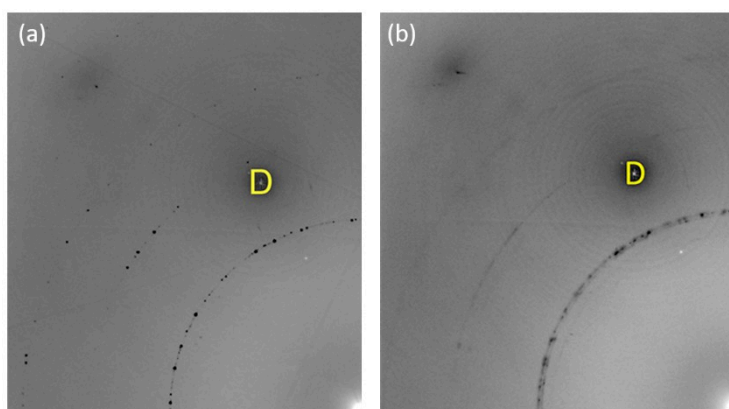


Figure 6.14. XRD image of (a) AMH-VII at 15.5 GPa and 563 K (b) AMH-VIII at 15.2 GPa and 467 K.

Figure 6.13 and 6.14 compares the XRD patterns and images, respectively, of AMH-VII and AMH-VIII: as can be seen, the pattern of phase VIII is much more complex than that of phase VII, which shows that the structure of phase VIII has a lower symmetry and larger unit cell. The transition between the two phases is sharp, occurring over small temperature or pressure steps, and is reversible with little or no hysteresis.

The phase transition from AMH-VII to AMH-VIII was also studied by Raman scattering. As seen in Figure 6.15, the transition to AMH-VIII is accompanied by an intensity transfer between the two main bands of the stretching N-H / O-H region and the appearance of a broad band around 3000 cm^{-1} . Moreover, phase VIII has low-frequency Raman active lattice modes while the cubic phase VII has no active modes.

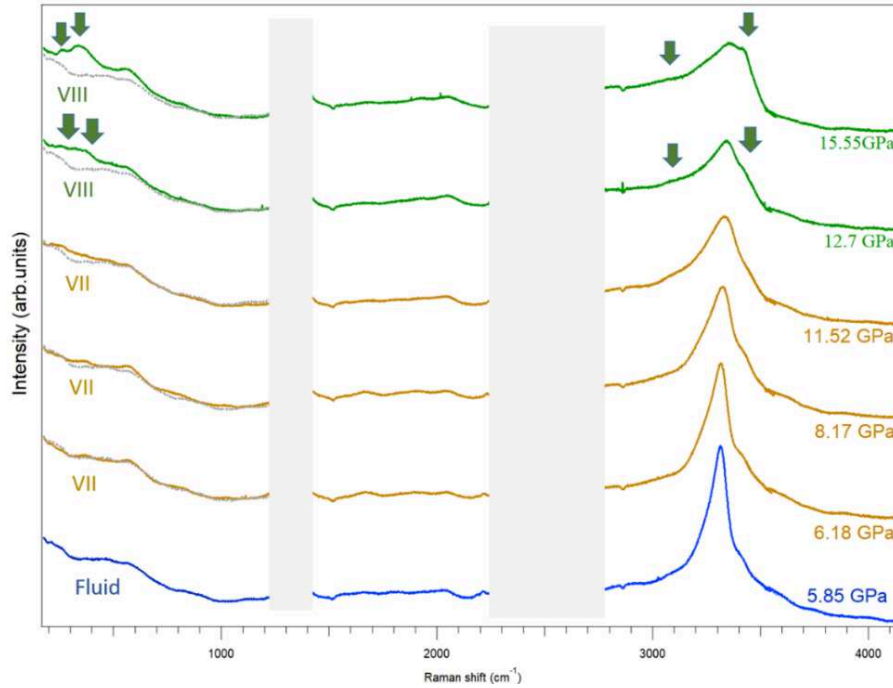


Figure 6.15. Evolution of the Raman spectra of AMH along the isotherm at 496 K on compression. The color represents the different phases: blue = fluid, brown = AMH-VII and green = AMH-VIII. In the lattice region, the grey curve shows the contribution of the diamond: it corresponds to the spectrum recorded in the fluid phase. At low frequencies, the two arrows indicate the apparition of at least two broad lattice modes in phase VIII. In the stretching region, the arrows show a broadening and a change in the relative intensities of the two main bands at the VII-VIII phase transition.

The visual appearance of the sample also changes at the phase transition, as seen in Figure 6.16, showing the photographs of the sample before and after the phase transition: phase VII is transparent whereas phase VIII appears as a strained phase. The Raman spectra of the sample at different positions are the same which indicates a homogeneous sample.

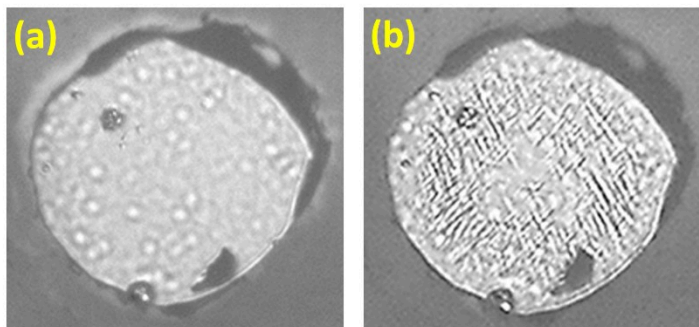


Figure 6.16. Photographs of the sample (a) AMH-VII at 460 K and 6.2 GPa (b) AMH-VIII at 413 K and 8.8 GPa. The phase VII is totally transparent whereas reticulations are visible in the sample of AMH-VIII.

6.4.2 Structure of AMH-VIII

A characteristic XRD 2D image of AMH-VIII has been presented in Figure 6.17: as can be seen, it corresponds to a poor powder sample. The integration of the XRD pattern, presented in

Figure 6.22, shows that phase VIII is characterized by a large number of diffractions peaks compared to the *bcc* phase VII. Qualitatively, the observation of peaks at high d_{spacing} indicates a large unit cell and thus more likely an ordered phase for AMH-VIII. To obtain structural information on phase VIII, we first tried to find a compatible unit cell with the list of the observed d_{spacing} using DICVOL and TREOR programs, but with no success. Because there is always no way to obtain a unit cell that can match all the XRD patterns we have got so far.

To go further and improve the quality of the structural data of phase VIII, we have thus tried to synthesize a single-crystal of phase VIII. To do so, we grew a crystal of phase VII by slowly compressing the fluid at 673 K up to the melting pressure. Once the single crystal of VII was formed, we lowered the temperature. Only visual observations were made during this process, so we did not determine the transition point to phase VIII. But thanks to our phase diagram, we can suppose that the phase transition between phase VIII and phase VII occurs around 430 K during the cooling between 8 and 9 GPa. The final pressure was 8.37 GPa and 300 K. We have then analyzed the structure of this sample by XRD experiment.

The XRD experiment was done at beamline ID27 of the ESRF. The DAC could be rotated along the vertical axis (ω rotation) perpendicular to the X-ray beam during data collection. The X-ray aperture of the DAC was 74° . A XRD image of the AMH-sample obtained at 8.37 GPa during a continuous ω rotation over the full angular range is shown in Figure 6.17. As can be seen, the diffraction pattern is characteristic of a single-crystal pattern although the mosaicist is quite large (several degrees) indicating a fragmentation of the initial single-crystal of phase VII through the VIII-VII phase transition.

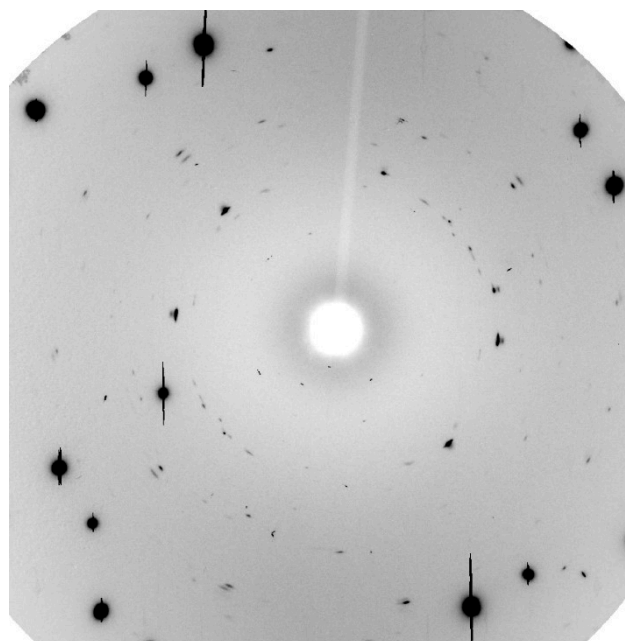


Figure 6.17. XRD image of the AMH-sample obtained at 300 K and 8.37 GPa after cooling a single crystal of AMH-VII at 673 K. The saturated point corresponds to the diamond diffraction peaks.

Positions		Coordinates				Reflection conditions
Multiplicity, Wyckoff letter, Site symmetry		$(0,0,0) + (\frac{1}{2}, \frac{1}{2}, 0) +$				General:
16	<i>g</i> 1	(1) x, y, z (5) $\bar{x}, \bar{y}, \bar{z}$	(2) $\bar{x}, \bar{y} + \frac{1}{2}, z + \frac{1}{2}$ (6) $x, y + \frac{1}{2}, \bar{z} + \frac{1}{2}$	(3) $\bar{x}, y + \frac{1}{2}, \bar{z} + \frac{1}{2}$ (7) $x, \bar{y} + \frac{1}{2}, z + \frac{1}{2}$	(4) x, \bar{y}, \bar{z} (8) \bar{x}, y, z	$hkl : h + k = 2n$ $0kl : k = 2n$ $h0l : h, l = 2n$ $hk0 : h, k = 2n$ $h00 : h = 2n$ $0k0 : k = 2n$ $00l : l = 2n$
8	<i>f</i> <i>m</i> ..	$0, y, z$	$0, \bar{y} + \frac{1}{2}, z + \frac{1}{2}$	$0, y + \frac{1}{2}, \bar{z} + \frac{1}{2}$	$0, \bar{y}, \bar{z}$	Special: as above, plus no extra conditions
8	<i>e</i> .2.	$\frac{1}{2}, y, \frac{1}{4}$	$\frac{3}{4}, \bar{y} + \frac{1}{2}, \frac{3}{4}$	$\frac{3}{4}, \bar{y}, \frac{3}{4}$	$\frac{1}{4}, y + \frac{1}{2}, \frac{1}{4}$	$hkl : h = 2n$
8	<i>d</i> 2..	$x, 0, 0$	$\bar{x}, \frac{1}{2}, \frac{1}{2}$	$\bar{x}, 0, 0$	$x, \frac{1}{2}, \frac{1}{2}$	$hkl : k + l = 2n$
8	<i>c</i> $\bar{1}$	$\frac{1}{2}, \frac{1}{2}, 0$	$\frac{3}{4}, \frac{3}{4}, \frac{1}{2}$	$\frac{3}{4}, \frac{3}{4}, \frac{1}{2}$	$\frac{1}{4}, \frac{3}{4}, 0$	$hkl : k, l = 2n$
4	<i>b</i> $2/m$..	$\frac{1}{2}, 0, 0$	$\frac{1}{2}, \frac{1}{2}, \frac{1}{2}$			$hkl : k + l = 2n$
4	<i>a</i> $2/m$..	$0, 0, 0$	$0, \frac{1}{2}, \frac{1}{2}$			$hkl : k + l = 2n$

Figure 6.19. Excerpt of the International Tables of Crystallography for space group *Cmca*.

The volume of the orthorhombic unit cell is 454 \AA^3 at 8.37 GPa. The number of molecules (NH_3 or H_2O) per unit cell was determined to be 24 by comparison with the volume per molecule in the DIMA phase at 8.37 GPa (19.1 \AA^3). The examination of the Wyckoff positions of the *Cmca* space group shows that several combinations are possible to accommodate 24 molecules, which doesn't allow us to determine the presence of a substitutional disorder of the water and ammonia molecules in phase VIII : without considering hydrogen atoms, the set 1 (16 in general positions + 8 in particular positions) would be compatible with an alloy whereas the set 2 (8 + 4 in particular positions for O and also for N atoms) would be compatible with an ordered of water and ammonia molecules. The data quality was not sufficient to determine the position of the atoms in the unit cell.

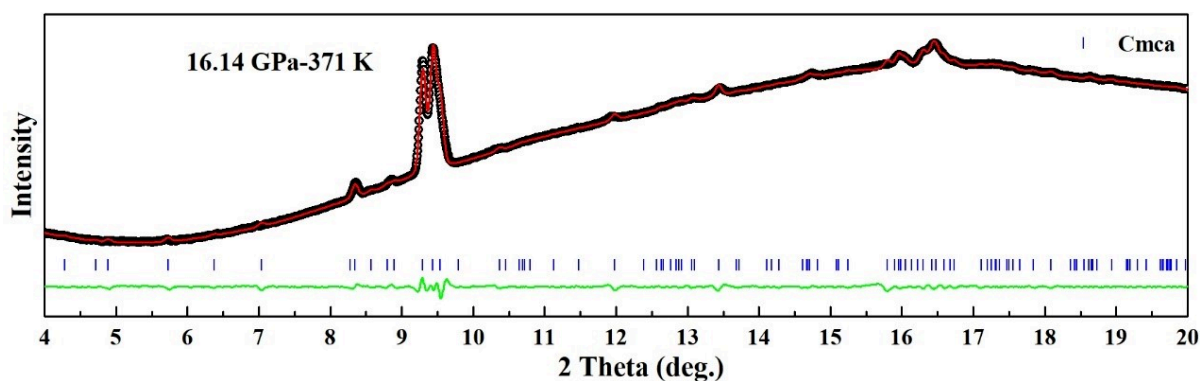


Figure 6.20. Le Bail fit of the XRD pattern (with background) of AMH at 16.14 GPa, 371 K. The symbols are experimental data and the red lines are Le Bail refinement. Sticks show the positions of Bragg reflections. The green line shows the difference between observed and calculated profiles.

Our previous XRD data on the powder samples of AMH-phase VIII was then analyzed by considering the orthorhombic unit cell with *Cmca* space group. The Le Bail fit of the XRD pattern of AMH-VIII at 16.14 GPa and 371 K (Figure 6.20) gives the lattice parameters $a = 4.4961 \text{ \AA}$, $b = 9.9985 \text{ \AA}$, $c = 9.0877 \text{ \AA}$ which correspond to a volume per molecules $V = 17.02 \text{ \AA}^3$.

This volume is close to the volume of the DIMA phase as can be seen in Figure 6.21. All the XRD patterns of AMH-VIII obtained in different experiments were fitted by the Le Bail method, and the pressure dependence of unit cell volume (all the symbols) is shown in Figure 6.21. It can be seen the unit cell volumes of phase VIII are in good agreement with the 300 K EOS of the DIMA phase. However, we also noted that the evolution of the volume of the single-crystal sample is different. For this sample, the pressure was increased from 8.37 GPa to 25.80 GPa at room temperature. The evolution with the pressure of the integrated XRD patterns of this sample is shown in Figure 6.22: no phase transition is observed but we observe a broadening of the diffraction peaks revealing the fragmentation of the single crystal under pressure. Moreover, our EOS of the single crystal sample is different from the ones observed in powder AMH-VIII samples as reported in Figure 6.21 which may be due to the fact that the compression is not hydrostatic (no transmitting medium): if the compressibility along with the a,b,c axis is very different, this would lead to a volume variation depending strongly on the crystal orientation.

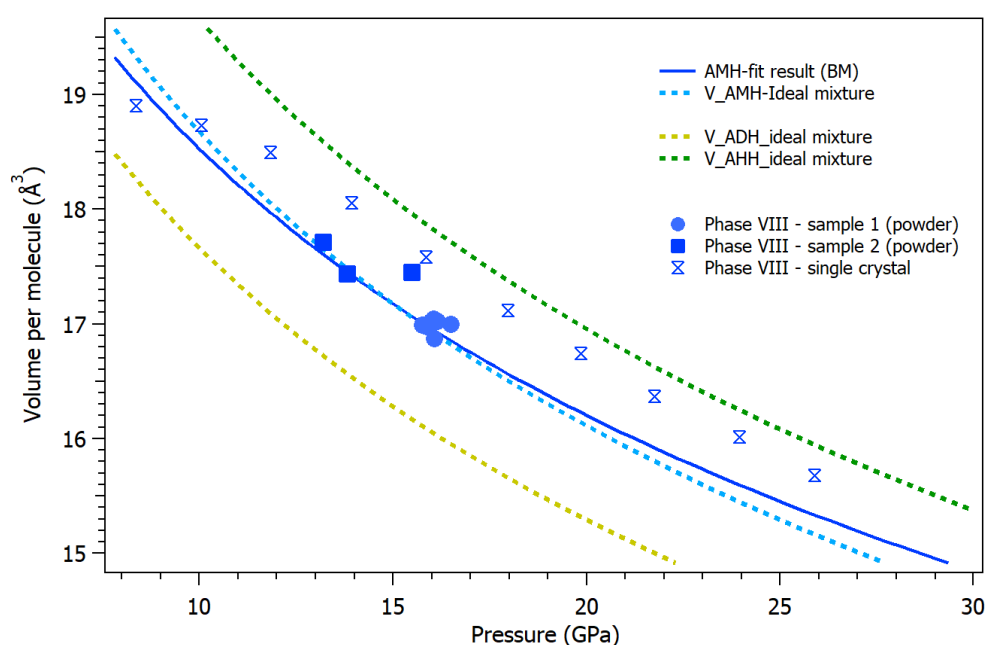


Figure 6.21. Comparison of the EOS of DIMA-AMH (blue line) with the EOS of AMH-phase VIII in the orthorhombic $Cmca$ space group. The different symbols represent the different samples (powder or single crystal) of AMH-VIII studied in this work. The dotted line represents the EOS of the ideal mixture for the three ammonia hydrates. The solid blue line represents the BM-EOS of the DIMA determined in this work (see Chapter 3).

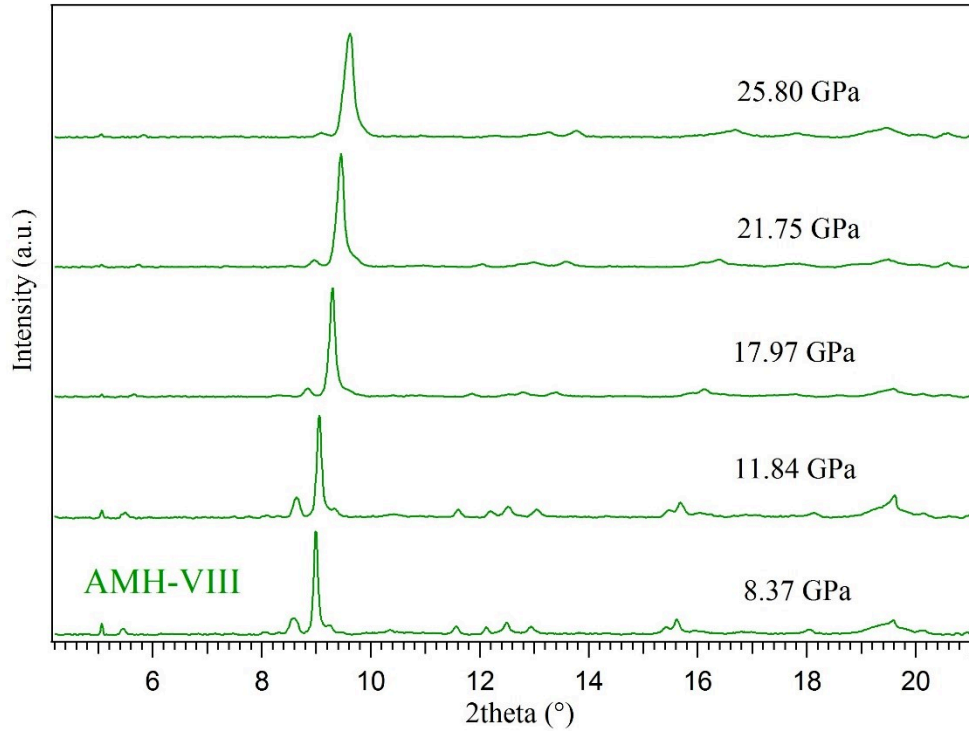


Figure 6.22. Evolution of the XRD pattern of AMH-VIII during compression at room temperature.

6.4.3 Raman spectra of AMH-VIII

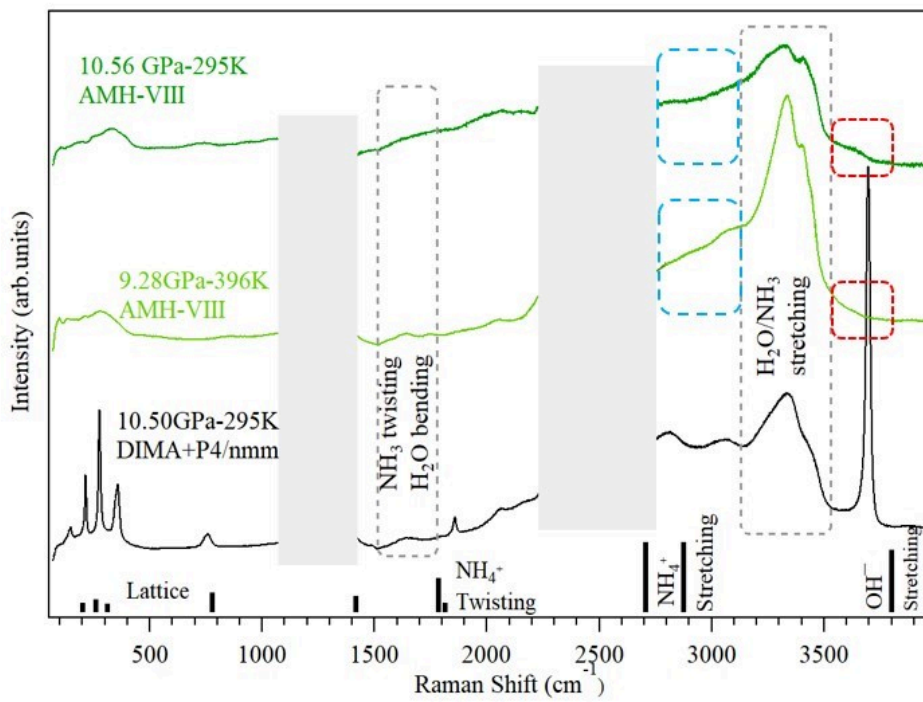


Figure 6.23. Comparison of the Raman spectra of the DIMA + P4/nmm phase and the Raman spectra of AMH-VIII at two different temperatures.

A typical Raman spectrum of AMH-VIII is presented in Figure 6.23 at two different temperatures and compared with the one of the DIMA+*P4/nmm* (AMH-VI) phase. In the latter, the signature of the *P4/nmm* phase is detected by the presence of the sharp peaks. As in the DIMA phase, we observe that the phase VIII is characterized by (1) broad bands around 3600 cm^{-1} and 2800-3100 cm^{-1} which we can assign to OH^- and NH_4^+ species; (2) a broad band assigned to molecular N-H and O-H stretching of water and ammonia is also clearly observed; (3) a broad band in the lattice region. These similarities in the Raman spectra of the DIMA and AMH-VIII phases suggest that AMH-phase VIII is also composed of molecular and ionic species. The intensity ratio of the molecular and ionic species Raman bands further indicates that the molecular species (H_2O and NH_3) are in a larger proportion than the ionic species (OH^- and NH_4^+).

The similarities in the Raman spectra of the two phases stands in contrast with the large difference in their respective XRD patterns. The latter indicates that phase VIII is more ordered than DIMA+*P4/nmm* since the large unit cell would suggest an ordering of the molecules and/or ions. Moreover, we have seen that phase VIII could be obtained by heating the nearly pure *P4/nmm* phase in the isobaric heating experiments starting with *P4/nmm*-rich samples which could indicate a structural relationship between the two phases. To go further, it is essential to determine the structure of phase VIII, which requires further investigations and in particular neutron diffraction experiments.

6.4.4 Transition line between AMH-VII and VIII

We have studied this phase transition by XRD and Raman scattering by following different thermodynamic pathways. Thanks to the different signatures of the phase transition, we have shown that starting from phase VII, phase VIII can be obtained by cooling and compression. Contrary to the DIMA+(*P4/nmm*) \rightarrow VII transition upon heating, the VII \rightarrow VIII transition is fully reversible as the heating or decompression of the phase VIII leads to phase VII. The forward and backward transition points obtained in our experiments are plotted in Figure 6.24, where the thermodynamic path is represented by the orientation of the triangles. As can be seen, the transition points between phase VII \rightarrow phase VIII or phase VIII \rightarrow phase VII coincide and allow us to draw a single VIII \leftrightarrow VII transition line.

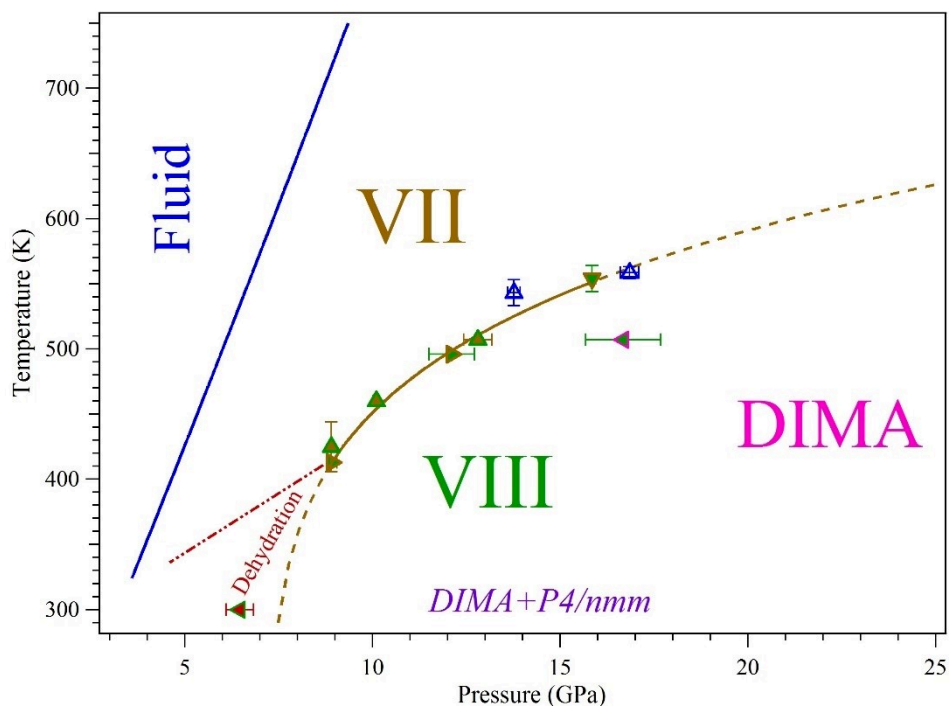


Figure 6.24. Experimental transition points determined in this square. The triangle plain colored symbols correspond respectively to the transitions points VII↔VIII and VII↔DIMA(+P4/nmm). For this transition, if phase VII has been formed, the presence of P4/nmm is then never observed. The continuous and dotted line represent respectively the Simon fit of the VII/VIII phase transition and its extrapolation. The red triangle corresponds to the phase transition between AMH-VIII → AHH-II + WRH at ambient temperature and the red dotted line represents the phase transition AHH-II + WRH ↔ AMH-VII. The open blue triangle corresponds to the transition between P4/nmm+VIII → VII observed in the two initial samples rich in P4/nmm.

The transition line can be well fitted by a Simon-Glatzel type equation, as found previously for the plastic III /ordered IV phase transition in pure ammonia^[4]:

$$T(P) = T_0 \left(1 + \frac{P - P_0}{a} \right)^{\frac{1}{c}}$$

By fixing $T_0=413$ K and $P_0=8.92$ GPa, which correspond to the lowest (P,T) conditions of the observation of the AMH-VII↔AMH-VIII phase transition, the fit gives $a = 1.65$ (83) GPa and $c=5.7$ (1.6).

6.4.5 Stability range of AMH-VIII

The stability range of phase VIII is also reported in Figure 6.24. Its representation is complex because, except for the transition line VII↔VIII (solid line), all the other observed transitions depend on the followed thermodynamic paths (they are thus represented with dotted lines). The orientation of the triangles in Figure 6.24 indicate the thermodynamic pathways.

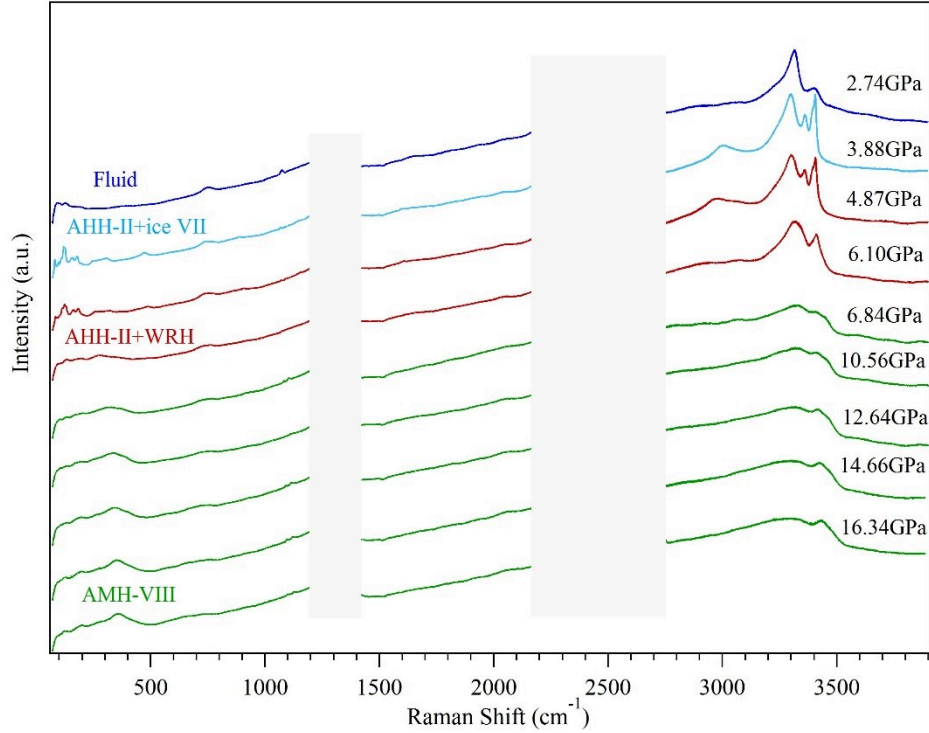


Figure 6.25. Evolution of the Raman spectra of AMH-VIII along with decompression at ambient temperature. Between 6.10 and 6.84 GPa, the dehydration of AMH-phase VIII into AHH-II and WRH is observed.

As we mentioned before, the formation of phase VIII requires high temperature (at least 400 K) and that it can be recovered down to ambient temperature and is then stable on compression up to at least 25 GPa. On decompression at ambient temperature, AMH-VIII is preserved down to 6.8 GPa, where the dehydration into AHH-II and a water-rich hydrate (called WRH) is observed as illustrated in Figure 6.25. This VIII \rightarrow WRH+AHH-II transition can only be observed on decompression, since the sample composed of AHH-II + ice VII is preserved upon compression to at least 20 GPa^[5]. At high temperature, we have shown that phase VIII can be obtained by decompression of the pure DIMA phase (see the XRD pattern evolution shown in Figure 6.12(b)): for this transition, we have a single (P, T) transition point (the pink triangle) at 16.7 GPa and 507 K.

6.5 Stability of the DIMA phase above 18 GPa

Above 18 GPa, AMH-VIII phase has never been detected upon cooling AMH-VII phase. Instead, we observe that the *bcc* (*Im-3m*) structure is preserved on cooling AMH-VII down to ambient temperature.

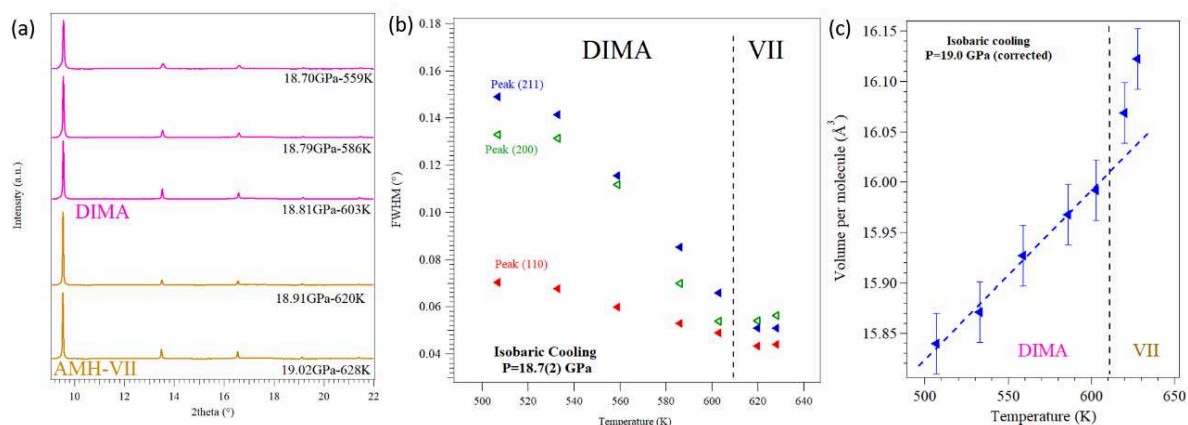


Figure 6.26. (a) Evolution of the XRD pattern during the cooling of AMH-VII along a quasi-isobar at 19 GPa. The bcc structure is preserved upon cooling and the VII→DIMA phase transition only involves subtle changes of the XRD patterns. (b) Linewidth evolution of the three first bcc peaks (110), (200) and (211). A progressive increase of the FWHM is observed at the beginning of the VII→DIMA phase transition. (c) Evolution of the volume as a function of temperature at 19 GPa. The volume measurements have been corrected to take into the small pressure variation along the P-T path, using the EOS parameters of AMH at 300 K.

The evolution of the XRD pattern during the cooling of phase VII along a quasi-isobar at 18.7(3) GPa is shown in Figure 6.26(a). As can be seen, all XRD patterns can be indexed by the same $Im\bar{3}m$ structure, and no apparent structural transition occurs. Nevertheless, by plotting the evolution of the linewidth of the first three XRD peaks of the *bcc* phase (the others peaks have too small intensity and have not been represented) as function of temperature along the quasi isobar at 18.7(3) GPa (see Figure 6.26(b)), we can detect a progressive increase of the linewidth on cooling below 610 K. Moreover, we observe a clear decrease of the volume thermal expansion coefficient at 610 K⁴ in Figure 6.26(c). Yet, no volume discontinuity can be inferred within uncertainties. As this phase transition occurs at nearly the same pressure than the phase transition from DIMA(+ $P4/nmm$) to AMH-VII, we interpret the low temperature phase as being the DIMA phase.

We have done the same analysis of the XRD data recorded during the cooling of phase VII along the isotherms at 27 GPa and 52 GPa. These results are presented in Figure 6.27. As can be seen, at 27 GPa (Figure 6.27(a)), the observations are less clear: we can detect only a progressive increase of the FWHM of phase VII followed by a flattening of the FWHM below 640 K but the volume variation seems continuous within uncertainties. Finally, at 52 GPa, no change is observed either on the linewidth or on the volume variation (see Figure 6.27(b)).

⁴ Since the pressure was not perfectly constant during the temperature decrease, the measured volume was corrected from the pressure effect by using the Birch Murnaghan EOS coefficient of AMH at 300 K. The volumes were calculated to correspond to a pressure of 19 GPa.

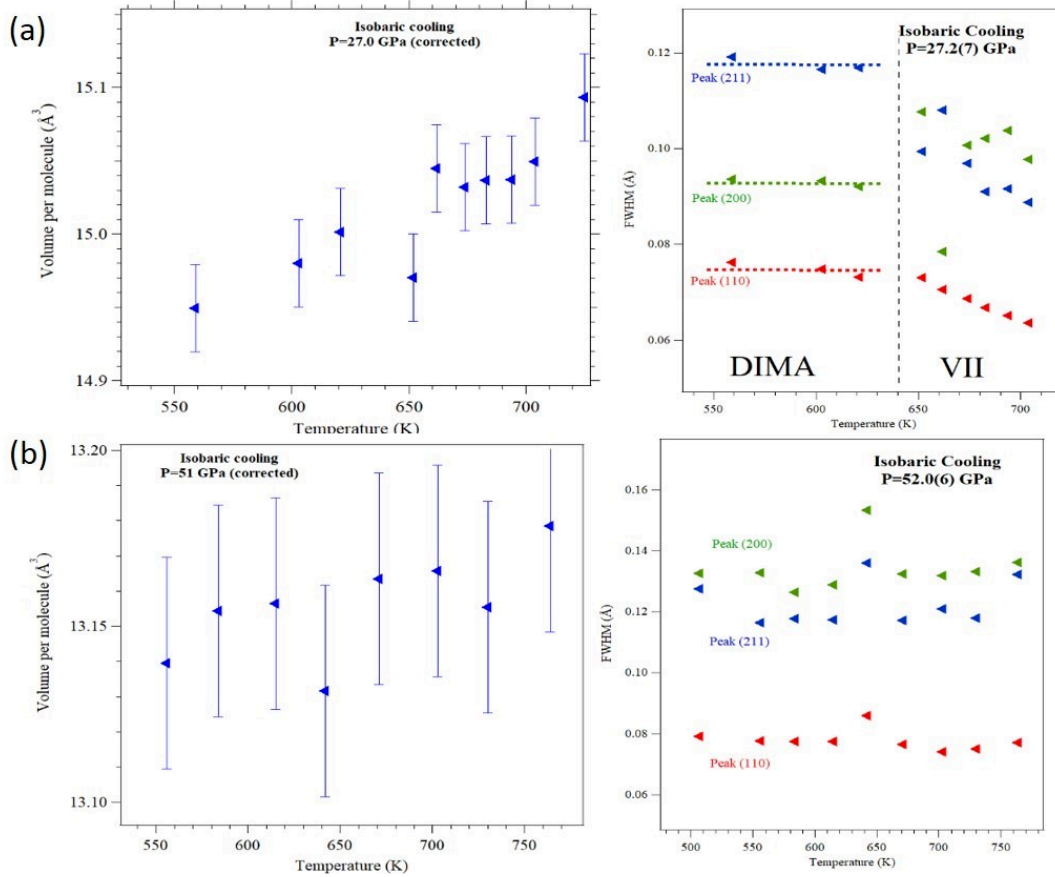


Figure 6.27. Volume variation (left) and evolution of FWHM (right) as a function of temperature for two quasi-isobars at (a) 27 GPa and (b) 52 GPa. For the volume variation (left), the measured volumes have been corrected using the 300 K Birch-Murnaghan EOS of AMH to take into account the small pressure variations upon cooling.

The different P-T points associated with the transition from phase VII to the *bcc* DIMA phase are presented in Figure 6.28 and compared with the ones obtained on heating the initial DIMA(+*P4/nmm*) samples and with the points corresponding to the VII \leftrightarrow VIII transition line. As can be seen, a slight deviation from the extrapolation of the VII \leftrightarrow VIII transition line is observed above 30 GPa. By fitting the VII \leftrightarrow DIMA(+*P4/nmm*) transition with a Simon-Glatzel equation, fixing P_0 and T_0 to the triple point VII-VIII-DIMA ($P_0=17.5$ GPa and $T_0=569$ K), we obtain $a=1.94(1.62)$ GPa and $c=17.19(6.84)$. The large uncertainties on a and c come from the dispersion of the transition points, which is much larger than for the VII \leftrightarrow VIII transition line.

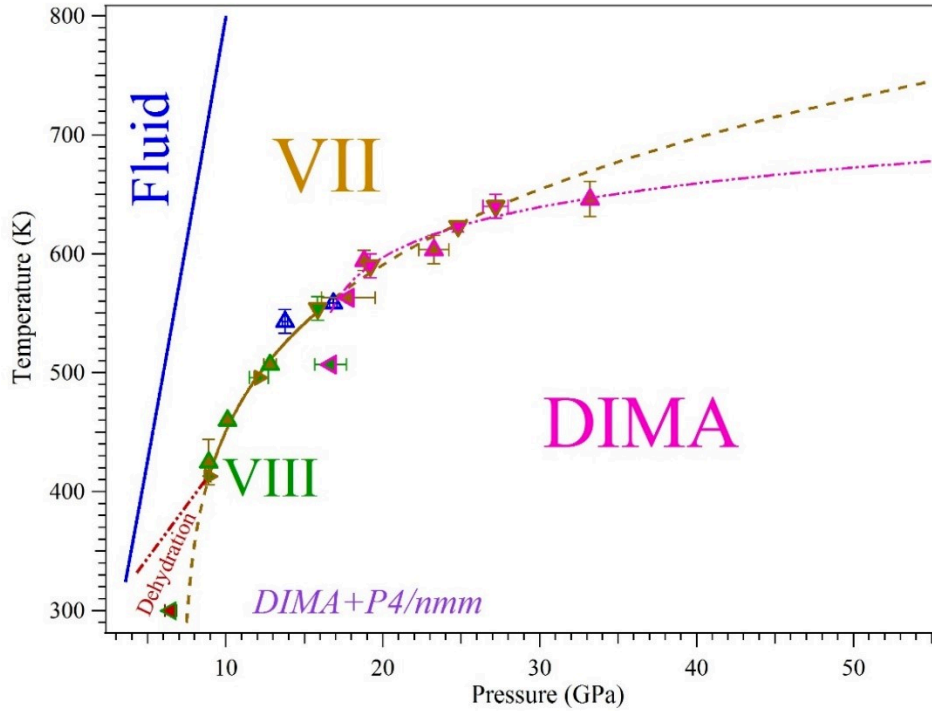


Figure 6.28. Experimental transition points determined in this work. The solid green/brown triangles and the pink/brown triangles respectively correspond to the transition points VII \leftrightarrow VIII and VII \leftrightarrow DIMA(+P4/nmm). The orientation of the triangle represents the thermodynamic paths. The contour color corresponds to the initial phase and the inside color, to the final phase. For the VII \leftrightarrow DIMA(+P4/nmm) phase transition, the P4/nmm phase is never observed in the forward (cooling) transition. The brown continuous and dotted line represent respectively the Simon-Glatzel fits of the VII \leftrightarrow VIII phase transition and its extrapolation. The red triangle corresponds to the transition AMH-VIII \rightarrow AHH-II + WRH at ambient temperature and the red dotted line represents the phase transition AHH-II + WRH \leftrightarrow AMH-VII. The blue triangle corresponds to the transition between P4/nmm+VIII \rightarrow VII observed in the two P4/nmm-rich samples.

6.6 Stability of AMH-VII at high pressure and high temperature

The stability of AMH-VII was studied in a compression experiment from 25 GPa to 52 GPa along an isotherm at 763 K using XRD. All the collected patterns could be indexed with the same $Im\bar{3}m$ structure in this pressure range. We determined the EOS of AMH at 763 K from this data set and compare it to the 300 K EOS in Figure 6.29. As can be seen, the two compression curves show the same behavior and there is no volume anomaly along the 763 K isotherm. Since in pure ammonia, the transition from the plastic to the superionic solid was detected by a sudden change in compressibility but no volume jump^[6], we computed the compressibility at 763 K and 300 K as a function of pressure using the XRD data. As can be seen in Figure 6.30, there is no obvious change, within the dispersion of the data, in the compressibility of AMH at the two temperatures.

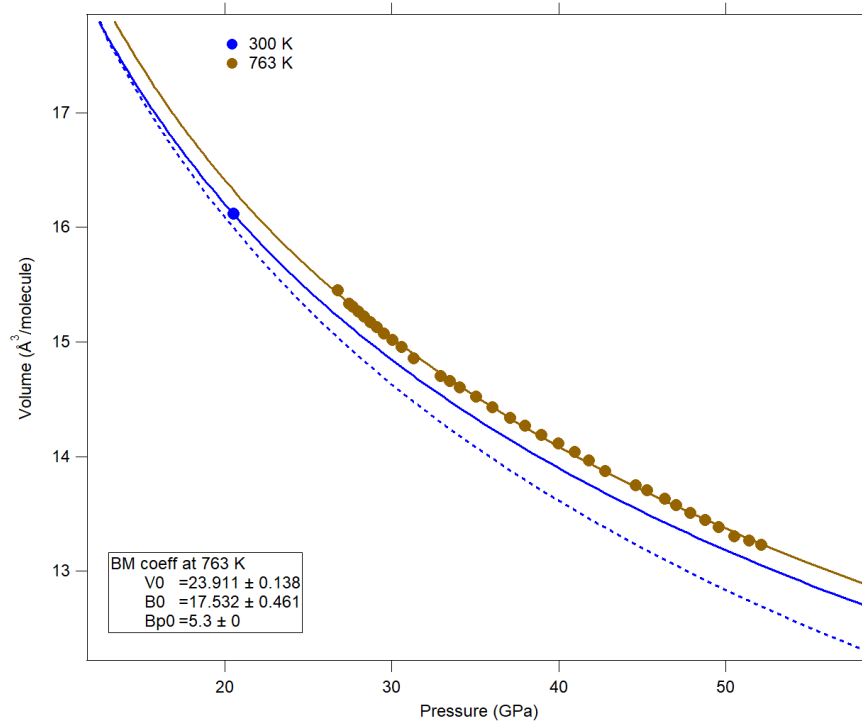


Figure 6.29. Comparison of the EOS of AMH at 300 K and 763 K, determined by XRD. For the experiment at 763 K, the pressure was measured with the EOS of gold using the gold liner between the sample and the rhenium gasket, whereas in the EOS measurements at 300 K the pressure was measured by ruby luminescence. We detected a volume difference between the two methods corresponding to the pressure difference of 2.05 GPa, so we corrected the gold pressure by adding an offset of 2.05 GPa.

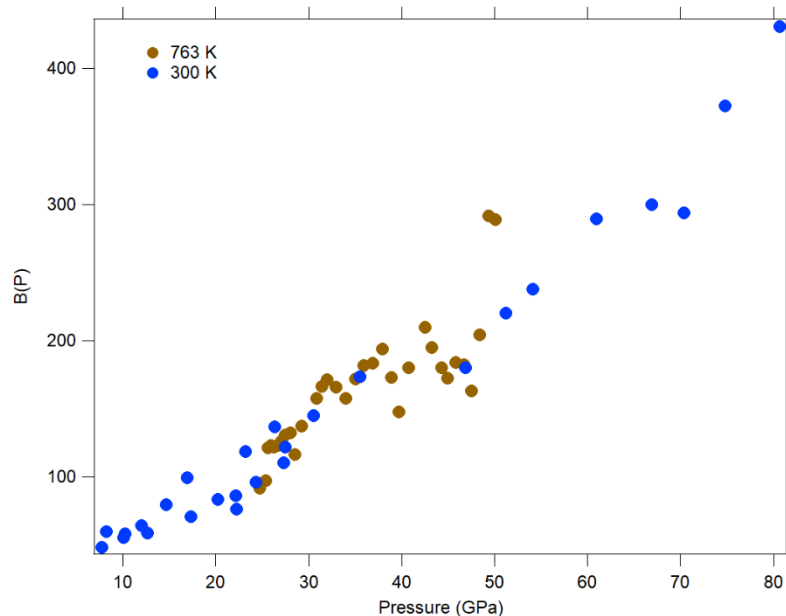


Figure 6.30. Isothermal compressibility modulus B (in GPa) of AMH as function of pressure for two isotherms at 300 K and 763 K.

To sum up, the isostructural phase transition VII→DIMA phase is difficult to observe on

cooling compared to the reverse transition DIMA+ $P4/nmm$ phase (AMH-VI)→VII. The main signature is a broadening of the *bcc* Bragg peaks in the DIMA phase. No volume jump was detected within uncertainties⁵. Above 27.2 GPa, we were not able to detect the signature of a phase transition on cooling phase VII. The three transition points obtained from 18.8 GPa to 27.2 GPa are shown in Figure 6.28 and compared to those determined on heating the DIMA+ $P4/nmm$ phases. Within uncertainties, the phase transition seems reversible. We also note that extrapolation of the VIII ↔ VII transition line coincides with that of the DIMA ↔ VII up to 27 GPa and then slightly deviates.

We have also shown that the AMH-VII is stable on compression from 25 GPa to 52 GPa at 763 K and we were not able to detect any phase transition by cooling phase VII down to 500 K at 52 GPa, although the extrapolation of the VII→DIMA places this transition around 650 K at this pressure. The discussion on the nature of phase VII at high pressure and high temperature will be done in the last section of this chapter.

6.7 Signature of superionicity in AMH-VII?

The theoretical phase diagram of AMH reported by Bethkenhagen *et al* using *ab initio* (DFT) molecular dynamics methods^[1] is reproduced in Figure 6.31. As can be seen, these calculations have been done in a very large domain of pressure [10-800 GPa] and temperature [500-7000 K] compared to our experimental work ([0-80 GPa] and [300-770 K]). At 500 K, purely ionic solid phases are predicted above 10 GPa. At 1000 K (the next temperature step in the calculations) and superionic conduction is observed in the solid phases in the pressure range 18-60 GPa.

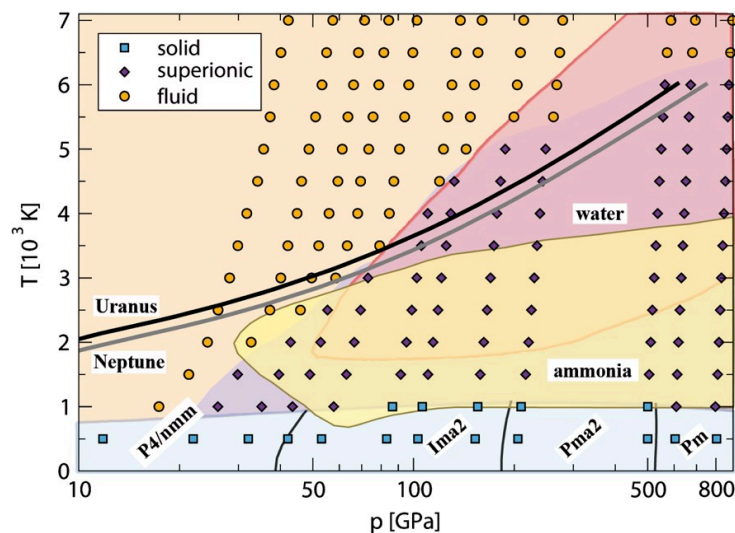


Figure 6.31. Theoretical phase diagram of AMH predicted by *ab initio* calculations^[1].

⁵ As said before, the only occasion where a volume jump has been detected from DIMA to VII was along the 563 K decompression isotherm, however we believe that the actual phase sequence was DIMA→VIII→VII, and the fact that we did not observe phase VIII was due to the too large pressure step between 19.5 GPa and 16.8 GPa and the proximity of the VII-VIII-DIMA triple point.

Compared to these calculations, we have shown in the present work that the phase diagram of AMH up to 50 GPa and 770 K is quite complex. Several metastable phases exist which leads to the observation of different phases in the same (P,T) domain depending on the followed thermodynamic path. Moreover, all the observed structures are not purely ionic or molecular but are in general ionico-molecular. Nevertheless, we have shown by XRD that, whatever the initial sample and whatever the thermodynamic pathways, the phase stable at high pressure and high temperature is the *bcc* AMH-VII phase. At low pressure (8 GPa) and 500 K, closed to the melting line, we have shown by QENS experiment the plastic nature of AMH-VII and by Raman scattering, we have also shown that this phase is mainly molecular but the presence of ionic species is not excluded even at low pressure. The presence of solid plasticity was not considered in the theoretical work of Bethkenhagen *et al.*

The ionic-superionic transition observed in the theoretical study occurs in the (P,T) range where we experimentally observed the DIMA \leftrightarrow VII transition, although we recall that the transition between the two phases become imperceptible above 30 GPa by XRD. Since the XRD technique is poorly sensitive to H atoms, we may hypothesize that the DIMA \leftrightarrow VII transition is mainly related to changes in the positions of H atoms. The latter may be either due to the onset of plasticity, as observed at $P < 10$ GPa, or to the onset of superionicity, as predicted by calculations.

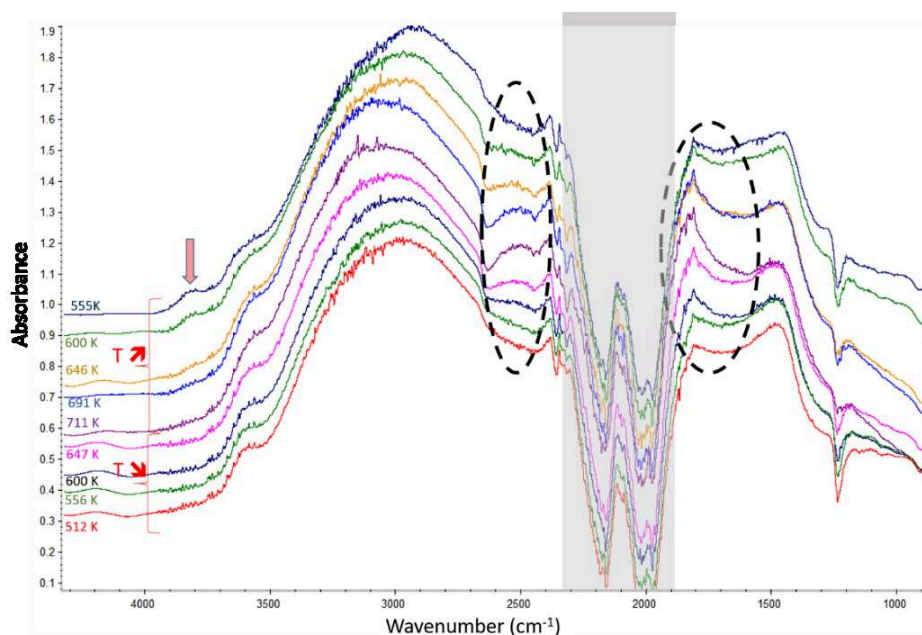


Figure 6.32. Evolution of IR absorbance of AMH as function of temperature on heating from 555 K to 711 K (top spectra) followed by cooling from 711 K to 512 K (bottom spectra). During this temperature cycle, the pressure varies from 42 to 37 GPa. The frequency window from 2000 to 2300 cm^{-1} is obscured by the strong absorption band of the diamond anvils. Temperatures are indicated on the left. The arrows indicate the presence of the band associated with OH^- stretching in the *P4/nmm* structure. The broad band between 2500 and 3700 cm^{-1} is characteristic of the stretching N-H and O-H in the DIMA phase and associated with NH_4^+ , H_2O , NH_3 and OH^- (see Chapter 3). *P4/nmm* disappears between 600 and 646 K. The dashed oval indicates the region where the absorption increases on heating and decreases on cooling.

To go further, we performed IR spectroscopy experiments at high P-T on the SMIS beamline of the SOLEIL synchrotron. Starting from an initial sample of DIMA (+ $P4/nmm$) phase, we have increased and decreased temperature from 300 K to 700 K along two quasi-isobars (40 and 67 GPa). The evolution of the absorbance as a function of temperature is presented in Figures 6.32 and 6.33, respectively at 40(3) GPa and 67(2) GPa. As can be seen in Figure 6.32, the initial sample was rich in DIMA phase but the $P4/nmm$ OH stretch of the OH^- ion at about 3800 cm^{-1} is observed at room temperature. This OH^- stretching mode disappeared on heating between 600 and 646 K (see Figure 6.32). We also note the appearance of a broad absorption near 1800 and 2500 cm^{-1} . These changes occur around 39.5(2.5) GPa and 623(23) K. The region [$1900\text{-}2400\text{ cm}^{-1}$] is not exploitable due to the strong absorption of the diamond. These broad absorption bands disappear reversibly when the sample is cooled between 647 K and 600 K. By contrast, the OH^- stretching mode of $P4/nmm$ structure is not recovered. These observations are consistent with our XRD results for the transition from DIMA+($P4/nmm$) to phase VII, and from phase VII to pure DIMA on cooling. On the same sample, we then followed the evolution of the absorption at 67 GPa as a function of temperature, shown in Figure 6.33. We also detected an increase of absorption around 1800 and 2500 cm^{-1} and a broadening of the broad peak around 3700 cm^{-1} associated to the OH^- stretching in the DIMA phase between 668 K and 711 K. We have not studied this process on cooling at this pressure.

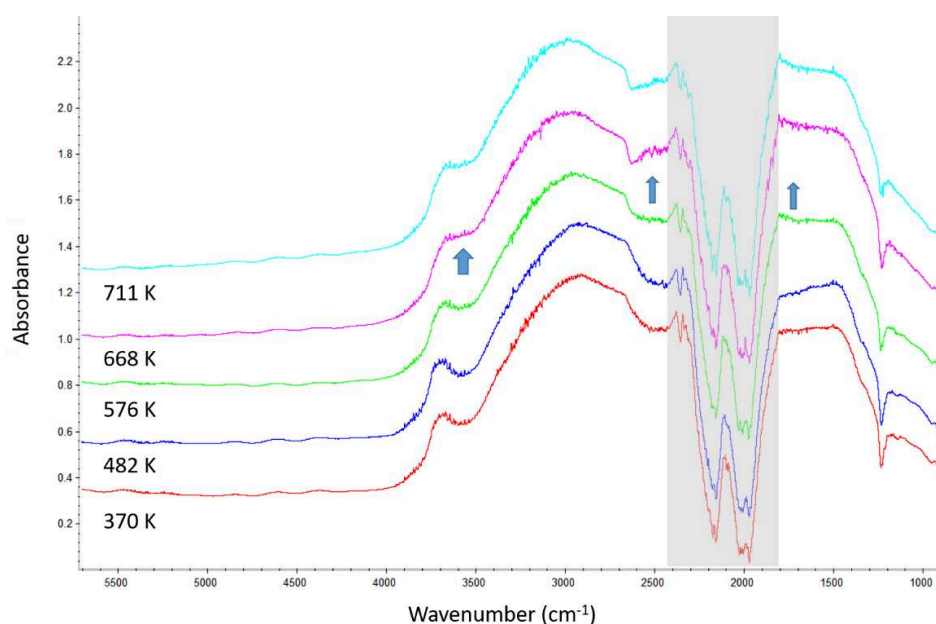


Figure 6.33. Evolution of IR absorbance of AMH as a function of temperature on heating from 370 K to 711 K along a quasi-isobar 69(2) GPa. The frequency window from $2000\text{ to }2300\text{ cm}^{-1}$ is obscured by the strong absorption band of the diamond anvils. Temperatures are indicated on the left. The arrows indicate the region where an increase of absorption is observed on heating.

If we report these two transition points on the phase diagram of AMH (see Figure 6.34), we can see that they are slightly below the extrapolation of the DIMA \leftrightarrow phase VII transition line and are independent of pressure as it occurs around 625(25) K at both pressures. These IR

observations are similar to the ones observed in pure ammonia at the onset of the transition to the superionic phase in ammonia^[6,7]. Figure 6.35 shows the evolution of the absorbance of pure ammonia across the ordered phase IV to superionic ammonia on heating and cooling. The increase of absorption is associated with the creation of new ionic species (mainly NH_4^+ and OH^- in our case). To obtain a superionic phase, the ionization needs to be dynamic and so associated with the creation/annihilation of ionic species with a short lifetime. In ammonia, this is revealed by a very strong broadening of the observed bands. In our experiment on AMH, this it is not as clear and perhaps corresponds to the beginning of the diffusion. High temperature experiments up to 900 K will be necessary to see the evolution of the broadening. Nevertheless, a more quantitative analysis of these linewidths is difficult because all the bands are very broad and a great part of the information is masked by the strong absorption of the diamond between 1900 and 2300 cm^{-1} . Thanks to the IR experiment, we have shown that this phase transition can be detected up to 70 GPa and that this transition is nearly independent of the pressure above 30 GPa. By comparison with pure ammonia, this phase transition is quite similar to the phase transition from the plastic NH_3 -III phase to the superionic phase. The observed AMH-VII above 30 GPa may thus also be the superionic phase.

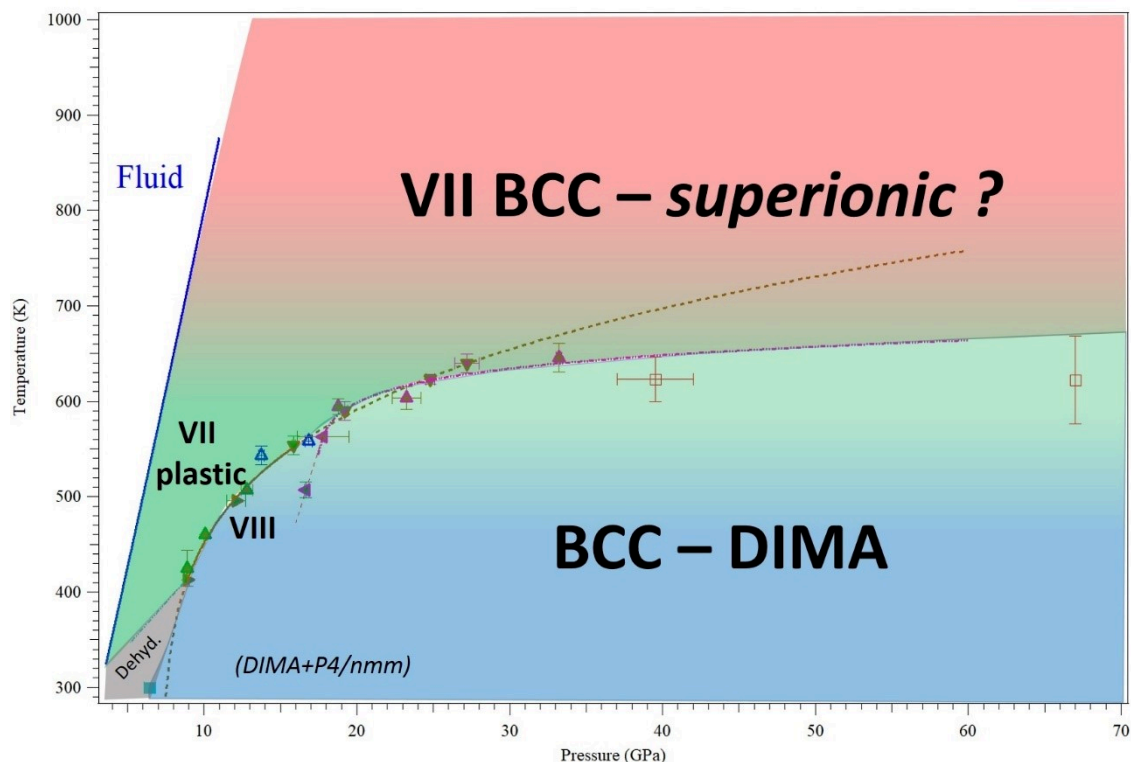


Figure 6.34. Phase diagram of AMH determined in this work. The different symbols represent our experimental data. The open red square corresponds to the (P,T) points determined by IR absorption experiments. The difference in color represents the hypothetical nature of the H atoms in the different phases: blue: ordered atoms; green: orientational disordered; red: diffusive.

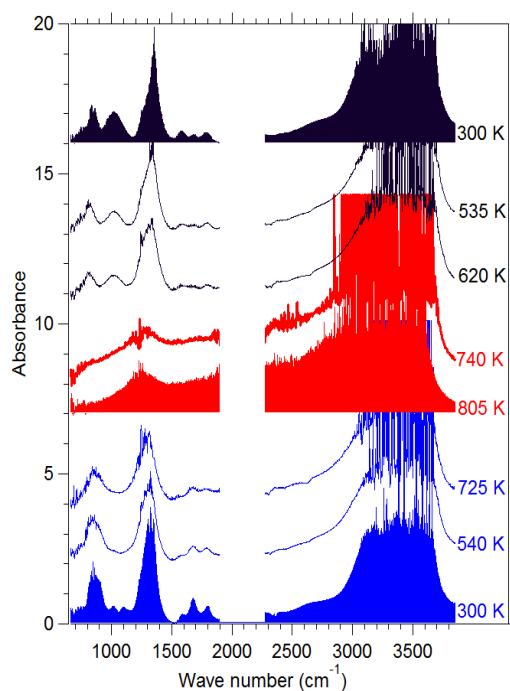


Figure 6.35 Evolution of IR absorbance of pure ammonia as a function of temperature on heating from 300 K to 805 K from 75 GPa to 83 GPa. The frequency window from 2000 to 2300 cm^{-1} is obscured by the strong absorption band of the diamond anvils.

6.8 Conclusions

In this chapter, we have investigated the phase diagram of AMH at high pressure and temperature (up to 70 GPa and 763.5 K) by XRD, Raman and infrared experiments. These studies have revealed a complex phase diagram of AMH with large metastabilities and the discovery of a new phase called AMH-VIII.

AMH-VIII is formed only at high temperature and is the stable phase between 8 and 18 GPa as the cooling of phase VII always leads to phase VIII. The DIMA phase and $P4/nmm$ phases observed in this P domain are thus considered as metastable phases. The phase transition between phase VIII and phase VII is well described by a Simon-Glatzel type equation. Since in a general manner, plasticity is not favored at high pressure, we can suppose that AMH-VIII is a rotationally ordered ionic-molecular phase. As this phase can be obtained from the totally ordered $P4/nmm$, we can also suppose that there is no substitutional disorder in phase VIII. This order associated with the coexistence of molecular and ionic species may lead to a large volume cell as observed in AMH-VIII. An orthorhombic unit cell with the space group $Cmca$ has been seen to comply with the XRD pattern of this phase.

Above 18 GPa, phase VIII is never observed and instead the cooling of the *bcc* phase VII leads to the initial pure *bcc* DIMA phase without any presence of the ionic $P4/nmm$ phase. The main characteristic of this transition is the broadening of the Bragg peaks in the DIMA phase. This becomes difficult to observe above 30 GPa, possibly due to the appearance of pressure gradients in the sample which artificially broadens the Bragg peaks and masks the transition. The Bragg peaks in the DIMA phase are intrinsically broadened due to the microstrain originating from the random distribution of NH_3 , H_2O , OH^- and NH_4^+ , combined to a static disorder of H atoms. The sharpening of the peaks in phase VII may be associated with local displacement of O and N atoms towards the perfect *bcc* lattice sites. To obtain such a

configuration, the main idea is to give more degrees of freedom to the hydrogen atoms. This is possible if the temperature allows rotation of all the molecules and this leads to plasticity in AMH-VII. Another possibility is to allow rotational and translational diffusion which will lead to a superionic phase. With only the basis of our XRD experiments, we cannot conclude on these two scenarios. Moreover, the transition from plastic to superionic phase with no change in the structure of the O/N lattice seems difficult to observe by XRD. Above 30 GPa, we have detected an increase in the infrared absorption at 40 and 70 GPa at nearly constant T (625 K), slightly below the extrapolation of the VII/DIMA phase transition. The same observation was previously made in pure ammonia at the molecular-superionic transition, but it is less clear in AMH as the IR bands are already very large in the low temperature phase. To confirm this, it will be necessary to perform the IR measurement to higher temperature to see if a broadening of all the peaks appears with temperature confirming the superionic nature of the HT phase.

References

- [1] Bethkenhagen, M., Cebulla, D., Redmer, R. *et al.* Superionic phases of the 1: 1 water–ammonia mixture. *The Journal of Physical Chemistry A* **119**, 10582-10588, (2015).
- [2] Liu, C., Mafety, A., Queyroux, J. *et al.* Topologically frustrated ionisation in a water-ammonia ice mixture. *Nature communications* **8**, 1065, (2017).
- [3] Rothkirch, A., Gatta, G. D., Meyer, M. *et al.* Single-crystal diffraction at the Extreme Conditions beamline P02. 2: procedure for collecting and analyzing high-pressure single-crystal data. *Journal of synchrotron radiation* **20**, 711-720, (2013).
- [4] Ninet, S. & Datchi, F. High pressure–high temperature phase diagram of ammonia. *The Journal of chemical physics* **128**, 154508, (2008).
- [5] Ma, C., Li, F., Zhou, Q. *et al.* Ammonia molecule rotation of pressure-induced phase transition in ammonia hemihydrates $2\text{NH}_3\cdot\text{H}_2\text{O}$. *RSC Advances* **2**, 4920-4924, (2012).
- [6] Ninet, S., Datchi, F. & Saitta, A. Proton disorder and superionicity in hot dense ammonia ice. *Physical review letters* **108**, 165702, (2012).
- [7] Ninet, S., Datchi, F., Dumas, P. *et al.* Experimental and theoretical evidence for an ionic crystal of ammonia at high pressure. *Physical Review B* **89**, 174103, (2014).

Conclusions

The aim of this thesis was to determine experimentally the properties of the ammonia monohydrate ($\text{NH}_3:\text{H}_2\text{O}$ - AMH) compound under high pressure and high temperature. This work was motivated by two main reasons: (a) for fundamental physics, this work allowed to study the evolution of H-bonds with density and determine whether the exotic states (ionic, superionic, symmetric ices) observed in pure water or ammonia ices also exist in mixtures at lower (P,T) conditions as predicted; (b) for planetary sciences, and in particular for icy planets and their satellites, knowing the properties of the ammonia hydrates under extreme (P,T) conditions is important to construct models of these bodies which can be compared to observations.

In this work, we have shown that the building of the phase diagram of AMH turned out to be a rather complex task, as different phases can be observed at the same P-T conditions depending on the followed thermodynamic paths. However, through detailed experimental investigations and analysis, we have obtained the phase diagram of AMH up to 70 GPa and 763 K.

At room temperature, our investigations allowed to explain the apparent discrepancy on the nature of AMH-VI between previous neutrons experiments^[1] and *ab initio* calculations^[2,3]. Our results, exposed in Chapter 3, have shown that AMH spontaneously ionizes under pressure ($P > 7.4$ GPa) at 300 K to form a peculiar alloy where the standard molecular forms of water and ammonia coexist with hydroxyl and ammonium ions. By combining X-ray diffraction, neutron diffraction and Raman scattering experiments, we demonstrated that AMH-VI is a mixture of a *bcc* (*Im-3m*) phase, called Disordered Ionico-Molecular Alloy (DIMA), and of the fully ionic *P4/nmm* phase predicted by *ab initio* (DFT) calculations^[2]. The partial ionization of the DIMA phase comes from a local topological frustration: the substitutional disorder is not compatible with the ionization of all water and ammonia molecules. This experimental result also shows that the static ionization in AMH appears at a much lower pressure (7.4 GPa) than in the pure ices (150 GPa in NH_3 , over 1.4 TPa in H_2O ^[2-4]), which originate from the lower energy cost for the proton transfer between water and ammonia. We have measured the EOS of the DIMA phase at room temperature and shown that the *bcc* phase is stable from 7.4 GPa to at least 80 GPa. No evidence of the symmetric and fully ionic *Ima2* phase, predicted by DFT to occur at 38.5 GPa^[3], has been observed by XRD. These findings are part of an article published in Nature Communication^[4].

We have then explored the evolution of AMH at simultaneous HP and HT conditions, in order to establish its phase diagram and look for possible superionic phases. First, we determined the melting curve of AMH up to 700 K by visual observations and Raman experiments (Chapter 4). Below 324 K, the melting line is non-congruent since the solid phase bordering the fluid is not a proper AMH phase but a mixture of AHH-II and ice VII. The solidus and liquidus pressure have been

determined at 300 K. Above 324 K, the solid-fluid equilibrium occurs at a unique (P, T) value and thus melting becomes congruent. Simultaneously, a new high temperature solid phase AMH-VII is observed in equilibrium with the fluid. AMH-VII phase has a similar refractive index and Raman spectra as the fluid, making it more difficult to detect melting by visual and Raman observations. By comparison with the melting curves of pure H₂O and pure NH₃, we found that there is a closer correspondence between AMH-VII and the plastic solid phase III of NH₃.

Subsequently, the properties of AMH-VII phase were investigated by XRD, Raman and QENS experiments, as presented in Chapter 5. The structure of AMH-VII has been determined by XRD: it is a body-centered cubic structure with space group *Im-3m* with substitutional and orientational disorder. Moreover, we have shown by Raman scattering that AMH-VII is a likely partly ionic and partly molecular. AMH-VII is thus very close to the DIMA phase. We have studied the hydrogen dynamics motion in AMH-VII by QENS experiments in the P-T range 6.3-8.2 GPa, 473-523 K. To our knowledge, these are the highest pressures at which QENS experiments have been performed to date. We used a sample where water is deuterated (NH₃·D₂O) to reduce neutron multiple scatterings. We have shown that the hydrogen atoms of ammonia molecules present rotational dynamics, confirming that AMH-VII is a plastic solid. Within error bars, the rotational diffusion coefficient D_R was found constant in the explored P-T range.

The phase diagram of AMH at much high pressure and temperature (up to 70 GPa and 763 K) was studied by XRD experiments, and the results presented in Chapter 6. Between 7 and 18 GPa, we have shown that the cooling of phase VII leads to a new phase, called phase VIII, whereas above 18 GPa, the cooling or compression of phase VII leads to the DIMA phase. We have demonstrated that AMH-VIII is formed only at high temperature (T>400 K) and is stable between 7 and 18 GPa. The DIMA phase and *P4/nmm* phase observed in this pressure range and below the transition temperature to AMH-VII are thus considered as metastable phases. The phase transition line between AMH-VII and AMH-VIII is reversible and well described by a Simon-Glatzel type equation. An orthorhombic unit cell with 24 molecules and *Cmca* space group were suggested for phase VIII based on single-crystal XRD experiment. Since phase VIII can be obtained from the fully ordered *P4/nmm* phase and has a large unit cell with low symmetry, we may confidently conjecture that the molecules and ions are more ordered in phase VIII compared to the *bcc* DIMA phase. AMH-VIII may thus correspond to an ordered ionico-molecular phase.

Above 18 GPa, AMH-VIII is never observed and instead the cooling of the *bcc* phase VII leads to the initial pure *bcc* DIMA phase, i.e without the presence of the ionic *P4/nmm* phase. As the main XRD signature of this transition is the broadening of the diffraction peaks in the DIMA phase, this phase transition is quite difficult to observe at high pressure (above 30 GPa). The sharpening of the peaks in phase VII may be induced by local displacement of O and N atoms towards the perfect *bcc* lattice sites: depending on the degree of freedom of the hydrogen atoms, a plastic or a superionic phase is expected. As the isostructural phase transition from the plastic AMH-VII phase

to the predicted superionic phase seems difficult to observe by XRD, we have investigated this transition by IR experiments. We have detected an increase in the infrared absorption at 40 and 70 GPa at nearly constant T (625 K), slightly below the extrapolation of the VII/DIMA phase transition. A similar effect was observed in pure ammonia at the onset of superionicity, however these results remain too qualitative at present to conclude on the superionic nature of the HT phase VII and further studies will be necessary.

In this work, we have focused our experimental studies on the solid phases with equimolar ammonia/water stoichiometry. Nevertheless, our investigations of the phase diagram of AMH have also revealed the existence of a P-T domain ($P < 10$ GPa, $T < 400$ K) where AMH dehydrates into AHH-II mixed either with a water-rich hydrate (WRH) or ice VII. We note that the WRH phase has been observed in the present work for the first time, always mixed with AHH-II or AMH-VII. Its identification will require further studies. At room temperature, we have shown that the dehydration of AMH occurs during decompression from the mixed DIMA+ $P4/nmm$ or from the phase VIII. We have also determined a phase transition line between AHH-II + WRH phase and the AMH-VII phase.

To confirm the presence of the superionic phase of AMH, it will be necessary to extend the IR spectroscopy measurements to higher temperature to see if a broadening of all the peaks appears and increases with temperature confirming the superionic nature of the HT phase. Simultaneously, AC impedance spectroscopy can be used to measure the resistance of a sample and it is an effective way to distinguish the electron conduction and ion conduction. Performing the AC impedance spectroscopy experiments on AMH at high temperature-pressure can help us to detect the presence of diffusive protons in AMH-VII phase.

References

- [1] Loveday, J. & Nelmes, R. Ammonia monohydrate VI: A hydrogen-bonded molecular alloy. *Physical review letters* **83**, 4329, (1999).
- [2] Griffiths, G. I., Misquitta, A. J., Fortes, A. D. *et al.* High pressure ionic and molecular crystals of ammonia monohydrate within density functional theory. *The Journal of chemical physics* **137**, 064506, (2012).
- [3] Bethkenhagen, M., Cebulla, D., Redmer, R. *et al.* Superionic phases of the 1: 1 water–ammonia mixture. *The Journal of Physical Chemistry A* **119**, 10582-10588, (2015).
- [4] Liu, C., Mafety, A., Queyroux, J. *et al.* Topologically frustrated ionisation in a water-ammonia ice mixture. *Nature communications* **8**, 1065, (2017).

Résumé en français de la thèse

«Experimental investigation of the phase diagram of ammonia monohydrate at high pressure and temperature»

Le but de cette thèse est de déterminer les propriétés du mélange équimolaire eau/ammoniac soumis à des conditions extrêmes de pression et de température. Il y a deux motivations principales sous-jacentes aux recherches sur le système eau/ammoniac. D'un point de vue fondamental et microscopique d'abord, le système ammoniac/eau présente les phases solides les plus simples dans lesquels les molécules sont liées par quatre types de liaisons hydrogène : les liaisons hydrogène homonucléaires O-H...O, N-H...N et les liaisons hydrogène hétéronucléaire O-H...N et N-H...O. Ces liaisons H sont particulièrement importantes de par leur fréquence dans la nature, en particulier dans les macromolécules biologiques telle que l'ADN et les protéines, et car elles sont à l'origine de nombreuses propriétés spécifiques de ces composés. L'étude des glaces pures et de leurs mélanges sous pression, et donc densité, variable permet de sonder les effets de la variation des longueurs et des angles de liaison hydrogène dans des systèmes simples, informations qui peuvent être ensuite utiles pour comprendre les propriétés de matériaux plus complexes.

Ces études sont également d'intérêt majeur pour les sciences de l'Univers. En effet l'eau, l'ammoniac et le méthane sont considérés comme des composants majoritaires des planètes et satellites du système Solaire qui se sont formés dans les régions les plus éloignées du Soleil, tel que les planètes Neptune et Uranus et les satellites Titan, Enceladus et Ganymède, ainsi que les exoplanètes dites « Planète Océan ». Les modèles actuels des intérieurs de Neptune et d'Uranus supposent l'existence d'une couche interne épaisse composée de ces glaces soumises à des conditions extrêmes de pression (20-700 GPa) et de température (2000-6000 K). Il est donc nécessaire de connaître les propriétés physico-chimiques des mélanges de glaces sur une large gamme de pression et de température pour construire des modèles de composition interne réalistes et compatibles avec les informations disponibles telles que le champ magnétique, les moments de gravitation et la composition atmosphérique.

Au cours des dernières décennies, de nombreuses études ont été consacrées aux propriétés des glaces d'eau et d'ammoniac pures à haute pression et à haute température (jusqu'à environ 200 GPa et 2500 K), recherches qui ont révélé un riche polymorphisme. En particulier, plusieurs phases solides « exotiques », telles que l'eau et l'ammoniac superionique, l'ammoniac ionique et la phase symétrique de l'eau ont été mises en évidence à des pressions proches ou au-delà de 100 GPa. En revanche, l'étude des mélanges eau/ammoniac est restée limitée à des pressions modestes, de l'ordre de 10 GPa, et à des températures inférieures à 300 K. Ce manque de connaissances sur les mélanges à haute pression et haute température est d'autant plus dommageable que ces systèmes sont plus pertinents pour l'étude des intérieurs planétaires : ils peuvent être vus comme des « minéraux » des planètes et satellites glacés plus réalistes que les glaces pures.

L'étude du système eau-ammoniac à pression ambiante et basse température ont montré que celui-ci peut cristalliser sous la forme de trois hydrates différents, en fonction de la concentration. Ces trois formes sont le dihydrate d'ammoniac, avec un rapport molaire ammoniac:eau de (1:2) (noté ADH : pour Ammonia DiHydrate), le monohydrate d'ammoniac

de stœchiométrie 1 :1 (noté AMH, pour Ammonia MonoHydrate), et l'hémihydrate d'ammoniac de stœchiométrie 2:1 (noté AHH : pour Ammonia HemiHydrate). Dans cette thèse, nos travaux ont porté essentiellement sur l'étude des propriétés du monohydrate d'ammoniac sous haute pression et haute température. Dans le **Chapitre 1** de ce manuscrit, nous passons en revue les principales motivations scientifiques de ce travail et l'état de l'art concernant les diagrammes de phase haute pression de l'eau, de l'ammoniac et des trois hydrates d'ammoniac. Bien que cette thèse soit centrée sur l'étude du monohydrate d'ammoniac, dans certaines régions de son diagramme de phase, l'AMH n'est pas stable et se déshydrate. Il est donc important de connaître également les diagrammes de phase des autres hydrates et des pôles purs.

Au début de cette thèse, la connaissance des diagrammes de phase des trois hydrates d'ammoniac était limitée à environ 9 GPa et à des températures comprises entre 100 et 300 K. En analysant les résultats expérimentaux (principalement des études de diffraction neutroniques) et théoriques antérieurs, nous avons constaté que de nombreuses questions sur le diagramme de phase de l'AMH persistaient et que certains résultats étaient contradictoires. En particulier, toutes les phases solides de l'AMH observées expérimentalement étaient décrites comme moléculaires, alors que les calculs théoriques basés sur la théorie de la fonctionnelle densité (DFT) prédisaient que l'AMH s'ionise et devient un solide d'hydroxyde d'ammonium NH_4OH ordonné (cristallisant dans le groupe d'espace $P4/nmm$) au-delà d'une pression variant entre 5 et 10 GPa^[1]. Or, dans cette gamme de pression, les études neutroniques décrivent la structure de l'AMH comme un alliage moléculaire désordonné, noté AMH-VI ou DMA pour « disordered molecular alloy »^[2]. Les structures expérimentale et théoriques sont illustrées sur la Figure 1 (gauche et droite, respectivement). Comme on peut le voir, la structure expérimentale de l'AMH-VI est cubique centrée et présente un désordre important : un désordre substitutionnel des molécules d'eau et d'ammoniac, d'une part, chaque site pouvant être occupé par l'une ou l'autre des molécules ; et un désordre positionnel des atomes d'hydrogène, d'autre part, qui résulte directement du précédent. Bien que la structure expérimentale de l'AMH-VI soit très éloignée de celle prédite par les calculs DFT qui est parfaitement ordonnée et de symétrie tétragonale, le désordre important révélé par l'étude neutronique pourrait avoir masqué une ionisation des molécules dans la structure DMA. Il nous est donc apparu important d'étudier la phase VI/ DMA de l'AMH plus en détail et en utilisant des techniques expérimentales tel que les spectroscopies Raman et infrarouge qui sont sensibles aux espèces chimiques. Il était également possible que l'ionisation prédite par la DFT intervient au-delà du domaine de pression précédemment étudié, d'où la nécessité d'étendre l'étude de l'AMH au-delà de 10 GPa. D'autre part, comprendre la nature exacte de la phase DMA n'est pas seulement pertinent pour le monohydrate AMH puisque celle-ci a également été observée à haute pression dans les deux autres hydrates, AHH et ADH. Cette phase pourrait donc être la phase pertinente à haute pression pour n'importe quelle composition du mélange eau/ammoniac, et donc connaître ses propriétés et son domaine de stabilité est important pour les modèles planétaires, sachant que le rapport eau/ammoniac planétaire est mal contraint. Une première étape de ce travail de thèse a donc été de déterminer précisément les propriétés de la phase VI à haute pression et température ambiante.

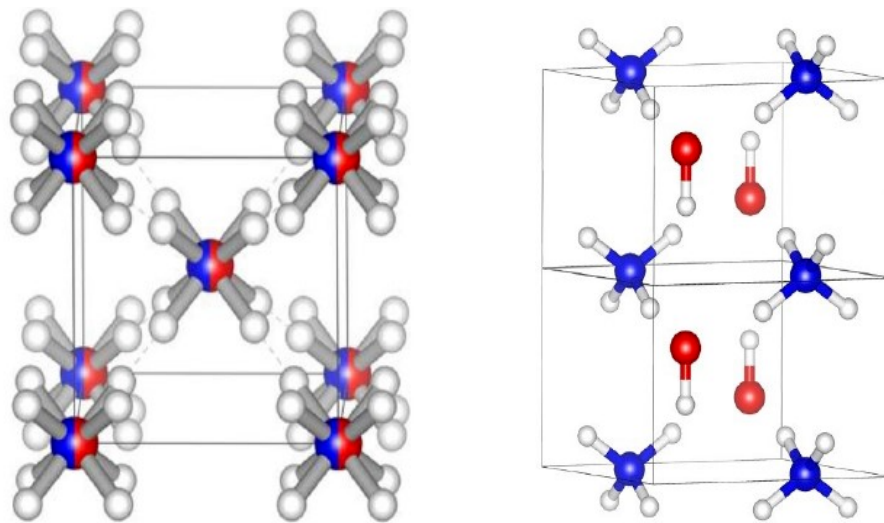


Figure 1 : (gauche) Structure de la phase VI de l'AMH déduite des expériences de diffraction neutronique. Cette phase cubique centrée (groupe d'espace $Im-3m$) est nommée DMA pour Disordered Molecular Alloy. Les molécules d'eau et d'ammoniac présentent un désordre substitutionnel : chaque site est occupé soit par une molécule d'eau ou une molécule d'ammoniac, avec une probabilité $\frac{1}{2}$. Ce désordre est représenté par des sphères bicolorées. Le désordre substitutionnel induit un désordre orientationnel des molécules et donc des atomes d'hydrogène. Sur la figure, nous avons représenté les positions majoritairement occupées par les atomes d'hydrogènes (sphère blanches). (droite) Structure ionique de groupe d'espace $P4/nmm$ prédite par les calculs *ab initio* (DFT). Cette phase ionique est totalement ordonnée et formée uniquement par des ions OH^- et NH_4^+ .

Dans une deuxième étape, nous avons exploré le diagramme de phase de l'AMH à haute pression et haute température ($T > 300$ K), un domaine resté quasiment vierge d'étude avant ce travail. Les questions qui se posaient au départ étaient : dans quelle domaine P-T l'AMH- VI est-elle stable ? l'AMH solide devient-il superionique, c'est-à-dire caractérisé par une forte diffusion protonique, à haute température comme les pôles purs ? Les simulations *ab initio*^[3] prédisent l'existence de cette phase superionique dans l'AMH, qui serait stable dans des conditions (P,T) plus douces (20 GPa – $T > 500$ K) que dans les glaces pures. La présence d'une couche de glace superionique, électriquement conductrice mais non ou faiblement convective, dans le manteau de Neptune et d'Uranus jouerait un rôle important dans la génération des champs magnétiques particuliers de ces planètes^[4,5]. Pouvons-nous faire confiance à ces prévisions théoriques, sachant que la structure de l'AMH solide prédite à basse température par les mêmes méthodes n'est pas en accord avec l'expérience ? Quels sont le domaine de stabilité et les caractéristiques de cette phase superionique si elle existe ?

Le but de cette thèse a donc été d'explorer le diagramme de phase de l'AMH dans un domaine pression-température plus étendu que ce qui a été fait jusqu'à présent, en utilisant diverses méthodes expérimentales pour répondre aux questions décrites ci-dessus.

Les méthodes expérimentales utilisées pour répondre à ces questions sont exposées dans le **Chapitre 2** de ce travail. Les dispositifs hautes pressions, principalement la cellule à enclumes de diamants, la procédure de chargement des échantillons et la métrologie haute pression-haute température associées sont présentés. Les techniques d'analyse, diffraction des rayons X,

spectroscopie Raman et Infrarouge et la diffusion quasi-élastique des neutrons (QENS) utilisées au cours de ce travail sont ensuite décrites. La description du principe des expériences de QENS, qui permettent de sonder la dynamique du proton, est plus développée que les autres car l'extension de cette technique à des pressions de plusieurs GPa est récente et encore peu exploitée.

Dans le **Chapitre 3**, nous présentons nos résultats concernant l'étude de l'AMH à température ambiante et basse température jusqu'à 80 GPa. Ce travail a permis de montrer que dans la phase VI, le monohydrate d'ammoniac se présente comme un état cristallin inhabituel, où les molécules d'eau et d'ammoniac coexistent avec des ions hydroxyle OH^- et ammonium NH_4^+ . Cette coexistence d'espèces ioniques et moléculaires est clairement détectée par nos expériences de spectroscopies Raman et infrarouge. Nos données spectroscopiques et structurales (par DRX et diffraction des neutrons) montrent par ailleurs la coexistence de deux phases dans la majorité des échantillons étudiés : la phase DMA de structure $Im-3m$, précédemment observée dans l'étude neutronique de Loveday et al^[2], et la phase $P4/nmm$, prédite par les calculs DFT^[1]. Dans la plupart des échantillons, la phase $Im-3m$ est majoritaire, et reste stable lors de la compression jusqu'au moins 80 GPa, pour des températures comprises entre 50 et 300 K.

La coexistence entre la phase DMA, décrite comme purement moléculaire, et la phase $P4/nmm$, purement ionique, nous paraissant surprenante, nous avons réalisé des calculs *ab initio* afin de mieux comprendre la nature de la phase DMA. Il est apparu que la phase DMA purement moléculaire n'est pas stable et qu'une partie des molécules s'auto-ionisent spontanément par transfert de proton depuis les molécules d'eau vers les molécules d'ammoniac. La phase DMA est donc en réalité un alliage ionico-moléculaire (voir Figure 2), que nous avons renommé DIMA pour « Disordered Ionico Molecular Alloy ». Cette phase DIMA est en moyenne une phase *bcc* mais l'arrangement des molécules/ions est différent de maille en maille. Cette ionisation partielle est observée à des pressions très douces (7.4 GPa) comparées aux pressions extrêmes requises dans les glaces pures (150 GPa dans la glace d'ammoniac, supérieures à 1.4 TPa dans la glace d'eau). Cette différence de pression montre que le transfert de protons entre l'eau et l'ammoniac demande beaucoup moins d'énergie que le saut de protons entre molécules de même espèce, en accord avec les travaux théoriques antérieurs.

Nos calculs confirment par ailleurs que la structure d'enthalpie la plus basse est bien la phase ordonnée et entièrement ionique $P4/nmm$ dans la plage de pressions 10–60 GPa. Cependant, à part quelques exceptions qui sont discutées plus loin, celle-ci est toujours observée en proportion mineure dans nos expériences. Pour expliquer cela, nous pouvons supposer que le système est piégé dans la phase DIMA et qu'il existe une barrière d'énergie importante entre la phase DIMA et $P4/nmm$. L'ionisation dans la phase DIMA est topologiquement frustrée du fait du désordre substitutionnel, lequel implique une probabilité importante que deux molécules de NH_3 soient premières voisines. Si l'une d'entre elles s'est ionisée par transfert de proton d'une molécule d'eau voisine, l'ionisation de la seconde sera défavorisée par la répulsion Coulombienne. La formation de la phase $P4/nmm$ requière que chaque molécule d'ammoniac soit exclusivement entourée de molécules d'eau, et vice versa, une configuration qui est peu probable, ce qui explique la faible proportion observée de cette phase.

Enfin, nous avons montré qu'en décompressant la phase VI à 300 K, les espèces ioniques disparaissent en deçà de 7.4 GPa. Simultanément, l'AMH se déshydrate et se décompose en

AHH-II et une autre phase qui, pour respecter la stœchiométrie globale, est forcément un hydrate riche en eau (noté WRH pour « Water-Rich Hydrate »). On peut supposer qu'il s'agit d'ADH, partant du principe que seule trois stœchiométries d'hydrate a été observée jusqu'à présent et qu'ADH est la plus riche en eau, mais la structure de WRH n'a pas encore été identifiée. La phase WRH elle-même se décompose vers 4 GPa et au final, on obtient un échantillon de AHH-II et de glace VII d'eau. Les travaux décrits ci-dessus ont fait l'objet d'une publication dans le journal Nature Communications en 2017^[6].

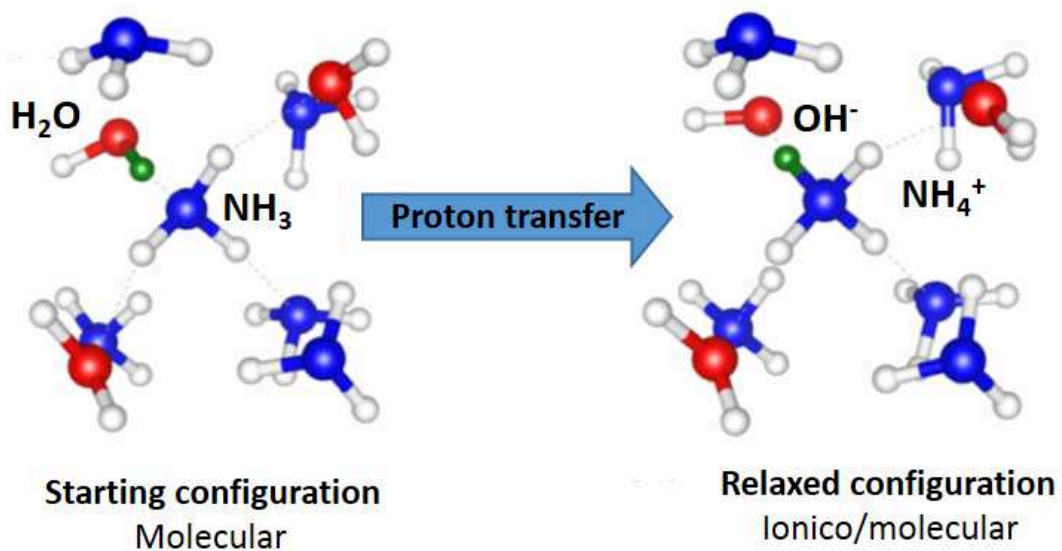


Figure 2 : illustration de l'auto-ionisation partielle de la phase DMA (non stable) sous pression vers la phase DIMA d'après les calculs ab initio de ce travail. La phase DIMA peut être vue comme une phase ionico moléculaire car des molécules d'ammoniac et d'eau coexistent avec les ions OH⁻ et NH₄⁺. L'apparition d'espèces ioniques est due au transfert d'un proton d'une molécule d'eau vers une molécule d'ammoniac. Toutes les molécules d'eau ne peuvent pas céder un proton, le transfert n'est possible que si l'environnement local initial y est favorable.

Une fois la structure de la phase VI comprise et corrigée par rapport à la littérature précédente, nous avons exploré le diagramme de phase à haute température. Dans une première étape, nous avons déterminé la courbe de fusion de l'AMH jusqu'à 675 K et 8.3 GPa. Cette étude est détaillée dans le **Chapitre 4** de cette thèse et a permis de mettre en évidence une nouvelle phase de l'AMH notée AMH-VII. La courbe de fusion de l'AMH a été déterminée par observation visuelle (coexistence fluide/solide) et les différentes phases ont été caractérisées par spectroscopie Raman. En dessous de 324 K, nous avons observé que la fusion n'est pas congruente et que la solidification du fluide conduit à un mélange composé de AHH-II et de glace VII. Les pressions de solidus et de liquidus ont été déterminées à 300 K. Au-dessus de 324 K, l'équilibre solide-fluide apparaît à une valeur unique (P, T) et la fusion devient donc congruente, jusqu'au moins 675 K. Le long de cette courbe de fusion, le fluide est en équilibre avec une nouvelle phase homogène, que nous avons nommé AMH-VII. L'indice de réfraction et le spectre Raman de cette phase sont très proches de ceux du liquide, néanmoins nous avons pu détecter visuellement l'équilibre solide/fluide jusqu'à 675 K et mesuré la pression de fusion dans l'intervalle 324-675 K. La courbe de fusion obtenue dans ce travail diffère notablement de la littérature en deçà de 400 K, et nos observations nous conduisent à conclure que les études

précédentes ont confondu la transition liquide-solide avec la ligne de transition entre la phase VII et la phase démixée AHH-II + WRH. Nous avons comparé la courbe de fusion de l'AMH-VII avec celles de l'ammoniac et de l'eau pure, en utilisant des unités réduites afin de mettre ces courbes sur la même échelle de densité. Cette comparaison révèle que la courbe de fusion de l'AMH suit une pente similaire à celle de l'ammoniac pur, suggérant une proximité plus forte entre AMH-VII et la phase III de l'ammoniac sur le plan des interactions intermoléculaires.

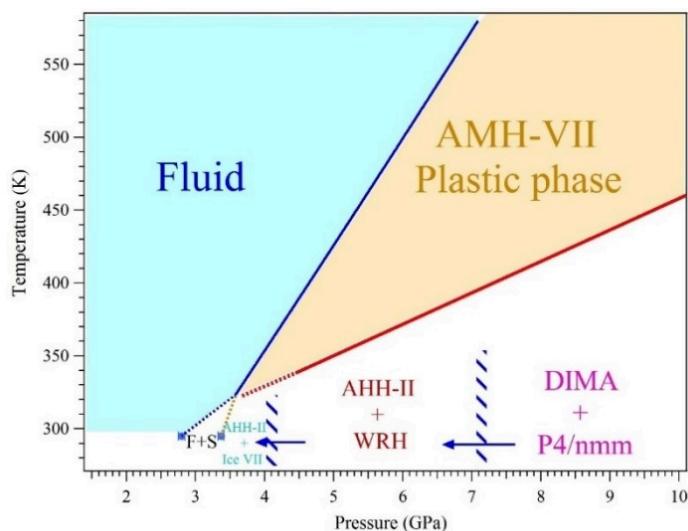


Figure 3 : Diagramme de phase de l'AMH dans le domaine des basses pressions ($P < 10$ GPa). La courbe de fusion devient congruente au-dessus de 324 K. A haute pression et haute température, une nouvelle phase homogène de l'AMH notée phase VII a été découverte. Une zone de deshydratation de l'AMH est observée à basse pression et basse température : la présence de l'hydrate d'ammoniac riche en eau (noté WRH) n'est observable qu'en décomprimant la phase VI (DIMA + P4/nmm). La deshydratation totale en AHH-II + ice VII est observée en dessous de 4 GPa à 300 K. Une fusion non congruente est alors visible (solidus et liquidus).

Après avoir mis en évidence l'existence de la phase VII, nous avons caractérisé ses propriétés vibrationnelles, structurales et les propriétés dynamiques du proton dans cette phase dans le domaine de pression inférieur à 10 GPa. Ces études sont détaillées dans le **Chapitre 5** de cette thèse. Le diagramme de phase de l'AMH jusqu'à 10 GPa – 700 K a été exploré par spectroscopie Raman et par diffraction des rayons X afin de déterminer le domaine de stabilité de la phase VII. La ligne de transition entre AMH-VII et la phase démixée AHH-II + WRH a été établie à haute température, ce qui a permis de délimiter le domaine de deshydratation de l'AMH comme représenté sur la Figure 3. Par diffraction des rayons X, nous avons démontré que la structure de la phase AMH-VII était une phase *bcc* avec le groupe d'espace *Im-3m*. Les spectres Raman montrent que des espèces ioniques peuvent également être présentes dans cette phase dès les basses pressions. La différence structurale entre la phase DIMA et la phase VII est révélée par la texture des échantillons, et en particulier la largeur des pics de diffraction : ils sont larges dans la phase DIMA et deviennent très fin dans la phase VII. Sachant que la largeur des pics de diffraction dans la phase DIMA provient des fluctuations du paramètre de maille, elles-mêmes liées au caractère local et partiel de l'ionisation qui fait fluctuer les distances entre molécules et ions, nous pouvons supposer que l'arrangement des atomes d'hydrogène dans la phase VII doit être différent de celui de la phase DIMA et plus isotrope. Afin d'obtenir un éclairage sur la dynamique des protons dans la phase VII, nous avons réalisé des mesures de diffusion quasi élastique incohérente des neutrons (QENS) sur un échantillon d'AMH partiellement deutéré ($\text{NH}_3 \cdot \text{D}_2\text{O}$) sur la plage 6.3-8.2 GPa et 473-523 K. Malgré la faible

intensité du signal quasi élastique mesuré, nous avons pu montrer que celui-ci est compatible avec une diffusion rotationnelle des atomes d'hydrogène des molécules d'ammoniac. Le coefficient de diffusion rotationnel D_R est, dans l'incertitude, constant ($D_R=0.7(2)$ meV) sur la gamme P-T de mesure. Ces résultats montrent que la phase AMH-VII est une phase plastique comme la phase III de l'ammoniac.

Le diagramme de phase de l'AMH a ensuite été étudié jusqu'à 760 K et 70 GPa et les résultats sont présentés dans le **Chapitre 6**. Etablir le domaine de stabilité thermodynamique des différentes phases observées au cours de cette étude s'est révélée une tâche complexe, du fait des fortes métastabilités de la plupart des formes solides de l'AMH. Nous avons mis en évidence l'existence d'une nouvelle phase de l'AMH nommée AMH-VIII dans un domaine de pression et de température modérée (7-18 GPa ; $T < 600$ K) (cf Figure 4). Nous avons montré que l'AMH-VIII ne pouvait être formée qu'à haute température ($T > 400$ K) mais qu'elle était ensuite récupérable à température ambiante. Nous avons montré que le refroidissement de la phase VII conduisait toujours à la phase VIII dans le domaine 7-18 GPa et que cette transition VII-VIII était réversible. La phase VIII est donc la phase stable entre 7 et 18 GPa et la phase VI, mélange de la phase DIMA et de la phase $P4/nmm$, observées initialement (après chargement de l'échantillon) dans ce domaine P-T est métastable. Nos points expérimentaux (P,T) de la transition VII/VIII peuvent être ajustés par une équation de type Simon-Glatzel. Afin de déterminer la structure de la phase VIII, nous avons fait croître un monocristal de cette phase et l'avons étudié par DRX. Bien que la structure complète n'ait pu être résolue, les clichés de diffraction sont indexables avec une maille orthorhombique et les extinctions systématiques compatibles avec le groupe d'espace $Cmca$. Le volume de la maille suggère un contenu de 24 molécules par maille, compte tenu du volume moléculaire mesuré dans la phase DIMA. Par ailleurs, les spectres Raman de la phase VIII sont compatibles avec la coexistence de molécules et d'ions. Nous avons aussi observé que la phase VIII est obtenue en chauffant la phase $P4/nmm$ lorsque cette dernière est obtenue quasi pure (par contre la transition inverse n'a jamais été observée). Toutes ces observations nous conduisent à penser qu'AMH-VIII est une phase ionico-moléculaire, non plastique et sans ou peu de désordre substitutionnel.

Au-dessus de 18 GPa, la phase VIII n'est jamais observée lors du refroidissement de la phase VII. De fait, celui-ci conduit à la phase DIMA initiale, mais pure, c'est-à-dire sans la présence de la phase ionique $P4/nmm$. La principale signature de cette transition est l'élargissement soudain des pics de Bragg dans la phase DIMA, tel que discuté ci-dessus pour la transition inverse. Par contre nous n'avons pu mettre en évidence un saut de volume à la transition. Au-delà de 30 GPa, l'élargissement des pics de Bragg n'est plus détecté, ce qui peut être dû à l'apparition de gradients de pression dans l'échantillon qui élargissent artificiellement les pics de Bragg et masque la transition.

Comme discuté plus haut, il est probable que la diminution de largeur des pics dans la phase VII comparé à la phase DIMA soit la conséquence de degrés de liberté supplémentaires des atomes d'hydrogène dans la phase VII. Si ces degrés de liberté sont uniquement de type rotationnel, on obtient une phase plastique comme observé à basse pression. A haute pression et température, les atomes d'hydrogène peuvent également acquérir un degré de liberté translationnel, i.e. sauter d'une molécule/ion à un(e) autre, ce qui conduirait à une phase superionique. Nos expériences XRD, peu sensibles aux atomes d'H, ne permettent pas de distinguer une phase plastique d'une phase superionique, d'autant plus qu'aucun changement de structure du réseau O/N n'est observé. Nous avons donc étudié la transition VII/DIMA par

spectroscopie infrarouge. A 40 et 70 GPa, nous avons détecté une augmentation globale de l'absorption infrarouge et un élargissement des bandes d'absorption au-delà de 625(25) K, soit légèrement en-dessous de l'extrapolation de la ligne de transition DIMA→VII déterminée par DRX. Des observations similaires ont été faites dans l'ammoniac pur à la transition entre solide moléculaire et solide superionique : l'augmentation d'absorption est associée à la création de nouvelles espèces ioniques, tandis que l'élargissement des bandes d'absorption reflète un temps de vie plus court des espèces. Cependant, la différence entre les spectre IR des phases basse et haute température est moins évidente dans l'AMH que dans l'ammoniac car les bandes IR sont déjà très larges dans la phase basse température du fait de l'existence d'ion et d'un désordre important.

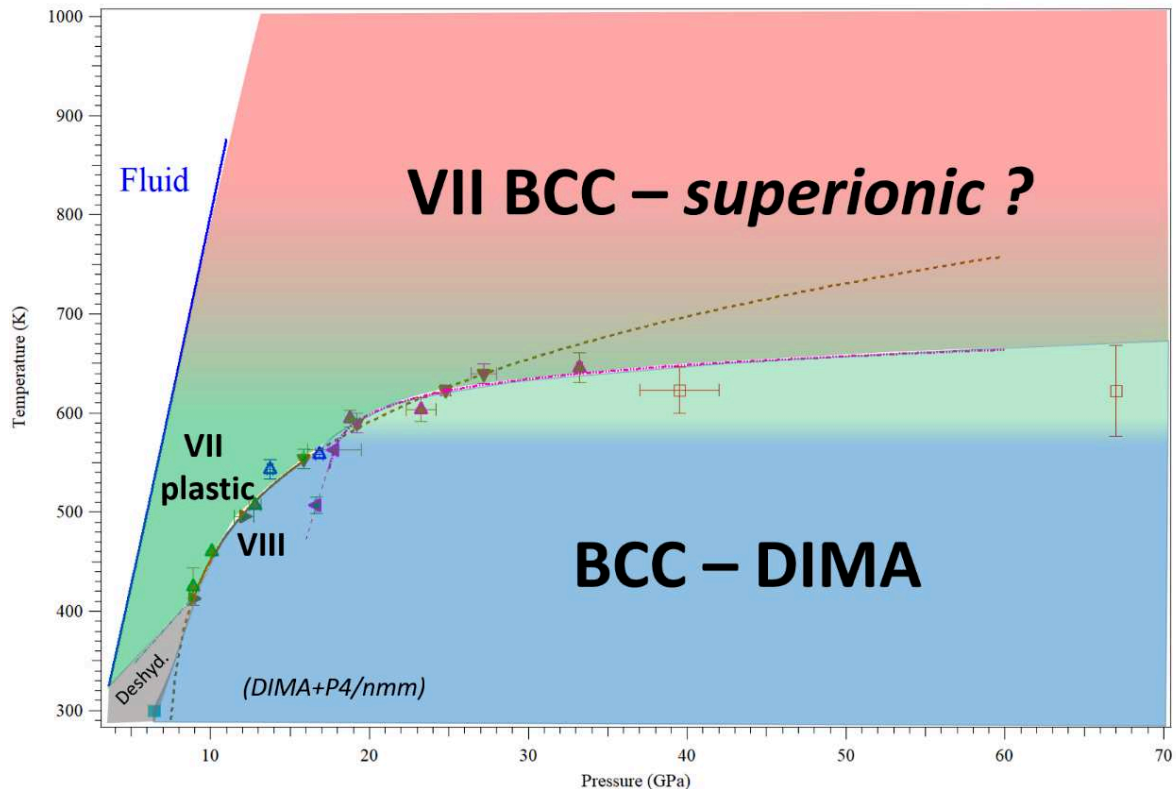


Figure 4 : Diagramme de phase de l'AMH déterminé au cours de cette thèse. Excepté le point de transition de phase entre la phase DIMA et la phase VIII à haute température (zone bleue vers 16 GPa – 500 K), tous les points expérimentaux délimitant la transition vers la phase VII sont représentés par les différents symboles. Les différentes couleurs représentent la nature du désordre associée aux atomes d'hydrogène dans les différentes phases. En bleu : désordre orientationnel statique. En vert : désordre orientationnel dynamique (plastique). En rouge : désordre dynamique translationnel et rotationnel. Le dégradé de couleur à haute pression bleu vers vert vers rouge montre que la localisation exacte n'a pas pu être déterminée dans ce travail.

En **conclusion**, le diagramme de phase final de l'AMH est représenté sur la Figure 4. Comparé au diagramme de phase initial, limité à 9 GPa et 400K, nous avons pu mettre en évidence deux nouvelles phases de l'AMH: la phase VII et la phase VIII. Dans la zone de deshydratation de l'AMH, nous avons également mis en évidence un nouvel hydrate d'ammoniac riche en eau dont la structure reste à déterminer. Nous avons montré que les phases stables de l'AMH (AMH-VII, AMH-VIII et la phase DIMA) sont toutes des phases ionico-moléculaires. La nature ionico-moléculaire de la phase *bcc* DIMA n'avait pas été comprise dans les études précédentes de

diffraction neutronique. Dans notre travail, en couplant des études de diffraction X/neutrons, des expériences de spectroscopie Raman et infrarouge avec des calculs *ab initio*, nous avons démontré cette coexistence et pu expliquer l'apparente contradiction qui existait entre les calculs et les précédentes expériences. Comme on peut le voir, le diagramme de phase est dominé par la présence de phases *bcc* (phase VII ou phase DIMA) et les différences entre ces deux phases sont dues aux atomes d'hydrogènes. Dans la phase DIMA, nous avons montré que les atomes d'hydrogène présentaient un désordre orientationnel statique dû au désordre substitutionnel des atomes d'azote (N) et d'oxygènes et la coexistence molécule/ion. Dans la phase VII à basse pression, nous avons pu démontrer la présence d'un désordre orientationnel dynamique des atomes hydrogène conduisant à définir la phase VII comme plastique dans cette zone. La nature, simplement plastique ou superionique de la phase VII, au-dessus de 650 K et 20 GPa reste à démontrer expérimentalement. Nous avons pu obtenir quelques éléments en faveur de cette superionicité dans la phase VII (domaine P,T compatible avec les calculs, augmentation du nombre d'espèces ioniques, réarrangement des atomes de N et O vers une structure *bcc* parfaite) mais pas de preuves expérimentales directes. De futures expériences (mesures de conductivité ionique, mesures IR à plus haute température) seront nécessaires pour en avoir la preuve directe expérimentale.

Bibliographie

- [1]Griffiths, G. I., Misquitta, A. J., Fortes, A. D. *et al.* High pressure ionic and molecular crystals of ammonia monohydrate within density functional theory. *The Journal of chemical physics* **137**, 064506, (2012).
- [2]Loveday, J. & Nelmes, R. Ammonia monohydrate VI: A hydrogen-bonded molecular alloy. *Physical review letters* **83**, 4329, (1999).
- [3]Bethkenhagen, M., Cebulla, D., Redmer, R. *et al.* Superionic phases of the 1: 1 water–ammonia mixture. *The Journal of Physical Chemistry A* **119**, 10582-10588, (2015).
- [4]Redmer, R., Mattsson, T. R., Nettelmann, N. *et al.* The phase diagram of water and the magnetic fields of Uranus and Neptune. *Icarus* **211**, 798-803, (2011).
- [5]Stanley, S. & Bloxham, J. Convective-region geometry as the cause of Uranus' and Neptune's unusual magnetic fields. *Nature* **428**, 151, (2004).
- [6]Liu, C., Mafety, A., Queyroux, J. *et al.* Topologically frustrated ionisation in a water-ammonia ice mixture. *Nature communications* **8**, 1065, (2017).